Studies of Dye-Titania Interactions in Dye-sensitised Solar Cells

Christopher Peter Kershaw

Thesis submitted in the fulfilment of the requirements for the degree of Doctor of Philosophy

Materials Engineering

College of Engineering

Swansea University

March 2020

Papers and conference presentations associated with this thesis

"Novel benzothiazole half-squaraines: model chromophores to study dye–TiO_2 interactions in dye-sensitized solar cells" Peter J. Holliman, **Christopher P. Kershaw**, Eurig W. Jones, Diana Meza-Rojas, Anthony Lewis, James McGettrick, Dawn Geatches, Kakali Sen,Sebastian Metz, Graham J. Tizzardd and Simon J. Coles, Journal of Materials Chemistry A, 2020, DOI: 10.1039/D0TA06016J

"A perspective on using experiment and theory to identify design principles in dye-sensitized solar cells" Peter J. Holliman, **Christopher Kershaw**, Arthur Connell, Eurig W. Jones, Robert Hobbs, Rosie Anthony, Leo Furnell, James McGettrick, Dawn Geatches & Sebastian Metz, Science and Technology of Advanced Materials, 19:1, 599-612, DOI: 10.1080/14686996.2018.1492858

"Metal Oxide Oxidation Catalysts as Scaffolds for Perovskite Solar Cells" Peter J. Holliman, Arthur Connell, Eurig W. Jones and **Christopher P. Kershaw**, Materials 2020, 13, 949

"Hybrid Al_2O_3-$CH_3NH_3PbI_3$ Perovskites towards Avoiding Toxic Solvents" Eurig Wyn Jones, Peter James Holliman, Leon Bowen, Arthur Connell, **Christopher Kershaw** and Diana Elizabeth Meza-Rojas, Materials 2020, 13, 243

"Quantitative chemical analysis of perovskite deposition using spin coating" Peter J. Holliman, Eurig W. Jones, Robert J. Hobbs, Arthur Connell, Leo Furnell, Rosie Anthony, **Christopher P. Kershaw**, Materials Letters: X 2 (2019) 100011

"Low cost triazatruxene hole transporting material for >20% efficient perovskite solar cells" Arthur Connell, Zhiping Wang, Yen-Hung Lin, Peter C. Greenwood, Alan A. Wiles, Eurig W. Jones, Leo Furnell, Rosie Anthony, **Christopher P. Kershaw**, Graeme Cooke, Henry J. Snaith and Peter J. Holliman, *J. Mater. Chem. C*, 2019,7, 5235-5243

"*Surface engineering dye solar cell devices by self-assembly."* Peter J. Holliman, **Christopher Kershaw**, Diana Meza-rojas, Rosie Anthony, Eurig Jones, Leo Furnell, Arthur Connell, Paper presented at PVSAT-15, 10-12 April 2019, Warwick University.

"*Low cost, scalable, hole transport materials for photovoltaic devices with improved solubility in green solvents for photovoltaic devices."* Arthur Connell, Zhiping Wang, - Alan A. Wiles, Eurig W. Jones, Leo Furnell, Rosie Anthony, **Christopher P. Kershaw**,

Graeme Cooke, Henry J. Snaith, Peter J. Holliman, Paper presented at PVSAT-15, 10-12 April 2019, Warwick University.

"Digital Imaging to Simultaneously Study Device Lifetimes of Multiple Dye-sensitized Solar Cells" Leo Furnell, Peter J. Holliman, Arthur Connell, Eurig W. Jones, Robert Hobbs, **Christopher P. Kershaw**, Rosie Anthony, Justin Searle, Trystan Watson and James McGettrick, Sustainable Energy Fuels, 2017,1, 362-370

"Studies of Dye Processing, Surface Interactions and Lifetimes for DSC Devices." P.J. Holliman, L. Furnell, R. Anthony, A. Connell, **C. Kershaw**, E. Jones, Paper presented at Dyenamo - DSSC strikes back conference, 16-17 October 2017, Uppsala, Sweden.

"Rapid processing and lifetime testing of dye-sensitized solar cells." Peter Holliman, Leo Furnell, Rosie Anthony, Arthur Connell, **Chris Kershaw**, Eurig Jones, Robert Hobbs and Alberto Fattori, Paper presented at Hybrid and Organic Photovoltaics conference - HOPV16, 28 June – 1 July 2016, Swansea, UK.

"Understanding and controlling electron transfer between sensitizer and electrolyte." **Chris Kershaw**, Peter Holliman, Leo Furnell, Rosie Anthony, Arthur Connell, Eurig Jones, Paper presented at PVSAT-13, 5-7 April 2017, Bangor.

"Towards low cost printable perovskite solar cells" Eurig W. Jones, Peter J. Holliman, Robert J. Hobbs, Arthur Connell, Leo Furnell, **Christopher P. Kershaw**, Rosie L. Anthony, Sanjay Ghosh, Cameron Pleydell-Pearce, Paper in Conf. Proceedings - PVSAT-12, 6-8 April 2016, Liverpool.

"Has my dye-sensitized solar cell dyed or died?" Peter Holliman, Leo Furnell, Sanjay Ghosh, Arthur Connell, **Chris Kershaw**, Eurig Jones, Robert Hobbs, Rosie Anthony, Alberto Fattori, Paper in Conf. Proceedings - PVSAT-12, 6-8 April 2016, Liverpool.

"Multiple linker Half-squarylium Dyes for Dye-Sensitized Solar Cells; Are Two Linkers Better than One?" A. Connell, P.J. Holliman, E.W. Jones, L. Furnell, **C. Kershaw**, M.L. Davies, C.D. Gwenin, M.B. Pitak, S.J. Coles, G. Cooke, *Journal of Materials Chemistry A*, 2015, **3**, 2883-2894.

Abstract

This work details the synthesis of several bespoke materials to derivatise the surface of titania (TiO_2) in order to obtain greater understanding of the sensitisation process in dye-sensitised solar cells and how this can influence device performance. In particular, this work has combined synthetic (dye synthesis), experimental (AR-XPS) and theoretical experiments (computer modelling) in order to investigate the self-assembly of organic dyes onto titania surfaces in dye-sensitised solar cell (DSC) devices.

To test the dyes and other materials in this thesis both liquid and solid-state dye-sensitised solar devices were made. The standard liquid DSC device utilised TEC 8 glass (3 cm x 1.5 cm) for both the photo and counter electrode. On the photoelectrode a mesoporous TiO_2 layer is deposited and sensitised with N719 dye. The counter electrode is coated with a thin layer of platinum PT-1 paste (GreatCellsolar). The two electrodes are bound together by melting 20 μm surlyn and a standard triiodide electrolyte is injected to the cell and the cell sealed. With this method we have managed to achieve 6.5 % using N719 dye.

Solid-state dye-sensitised solar cell (ssDSC) devices we made using TEC 7 glass (2.8 cm^2). Onto the glass a compact layer of TiO_2 has been deposited via spray coating, thereafter a thin layer of mesoporous TiO_2 is spin coated and sensitised overnight in a dye bath. After which, a thin layer of Spiro-OMeTAD is deposited via spin coating, after which Au is deposited under vacuum. With this method 4.0 % has been achieved using LEG4 dye.

This thesis reports the first synthesis of ten novel half-squaraine (HfSQ) dyes, five containing a benzothiazole backbone and another five identical dyes with a dimethyl-derivatised carbon. These new dyes have been purified using various preparative (column and flash) chromatography. Once purified the dyes have been analysed using nuclear magnetic resonance (NMR), attenuated total reflectance infra-red (ATR-IR), ultraviolet-visible spectroscopy (UV-Vis) and mass spectrometry. These novel dye materials have then been used to derivatise the titania surface in DSC devices. The dyes have been designed so that a sulphur heteroatom can be used as an atomic probe of the dye-TiO_2 interface in order to study surface coverage, dye orientation and dye-electrolyte interactions in dye-sensitized solar cell (DSC) devices. X-ray single crystal structural and opto-electronic data have also been correlated with density functional

theory/computer modelling to better understand the widely reported but poorly understood influence of S heteroatoms on dye photochemistry, DSC device performance and lifetime. To the best of our knowledge, for the first time, the S heteroatom in the dyes has been used as a molecular probe along with angle-resolved X-ray photoelectron (ARXPS) data to study how the dye-TiO_2 orientation varies with the position of the carboxylate linker on the dye periphery.

In further work, a one-step synthesis has been used to link two dye-sensitized solar cell (DSC) dyes together through an anhydride moiety. The dyes we have attempted to combine are triphenylamine dye "Yellow dye" to another Yellow dye and squaraine dye SQ2 to other moieties such as Chenodeoxycholic acid and stearic acid. To the best of our knowledge, this is also the first time this has been attempted in DSC dyes. The resulting anhydride precursor has been used to self-assemble the two dyes onto TiO_2 surfaces in a controlled manner. Hence, this represents a brand-new method of sensitising two dyes, in a single sorption process; providing a new method to control dye-sorption kinetics, dye loading and surface organisation. When two dyes are introduced to the titania surface at the same time it is possible to control the positions of the two dyes without the need of bulky co-sorbents (e.g. CDCA) to supress dye aggregation. This one-step synthesis method was applied to combine two different dye materials into one anhydride moiety. Attempts have been made to combine SQ2 dye to co-adsorbent CDCA and SQ2 dye to stearic acid. The photo-physical properties of the anhydride and its precursor dyes have been studied (via UV-Vis, ATR-IR NMR and tested in ssDSC devices) and compared highlighting the potential of this new method for co-sensitisation.

Contents

Declarations 8
Acknowledgements 9
Abbreviations 10
Area of study 12
1 Introduction 17
1.1 Shockley-Queisser limit 21
1.1.1 Entropy and thermal losses 21
1.1.2 Recombination 22
1.1.3 Bandgap losses 23
1.2 Multi-junction devices 24
1.3 Current solar technologies 25
1.3.1 1st, 2nd and 3rd generation photovoltaic materials 25
1.4 Dye-sensitized solar cells (DSC devices) 30
1.4.1 History and concept 30
1.4.2 Light harvesting dyes/sensitizers 33
1.4.3 Dying methods 46
1.4.4 Metal oxide semi-conductor scaffolds 47
1.4.5 The role of electrolytes 49
2 Experimental 53
2.1 Materials and General Techniques 53
2.2 Angle-resolved X-ray photoelectron spectroscopy (ARXPS) 53
2.3 X-ray crystallography 53
2.4 Dye synthesis 54
2.5 DFT Modelling procedure 77
2.5.1 Computational details 77
2.5.2 Anatase (1 0 1) TiO_2 Surface 78
2.6 Dye-sensitised solar cell fabrication 79
2.6.1 Liquid dye-sensitised solar cells 79
2.6.2 Solid state dye-sensitised solar cell (ssDSC) device manufacture 83
2.6.3 Device testing 85
2.6.4 Experiment 1 (Doping with FK209) 88
2.6.5 Experiment 2 (Effect of the “blocking” layer) 88
2.6.6 Experiment 3 (Optimisation of TiO_2 thickness) 88

2.6.7 Experiment 4 (Effect of $TiCl_4$ treatment) 89
2.6.8 Experiment 5 (Effect of dyeing time) 89
2.6.9 Experiment 6 (Effect of HTM thickness on ssDSC device performance) 89
2.6.10 Experiment 7 (Testing of novel materials for ssDSC devices) 89
2.6.11 Experiment 8 (Lifetime testing of ssDSC devices) 90
2.7 Dye loading 90
3 Novel Benzothiazole Half-Squaraines: Model Chromophores to Study Dye-TiO_2 Interactions in Dye-Sensitized Solar Cells 91
3.1 Introduction 91
3.1.1 X-ray Photoelectron spectroscopy (XPS) 94
3.1.2 Angle resolved X-ray Photoelectron spectroscopy (ARXPS) 94
3.2 Results and discussion 96
3.2.1 Dye synthesis 96
3.2.2 Counter Ion effects on DSC performance 104
3.2.3 Spectroscopic analysis 106
3.2.4 Dye orientation studies (DFT modelling) 110
3.2.5 Angle-resolved X-ray photoelectron spectroscopy (ARXPS) 113
3.2.6 ARXPS analysis of dyes 119
3.2.7 X-ray crystallography 135
3.2.8 Device data 137
4 Developing solid state dye-sensitised solar cell (ssDSC) devices for the testing of novel dyes and other materials 145
4.1 Introduction 145
4.1.1 Aim of this chapter 146
4.2 Results and discussion 147
4.2.1 Deposition of TiO_2 "blocking layer" 147
4.2.2 $TiCl_4$ Treatment 147
4.2.3 Mesoporous TiO_2 semi-conductors in ssDSC devices 148
4.2.4 Manufacturing ssDSC devices 149
4.2.5 Developing the ssDSC devices 152
5 Anhydrides 174
5.1 Introduction 174
5.1.1 Anhydrides 176
5.1.2 Co-sensitisation 176
5.2 Results and discussion 180

5.2.1 Dye synthesis 180
5.2.2 Device testing 188
6 Conclusions and Future work 190
6.1 Chapter 3 190
6.2 Chapter 4 191
6.3 Chapter 5 193
7 References 196
8 Appendix 213
8.1 NMR Spectra 213
8.2 Mass spectrometry 235
8.3 ATR-IR spectroscopy 254
8.4 UV-visible spectroscopy 264
..... 265
8.5 Crystal data 269
8.6 Profilometry 271
8.7 Dye injection measurements 276

Declarations

This work has not previously been accepted in substance for any degree and is not being concurrently submitted in candidature for any degree.

Signed.....  .....
.....

30th March 2020

Date.....
.....

This thesis is the result of my own investigations, except where otherwise stated. Other sources are acknowledged by footnotes giving explicit references.A bibliography is appended.

Signed..... 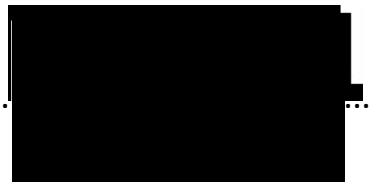 .....
.....

30th March 2020

Date.....
.....

I hereby give my consent for my work, if relevant and accepted, to be available for photocopying and for inter-library loans **after expiry of a bar on access approved by the University.**


.....

30th March 2020

Date.....
.....

Acknowledgements

I would like to thank Dr Peter Holliman, the NRN, GCell and the Welsh government for giving me the opportunity to undertake this PhD. I wish to thank my supervisors; Prof. Peter Holliman and Dr Chris Gwenin (BU) for their constant support and guidance throughout the project. The journey through this work has had its ups and downs especially during the move from Bangor to Swansea University but I could not have asked for more supportive supervisors.

I wish to thank Dr James McGettrick (Swansea University – SPECIFIC) for helping me run X-ray photoelectron spectroscopy, Dr Dawn Geatches, Dr Sebastian Metz and Dr Kakali Sen (STFC) for running DFT and other computer calculations on many of my materials. Thank you to the Dr Joel Loveridge for training me to use the Swansea NMR spectrometer and Swansea mass spectrometry service for running mass spectrometry on my samples. Thank you to Dr Alan Wiles (Glasgow University) for running electron injection measurements on my dyes. Thank you to Dr Graham J. Tizzardd and Dr Simon J. Coles (UK National Crystalography Service, University of Southampton) for running crystalography on my dyes.

My thanks go out to the P. J. Holliman research group (Dr Arthur Connell, Dr Eurig Jones, Dr Robert. J. Hobbs, Dr Diana Meza-Rojas, Dr Anthony Lewis, Dr Leo Furnell, Dr Rosie Anthony). My appreciation goes out to all the technicians at both Bangor and Swansea University, Dr David Hughes (Bangor) and Ian Matthews (Swansea) as they have been a continuous help throughout my studies.

I want to thank my family for their continued support and guidance. My parents Lynn and David have believed in me and supported me at every opportunity, and I hope to live up to their example. My brother Ciarán is someone I can rely on and has grown up to be a man I will always admire.

Thank you to my girlfriend Rebecca Hudson, for all her love and support throughout.

Abbreviations

Abs	-	Absorbance
AO	-	Dyesol® 18NR Active Opaque Titania paste
ARXPS	-	Angle resolved X-ray photoelectron spectroscopy
a-Si	-	Amorphous Silicon
ATR-IR	-	Attenuated total reflectance Infra-red spectroscopy
CB	-	Conduction band
CDCA	-	Chenodeoxycholic acid
CNT's	-	Carbon nanotubes
c-Si	-	Crystalline Silicon
DFT	-	Density functional theory
DMSO	-	Dimethyl sulfoxide
DSC	-	Dye-sensitised solar cell
ESI	-	Electrospray ionisation
eV	-	Electron volt
FF	-	Fill factor
FID	-	Flame ionisation detector
FTIR	-	Fourier transform infra-red spectroscopy
FTO	-	Fluoride-doped tin oxide
GCMS	-	Gas chromatography/ Mass spectrometry
HfSQ	-	Half squaraine dyes
HOMO	-	Highest occupied molecular orbital
HTM	-	Hole transport material
IPCE	-	Incident photon conversion efficiency
J_{sc}	-	Short circuit current density
K_d	-	Partition co-efficient
KWh	-	kilowatt-hour
LCOE	-	Levelized cost of energy
LUMO	-	Lowest unoccupied molecular orbital
Mesoporous	-	A material that contains pores between 2 and 50 nm

Mtoe	-	Million Tonnes of Oil Equivalent
NIR	-	Near infrared
OPV	-	Organic photovoltaics
PES	-	Photoelectron spectroscopy
PID	-	Photoionisation detector
PSC	-	Perovskite solar cell
PV	-	Photovoltaics
RoHS	-	Restriction of Hazardous Substances
sHfSQ	-	Sulphur half squaraine dyes
ssDSC	-	Solid state dye-sensitised solar cell
SQ	-	Shockley-Queisser limit
TBA^+	-	Tetrabutylammonium ion
TCO	-	Transparent conductive oxide
TPA	-	Triphenylamine
TWh	-	Terawatt-hour
UV-Vis	-	Ultra-violet visible spectroscopy
VOC	-	Volatile organic compound
VB	-	Valence band
V_{oc}	-	Open circuit voltage
XPS	-	X-ray photoelectron spectroscopy

Area of study

Dye-sensitised solar cells (DSC devices) are a technology which comes close to replicating natural photosynthesis.[1] Like chlorophyll in leaves DSC devices use a dye to absorb light and convert the light into a useable form of energy. DSC devices have lower efficiencies (14.7 %)[1] when compared with other photovoltaic devices (> 20 % for perovskites)[2] however this is often offset by low cost ($\$0.5/W_{peak}$)[3] when compared to other PV technologies. The efficiencies of DSC's have been increasing recently, with a recent high of 14.7%.[1] This thesis aims to study the DSC photoelectrode surface to understand and then control how it interfaces with the rest of the device. Several bespoke dye materials have been synthesised with the aim of studying how they self-assemble to titania (TiO_2) surfaces. By feeding back new knowledge into designing new bespoke actives, the aim is that greater control will be possible during the dye sensitization process, thus allowing better optimisation of the TiO_2 interface for DSC applications.

The general operation of a liquid based DSC device is as follows: a photon emitted from the sun passes through glass or plastic substrate hitting a photosensitive dye which is adsorbed onto a mesoporous oxide (usually ZnO or TiO_2).[4] If the dye absorbs the photon, an electron from the dye can be promoted from the dye HOMO (highest occupied molecular orbital) to the dye LUMO (lowest unoccupied molecular orbital). The excited electron can then be injected into the conduction band of the mesoporous oxide layer (known as the working electrode or photoanode)[4]. The electron passes from the working electrode to a conducting oxide (TCO) coating on the glass or plastic substrate. From here the electron flows to a load in the circuit. Then the oxidised photosensitive dye is restored to its ground state by electron injection from iodide in the electrolyte (mediator). The triiodide in the electrolyte diffuses to the platinum coated counter electrode. Here the triiodide is reduced back to iodide, completing the cycle (see **Figure 0.1**).[5]

Several commercial companies have been working on DSC device technology (e.g. G24[5], Exeger[6], GreatCellSolar[7], Solaronix[8]). DSC devices have been used in small electronic items such as backpacks and keypads (GCell)[5] and more importantly they have been used in buildings such as the SwissTech Convention centre (made by Solaronix).[8] Although initially appearing unfavourable (after all, the larger the

absorption range the more photons that can be absorbed), the tuneable absorption of DSC devices can offer a big advantage for DSC devices. Though silicon cells can absorb more wavelengths, most are not optimised meaning a lot of energy is wasted. This is because the band gap of silicon is fixed and therefore the voltage is not optimised. In DSC devices it is possible to co-sensitise many dyes with differing bandgaps allowing the device to absorb more photons with fewer losses (see **Figure 0.2**), though this is not without its difficulties and the band-gaps of the dyes must be carefully selected in order to avoid further recombination pathways. Hence, later in this thesis co-sensitisation with bespoke dyes synthesized in this work will be explored.

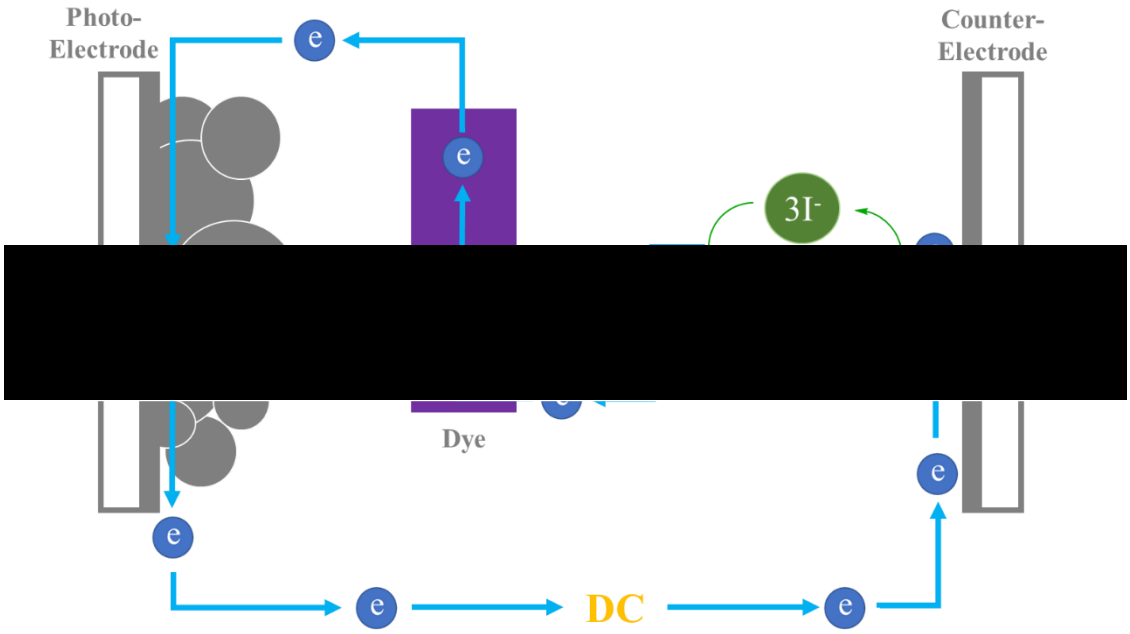

Figure 0.1 - Schematic of DSC device showing key steps for device operation. Figure adapted from GCell[5]

Other chapters in this thesis describe the targeted synthesis of bespoke materials that self-assemble in such a way that gives us a deeper understanding of the way in which dye molecules self-organise themselves on the titania surface during sensitisation. This inevitably has important effects on the subsequent device processes that take place

during DSC device operation (i.e. electron injection, dye regeneration, recombination etc).

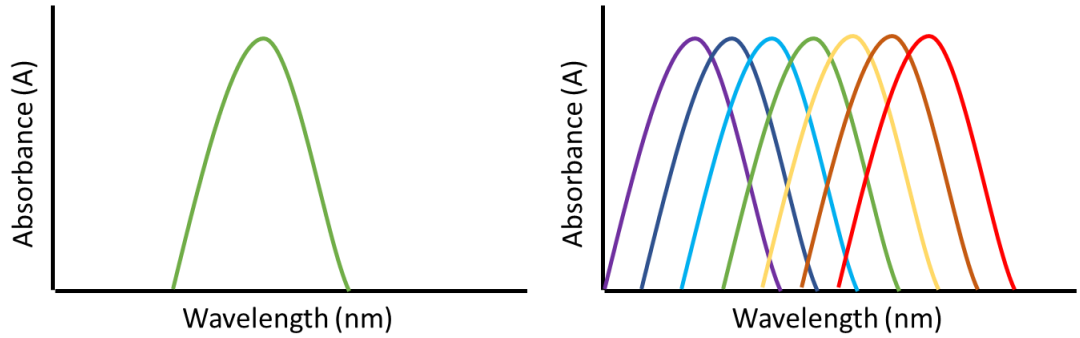

Figure 0.2 – Absorbance of a single dye (left), compared to the panchromatic absorption of multiple co-sensitised dyes (right)

In this context, self-assembly can be described as the processes which take place when two or more chemical entities encounter each other (whether it be in the gas, liquid or solid phase) and the two chemical entities undergo a recognition event. During this event, the two chemical entities have very weak interactions between their intermolecular forces which result in a particular chemical configuration.[9,10] For example, self-assembled nanolayers are used quite extensively in advanced devices (e.g. chemical sensors[11], DSC's[12], anti-microbial mirrors[13] and photonic crystal dye

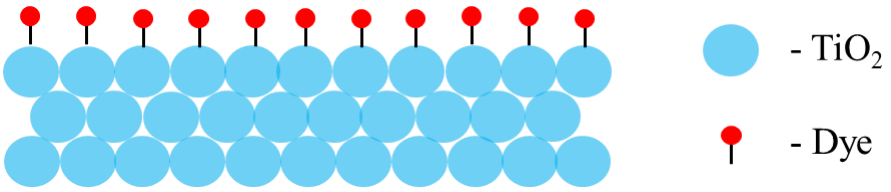

Figure 0.3 – Graphical representation of a monolayer of dye adsorbed onto TiO_2[16]

lasers[14]). This is down to the ability to assemble nanoparticles into well-defined configurations which can lead to more and more complicated devices. This is particularly useful in DSC devices where a monolayer of the dye self-assembles onto TiO_2 (see **Figure 0.3**).[15] The need to further understand this process forms the basis of this thesis. DSC devices are not the only photovoltaic device to make use of self-assembled nanolayers. The most efficient lab scale photovoltaic devices are tested and then recorded National Renewable Energy Laboratory (NREL)[16] and can be seen in **Figure 0.4**.

The National Renewable Energy Laboratory (NREL) is a national laboratory aiming to drive advanced energy research and has three national centres dedicated to this (National Bioenergy centre, National Centre for Photovoltaics and National Wind Technology Centre). The National centre for Photovoltaics (NCPV) is charged with testing and recording the best (confirmed) solar energy conversion efficiencies for a vast range of photovoltaic technologies.

The devices shown here in the NREL table are arguably not representative of devices that would be used commercially because they are almost always small laboratory-sized devices (sometimes with an active area 1 cm^2 or less).[17] Therefore, these devices are optimised for laboratory testing and not necessarily for reality where modules can exceed 1 m^2.[18] Therefore, Progress In Photovoltaics publish consolidated tables showing an the highest independently confirmed efficiencies for solar cells and modules are presented.[19]

Though these devices are small they can often show the potential of what larger devices could become. Almost all lab scale (PV) devices are recorded in the NREL chart; multi-junction cells, single-junction gallium arsenide cells, crystalline silicon cells, thin-film technologies and 3rd generation PV materials such as DSC devices (which is the main focus of this thesis).[16]

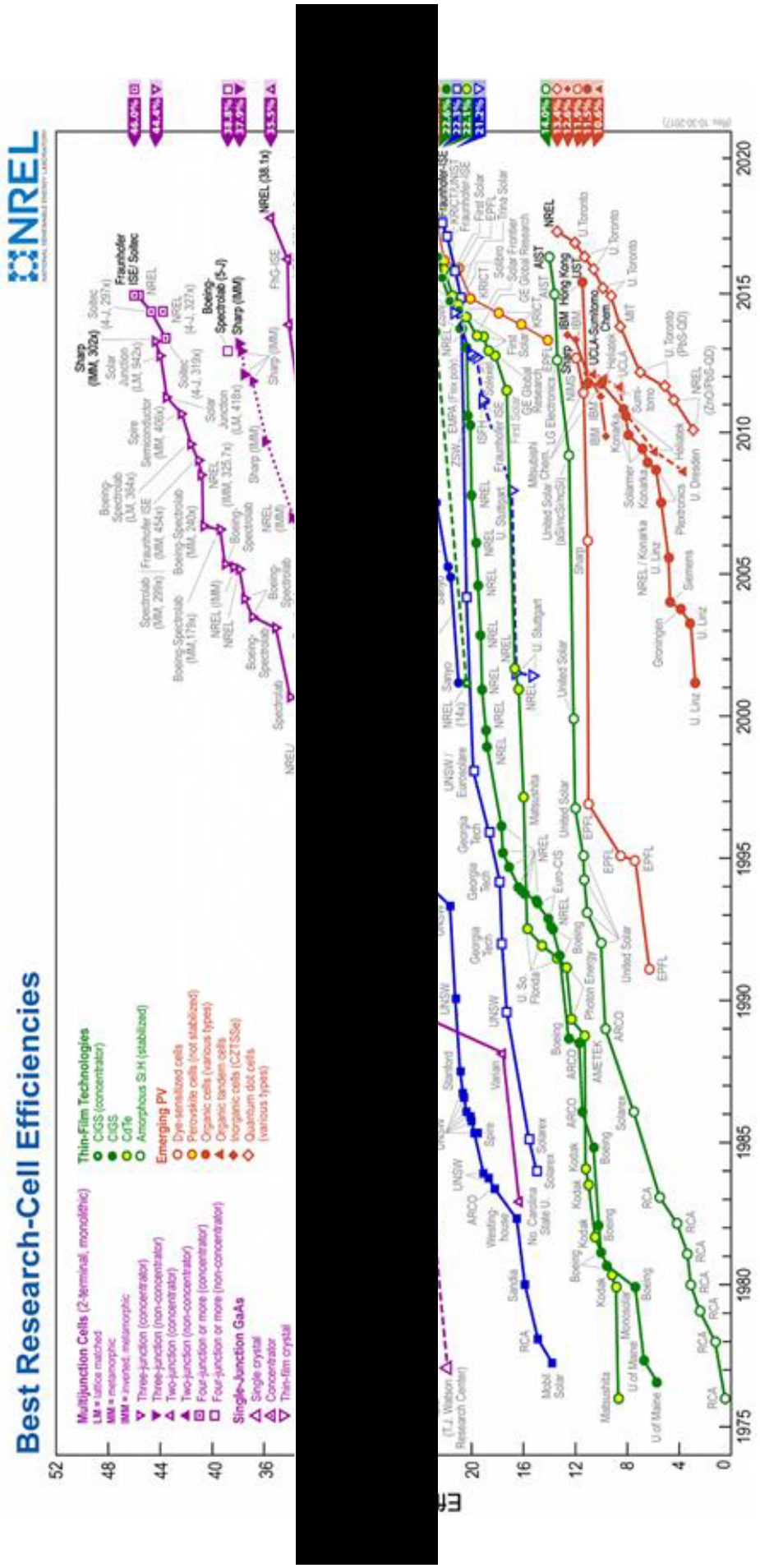

Figure 0.4 – Best lab scale research cell efficiencies, certified by NREL[17]

1 Introduction

The total energy consumption of the Earth during the year 2016 was estimated to be 21.8 TW (terawatts).[20] With developing countries starting to depend more on electricity and a rapidly increasing global population, this energy demand is only likely to increase. This has been estimated that energy consumption could reach 28 TW in 2050.[21] To put this into perspective an average family house in Wales in 2017 used 3681 kWh of power (power is energy per unit of time, whilst energy is total amount of work done). This energy consumption is unsustainable, as we have very few resources that are able to provide this energy without disastrous consequences. Global warming has proven to have a negative impact on the environment[22], wildlife[23] and human life[24].

As such, the world is reaching a tipping point in terms of energy.[25] An increase in the global temperature is believed to be causing the ice caps to melt. Burning fossil fuels releases CO_2. CO_2 is a greenhouse gas and is a major contributor to global warming. As the global temperature increases the ice caps begin to melt. During the last ice age atmospheric oceans froze whilst holding higher levels of CO_2 therefore if the icecaps melt this captured CO_2 will be released. This is a vicious circle and in the not so distant future could become unstoppable and potentially lead to catastrophe. At the moment humankind's main source of energy is fossil fuel; in particular oil.

The UK consumed the equivalent of 142.0 million tonnes of oil equivalent (Mtoe) in 2019.[26] Therefore, we need to find cleaner renewable forms of energy. The use of renewable energy is on the rise but still only accounted for 12.3 % of the overall energy consumed within the UK in 2019 (See **Figure 1.1**).[27,28] Whilst this need is increasing the world's supply of oil, gas and coal are finite and are therefore running out.[29] This, alongside greater demand for electricity that are the main driving force behind climate change and its effects. Therefore there has been a shift in perception and use to renewable energy (energy from a source that is not depleted when used) in order to solve the worlds energy requirements.[30]

Another alternative is nuclear energy. Currently nuclear power provides a huge amount of electricity (~21 %)[24] to the UK however, approximately half of these power stations are due to go offline by 2025.[24] Nuclear power stations also have a limited lifespan (due to the impact of radiation on materials such as steel, graphite and

concrete)[31]. Nuclear power is also very expensive, which means less developed nations lack the resources to establish and maintain such power stations and more developed nations are building fewer.

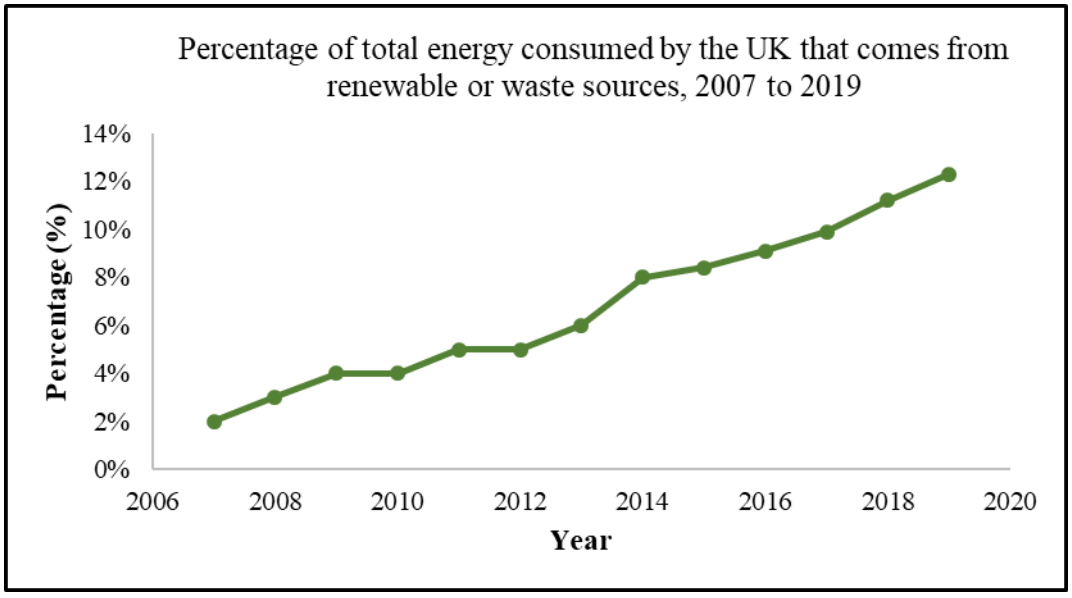

Figure 1.1 - Percentage of total energy consumed by the UK that comes from renewable or waste sources, 2007 to 2019[27,28]

Besides nuclear power, renewable energies (solar, wind and tidal) energies are probably the most likely solution for the world's energy needs.[32] Sunlight delivers more energy in one hour than the Earth uses in one year.[32] The estimated energy that reaches earth from the sun is estimated to be around 600 TWh per year. The daylight mid average latitude solar flux allows solar technology to access 230 W/m^2, whereas wind and geothermal energy resources can only obtain access to 2 W/m^2 and 0.05 W/m^2 respectively.[21] Therefore, it is sensible to take advantage of our largest energy source, i.e. the sun. If just a fraction of this could be harvested (less than 10%), it could provide 60 TWh of power, far more than the 28 TWh demand predicted by Hagfeldt *et al.*[21] and more than enough power to meet the world's current energy demands.[21]

So, with all these differing energy sources how can we determine which has the best value for money? This is where the levelized cost of energy (LCOE) comes in. According to the US Energy Information Administration (EIA), LCOE "represents the average revenue per unit of electricity generated that would be required to cover the costs of building and operating a generating plant during an assumed financial life and duty cycle".[33] Therefore, the LCOE tells us whether paying for a particular PV device now will be cheaper than paying for the electricity for the lifetime of the product even

considering a large upfront payment. A table demonstarating the LCOE of various renewable and non-renewable energy technologies can be seen in **Table 1.1**.[34]

Table 1.1 – Levelised cost of energy (LCOE) comparison of various renewable and conventional energy generation technologies.[35]

Energy technology	LCOE (lowest)	LCOE (highest)
Solar PV-Rooftop Residential	$150	$227
Solar PV-Rooftop C&I	$74	$179
Solar PV-Community	$63	$94
Solar PV-Crystalline Utility Scale	$31	$42
Solar PV-Thin Film Utility Scale	$29	$38
Solar Thermal Tower with Storage	$126	$156
Geothermal	$59	$101
Wind	$26	$54
Gas Peaking	$151	$198
Nuclear	$129	$198
Coal	$65	$159
Gas combined cycle	$44	$73

Solar energy can be harvested in the following ways:

(i) *Solar thermal technology.*[36,37]

Solar thermal technologies collect and concentrate the sun's light using reflectors and focus the sunlight onto a receiver. This harvests solar radiation that can be transferred to a fluid such as water. The water turns to steam, and the steam powers a turbine which generates electricity. This is particularly useful in areas of high solar intensity such as South America, Australia, middle east and Africa.

(ii) Photovoltaic energy conversion.[21,38,39]

Photovoltaic (PV) energy conversion technologies convert sunlight into electrical energy and is the main focus of this thesis (in the form of DSC devices). PV materials

come in many forms; multi-junction, silicon, perovskite, organic photovoltaic (OPV) and dye-sensitised solar cell (DSC).

It was the French scientist Edmund Becquerel (1839) who first identified that light could be used to produce electricity.[40] Becquerel's first photovoltaic cell consisted of two electrodes in an acidic solution separated by a thin membrane (see **Figure 1.2**, adapted from [41]). When Becquerel illuminated one of the electrodes, he noticed electricity was being produced and hence the first photovoltaic effect was discovered. When the light hit the semi-conductor (Pt) it released electrons from its atoms. The released electrons are then pulled to the anode through an electric field, where a current is then produced.

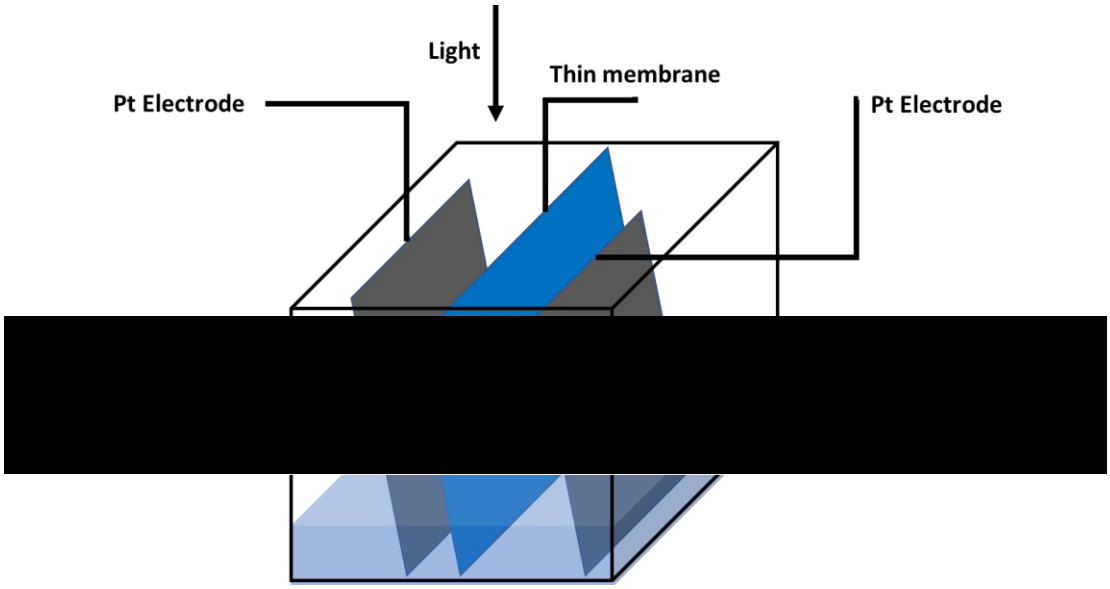

Figure 1.2 - Diagram of apparatus described by Becquerel (1839)[40]

It wasn't until 38 years later in 1877 when G. Adams and R. E. Day discovered the photovoltaic effect in a solid material (selenium)[42]. They reported that when a candle was lit an inch away from the selenium a current was detected. Hence, the investigators concluded, "it was clear that a current could be started in the selenium by the action of light alone".[42] Years later (1950's), scientists began studying the effects of light on semi-conductors such as silicon and germanium which have since gone on to dominate the current PV market. In order to know the true potential of these devices a lot of research has looked at their theoretical performance limits. A paper published by William B. Shockley and Hans-Joachim Queisser describes such limits for a single junction solar device (see below).[43]

1.1 Shockley-Queisser limit

The Shockley–Queisser (SQ) limit is the theoretical limit for single-junction solar devices.[43] William B. Shockley and Hans-Joachim Queisser used physical assumptions (such as T_{sun} = 6000 K and T_{cell} 300 K) [43] to calculate inherent losses of single-junction solar devices to derive their theoretical maximum efficiency of 33 %.[44] 33% corresponds to a bandgap of around 1.3 eV (because of the trade-off between current and voltage occurs around 1.3 eV).[45] The theoretical maximum efficiency of a photonic device can be seen in **Figure 1.3**[44] however for more details regarding the current/ voltage trade-off can be found in **section 1.1.3**.

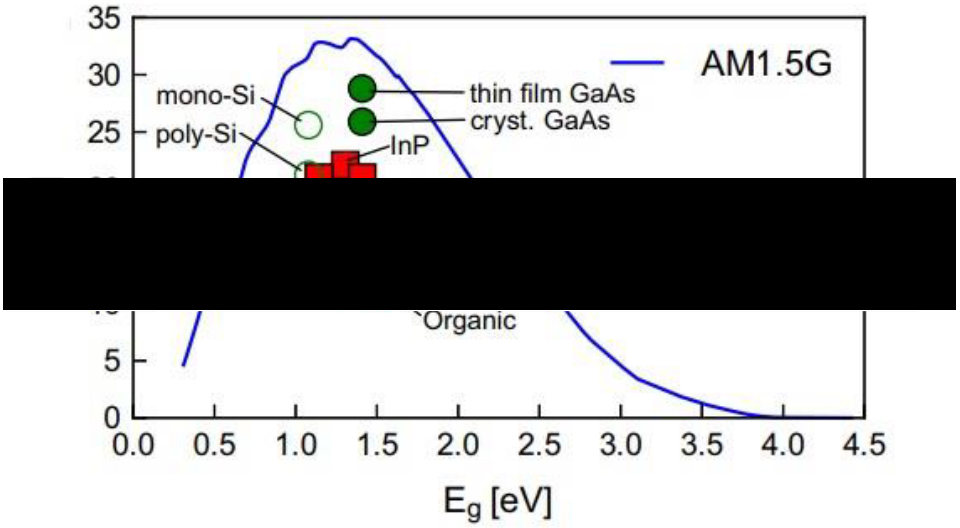

Figure 1.3 - The theoretical maximum efficiency of a photonic device according to the Shockley-Queisser limit. Highest recorded efficiency of current solar devices has been marked to compare against bandgap theoretical limit.[45]

The losses of efficiency they attributed to one of following processes:

1) Entropy and thermal losses

2) Recombination

3) Bandgap Losses

1.1.1 Entropy and thermal losses

Any energy that a PV device is unable to absorb turns into heat. As the temperature of the devices increases, the outgoing radiation and heat loss also increase until an equilibrium is achieved.[46,47]

As the temperature of the cells increases, the blackbody radiation also increases, until a new equilibrium is reached.[47] The temperature at equilibrium can vary depending in

which climate the solar panel is placed. Thus, the temperature of a solar cell on a roof sub-Saharan Africa would be considerably different to one placed on a roof in the UK. For example, Viridian Solar fixed monocrystalline PV panels onto UK houses with several different types of roofs in order to see how the temperature of the panels varied.[48] The largest temperature variation was seen from panel placed on a shingle roof where the temperature varied from 0 ^{o}C to 40 ^{o}C. Manufactured solar panels are supplied with a data sheet. In the data sheet the manufacturer will refer to the temperature coefficient (pMax).[28] This value corresponds to the loss of efficiency of the for every 1^{o}C the PV device rises in temperature. Monocrystalline and polycrystalline cells have a pMax between -0.45 to -0.5 %. Amorphous thin film PV devices have a pMax between -0.2 to -0.25 %.[28] Not only does device efficiency decrease as temperature rises DSC devices can be at particular risk due to their liquid electrolyte. As the temperature of the device rises it causes the organic solvent in the liquid electrolyte to expand, potentially causing devices to break and leak.[49]

1.1.2 Recombination

The second Shockley-Queisser loss is recombination is "the process in which an electron, which has been excited from the valence band to the conduction band of a semiconductor, falls back into an empty state in the valence band, and recombines". [43] In the Shockley-Queisser model the voltage is limited by the rate of recombination. Because charge separation occurs at the dye-TiO_2 interface in DSC devices, there are different routes of recombination for DSC technology compared to Si PV (see **Figure 1.10**).[50] Recombination can occur between the dye/ electrolyte or HTM, between the dye and TiO_2 and between the TiO_2 and the electrolyte or HTM. However, the largest contributorto recombination is regeneration of the dye by the electrolyte.[50] This process is several orders of magnitude slower than the other electron transfer steps.[50] The slower the step the higher likelihood of recombination.

1.1.3 Bandgap losses

The third and final factor that makes up the Shockley-Queisser limit is bandgap losses. The bandgap is the energy required to promote an electron from the HOMO to the LUMO. The Shockley-Queisser limit of 33 %[44] corresponds to a bandgap of around 1.3 eV.[45] There are lots of photons lower than 1.3 eV hitting the earth's surface (see **Figure 1.4**).[51] Therefore, if absorbed, the increased number of photons will lead to an increase in J_{sc}. However, the J_{sc} will inevitably drop as the bandgap is fixed and therefore any photons lower in energy than the bandgap will not be absorbed, and any photons absorbed are low in energy. Photons with energy > 1.3 eV have the opposite effect. There are fewer photons available in this region but, the photons that are available are much higher in energy leading to an increase in V_{oc} but a decrease in J_{sc}. However, most of the photons are too high in energy and their excess energy is converted into heat a process that is referred to as "thermalisation" (see **Figure 1.4**).

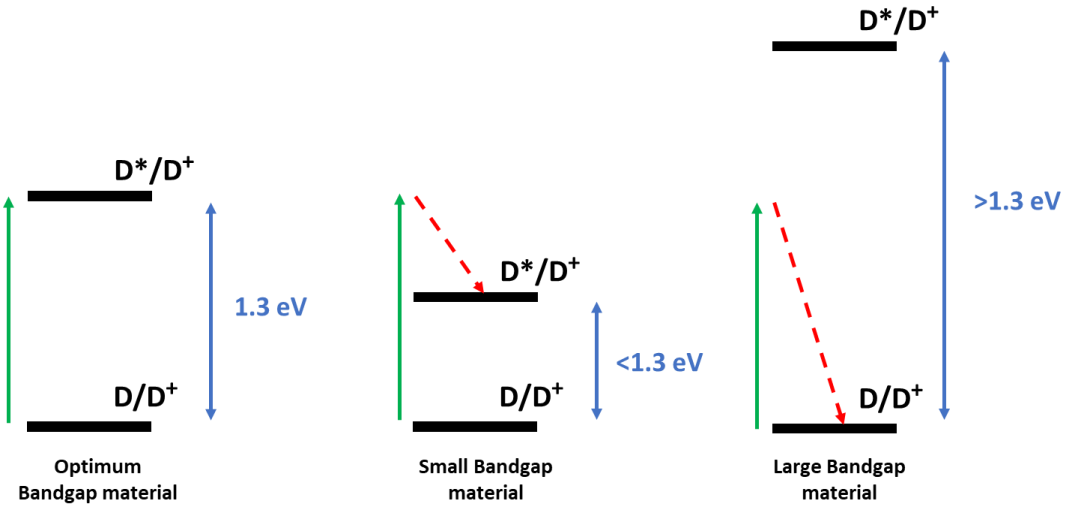

Figure 1.4 - Diagram to represent the energy required to promote and electron from the HOMO to the LUMO of a dye in a DSC device (Green is the energy of the electron, blue is the bandgap, red is the recombination pathway and ultimately the loss of energy from the system).

By comparison, one advantage of a DSC device is the ability to vary the spectral response of the device because a molecular sensitiser (a dye) is used to harvest the light. Various sensitisers have been synthesised that absorb small bands across the AM 1.5 solar spectrum (see **Figure 1.5**).[51] The ability to change the sensitiser means we can tune the device to absorb light in the region we want the most.

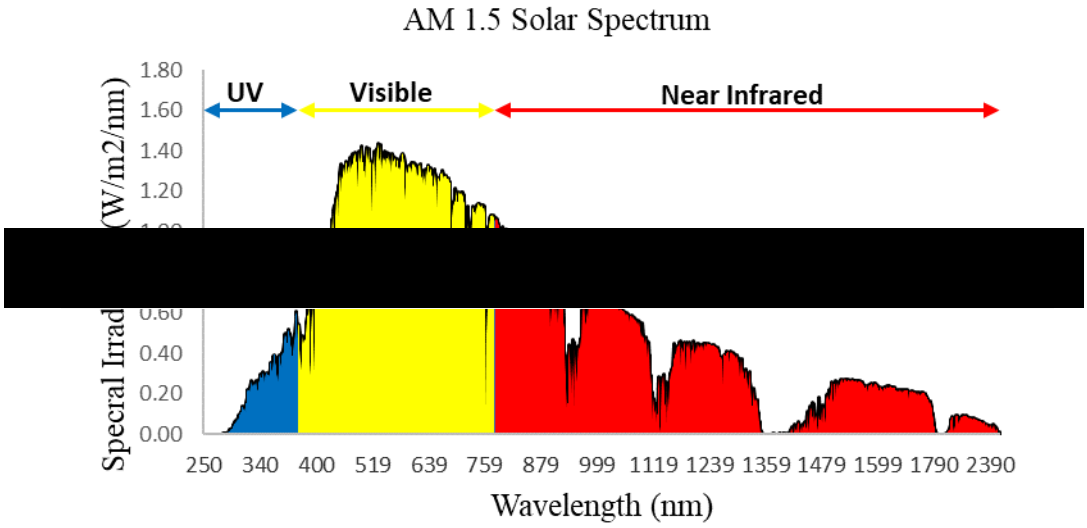

Figure 1.5 - AM 1.5 solar spectrum[51]

1.2 Multi-junction devices

Multi-junction devices work by splitting the AM 1.5 solar spectrum into separate sections and then aim to optimise each section in order to increase efficiency. Multi-junction devices use multiple materials with varying band-gaps to absorb photons with differing energy levels (see **Figure 1.6**).[52,53] This process can increase device efficiency but, because each layer requires good quality crystals of each material, grown one layer at a time epitaxially, making it quite costly.[54] Therefore, these devices are usually reserved for space exploration where the power to weight ratio of the module takes priority over its cost.[54]

A cheaper alternative to multi-junction devices are tandem solar cells. Like multi-junction solar cells tandem devices split the AM 1.5 solar spectrum in to separate sections. However, unlike multi-junction devices tandem solar cells utilise two or more sub-cells in order to harvest more sunlight to increase their efficiency. One recent example of a tandem device was a silicon/ perovskite solar cell developed by Oxford PV which has achieved 28 % efficiency (on a 1 cm^2) device.[55]

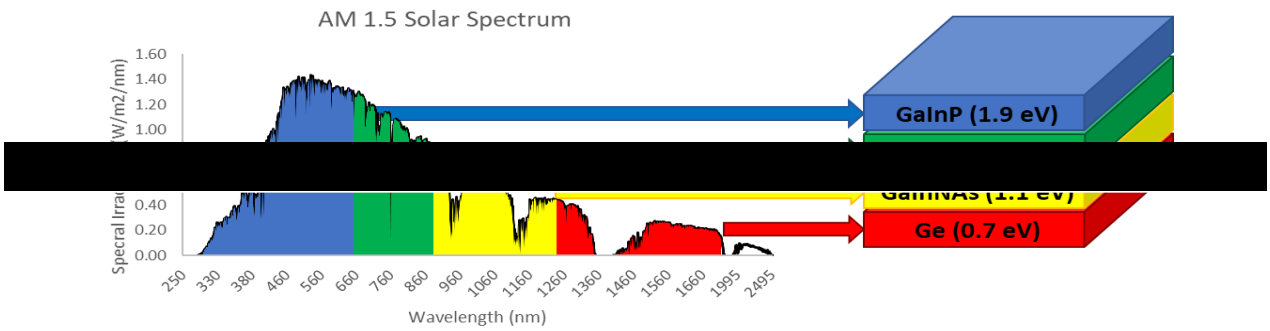

Figure 1.6 – A typical example of a multi-junction PV device. Made up of GaInP, GaInAs, GaInNAs and Ge, together which absorb almost the entire AM 1.5 solar spectrum[52,53]

1.3 Current solar technologies

1.3.1 1st, 2nd and 3rd generation photovoltaic materials

Silicon (Si) wafer based solar devices currently occupy the largest share of the PV market (approx. 95 %)[56], the remaining 5 % contains a variety of thin-film solar devices, mainly CdTe (cadmium telluride)[57], CIGS (copper indium gallium selenide)[58] and GaAs (gallium arsenide)[59].

There are various types of PV technologies including (but not limited to) silicon[60], multi-junction[52], CdTe[16], GaAs[61], perovskite[62], OPV[63] and DSC[64]. Each device has its advantages and disadvantages making them ideal for certain situations, i.e. DSC devices can operate more efficiently at lower light intensities and therefore perform better indoors.[65] The performance of silicon PV devices strongly depends on the angle of the incident light and therefore perform poorly in the morning, evening and cloudy days. At an angle, PV devices are likely to reflect more light and absorb less light then when facing the sunlight directly.[66] DSC devices are less affected by the angle of incident light and therefore still perform well under diffuse light conditions (**see Figure 1.7**).[67] OPV can be manufactured/printed on flexible substrates[68], which is very encouraging for use in wearable electronics[69] and multi-junction devices are expensive but also incredibly efficient (47.1 %)[16] and are therefore used in space exploration where cost is less of an issue[70]. A typical communications satellite solar panel weighs about 20 kilograms.[71] It costs approximately $10,000 per kilogram to send anything into space.[71] Therefore, the cost of sending that solar panel comes to $200 per watt. This is approximately 100 times higher than a competitive utility price.[71]

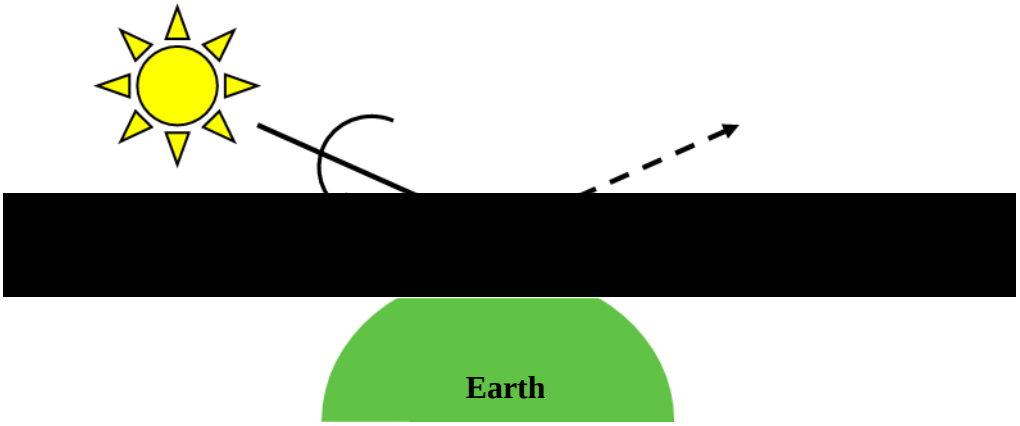

Figure 1.7 - A figure representing the angle of incidence on a PV device[67]

Further information on 1st, 2nd and 3rd generation PV devices can be found in the next sections. However, this thesis will focus' on 3rd generation PV devices as the work undertaken is predominantly to do with dye-sensitised solar cells which is a form of 3rd generation PV.

1.3.1.1 1st generation photovoltaic materials (silicon solar cells)

Silicon solar cells belong to a group of devices called p/n type PV devices, a name given to them because of the junction formed between an n-type and p-type semiconductor.[72] A p-type or positive-type semiconductor is made up of crystalline silicon doped with a material that is electron deficient leading to a net positive charge (e.g. silicon doped with boron).[73] A n-type or negative type semiconductor is made up of crystalline silicon doped with a material that is electron rich (i.e. has more valence electrons than Si, e.g. silicon doped with phosphorous).[73] **Figure 1.8** gives an example of n-type and p-type doping. On the left silicon is doped with boron, boron has one less electron in its outer shell compared to silicon. This leaves behind an electron "hole" or net positive (p) charge. On the right silicon is doped with phosphorous. Phosphorous has one more electron in its outer shell compared when compared to silicon. This gives the lattice a free electron and therefore a net negative (n) charge. A p/n type device makes use of these electron-hole pairs and use the electric field to generate a potential.[73]). 1st generation PV devices possess indirect band-gaps which can affect the probability of light being absorbed and therefore impact device efficiency. The band gap is the energy between the valence band (HOMO equivalent) and conduction band (LUMO equivalent). If the momentum of the electrons and holes are equal in both the valence band and the conduction band

then the material has a direct band gap. If the electron needs to pass through an intermediate state then it is an indirect band gap.[74]

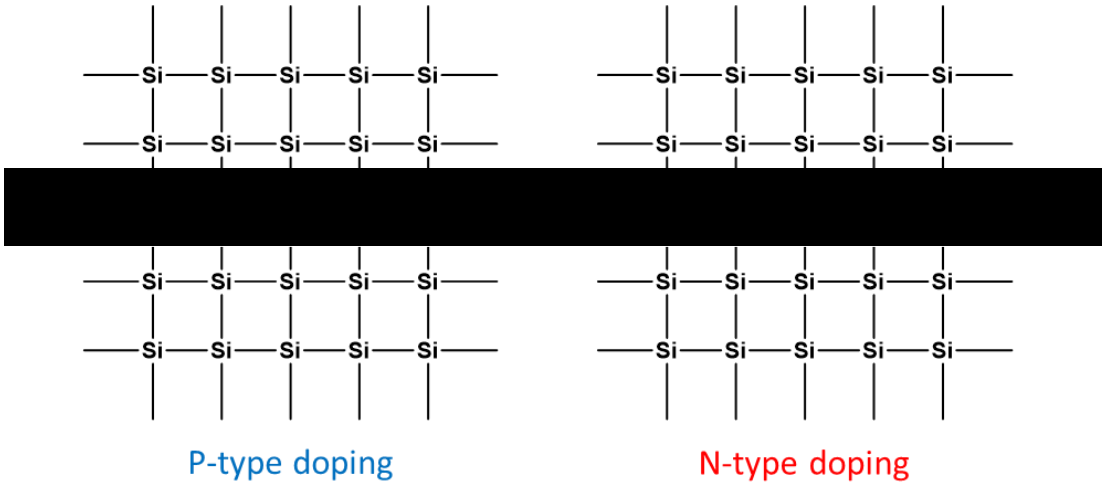

Figure 1.8 - P and N – type doping in a silicon semiconductor.[74]

1.3.1.2 Second generation photovoltaic materials (thin film solar cells)

The second generation of solar devices include amorphous silicon, CIGS and CdTe, and are often referred to as "thin film technologies" (see **Table 1.2**).[75] Second generation PV devices are given this name because their absorber layer has a much higher extinction coefficient (ε) and therefore require less materials to be as or more efficient that Si. Unlike Si, thin films possess a direct band gap which increases the probability of light harvesting within a thin layer of material (usually just a few micrometres or less).[69] Because much thinner layers of absorber material are required, these thin film solar cells once offered a cheaper alternative to crystalline silicon (c-Si). However, in recent years 2nd generation PV costs are now much more comparable to c-Si costing around an \$0.42-0.36/W^{-1} in 2018[76]. Nevertheless, these materials can be deposited on cheap flexible substrates such as glass, plastic or even stainless steel giving them a wider range of applications.[77] The cost of PV devices is determined by a multitude of factors including (but not limited to), the price of the raw materials, cost of manufacturing, installation costs as well as the efficiency of the PV device being used.[78] If these factors change then the cost of that particular type of solar technology will likely also change.

Table 1.2 - Physical properties for three different thin film materials. For abundancy least abundant material of the compound has been used and has been written in bold underneath for clarification. Adapted from[75,79]

	a-Si	CdTe	CIGS
Absorption coefficient	1.7442 x 10^6 cm^{-1}	1.1148 x 10^6 cm^{-1}	> 1 x10^5 cm^{-1}
Bandgap	Direct 1.75 eV	Direct 1.44 eV	Direct 1.0 - 1.6 eV
Sufficient thickness (for device operation)	1 µm	3 - 5 µm	1 - 2 µm
Temperature coefficient	-0.3 %/ºC	-0.25 %/ºC	-0.26 %/ºC
Toxicity	None	Cadmium	None
Abundance (Earth's Crust)	2.82 x 10^5 mg/ L (**Si**)	1 x 10^{-3} mg/ L (**Te**)	5 x 10^{-2} mg/ L (**Se**)

Amorphous silicon is the most widely used form of thin film technology, having been used as a power source in clocks and calculators since the late 1980's.[75] Typically the efficiencies of amorphous silicon (a-Si) tend to be much lower than c-Si (13.4 % compared to 25.0 % for c-Si).[80] However a-Si is much cheaper ($0.34 – 0.27/$W^{-1}$)[76] and each module is less bulky than their c-Si counterparts.[81] The efficiencies of CIGS (23.4 %)[82] and CdTe (22.1 %)[16] solar devices are generally higher than a-Si but the materials used in their manufacture are toxic and/or low in abundance[75,80] in the earth's crust, which is something that would impede mass production due to scarce resources driving up raw material costs. Unfortunately, many forms of solar technology rely on the use of toxic, regulated elements (e.g. Cd in CdTe and Pb in organolead perovskites) and on rare (low abundancy) elements (Te, In, Se in CIGS and CdTe).[83] However, a large emphasis on developing thinner films could potentially reduce the amount of these materials present.[75] Some of these issues led to the production of a new generation of PV devices that utilise highly absorbing films to minimise cost of materials often referred to 3rd generation photovoltaics.

1.3.1.3 3rd generation photovoltaic materials (PV able to overcome the Shockley-Queisser limit)

The most recent PV technologies are referred to as 3rd generation are made up of DSC, CZTS (copper zinc tin sulphide), organic photovoltaics (OPV), perovskite solar cells (PSC) and quantum dot solar cells. These solar cells can potentially reach higher device efficiencies than their predecessors whist still utilising thin films.[82] Hence, this provides the potential for large scale, renewable power generation whilst being able to offer a significant reductions in raw material costs.[84,85]

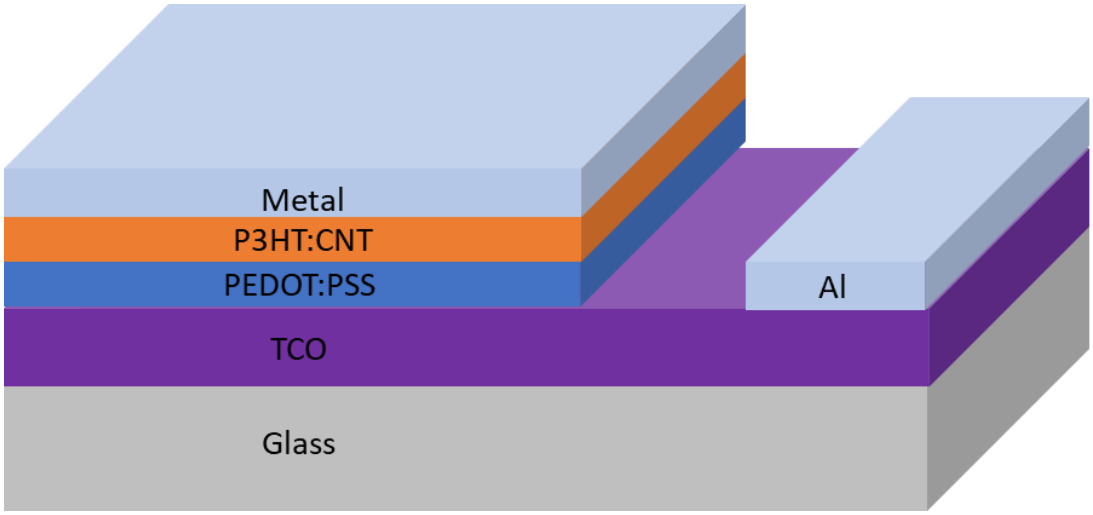

Figure 1.9 – A schematic diagram for a typical basic organic cell with CNT's as an acceptor within the active layer. Adapted from[88]

An alternative to perovskite solar cells are organic photovoltaics or OPV[86] which are another promising form of thin film technology.[87] The structure of a typical basic OPV device can be seen below in **Figure 1.9**[88]. OPV have many advantages including lower costs, flexibility and large area printability.[86] Unfortunately the efficiencies of OPV devices are still below (17.5 %)[89] other PV technologies mainly due to the low charge mobility of organic materials.[90,91] One way around this is to fix the organic molecules in place and use an electrolyte to move electrons and holes. As such, dye-sensitised solar cells (DSC devices), which are the main subject of this thesis, combine both organic and inorganic sub-components and make use of electrolytes and/or mobile organic molecules to transfer electrons.

Perovskites were first used for solar applications in 2012, though perovskites themselves were discovered 1839.[92] Organo-lead halide perovskites solar device efficiencies have increased to > 20 % in just seven years.[2] This meteoric rise in power conversion efficiency (PCE) has come from improvements in perovskite formulations and advanced deposition methods.[2] The high efficiencies make for a promising future

PV technology. Despite this, these solar cells currently have major drawbacks. Perovskite materials tend to degrade rapidly under exposure to moisture, heat, or prolonged illumination in air [93]. Yet, it is the lead component that presents the biggest issue. The lead in these perovskites is water soluble and therefore can leach out into the environment if not encapsulated correctly.[94] Lead exposure in humans has been shown to cause brain malfunction, premature infants and low birth rate, damage to the circulatory system and kidney malfunction.[94] As of July 1st 2006, a European Union directive on the restriction of hazardous substances (RoHS) restricts the use of lead (and other similar materials) in electrical and electronic equipment.[95] This will have serious ramifications on new PV technologies like PSC devices. There have been many replacements suggested for lead, usually other group 14 metals, such as Sn or Ge. But, when the lead is replaced the efficiencies of these materials drop significantly (< 10 %),[94] although PCE = 15% has been achieved for organotin perovskites in an oxygen deficient environment[96] by device encapsulation with cover glass and UV-curable epoxy in a N_2 filled glove box.[96] The main problem is the stability of Sn^{4+}. SnF_2 has been used to help stabilise the Sn based perovskite.[97] Other methods include encapsulation, which has proven to maintain Sn perovskite stability over 100 days[94] however, this is still low compared to 30 years for 1st generation PV.[98]

1.4 Dye-sensitized solar cells (DSC devices)

1.4.1 History and concept

Discovered in the late 1980s[4], DSC devices are a form of photoelectrochemical cells, that make use of a sensitiser/dye to harvest light and convert solar energy into electricity. Not only are DSC devices relatively environmentally friendly (most of the materials for manufacturing are classed as "non-hazardous") they are low-cost, easy to scale up and show good performance under diffuse light.[99] A big advantage for DSC is the fact they can be manufactured on glass and flexible substrates giving them a broader range of applications compared to 1st generation PV.[21]

The working principle of DSC's involve some key processes, light absorption, charge separation and charge collection see **Figure 1.10** (processes i-v).[4]

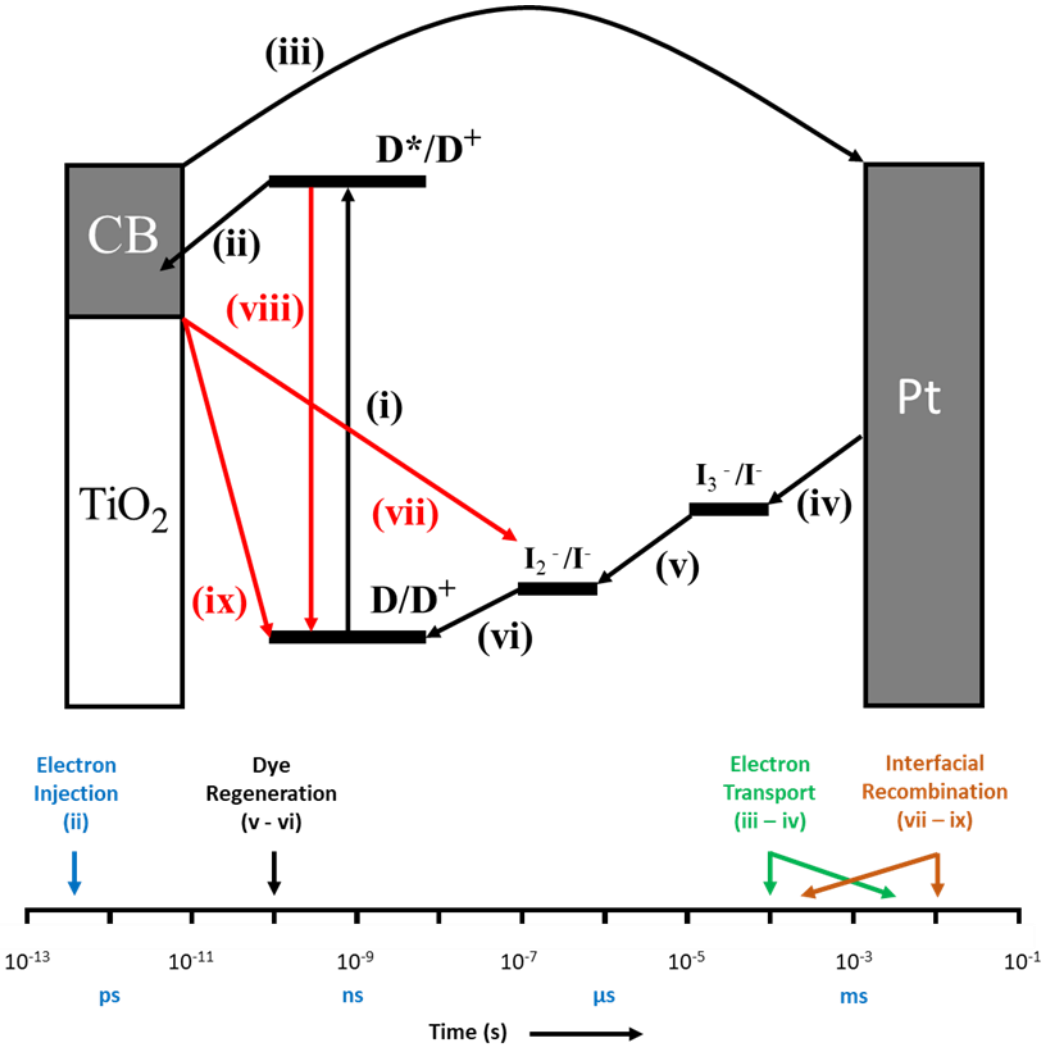

Figure 1.10 - Schematic of DSC device showing key steps for device operation (in black) and competing processes (in red) and their respective timeframe.[4,50] Where D/D^+ is the HOMO, D^*/D^+ is the LUMO.

Recombination is largely down to the speed of the electron transfer processes. Generally, if the processes in black (10^{-12} to 10^{-4}) [50] are faster than the process in red (10^{-4} to 10^{-2})[50] then recombination is less likely to occur. Henry Snaith postulates that by increase the absorption onset to 940 nm and reducing the overpotential required to drive dye regeneration by 0.3 eV then a DSC device could achieve 20.25 %.[100]

The components of DSC devices can be broken down into three main areas:

I) Light harvesting dyes/sensitizers[101]

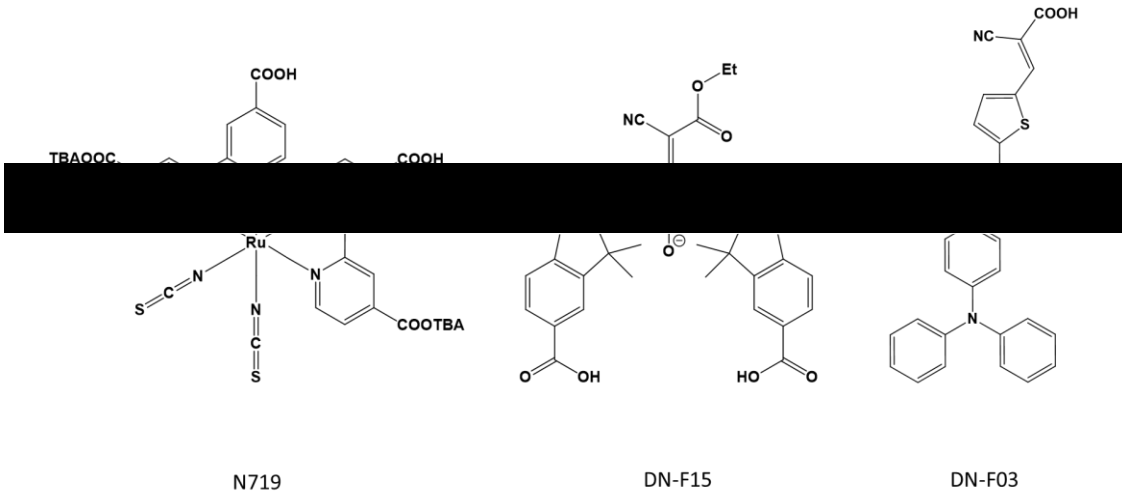

Figure 1.11 – Chemical structures of three different dyes used in DSC devices. Inorganic dye N719 (left), organic squaraine dye DN-F15 (middle) and organic triphenylamine dye DN-F03 (right).[102]

II) Metal oxide semi-conductor scaffolds[102]

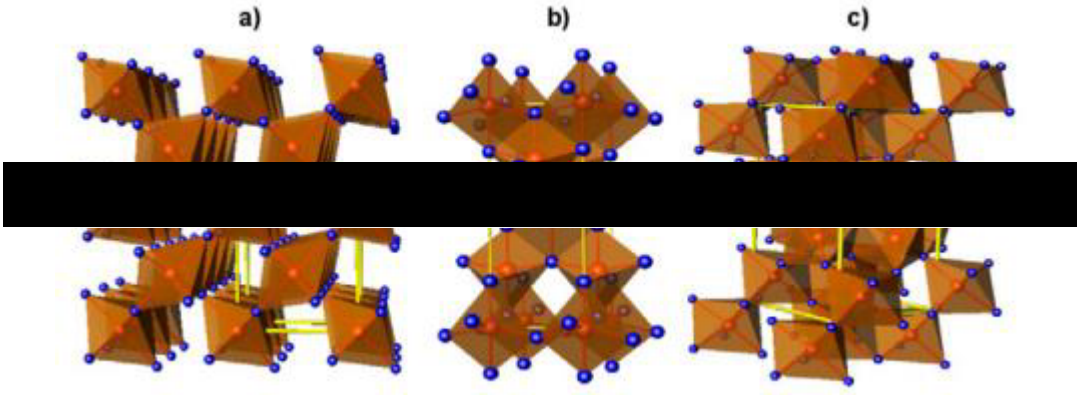

Figure 1.12 - Crystal structures of the various forms of TiO_2. (a) Rutile, (b) Anatase and (c) Brookite. Blue dots represent O^{2-}, red dots represent Ti^{4+} and the yellow lines indicate the unit cell.[187]

III) The role of electrolytes

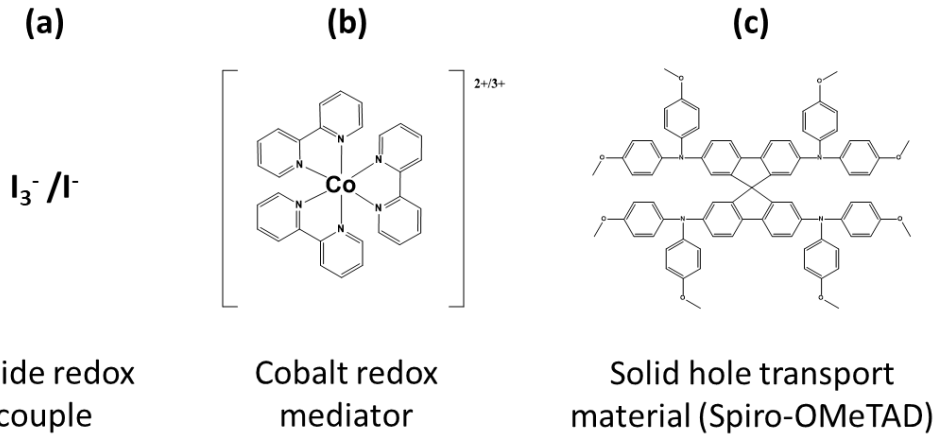

Figure 1.13 - Chemical structures of Iodide redox couple (left), a cobalt redox mediator (centre) and a solid-state hole transport material (Spiro-OMeTAD – Left)

1.4.2 Light harvesting dyes/sensitizers

Dyes (or sensitizers as they are sometimes referred to) are the part of the device that harvests light and injects excited electrons into the conduction band of the TiO_2 semiconductor. After absorbing light a "good" dye should be able to use this energy to promote an electron from the HOMO to the LUMO. The electron is injected into the conduction band of the TiO_2. In terms of solar energy harvesting, the sensitisation of semiconductors began all the way back in the 1960's when Gerischer[103], Tsubomura[104] and their co-workers began sensitising wide band gap semiconductors such as ZnO with dyes like rose bengal (due to its low cost)[105]. Rose bengal is an organic dye synthesised by Chnem in 1882, there are various groups of dyes used in DSC devices these are inorganic, organic and natural.

Taking natural dyes first, these are extracted from biological sources, usually plants.[106] Such dyes include anthocyanin, betacyanin, carotene, tannin, and chlorophyll.[107] Natural dyes have an advantage over other types of dye as usually very little synthesis is required, meaning the dyes can be widely available assuming the yield from the crop is high. Perhaps the major selling point for natural dyes is that they are non-toxic and biodegradable which means the dyes do not pose a threat to wildlife and the environment.[108] Though this statement is true of the dyes themselves it does not however take into account the purification process of the dyes. Purification is difficult and it often uses a huge amount of toxic/harmful solvents which creates lots of waste

and only yields a small amount of material. These factors, alongside low efficiencies, have made natural sensitisers undesirable when compared to synthesised dyes.[108] For example, DSC devices fabricated with chlorophyll have achieved efficiencies greater than 4 %[109]. However, most devices made with natural dyes rarely achieve efficiencies higher than 1 %.[110] The main problem with natural dyes is that they have evolved to serve multiple roles not just solar energy harvesting. This means materials such as chlorophyll are not optimally designed for PV applications.[111] This has led to some researchers taking natural dyes and modifying them for use in DSC.[112,113] Thus, Grätzel and Kay managed to extract chlorophyll and introduced different metals (Cu and Mg) to form complexes. In doing so they managed to achieve a PCE of 2.6 %.[112] Although 2.6 % is a good result for a DSC device utilising a natural dye, Grätzel and O'Regan proved much higher efficiencies can be obtained with synthetic dyes.[99]

This new breakthrough occurred in 1991 when O'Regan and Grätzel[99] showed the success of using ruthenium bipyridyl dyes. Since then, this family of dyes have gone on to be one of the most commonly used inorganic dyes.[114–117] Ruthenium based dyes tend to have a wide absorption range (400 - 700 nm for N719)[118] (see **Figure 1.14**)[119] and reasonable molar extinction coefficients (ε_N719 = 13,500 mol^{-1} cm^{-1}).[4] They also have long term stability (1200 h at open circuit exposed to light)[120] under thermal stress and light soaking. However, despite these great attributes, device efficiencies have plateaued at around 10 – 11 %. This, alongside high cost and lack of availability of ruthenium and other metal-based dyes, has become a major limitation holding these dyes back.[117] The use of Ru based dyes has yielded good performing devices (in 1993 a PCE of greater than 10 % was achieved with N3 dye). However, since 1993 there have only been small advances in performance of Ru based dyes.[117] This has led to further interest in organic dyes that have much higher molar extinction coefficients (ε).[117]

There are several reasons why organic dyes generally have better (ε); the first being organic dyes are generally large conjugated systems with delocalised elections allowing for electronic transitions involving π orbitals. Normally, the longer the conjugated system the longer the λ_{max} and the larger the value of ε (see **Table 1.3**).[121]

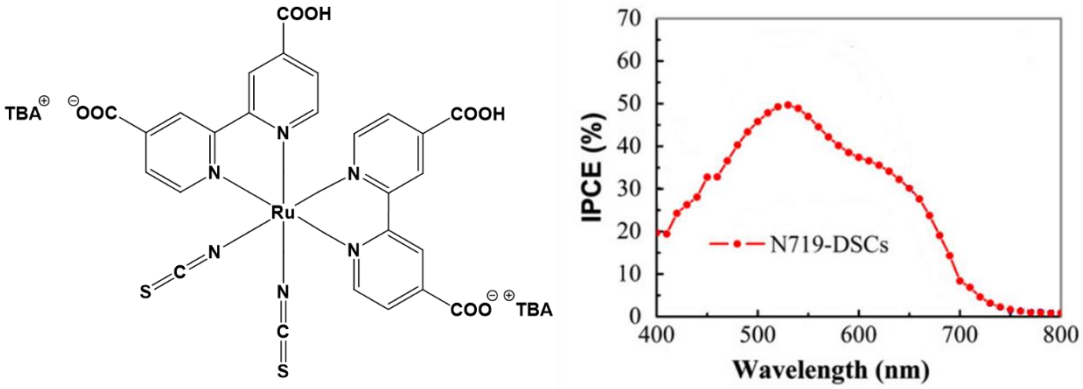

Figure 1.14 - Structure of N719 dye (left). IPCE of N719 (right) showing N719's wide absorption range (measured in % IPCE).[119] IPCE or Incident photon conversion efficiency is the number of electrons in the external circuit produced by ab incident photon of a given wavelength.

Table 1.3 – Effect of conjugation on λ_{max} and ε_{max} in the UV/VIS spectra of ethene and some conjugated polyenes[121]

Compound	Structure	λ_{max}/ nm	ε_{max}/ dm^3 mol^{-1} cm^{-1}
E-1,3,5-Hexatriene	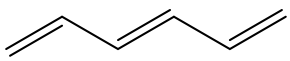	258	35,000

Another factor affecting the absorbance of inorganic dyes are orbital selection rules. Most inorganic dyes are octahedral complexes which normally means d-d* transitions which are forbidden.[122] However, as most inorganic dyes for DSC are non-centrosymmetric, d-d transitions are not completely forbidden and so the e_g-t_{2g} (molecular orbital) transition becomes weakly allowed.[122] Transition metals may also absorb light as a result of electron transfer from its associated ligands to the metals d – orbital (or vice versa). During these transitions, the electron moves a considerable

distance, which means the transition dipole may not be as large and therefore the absorption is less intense.[122]

In liquid cells, the lower ε of inorganic dyes can be counteracted by using a thicker film of mesoporous TiO_2 (~ 7-10 µm). A thicker layer of TiO_2 should adsorb more dye increasing pathlength (Beer lambert law, A = εlc) and therefore harvest more photons. However, in the case of ssDSC devices much thinner films (~ 2 µm) have better performance then the same devices with thicker films. This is because ssDSC devices utilise a solid HTM rather than a liquid electrolyte. HTMs can often struggle to penetrate the pores of the mesoporous TiO_2. A thinner layer can also offer many advantages, including cost savings, reduction in dye aggregation and a smaller pathway for injected electrons to travel.

Organic dyes are commonly based on a D–π–A-based architecture (see **Figure 1.15**).[51] In this system, after the dye is excited by a photon, the donor (D) or HOMO promotes an electron to the acceptor (A) or LUMO through a π bond where the electron is

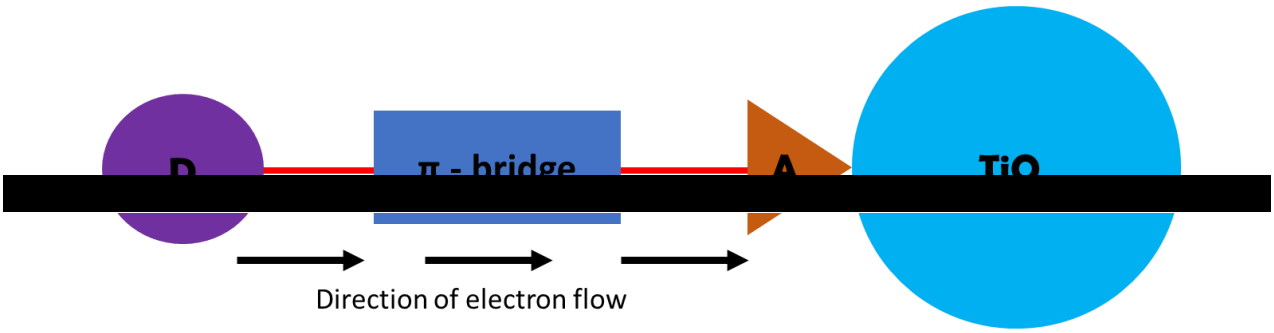

Figure 1.15 – An image to show the most common architecture of organic dyes for DSC. Flow of electrons goes from Donor (D) to π-bridge to acceptor (A) before being injected into the TiO_2[51]

injected into the conduction band of the TiO_2. There is a large literature of different organic dyes which utilise the D–π–A orientation; suggesting that is the most successful for efficient electron injection (assuming the dye has a perpendicular orientation to the TiO_2 surface)[123,124]. For dyes that are not perpendicular to the TiO_2 such as symmetrical squaraine dyes a different architecture is used. For more information please see **section 1.4.2.2**.

Common electron donor units include triarylamine, indoline, coumarin, and fluorene, whereas carboxylic acid, cyanoacrylic acid, and rhodamine units act as electron acceptors to form the system (see **Figure 1.16**)[125].

1.4.2.1 Designing highly efficient dyes for DSC devices

When designing DSC dyes, not only must the dye be understood, but the chemical

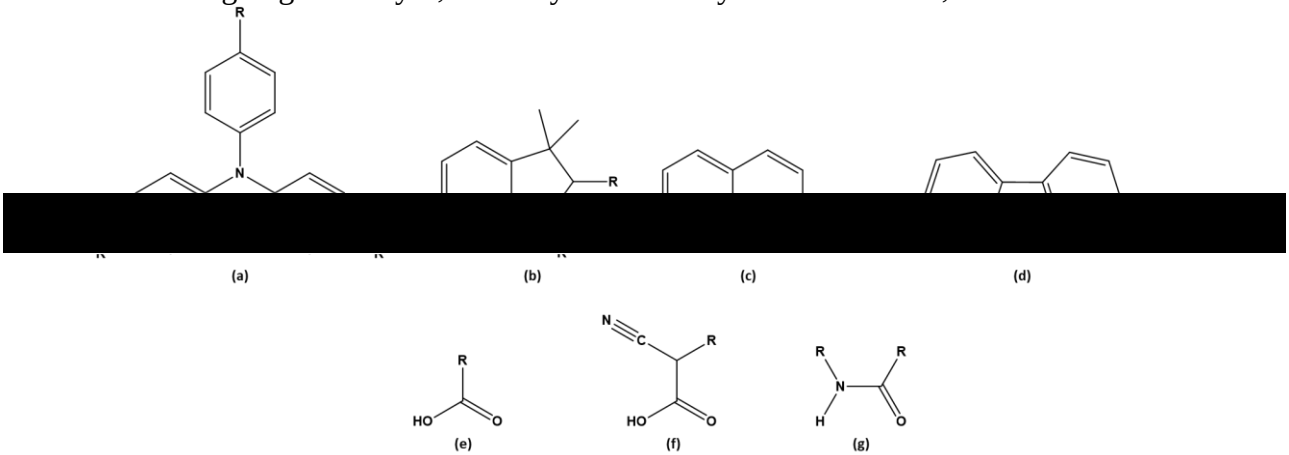

Figure 1.16 – Common electron donor (a-d) and electron acceptor units (e-g) that make up organic dyes for DSC devices. A - Triarylamine, B - indoline, C - coumarin, D - fluorene., E - carboxylic acid, F - cyanoacrylic acid and G - rhodamine.[125]

nature of the TiO_2 must also be considered. The bulk and surface of the TiO_2 are very different in terms of their molecular structure. The surface of amorphous TiO_2 is atomically rough and usually has surface defects with oxygen vacancies.[126] This in turn can make the surface polar in nature and, as such, make it more attractive to functional groups with similar polarities. Therefore, generally polar functional groups (e.g. OH, NH_2 etc) would be expected to orientate towards the TiO_2 and non-polar substituents (e.g. alkyl chains) to point away from the TiO_2 surface. However, testing DSC materials can be challenging. DSC devices contain multiple components that if not optimised can interfere with the efficiency of the whole device (even if it's not the component that is being tested).[4] Therefore multiple DSC devices need to be manufactured with a control device which can be time consuming.[4] Nowadays a lot of research centres have access to high performance computers to run simulations of various dyes and other materials to see which are likely to perform the best. There have been several reports using density functional theory (DFT) calculations on DSC devices.[127–129] Some of these papers have modelled device kinetics.[130] By determining slow internal transfer processes researchers have identified problem areas for recombination and then made efforts to combat them. Among the most popular methods to combat recombination are; use of additives, co-adsorbents and metal oxides with the use of co-adsorbents proving the most effective.[131] The role of these co-adsorbents isn't entirely understood however, it is believed that the bulky nature of these materials is able to inhibit aggregation between dyes. If aggregation decreases

then dyes become more efficient and yield better devices.[132] Other researchers have investigated and modelled the mesoporous TiO_2, to try and understand its surface area and porosity. However, most reports look at the performance of the dyes. By modelling the molecular orbitals of the dyes and TiO_2, their energies can be matched to minimise internal losses.[133–136] Despite this, there seems to be no reports specifically using modelling to look at how dyes self-assemble to the TiO_2.[137] As such, in **Chapter 3** of this thesis, a combination of computer modelling, ARXPS and device data have been used to try and understand how half-squaraine dyes self-assemble to TiO_2 and then discuss how the results can be applied to other organic dyes in DSC devices.

Co-sensitisation is when two or more dyes are used in a single device to harvest more of the AM 1.5 solar spectrum. Durrant *et al.*[138] first reported a step-wise approach to co-sensitisation by first sorbing a Ru-bipyridyl dye onto TiO_2, followed by treatment with aluminium isopropoxide to deposit an Al_2O_3 layer before sorbing a Ru-phthalocyanine dye.[138] More recently researchers have passively co-sensitised multiple dyes that are able to work in tandem to enhance electron injection. This approach has been used by Kakiage *et al.*[1] to achieve devices greater than 14 % showing the huge potential behind co-sensitisation. Though many dyes have been co-sensitised in DSC devices this thesis will focus predominantly on "squaraine" dyes. Squaraine dyes are relatively straight forward to synthesise and modify allowing for incorporation of specific atoms and functional groups that control how the dyes behave when sensitised to a surface.

1.4.2.2 Squaraine dyes

Initially synthesised in the 1960s, squaraine dyes are typically an intense blue colour with a λ_{max} around 650 nm (λ_{max} of SQ2 = 651 nm).[139] Squaraines have a significant number of technological applications including electrophotography[140], optical recording[141,142], nonlinear optics[143], pH responsive probes[144] and solar energy conversion.[145] As well as ease of synthesis squaraine dyes are also desirable because of their ease of purification.[146] Squaraine dyes absorb in the near infrared (NIR)[147] are

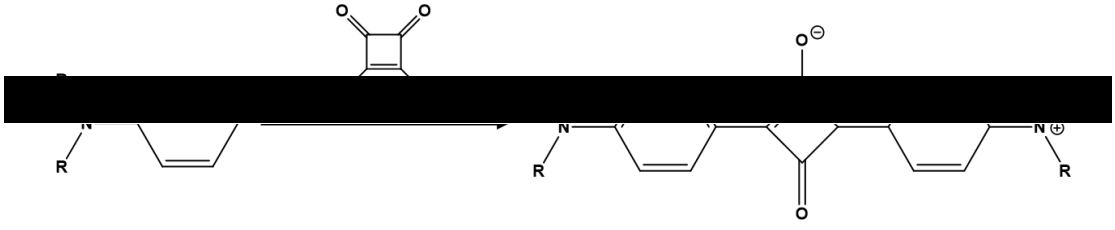

Figure 1.17 - Synthesis of aniline based symmetrical squaraine dye[148]

low cost and have high molar extinction co-efficient (ε_DN-F14 = 295,000 mol^{-1} cm^{-1})[101] Squaraines are synthesised via a condensation reaction of 3,4-dihydroxy-3-cyclobutene-1,2-dione (squaric acid) with an activated aromatic or heterocyclic component. **Figure 1.17**[148] shows the general synthesis of squaraine using an aniline ($C_6H_5NH_2$) based component as an example.

Squaraines are also very useful as we can easily modify the aromatic/ heterocyclic donor moieties (e.g. N, N-dialkylanilines, phenols, pyrroles, indoles, benzothiazoles and quinolones), allowing us to tune their physical and optical properties. By adding large bulky groups aggregation can be reduced.[149] Synthesising squaraines with vinyl dicyano moieties are known to push absorption into the near infrared.[150] Squaraines are known to have a very dense electron distribution over the central ring of the dye HOMO, this alongside their planar structure and zwitterionic properties is what gives squaraines their high absorption coefficients.[146] Squaraines strong, consistent chromophore, NIR absorption band and synthetic flexibility make them ideal for the investigation of organic dyes in DSC devices.

However, despite squaraines having a strong photon absorption, they generally have poor device efficiency (ca. 1 - 4 %)[147,151]. This surprising lack of efficiency has been reported to be largely down to dye aggregation[147] and a lack of directionality during electron injection from the dye to the semiconductor. To address the lack of direction in symmetrical squaraines, researchers have looked into unsymmetrical squaraines.

1.4.2.3 Unsymmetrical squaraine dyes

Unsymmetrical squaraine dyes have different functional groups on each end of the dye. It has been reported that this causes a hypochromic shift and a broadening of the light absorbance.[147] An example structure of an unsymmetrical squaraine can be seen in Figure 1.18.[147]

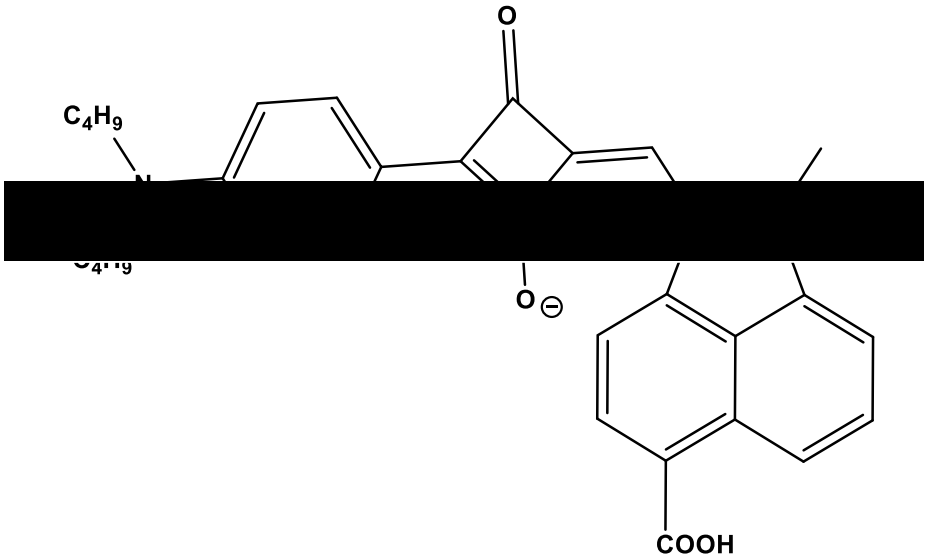

Figure 1.18 - A typical example of a NIR absorbing unsymmetrical squaraine dye (SQCBI-a) [147]

Unsymmetrical squaraines suffer from fewer recombination losses due to a reduction in aggregation. The bulky nature of unsymmetrical squaraines compared to symmetrical squaraine inhibits dye aggregation. Pandey *et al.*[152] synthesised both symmetrical and unsymmetrical squaraine dyes and tested their performance with and without chenodeoxycholic acid (CDCA). Pandey observed a huge increase in the performance of the symmetrical dye but little/no effect for the unsymmetrical dye.[152] The symmetrical squaraine (SQ-3) achieved 1.46 % without CDCA and 2.49 % with CDCA showing a huge increase in performance.[152] Whereas the unsymmetrical dye (SQ-4) achieved 2.43 % without any additives.[152] CDCA has many beneficial properties in DSC devices. However, its main use is to reduce dye aggregation by protonating the TiO_2 surface and acting as a spacer for the dyes, encouraging favourable electron injection.[153] CDCAs larger impact on symmetrical dyes suggest they are more susceptible to aggregation compared to their unsymmetrical counter parts[146], which is supported by the lower efficiencies of symmetrical squaraines.

Nithyanandhan *et al.*[147] looked at using density functional theory on synthesised symmetrical and unsymmetrical dyes. Nithyanandhan found a clear distinction of where the HOMO and LUMO sit on the dyes.[147] Unlike symmetrical squaraines where the HOMO and LUMO electron density resides on the centre of the dye, the electron density shifts towards the group linked to the TiO_2 surface.[147] It has been reported that this directional flow of electron distribution should lead to improved charge separation and electron injection in DSC devices (see **Figure 1.19**).[146]

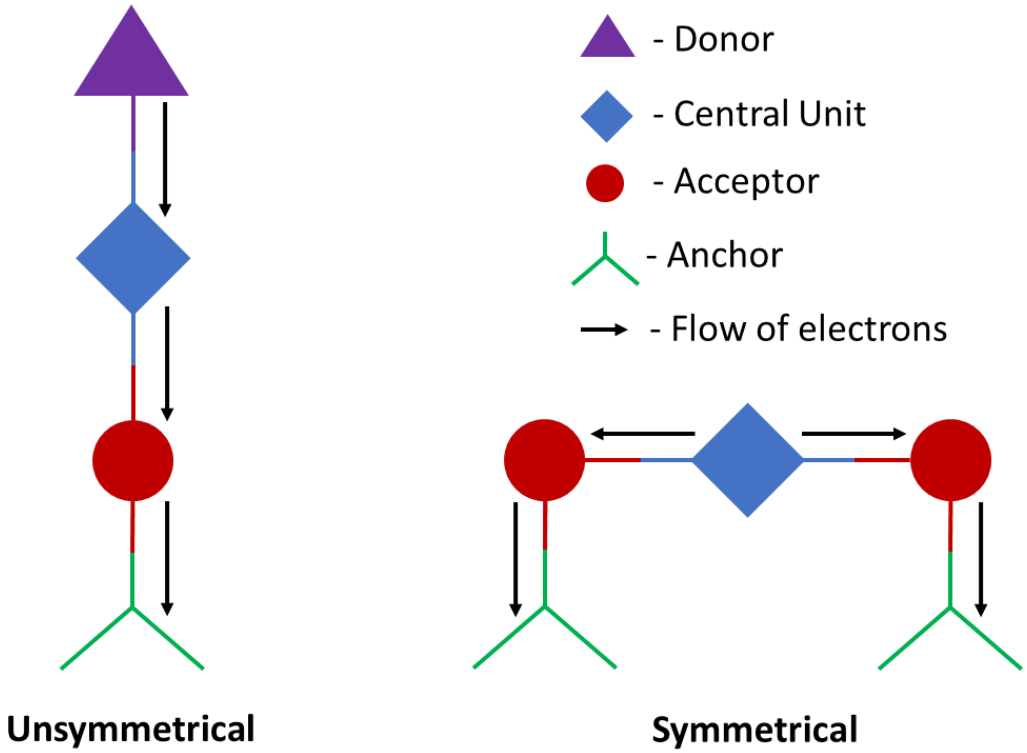

Figure 1.19 - Charge injection directionality in unsymmetrical and symmetrical squaraine dyes. In unsymmetrical squaraines (left) electrons flow from the top of the dye to the bottom where they are injected into the CB of the TiO_2 creating a "directional flow" of electrons. In symmetrical squaraines, the electrons have a choice "left or right" this creates a lack of directionality and therefore decrease injection efficiency.

Though this is agreed upon in most of the literature there are some recent publications disputing its effect on performance. Barolo *et al.*[146] notes that both symmetrical and unsymmetrical squaraines have comparable efficiencies and it's the number of anchoring groups as well as the length and nature of the alkyl chain plays a far greater role when it comes to charge injection.[146]

It has been reported that one downside to unsymmetrical squaraines is their difficult synthesis. They require at least four steps whereas symmetrical squaraines require just

one (though normally two steps are used in order to first modify the electron rich aromatic compound).[146]

1.4.2.4 Half-squaraine dyes

Half-squaraine (HfSQ) dyes are produced as an intermediate during the synthesis of unsymmetrical squaraine dyes.[4] HfSQ dyes are synthetically versatile, exhibit a high ε (18,400 M^{-1} cm^{-1} +/- 200 M^{-1} cm^{-1})[123] and have absorption maxima at ≈ 450-500 nm, similar to Ru-bipy dyes.[123] Half-squaraines have been tested in ZnO devices giving η = 0.27 %[154] and 0.53 %[155] with η = 3.54 %[156] in TiO_2 devices. The highest performance of a HfSQ dyed device was η = 5.5 % achieved by Connell *et al* (see **Figure 1.20**).[123] In the context of this thesis, HfSQ dyes can be used as a potential replacement to their more expensive Ru-bipy inorganic counterpart[146] because they absorb light in a similar part of the solar spectrum. The absorption of HfSQ dyes (450-500 nm) are also complementary to the highly absorbing squaraines (λ_{max} ~ 650 nm), resulting in a co-sensitised device with a better spectral response and improved device efficiency.[157] The HfSQ chromophore is also of interest as it can easily be modified as shown by Holliman *et al.*[157] Holliman exploited the synthetic flexibility of HfSQ dyes, by incorporating carboxylic anchoring groups at four different points to study and then studying the influence of the anchoring group position on DSC device performance.[157]

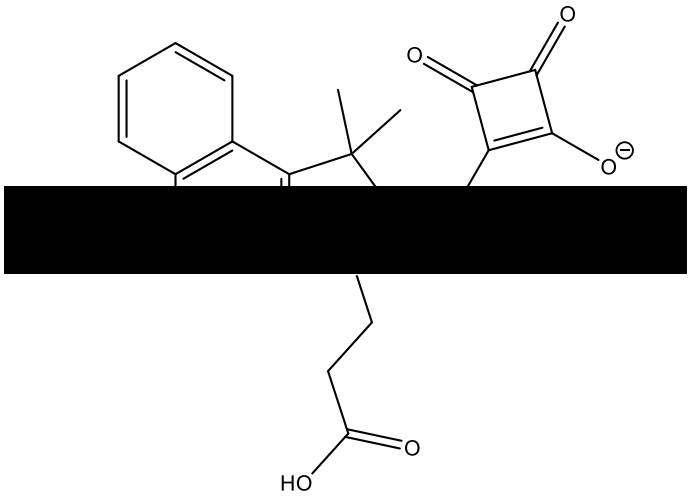

Figure 1.20 – Chemical structure of highest performing half-squaraine (achieved 5.5 %)[121]

Despite this, the self-assembly of dyes onto TiO_2 is a process not entirely understood. In this thesis we attempt to utilise the synthetic flexibility of the HfSQ chromophore to develop several bespoke dyes. These bespoke dyes have been designed to self-assemble in certain orientations on the TiO_2. Experimental and computational data

has been run side by side to determine exactly how HfSQ dyes self-assemble to TiO_2 during the sensitisation process. This knowledge has then been applied to other dyes and help develop our understanding of what happens at the TiO_2 surface during dye uptake. This could be further applied during co-sensitisation to further optimise the TiO_2 electrode. By optimising the co-sensitisation process the hope is to be able to produce devices with panchromatic (UV, visible and NIR) responses but at a much cheaper cost then other panchromatic sensitizers currently available.[157]

1.4.2.5 Self-assembly of Dye Anchoring groups

An example of self-assembly in DSC devices could be when we dye the photoelectrode for DSC devices. When a dye is initially introduced to the TiO_2 surface, the hydrophilic groups interact positively with the hydroxy groups of the TiO_2. At the same time the hydrophobic groups will point away and it's this interaction that will have a large influence on how the dye orientates itself on the TiO_2 (see **Figure 1.21**).

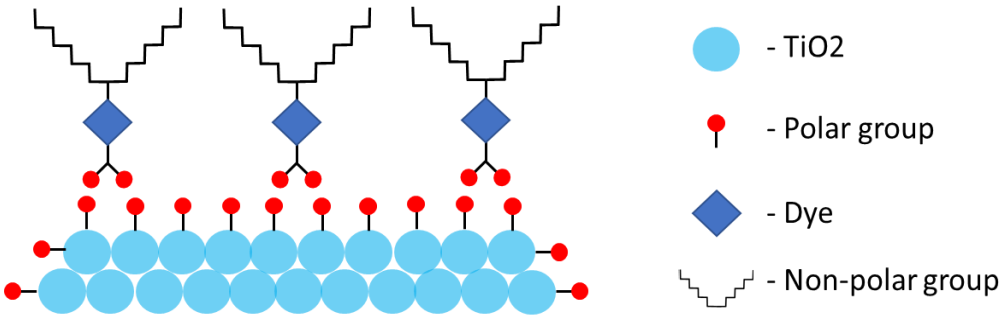

Figure 1.21 – Dye molecules "self-assembling" on TiO_2 in DSC devices

In an ideal scenario for DSC devices the mesoporous TiO_2 should have a monolayer of dye adsorbed on its surface.[158] Dye loading has a direct impact on short circuit current (J_{sc}). Too little dye and there will be gaps on the TiO_2 surface. These gaps are wasted space that could have been used to harvest more photons.[158] Too much dye means some of the dye molecules will not be directly bound to the TiO_2 but will interact with other dye molecules through aggregation. Therefore, the dye will absorb photons but be unable to inject the excited electrons into the CB of the TiO_2 limiting the amount of light that can reach dye molecules on the TiO_2 surface.

DSC dyes are designed to self-assemble to the TiO_2 surface. However, the way they organise themselves is down to what orientation is most energetically favourable, not necessarily the best for solar energy conversion. In most models it is assumed that

dyes self-assemble to TiO_2 at a perpendicular angle to the TiO_2. However, this has not yet been proven and it is possible that the dyes sit anywhere between 0 and 90° to the TiO_2 surface (see **Figure 1.22**) and hence the need for this investigation. Although this may seem trivial, the angle of the dyes can affect how much dye can be adsorbed which can have a huge impact on the efficiency of the device. Hence, dye orientation is looked at in more depth in chapter 2.

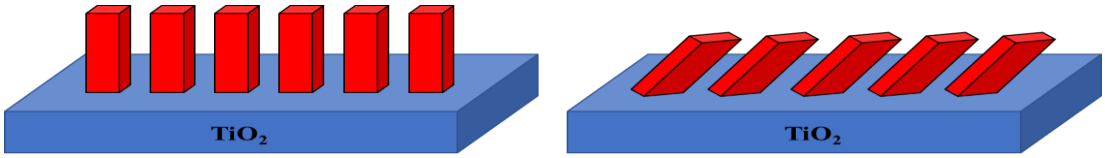

Figure 1.22 – Dye orientation on TiO_2. Dyes perpendicular to TiO_2 (left). Dyes at a 45° angle to TiO_2. Dyes in red, TiO_2 in blue.

Because, it is very important that we develop better understanding of how dyes assemble on the TiO_2 surface. The more understanding the greater the control on surface organisation.

A key part of dye absorption on to the metal oxide substrate is that the dye must have a chemical "anchor". Most DSC dyes are anionic and chemisorb to the TiO_2 surface by forming carboxylate ester bonds with the oxygen on the TiO_2 surface.[159] Understanding how the chemical anchors affect dyes (electron injection and recombination) and their ability to inject electrons into the metal oxide is imperative for the development of new bespoke DSC devices with record efficiencies.

Dye molecules can self-assemble at the metal oxide surface mainly through covalent bonding, but other interactions still take place including hydrogen bonding, electrostatic interaction, van der Waals forces, hydrophobic interaction or physical entrapment. Most of these interactions tend to be weak and unstable.[160] However, the strong covalent bonds ensure strong coupling. There are many theories for every linker group ever produced **Figure 1.23**[124] displays eight possibilities for just a carboxylic acid (COOH) anchor.

These acidic "anchors" all ester like linkages (bonds) with metal oxides by reacting with hydroxyl groups on the surface. This process is reversible, and the anchors are typically removed under basic conditions (pH > 9).[161]

The specific techniques which have been used to study anchoring points at the anchor substrate interface include Fourier transform infrared spectroscopy (FTIR) in

transmission geometry, attenuated total reflectance FTIR (ATR-FTIR) and photoelectron spectroscopy (PES).[162]

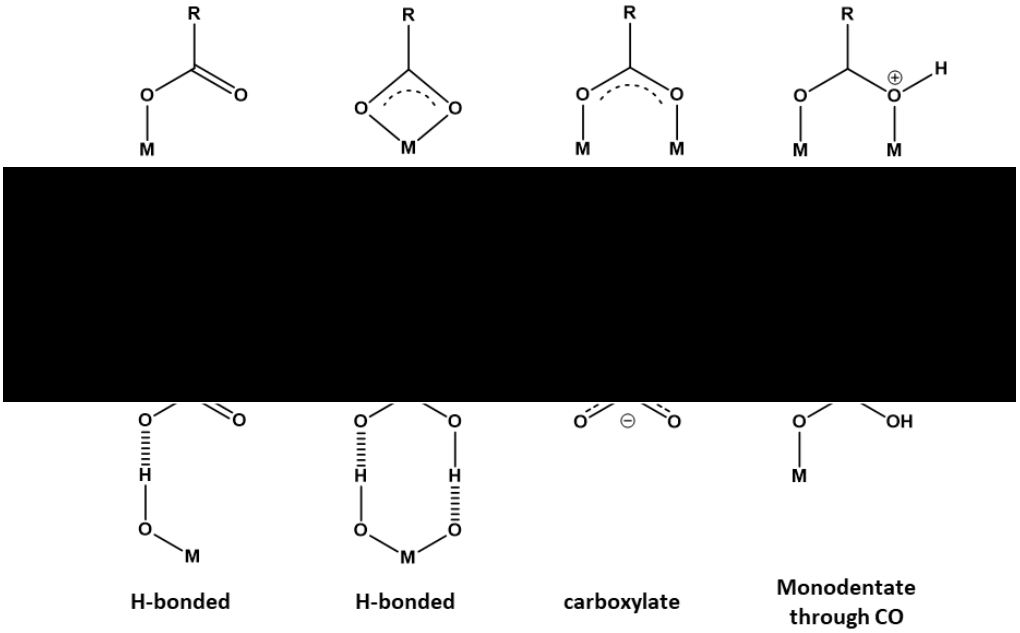

Figure 1.23 - Possible binding modes for a carboxylate anchor group binding to a metal oxide surface.[125] M represents the metal ion of the metal oxide surface (usually titanium or Zinc).[124]

FTIR uses infrared radiation to measure vibrational frequencies typically between 4000 and 400 cm^{-1}.[125] Unfortunately, transmission FTIR can give a poor signal to noise ratio and sample preparation can be complicated by the need to disperse the target analyte either in KBr or Nujol Mull. Because of this ATR-FTIR is more commonly used instead.[125] ATR-FTIR gives a better signal to noise ratio by allowing the IR wave to propagate near the TiO_2-dye interface enhancing the anchor-specific signal. This also means that samples can simply be placed on top of the ATR crystal which means that neat dye powder or dye sensitized TiO_2 films can easily be studied using this method. Using this technique, symmetrical and asymmetrical vibrational frequencies can be identified.[125] The difference between the two frequencies can be used to accurately to determine if the anchor is in a bidentate adsorption mode (either bridging or chelating) dominates; otherwise, a monodentate anchoring mode exists.[125] However making an efficient DSC dye doesn't just stop at the design stage, the adsorption process itself must be a primary consideration.[163]

1.4.3 Dying methods

1.4.3.1 Passive dying

As stated previously the process of passive dying involves submerging a mesoporous film such as TiO_2 in a known concentration of dye solution. Using passive (immersive) sensitisation of TiO_2, the process can take anywhere between 18 to 24 hours to ensure what appears to the naked eye to be full dye coverage. Though this timescale is not much of a problem for laboratory scale production of DSC devices, in an industrial environment the slow process could potentially create a bottleneck, limiting production and increasing costs. DSC devices would have to be made in batches rather than a continuous roll-to-roll (R2R) process. Scalability would also be an issue; small scale devices (e.g. 1 cm^2) only require a small amount of dye solution. However, a significant amount of dye would need to be used to passive dye larger devices. Dyes generally are one the most expensive parts of a DSC device. Therefore, having to use more will have a negative impact on the manufacturing cost.

Yet, the timescales for passive dyeing are too long (e.g. 18 h), if DSC devices are truly ever going to be considered as a low-cost photovoltaic technology then the process needs to be improved. In 2010, Holliman *et al.* reported the first ultra-fast (5 min) co-sensitization using N719 and SQ1 ($\eta = 7.9\%$).[164] The manufacture of the devices used a simple procedure (pumping dye solution through pre-sealed devices). This process operates by overcoming the mass transfer issues present within passive dyeing allowing it to be scaled for industry. This has since been developed further with ultra-fast tri-sensitization reported in 2012 by Holliman *et al*.[165]

1.4.3.2 Pump dying

As stated previously ultra-fast dying or "Pump" dying technique was developed in 2010 by Holliman *et al*.[164] This new dying method of dying relies on the device being sealed before dye sensitisation (see **Figure 1.24**). Once sealed the dye solution is pumped through a cavity in the counter electrode, this process is then repeated approximately 10-20 times depending on dye uptake. This method allows rapid uptake of a single dye as well as giving a fast and efficient procedure to co-sensitise devices in a way that could be easily replicated on a much larger scale. The next step is to choose a suitable dye or dyes that co-sensitise well. A good set of dyes proven to be efficient in co-sensitised systems are "squaraine" dyes (SQ-dye[166], HSQ3[167], HSQ4[167], SQ2[168] and SQ1[169]). In order for dyes to perform well in a co-sensitised system their

absorbances must be spectrally matched. If the dyes are not spectrally matched they will compete for the same photons therefore reducing efficiency.[170]

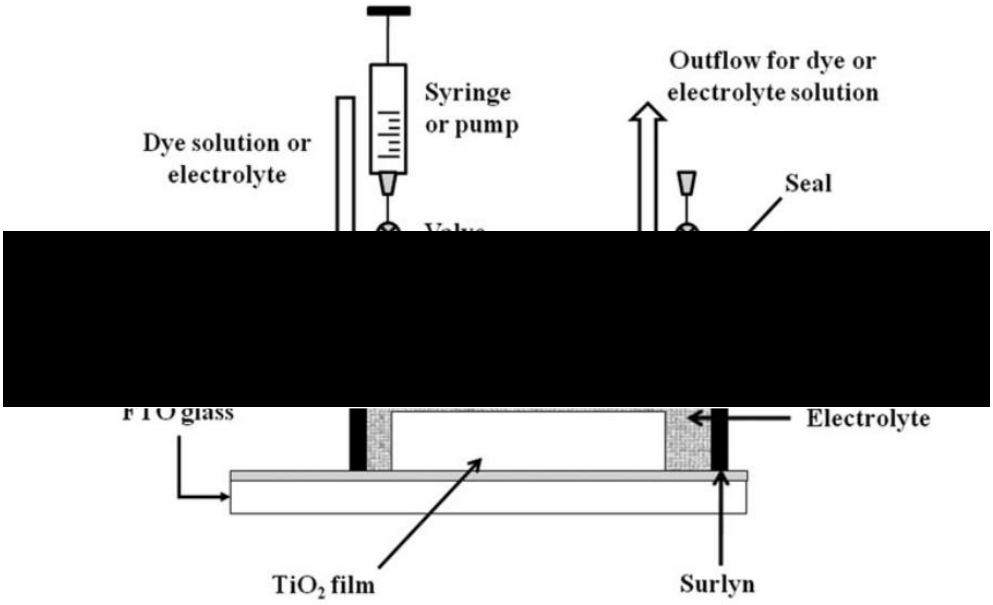

Figure 1.24 - Pump dying of a dye-sensitised solar cell as proposed by Holliman et al.[164]

1.4.4 Metal oxide semi-conductor scaffolds

A semi-conductor is "a material with a relatively small energy gap (3.2 eV for TiO_2 anatase)[171] between the conduction band (CB) and the valence band (VB)" thus allowing the material to conduct electricity when a small amount of energy is applied.[172] A generic example of a conductor, insulator and semiconductor can be seen in **Figure 1.25**.[172]

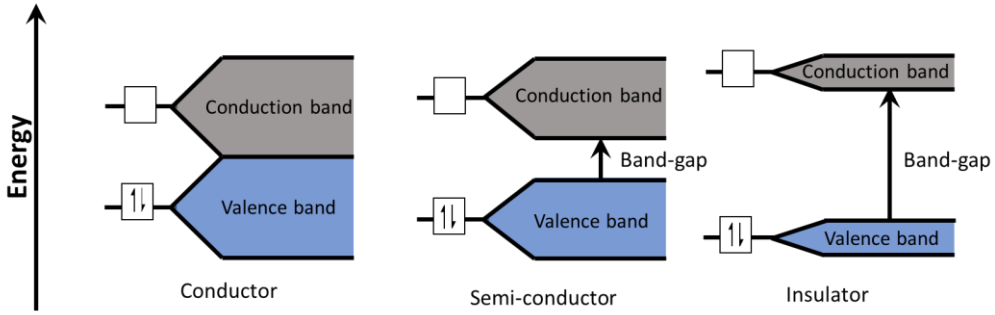

Figure 1.25 - Band structure diagrams for metals, semiconductors and insulators. Note that metals either have a single partially filled band or two overlapping bands. Diagram redrawn from literature[172]

The mesoporous metal oxide semi-conductor is also called the photoelectrode, photoanode or working electrode. This is responsible for accepting electrons from the dye LUMO and transporting them to the transparent conducting oxide (TCO). The photoelectrode is most commonly made up of a mesoporous semiconductor, sintered on a glass substrate that has been coated with a TCO (e.g. fluoride-doped tin oxide – FTO or indium-doped tin oxide - ITO).

As stated previously, a key breakthrough for DSC devices was when O'Regan and Grätzel decided to sensitise a mesoporous TiO_2 film with N3 dye.[99] They found that the combination of the high surface area of the TiO_2 and the "ideal spectral characteristics of the dyes" gave a sharp increase in efficiency over previous DSC devices.[99] Although the metal oxide film is not directly the main focus of this thesis, the following section is included because the metal oxide surface is the substrate for all the dye sorption studies.

Since O'Regan and Grätzel's 1991 Nature paper, mesoporous TiO_2 has become the most common semiconductor in DSC devices although, materials such as ZnO, Nb_2O_5, $SrTiO_3$, Zn_2SnO_4 and SnO_2 have also been used.[173,21] ZnO and SnO_2 are considered to be two of the most promising alternatives to TiO_2 for DSC devices.[174] ZnO and SnO_2 have an almost identical band-gaps to TiO_2 (i.e. 3.3 eV[174], 3.62 eV[175] and 3.2 eV[171] respectively). Both ZnO and SnO_2 have high electron mobilities (115-155 $cm^2V^{-1}s^{-1}$ for ZnO[176] and 100-200 $cm^2V^{-1}s^{-1}$ for SnO[177]). Despite this, the efficiencies of both SnO_2 and ZnO devices are yet to equal those of TiO_2. For ZnO devices it is thought to be down to the basic nature of ZnO being prone to attack from the acidic dye.[178] This attack forms agglomerates of Zn^{2+} reducing the performance of ZnO devices.[179,180] SnO_2 devices are reportedly more prone to fast recombination due to the positive shift of 300 mV of the conduction band.[181] SnO_2 devices are also plagued by intrinsic defects (Sn interstitial and O_2 vacancies) that act as trap sites for recombination to occur.[182]

By comparison, the properties of TiO_2 make it an ideal candidate for use in DSC devices[172]. TiO_2 is cheap to purchase, almost completely inert, resistant to photo-induced reactions and is non-toxic (e.g. it is used in sun cream).[183] TiO_2 crystallinity and pore size have both been reported to have a profound effect on dye loading,

electron transport, collection, recombination and therefore a devices performance.[184] For example, one of the main functions of the mesoporous TiO_2 is to maximise the light harvesting capability of a device by providing a large surface area for the dye to absorb. The more dye on the surface the more photons that can be absorbed.[12] Smaller TiO_2 nanoparticles will have a higher surface area, therefore increase dye loading. However, smaller TiO_2 nanoparticles will also have smaller pores reducing the ability of dye molecules or electrolyte to penetrate the TiO_2 layer. This problem is then reversed for larger TiO_2 nanoparticles.[185,186]

Though anatase is the most common form of TiO_2 found in DSC devices, TiO_2 itself can be found naturally in three forms (see **Figure 1.13**)[102], these are;

a) Rutile (Tetragonal geometry)[187]

b) Brookite (Orthorhombic geometry)[188]

c) Anatase (Tetragonal geometry)[189]

All three forms of TiO_2 have a band-gap greater than 3 eV[171,190,191] this means they absorb in the UV region ($\lambda < 400$ nm) of the AM 1.5 solar spectrum and thus ideal for use in DSC devices.[102]

1.4.5 The role of electrolytes

The role of the electrolyte is to regenerate the oxidised dye and transport the charge through the cell through a series of redox reactions.[192] Although other materials can be used I_3^- / I^- is the most common redox mediator used in liquid DSC devices.

$$I_3^- + 2e^- (TiO_2) \longrightarrow 3I^- \qquad \text{Equation 1.1}[193]$$

In order to transport electrons through the electrolyte triiodide is converted in to iodide as seen in equation 1.1.[194]

$$D \mid TiO_2 + h\nu \ ^{(i)} \longrightarrow D^* \mid TiO_2 \ ^{(ii)} \longrightarrow D^+ \mid TiO_2 + e^-_{cb} (TiO_2) \qquad \text{Equation 1.2}$$

$$D^+ \mid TiO_2 + E \ ^{(iii)} \longrightarrow D \mid TiO_2 + E^+ \qquad \text{Equation 1.3}$$

$$D^+ \mid TiO_2 + e^-_{cb} (TiO_2) \ ^{(iv)} \longrightarrow D \mid TiO_2 \qquad \text{Equation 1.4}$$

Key: $D \mid TiO_2$ = dye absorbed on TiO_2

The first part (i) of equation 1.2 shows a photon excitation of the dye leading to an electron being promoted from the dye HOMO to the dye LUMO. Equation 1.2 part

two (ii) shows the electron being injected into the conduction band of the TiO_2. Equation 1.3 (iii) shows the electron transfer between the electrolyte and the oxidised dye. This reduction regenerates the dye ready for a new cycle to begin. Equation 1.4 (iv) show the recombination pathway of a promoted electron returning to the dye.

In reality, using a I_3^-/I^- based electrolyte is one of the largest contributors to device efficiency loss. To regenerate the dye, electrons must travel from the electrolyte to the HOMO of the dye. This process takes several steps (with varying energy states, see **Figure 1.26**) converting between I_3^- and I^-.[194] Each of these steps including the regeneration of the dye itself usually requires an over-potential of ~ 0.5 eV. This over-potential drives the process forward but also limits the V_{oc} (~ 0.8 V).

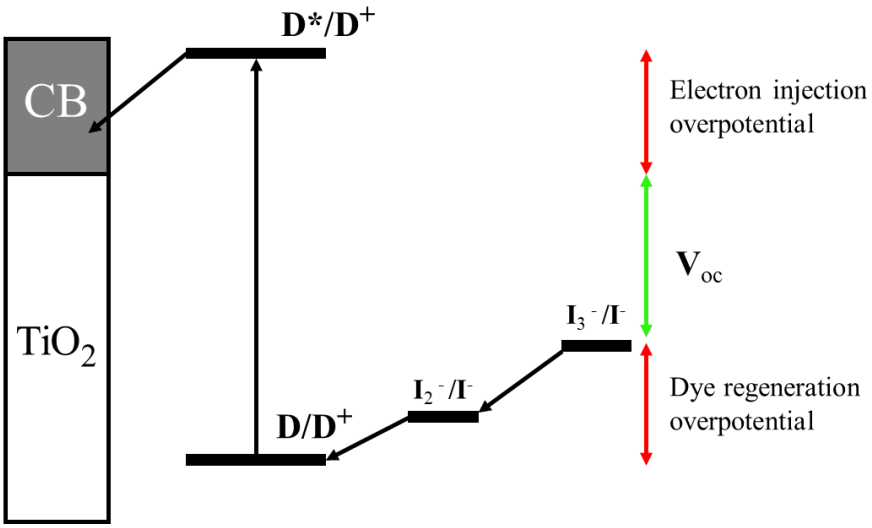

Figure 1.26 - Schematic of liquid DSC device showing the overpotential required for dye regeneration and the losses therein.

One way to reduce the losses occurred during the dye regeneration process has been reported to involve the use of single electron-change redox couples (e.g. based on Co complexes). The first reported use of a cobalt complex redox shuttle was by Nusbaumer *et al.* (2001).[195] Nusbaumer was able to achieve 2.2 % power conversion efficiency (PCE) using 2,6-bis(1′-butylbenzimidazol-2′-yl)pyridine, $[Co(dbbip)_2]^{3+/2+}$ and Z316 dye under one sun illumination. Nusbaumer was also able to achieve 5.2 % efficiency with the same material. However, this was under $1/10^{th}$ of a sun illumination. With the discrepancy being attributed to mass transport limitations when under at higher light intensities.[195] This result can be confirmed by a light soaking experiment carried out by O'Regan *et al.*[196] O'Regan found as the photocurrent increased so did the series resistance. This increase in series resistance was found to

be down to the diffusion resistance of the electrolyte. The more viscous the electrolyte the worse this problem becomes. This diffusion resistance limits overall device performance.[197]

Cobalt based redox shuttles have many advantages over its triiodide counterpart. Co complexes are less corrosive[198] and absorb less light in the visible region allowing more photons to reach the sensitiser. The redox potential of Co complexes is also tuneable allowing them to better match to the energy levels of the rest of the device.[197] It has also been noted that some dyes are more easily regenerated when a Co electrolyte is used.[197]

Like cobalt based redox shuttles, copper-based mediators are another promising alternative to triiodide-based electrolytes. Copper-based mediators are becoming more popular due to the extremely small driving force potentials required for dye regeneration, high photovoltages (~1.0 V) without any compromise on photocurrent densities and slower recombination rates. Recent work has also demonstrated that DSC devices containing copper-based electrolytes perform better under low light intensities compared to other types of thin film solar cells.[199]

For all of these liquid-based electrolytes, there needs to be a solvent, and this is usually an organic solvent (i.e. acetonitrile or 3-methoxypropionitrile) containing the redox mediator (e.g. iodide/triiodide or cobalt complex etc.). These solvents often have low boiling points, which can cause internal pressure potentially leading to leakage and instability problems. One way around this problem is to use a solid hole transport materials (HTMs) like those used in perovskites.[49]

Hole transport materials (HTMs) are another promising material that could potentially replace liquid electrolytes. HTMs are most commonly seen in PSC devices, with materials like spiro-OMeTAD[200] and TAT-^{t}BuSty[201] helping perovskite devices achieve PCEs greater than 20 %.[201–203] The first reported use of a HTM in a DSC device was in 1997 by Yanigida *et al.*[204] Yanigida used a polypyrole (HTM) instead of a typical liquid electrolyte. In doing so, they discovered that they were able to significantly reduce the amount of charge transfer processes required. HTM's can achieve much higher voltages (i.e. ~ 1.0 V) because they carry charge through a partially filled valence band. Therefore a smaller over-potential is required.[4]

HTMs are synthetically versatile and can be cheap to synthesise although, the widely used spiro-OMeTAD is expensive (e.g. *ca.* £300/g). Despite this, solid state dye-sensitised solar cell (ssDSC) devices are still behind their liquid counterparts with a current best efficiency of 11.0 %[205] compared to 14.7 %[1] for a liquid (Co electrolyte) device. However, in this thesis, devices have focussed on liquid electrolytes to try to understand the effects of any interaction between the sulphur heteroatom in the dye with the iodide-based electrolyte. An example of an iodide redox shuttle, a cobalt redox mediator and a solid HTM can be seen in **Figure 1.13**.

Understanding what's happening at the TiO_2 interface is critical to improving DSC device performance. Though self-assembly of sensitisers is well researched, the orientation and position of the sensitisers and its effect on performance is not as well studied. Developing novel materials and methods of dyeing can all effect how the sensitisers assemble to the TiO_2. How these materials orientate themselves influences light absorption, dye injection as well as how quickly and efficiently the dyes can be regenerated.

2 Experimental

2.1 Materials and General Techniques

All chemicals were purchased from Sigma Aldrich and used as supplied unless otherwise stated. Anhydrous solvents were used as supplied. NMR spectra were recorded on a Bruker AC500 and Avance III at 500 and 400 MHz for ^{1}H and 125 and 101 MHz for ^{13}C. Chemical shifts (δ) are given in ppm relative to tetramethyl silane and J values (in Hz) refer to H coupling constants unless otherwise stated. Mass spectra were recorded at the EPSRC National Mass Spectrometry service at the University of Swansea. Attenuated infrared spectra were recorded on a Perkin Elmer Spectrum Two FT-IR spectrometer (resolution: 8 cm^{-1}, 16 scans for dye powder, 300 scans for TiO_2 films). UV-Vis spectra and ε were measured on a Perkin Elmer Lambda 35 UV/Vis spectrometer. Flash chromatography purification was done using a Teledyne Isco Combiflash Nextgen 300+ instrument. X-ray photoelectron spectroscopy was measured by myself and Dr James McGettrick in the College of Engineering, Swansea University. Density functional theory calculations were carried out by Dr Dawn Geatches, Dr Sebastian Metz and Dr Kakali Sen of the scientific computing department at STFC Daresbury laboratory (Daresbury, Warrington - UK).

2.2 Angle-resolved X-ray photoelectron spectroscopy (ARXPS)

XPS data were recorded on an Axis Supra XPS using a monochromated Al K_α source and large area slot mode detector (300 x 800μm analysis area). Data were recorded using a charge neutralizer to limit differential charging and binding energies were calibrated to the main hydrocarbon peak (BE 284.8 eV). Survey scans were performed using a pass energy of 160 eV and high resolution spectra were recorded using a 0.1 eV step size and a pass energy of 20 eV. Number of scans for each element was as follows: carbon (8), nitrogen (8), titanium (2), oxygen (3) and sulphur (20). Data were fitted using CASA software with Shirley backgrounds.

2.3 X-ray crystallography

In each experiment a suitable crystal was selected and mounted on a MITIGEN holder in perfluoroether oil on a Rigaku FRE+ equipped with either HF Varimax confocal mirrors (**D3**) or VHF Varimax confocal mirrors (**4**, **5**, **7** and **D4**) and an AFC12 goniometer and HG Saturn 724+ detector (**4**, **5**, **7** and **D3**) or HyPix

6000 detector (**D4**). The crystal was kept at T ¼ 100(2) K during data collection. Using Olex2 the structure was solved with the ShelXT44 structure solution program, using the Intrinsic Phasing solution method. The model was re□ned with ShelXL45 using Least Squares Minimisation. All non-hydrogen atoms were refined anisotropically and all hydrogen atom positions were calculated geometrically except those bonded to

2.4 Dye synthesis

Preparation of 3-dodecyl-2-methylbenzothiazol-3-ium bromide (1)[206]

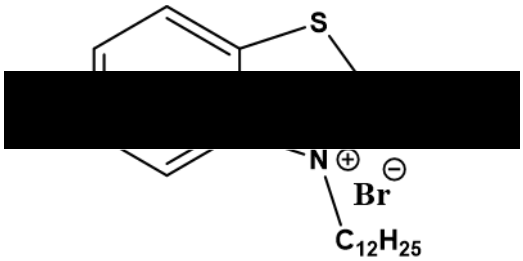

A mixture of 2-methylbenzothiazole (5.0 g, 33.51 mmol) and 1-bromododecane (16.70 g, 67.02 mmol) was heated for 48 h under nitrogen in anhydrous reagent alcohol (80 ml). After cooling, the solvent was removed *in vacuo.* Diethyl ether (100 ml) was added to the round bottom flask and the mixture was refluxed for 8 h. After cooling the mixture was filtered into a thimble and the solid was washed with diethyl ether using a soxhlet for 8 h to give a white solid. (Yield 3.31 g, 24.79 %)

^{1}H NMR (400 MHz, DMSO) δ 8.45 (1H, d, -Ph-**H-** J 8.1), 8.34 (1H, d, -Ph-**H-**, J 8.4), 7.90 (1H, t, -Ph-**H-**, J 7.8), 7.81 (1H, t, -Ph-**H-**, J 7.7), 4.71 (2H, t, -**CH$_2$**-CH$_3$-), 3.21 (3H, s, -**CH$_3$**-CHCC-), 1.94 – 1.73 (2H, m, -CH$_2$-**CH$_2$**-CH$_2$-), 1.43 (2H, dd, -CH$_2$-**CH$_2$**-CH$_2$-, J 14.4, 7.2), 1.24 (15H, s, alkyl chain), 0.86 (3H, t, -CH$_2$-**CH$_3$**- J 6.6).

^{13}C NMR (101 MHz, DMSO) δ 177.07, 140.83, 129.36, 129.11, 128.10, 124.64, 116.87, 49.17, 31.28, 28.99, 28.97, 28.91, 28.84, 28.68, 28.57, 27.78, 25.86, 22.08, 16.80, 13.95.

MS (FTMS $^{+}$) $[M - Br]^{+}$ calculated = 318.00, $[M - Br]^{+}$ observed = 318.00

Preparation of 3,4-Diethoxy-3-cyclobutene-1,2-dione (2)[123]

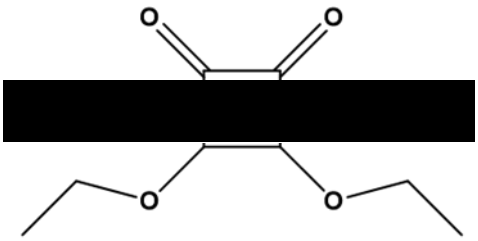

Squaric acid (5 g, 44 mmol) was suspended in ethanol (50 ml) and refluxed for 3 h. The reaction was cooled to room temperature and the solvent was removed *in vacuo*. The white solid material obtained from the reaction was dissolved in fresh ethanol (50 ml), the mixture was heated under reflux for 30 min and the solvent was removed *in vacuo*. This step was repeated three times. The product was used without any further purification (Yield 7.50 g, quantitative).

^{1}H NMR spectrum (400 MHz, DMSO): δ 4.66 (2 H, q, CH_3-**CH_2**-O-, J 7.1), 1.38 (3 H, t, **CH_3**-CH_2-O-, J 7.1).

^{13}C NMR (101 MHz, DMSO) δ 189.52, 184.11, 70.64, 15.68.

MS (TOF MS $^{+}$) M^{+} calculated = 171.07, M^{+} observed = 171.07, m/e

Preparation of 1-dodecyl-2,3,3-trimethylindol-1-ium bromide (3)[207]

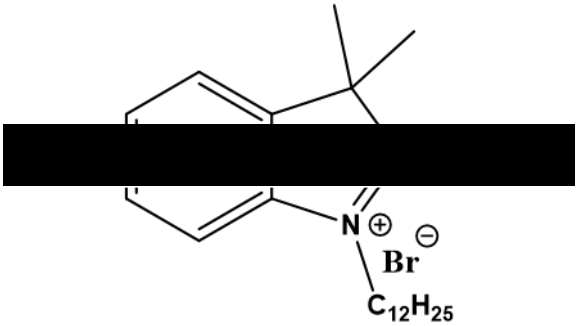

A mixture of 2,3,3-trimethylindolenine (5.00 g, 31.40 mmol) and 1-bromododecane (15.65 g, 62.80 mmol) was heated overnight under nitrogen in anhydrous acetonitrile (80 ml). After cooling, the solvent was removed *in vacuo*. Diethyl ether (100 ml) was added to the round bottom flask and the mixture was refluxed for 8 h. The mixture was filtered through a thimble and the solid was washed with diethyl ether using a soxhlet for 8 h to give a purple solid. (Yield 8.31 g, 64.77 %)

^{1}H NMR (400 MHz, DMSO) δ 8.02 – 7.93 (1 H, m, -Ph-**H**), 7.88 – 7.79 (1 H, m, -Ph-**H**), 7.67 – 7.59 (2 H, m, **H**-Ph-**H**), 4.45 (2 H, t, -**CH$_2$**-CH$_2$-, J 7.7), 2.85 (3 H, s, **CH$_3$**-C-), 1.91 – 1.76 (2 H, m, -CH$_2$-**CH$_2$**-), 1.54 (6 H, s, **CH$_3$**-C-**CH$_3$**), 1.47 – 1.37 (2 H, m, -**CH$_2$**-CH$_3$), 1.24 (12 H, s, alkyl chain), 0.85 (3 H, t, -CH$_2$-**CH$_3$**, J 6.6).

^{13}C NMR (101 MHz, DMSO) δ 196.76, 174.93, 138.98, 137.45, 133.51, 131.16, 130.19, 128.88, 127.73, 123.90, 113.83, 55.96, 48.33, 34.12, 29.21, 29.14, 29.07, 28.97, 27.92, 26.31, 24.92, 22.10, 14.30

MS (FTMS $^{+}$) $[M\text{-}C_2H_4]^+$ calculated = 300.51, $[M\text{-}C_2H_4]^+$ observed = 300.27, m/e

Preparation of 3-(2-carboxyethyl)-2-methylbenzothiazol-3-ium bromide (4)[208,209]

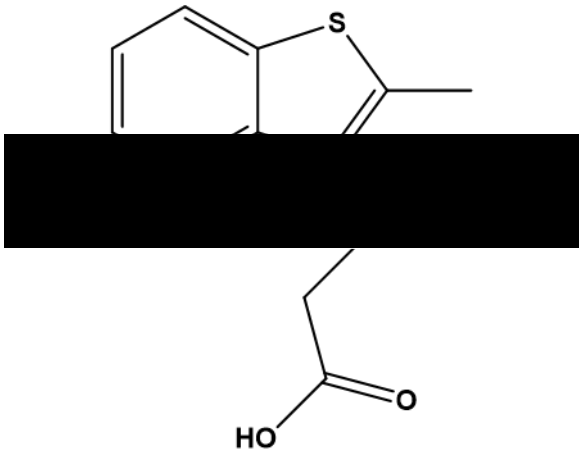

A mixture of 2-methylbenzothiazole (2.00 g, 13.40 mmol) and 3-bromopropionic acid (5.00 g, 32.67 mmol) was heated for 48 h under nitrogen under in anhydrous reagent alcohol (80 ml). After cooling, the solvent was removed *in vacuo*. Diethyl ether (100 ml) was added to the round bottom flask and the mixture was refluxed for 8 h. After cooling the mixture was filtered into a thimble and the solid was washed with diethyl ether using a soxhlet for 8 h to give a white/ pink solid. (Yield 2.68 g, 66.17 %)

^{1}H NMR (400 MHz, DMSO) δ 8.46 (1H, d, -Ph-**H** J 8.1), 8.36 (1H, d, -Ph-**H** J 8.5), 7.88 (1H, t, -Ph-**H** J 7.8), 7.80 (1H, t, -Ph-**H** J 7.7), 4.90 (2H, t, -CH_2-**CH_2**- J 7.2), 3.26 (3H, s, -**CH_3**-CHCC-), 2.99 (2H, t, -CH_2-**CH_2**- J 7.2).

^{13}C NMR (101 MHz, DMSO) δ 178.62, 171.93, 141.20, 129.85, 129.40, 128.53, 125.12, 117.40, 45.46, 32.24, 17.59.

MS (TOF MS ES $^{+}$) $[M]^{+}$ calculated = 222.06, $[M]^{+}$ observed = 222.06, m/e

Preparation of 1-(2-carboxyethyl)-2,3,3-trimethyl-indol-1-ium bromide (5)[209]

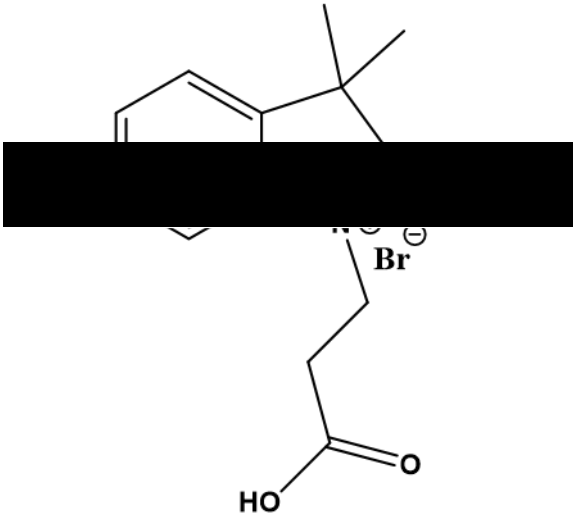

A mixture of 2,3,3-trimethylindolenine (5.0 g, 31.40 mmol) and 3-bromopropionic acid (10.00 g, 65.37 mmol) was heated overnight under nitrogen in anhydrous toluene (80 ml). After cooling, the solvent was removed *in vacuo.* Diethyl ether (100 ml) was added to the round bottom flask and the mixture was refluxed for 8 h. After cooling the mixture was filtered into a thimble and the solid was washed with diethyl ether using a soxhlet for 8 h to give a purple solid. (Yield 7.13 g, 72.76 %)

1H NMR (400 MHz, DMSO) δ 8.00 (1H, dd, -Ph-**H**, J 6.0, 2.9), 7.85 (1H, dd, -Ph-**H**, J 5.3, 3.3), 7.67 – 7.58 (2H, m) **H**-Ph-**H**, 4.66 (2H, t, -**CH$_2$**-CH$_2$-, J 7.0), 2.99 (2H, t, -CH$_2$-**CH$_2$**-, J 7.0), 2.87 (3H, **CH$_3$**-C-, s), 1.54 (6H, s, -**CH$_3$**-C-**CH$_3$**-).

13C NMR (101 MHz, DMSO) δ 198.38, 171.99, 142.23, 141.30, 129.82, 129.39, 123.96, 116.04, 54.74, 44.03, 31.58, 22.35, 14.90.

MS (FTMS $^+$) [M$^+$] calculated = 232.30, [M$^+$] observed = 232.13, m/e

Preparation of 3-((3-dodecylbenzothiazol-2-ylidene)methyl)-4-ethoxycyclobut-3-ene-1,2-dione (6)

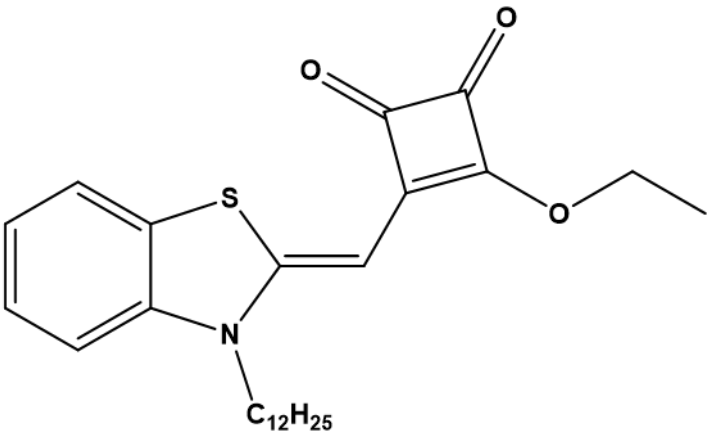

2.00 g (5.02 mmol) of 3-dodecyl-2-methylbenzothiazol-3-ium bromide (**1**) and (0.86 g, 5.05 mmol) of 3,4-diethoxy-3-cyclobutene-1,2-dione (**2**) and triethylamine (2 ml) were dissolved in ethanol (25 ml) and vigorously refluxed for 30 minutes. The solvent was removed from the red solution *in vacuo* and the crude product was purified by column chromatography (SiO_2) with ethyl acetate and petroleum ether (80:20) as eluent. (Yield 1.03 g, 46.61 %).

^{1}H NMR (400 MHz, DMSO): δ 7.81 (1H, d, -Ph-**H**, J 7.8), 7.48 (1H, d, -Ph-**H**, J 8.2), 7.40 (1H, t, Ph-**H**, J 7.7), 7.22 (1H, t, -Ph-**H**, J 7.6), 5.54 (1H, s, -C-**CH**-C-), 4.75 (2H, q, -**CH$_2$**-CH_3-, J 7.0), 4.16 (2H, t, -**CH$_2$**-CH_2-, J 7.3), 1.72 – 1.59 (2H, m, -**CH$_2$**-CH_3-), 1.43 (3H, t, -**CH$_3$**-CH_2- J 7.1), 1.22 (16H, s, alkyl chain), 0.84 (3H, t, -**CH$_3$**-CH_2- J 6.7).

^{13}C NMR (126 MHz, DMSO): δ 180.93, 180.47, 154.81, 136.34, 122.14, 122.05, 118.71, 117.22, 106.15, 74.26, 64.90, 41.05, 27.16, 24.85, 24.78, 24.71, 24.58, 24.52, 22.16, 22.01, 17.94, 11.17, 9.37.

MS (FTMS $^{+}$) [M^{+}] calculated = 441.13, [M^{+}] observed = 441.13, m/e

FT-IR (ATR) ν/cm-1 2957 (m), 2920 (s), 2851 (s), 1724 (s), 1675 (s), 1470 (m), 741 (s), 718 (s)

UV-visible λ_{max} 441 nm (47,804 M^{-1} cm^{-1} ± 2,175 M^{-1} cm^{-1}) in ethanol.

Preparation of 3-((1-dodecyl-3,3-dimethylindolin-2-ylidene)methyl)-4-ethoxycyclobut-3-ene-1,2-dione (7)[210]

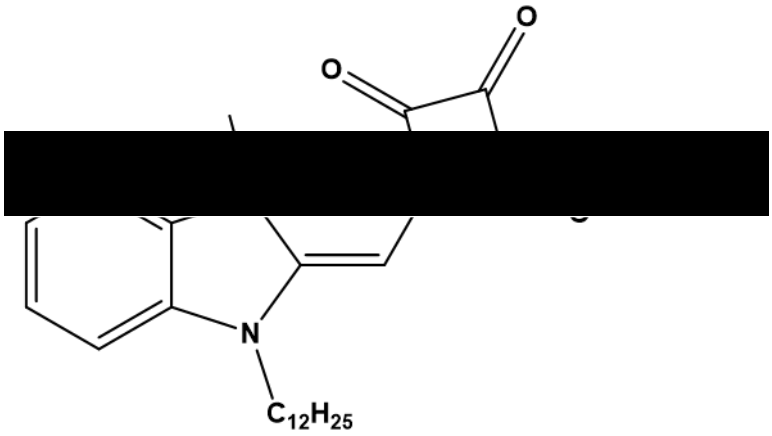

3.00 g (7.34 mmol) of 1-dodecyl-2,3,3-trimethyl-indol-1-ium bromide (**3**), 1.25 g (7.34 mmol) of 3,4-Diethoxy-3-cyclobutene-1,2-dione (**2**) and triethylamine (3 ml) were dissolved in 25 ml of ethanol and refluxed for 30 minutes under nitrogen. The solvent was removed from the green solution and the crude product was purified by column chromatography (SiO_2) with petroleum ether and ethyl acetate (80:20) as eluent. (Yield 1.39 g, 41.87 %).

^{1}H NMR (400 MHz, DMSO) δ 7.43 (1H, d, -Ph-**H**, J 7.3), 7.28 (1H, t, -Ph-**H**, J 7.6), 7.17 (1H, d, -Ph-**H**, J 7.9), 7.06 (1H, t, -Ph-**H**, J 7.4), 5.36 (1H, s, -C-**CH**-C-), 4.81 (2H, q, -**CH$_2$**-CH_3, J 7.1), 3.90 (2H, t, -**CH$_2$**-CH_2- J 7.2), 1.70 – 1.58 (2H, m, -CH_2-**CH$_2$**-), 1.54 (6H, s, **CH$_3$**-C-**CH$_3$**), 1.44 (3H, t, J 7.1), 1.31 (4H, s, alkyl chain), 1.21 (10H, s, alkyl chain), 0.83 (3H, t, -CH_2-**CH$_3$**-, J 6.7).

^{13}C NMR (101 MHz, DMSO) δ 192.16, 187.69, 186.22, 172.55, 167.74, 142.42, 140.31, 127.83, 122.51, 121.93, 109.19, 80.70, 69.72, 47.41, 42.11, 31.24, 28.79, 28.77, 28.60, 28.53, 26.47, 26.03, 25.69, 22.04, 15.64, 13.92

FT-IR (ATR) ν/cm^{-1} 2974 (br), 2958 (br), 2924 (br), 2845 (br), 1770 (s), 1717 (s), 1687 (s), 1534 (s), 1514 (s), 1424 (s), 1290 (s).

UV-visible λmax 424 nm (71,704 M^{-1} cm^{-1} ± 1,993 M^{-1} cm^{-1}) in ethanol.

Preparation of 3-((3-dodecylbenzothiazol-2-ylidene)methyl)-4-hydroxycyclobut-3-ene-1,2-dione (D1)

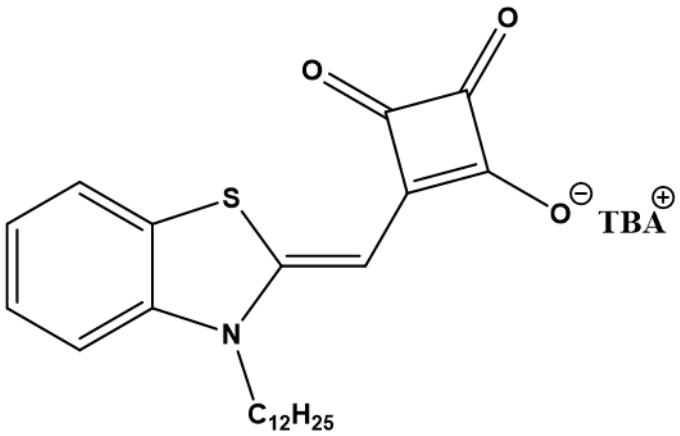

3-((3-dodecylbenzothiazol-2-ylidene)methyl)-4-ethoxycyclobut-3-ene-1,2-dione (**6**) (1.00 g, 2.27 mmol) was dissolved in ethanol (10 ml) and was heated to reflux. Tetrabutylammonium hydroxide solution (2 ml, 40 %) was added and the solution was refluxed for 1 h and the resulting mixture was purified by column chromatography (SiO_2) with ethyl acetate and petroleum ether as eluent to remove impurities. Pure product can then be run off the column with a dichloromethane: methanol mix (90:10). Yield (0.29 g, 19.46 %)

^{1}H (400 MHz, DMSO) δ 7.44 (1H, d, -Ph-**H**-, J 7.6), 7.17 (1H, t, -Ph-**H**-, J 7.7), 7.03 (1H, d, -Ph-**H**-, J 8.1), 6.91 (1H, t, -Ph-**H**-, J 7.5), 5.39 (1H, s, -C-**CH**-C-), 3.83 (2H, t, -CH_2-**CH_2**- J 7.5), 1.23 (14 H, s, alkyl chain), 0.85 (3 H, t, -CH_2-**CH_3**- J 6.7).

^{13}C (101 MHz, DMSO) δ 208.61, 194.54, 179.30, 147.80, 142.16, 126.31, 126.00, 121.17, 120.79, 109.26, 81.67, 57.52, 43.94, 31.29, 28.99, 28.95, 28.83, 28.69, 26.23, 25.79, 23.06, 22.09, 19.21, 13.95, 13.49.

MS (FTMS $^{-}$) $[M\text{-}TBA]^{-}$ calculated = 412.19, $[M\text{-}TBA]^{-}$ observed = 412.20, m/e

FT-IR (ATR) ν/cm^{-1} 3334 (br), 2958 (m), 2923 (s), 2872 (m), 2851 (m), 1748 (s), 1670 (s), 1524 (m).

UV-visible λ_{max} 446 nm (31,225 M^{-1} cm^{-1} ± 231 M^{-1} cm^{-1}) in ethanol.

Preparation of 3-((1-dodecyl-3,3-dimethylindolin-2-ylidene)methyl)-4-hydroxycyclobut-3-ene-1,2-dione (D2)[210]

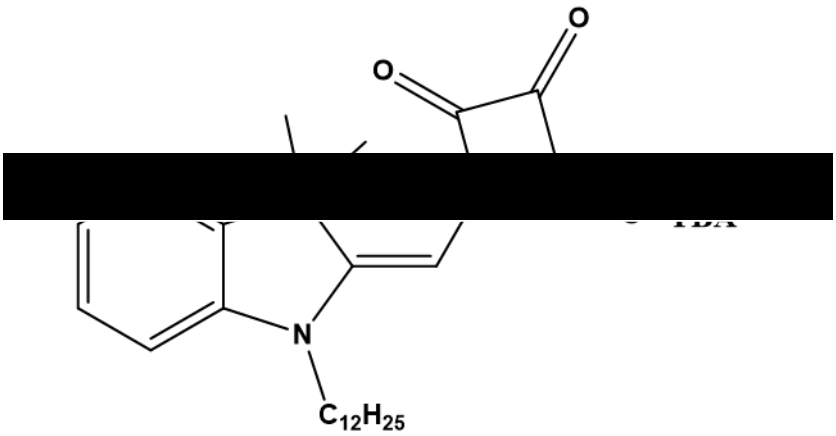

3-((1-dodecyl-3,3-dimethylindolin-2-ylidene)methyl)-4-ethoxycyclobut-3-ene-1,2-dione (**7**) (1.00 g, 2.21 mmol) was dissolved in ethanol (10 ml) and heated under reflux. Tetrabutylammonium hydroxide solution (2 ml, 40 %) was added and the mixture was refluxed for 1 h. After cooling the solvent was removed *in vacuo* and the product was obtained as a red solid after purification by column chromatography (SiO_2) with ethyl acetate and petroleum ether as eluent to remove impurities. Pure product can then be run off the column with a dichloromethane: methanol mix (90:10). Yield (0.48 g, 32.65 %)

^{1}H NMR (500 MHz, DMSO) δ 7.23 (1H, d, -Ph-**H**, J 7.3), 7.13 (1H, td, -Ph-**H**, J 7.8, 1.2), 6.82 (2H, t, **H**-Ph-**H** J 7.5), 5.39 (1H, s, -C-**CH**-C-), 3.69 (2H, t, -**CH$_2$**-CH_2-, J 7.3), 1.59 (8H, m**,** J 7.3, 6.2), 1.55 (6H, s, CH_3-C-CH_3), 1.22 (12H, s, alkyl chain), 0.85 (3H, t, -CH_2-**CH$_3$**- J 6.9).

^{13}C NMR (126 MHz, DMSO) δ 210.50, 195.58, 179.18, 157.86, 144.52, 140.30, 127.68, 122.00, 119.85, 107.08, 84.66, 49.06, 46.21, 41.93, 31.75, 29.46, 29.43, 29.37, 29.31, 29.15, 28.06, 26.86, 26.17, 23.53, 22.56, 19.68, 14.42, 13.96.

MS (FTMS $^-$) $[M\text{-}TBA]^-$ calculated = 422.27, $[M\text{-}TBA]^-$ observed = 422.85, m/e

FT-IR (ATR) ν/cm^{-1} 2954 (m), 2924 (m), 2856 (m), 1748 (s), 1552 (vs), 1460 (m), 1360 (m), 1308 (m)

UV-visible λmax 423 nm (38,218 M^{-1} cm^1 ± 478 M^{-1} cm^1) in ethanol.

3-(2-((2-ethoxy-3,4-dioxocyclobut-1-en-1-yl)methylene)benzothiazol-3-yl)propanoic acid (D3)

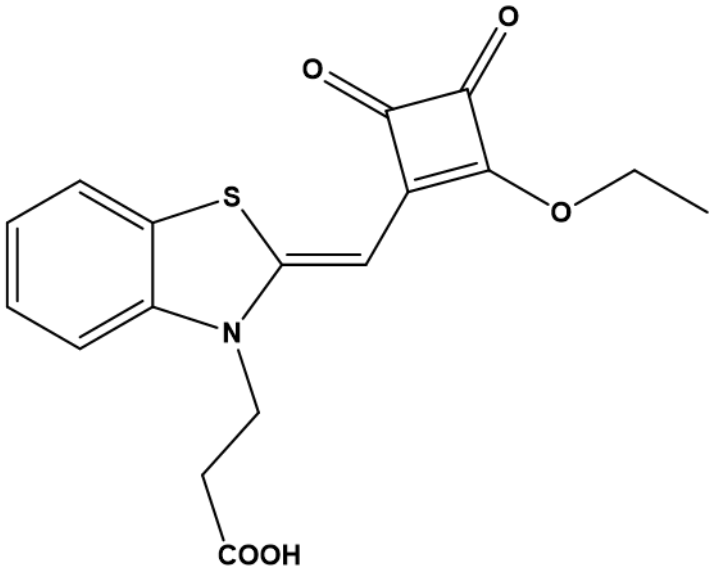

2.00 g (6.62 mmol) of 3-(2-carboxyethyl)-2-methylbenzothiazol-3-ium bromide (**4**), 1.13 g (6.64 mmol) of 3,4-Diethoxy-3-cyclobutene-1,2-dione (**2**) and triethylamine (2 ml) were dissolved in 25 ml of ethanol and refluxed under nitrogen for 30 minutes. After cooling the solvent was removed was removed *in vacuo* and the crude product was purified by column chromatography (SiO_2) with dichloromethane and methanol (90:10) as eluent. (Yield 1.46 g, 63.76 %).

^{1}H NMR (400 MHz, DMSO) δ 7.80 (1H, d, -Ph-**H**, J 7.8), 7.48 (1H, d, -Ph-**H**, J 8.2), 7.39 (1H, t, -Ph-**H**, J 7.3), 7.21 (1H, t, -Ph-**H**, J 7.3), 5.59 (1H, s, -C-**CH**-C-), 4.75 (2H, q, -**CH$_2$**-CH_3- J 7.1), 4.37 (2H, t, -**CH$_2$**-CH_2-, J 7.2), 2.67 (2H, t, -CH_2-**CH$_2$**-, J 7.2), 1.43 (3H, t, -CH_2-**CH$_3$**-, J 7.1).

^{13}C NMR (101 MHz, DMSO) δ 185.22, 184.68, 172.19, 171.89, 158.97, 140.63, 127.11, 125.74, 123.53, 123.33, 112.10, 79.27, 69.29, 41.19, 31.15, 15.69

MS (FTMS $^{+}$) $[M+H]^+$ calculated = 346.07, $[M+H]^+$ observed = 346.07, m/e

FT-IR (ATR) ν/cm^{-1} 2925 (br), 1770 (s), 1710 (s), 1676 (s), 1496 (s), 1410 (s).

UV-visible λ_{max} = 424 nm (18,411 M^{-1} cm^{-1} ± 510 M^{-1} cm^{-1}) in ethanol.

Preparation of 3-(2-((2-ethoxy-3,4-dioxocyclobut-1-en-1-yl)methylene)-3,3-dimethylindolin-1-yl)propanoic acid (D4)

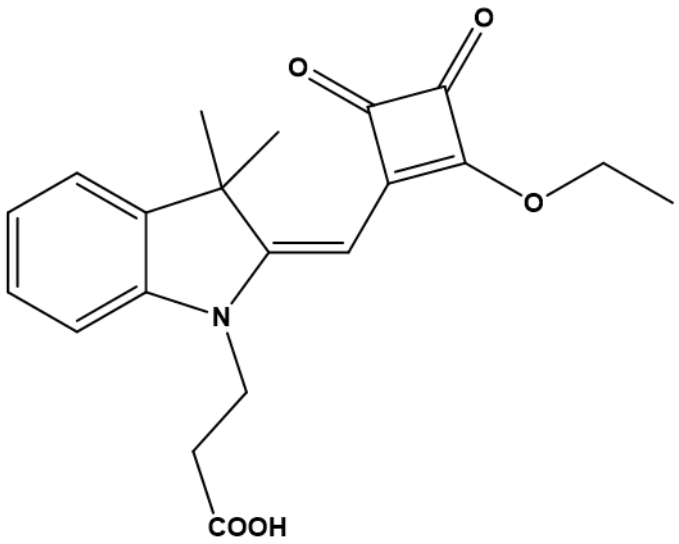

2.00 g (6.41 mmol) of 1-(2-carboxyethyl)-2,3,3-trimethyl-indol-1-ium bromide (**5**), 1.09 g (6.41 mmol) of 3,4-Diethoxy-3-cyclobutene-1,2-dione (**2**) and triethylamine (2 ml) were dissolved in 25 ml of ethanol and refluxed under nitrogen for 30 minutes. The solvent was removed *in vacuo* and the crude product was purified by column chromatography (SiO_2) with dichloromethane and methanol (90:10) as eluent. (Yield 0.80 g, 35.09 %).

^{1}H NMR (400 MHz, DMSO) δ 7.42 (1 H, d, -Ph-**H,** J 7.3), 7.28 (1 H, t, -Ph-**H,** J 7.7), 7.18 (1 H, d, -Ph-**H,** J 7.9), 7.06 (1 H, t, -Ph-**H,** J 7.4), 5.39 (1 H, s, -C-**CH**-C-), 4.81 (2 H, q, -**CH$_2$**-CH$_3$-, J 7.1), 4.15 (2 H, t, -**CH$_2$**-CH$_2$-, J 7.0), 2.61 (2 H, t, -CH$_2$-**CH$_2$**-, J 7.0), 1.54 (6 H, s, -**CH$_3$**-C-**CH$_3$**-), 1.44 (3 H, t, -CH$_2$-**CH$_3$**-, J 7.1).

^{13}C NMR (101 MHz, DMSO) δ 192.08, 188.09, 186.61, 172.75, 167.35, 142.02, 140.26, 127.79, 122.53, 121.90, 109.25, 81.08, 69.82, 47.37, 45.66, 30.95, 26.49, 15.68.

MS (FTMS $^{+}$) [M^{+}] calculated = 355.14, [M^{+}] observed = 355.04, m/e

FT-IR (ATR) ν/cm^{-1} 3425 (br), 2976 (m), 2933 (m), 2682 (w), 1770 (vs), 1722 (s), 1702 (s), 1535 (s), 1309 (s) 1175 (s), 1035 (s), 930 (s), 754 (s).

UV-visible λ_{max} 423 nm (51,672 M^{-1} cm^{-1} ± 1,519 M^{-1} cm^{-1}) in ethanol.

Preparation of 3-(2-((2-hydroxy-3,4-dioxocyclobut-1-en-1-yl)methylene)benzothiazol-3-yl)propanoic acid (D5)

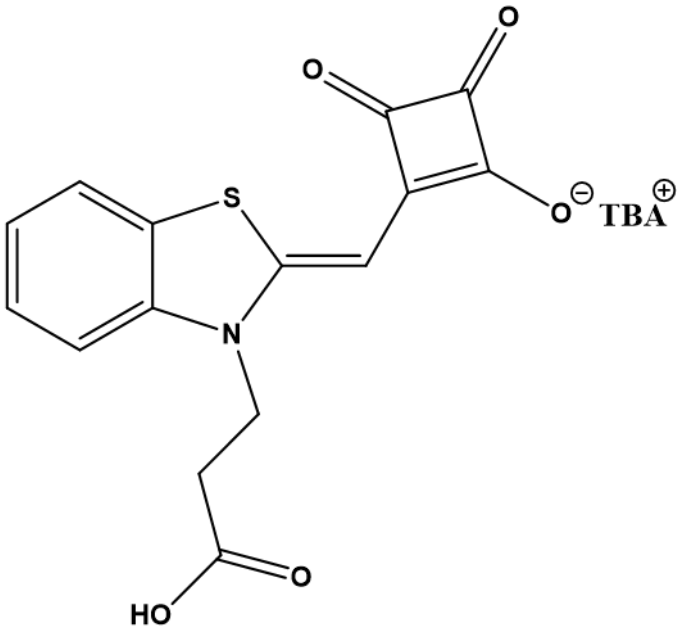

3-(2-((2-ethoxy-3,4-dioxocyclobut-1-en-1-yl)methylene)benzothiazol-3-yl)propanoic acid (**D3**) (1.00 g, 1.45 mmol) was dissolved in ethanol (10 ml) and heated under reflux. Tetrabutylammonium hydroxide (1 ml, 40 %) was added and the mixture was refluxed for 1 h. After cooling the solvent was removed in vacuo and the solvent was removed *in vacuo* and the resulting mixture was purified by column chromatography (SiO_2) with dichloromethane and methanol (90:10) as eluent. After purification the solution was concentrated, and the pure product precipitated with ethanol. (Yield 0.32 g, 39.51 %)

^{1}H NMR (500 MHz, DMSO) δ 7.44 (1H, d, -Ph-**H,** J 7.6), 7.18 (1H, t, -Ph-**H,** J 7.7), 7.09 (1H, d, -Ph-**H,** J 8.1), 6.93 (1H, t, -Ph-**H,** J 7.4), 5.42 (1H, s, -C-**CH**-C-), 4.09 (2H, t, -**CH$_2$**-CH$_2$-, J 7.4), 2.58 (2H, t, -CH$_2$-**CH$_2$**-, J 7.4)

^{13}C NMR (126 MHz, DMSO) δ 209.39, 195.06, 179.61, 172.84, 147.78, 142.22, 126.71, 126.50, 121.63, 121.44, 109.87, 82.37, 58.00, 31.36, 23.53, 19.68, 13.96

MS (FTMS $^{-}$) $[M-H]^-$ calculated = 316.03, $[M-H]^-$ observed = 316.03, m/e

FT-IR (ATR) ν/cm^{-1} 2958 (m), 2930 (s), 1750 (s), 1523 (m), 1424 (s).

UV-visible λ_{max} = 446 nm (36,409 M^{-1} cm^{-1} ± 455 M^{-1} cm^{-1}) in ethanol.

Preparation of 3-(2-((2-hydroxy-3,4-dioxocyclobut-1-en-1-yl)methylene)-3,3-dimethylindolin-1-yl)propanoic acid (D6)

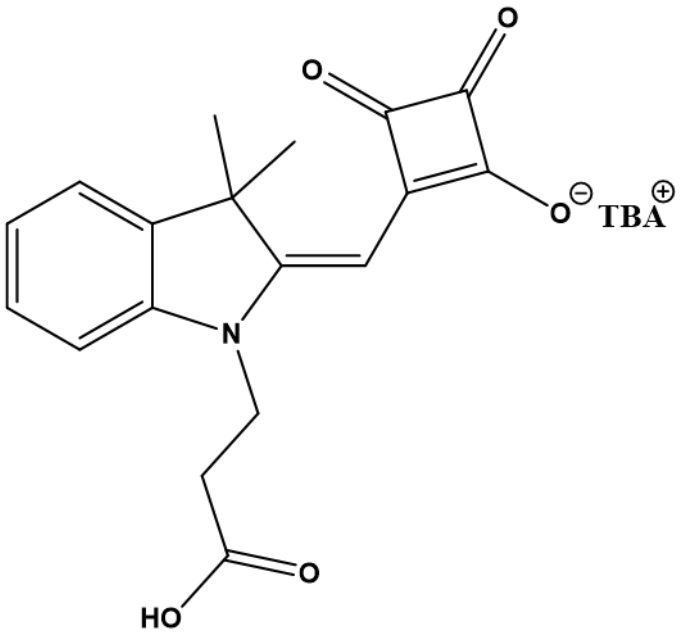

3-(2-((2-ethoxy-3,4-dioxocyclobut-1-en-1-yl)methylene)-3,3-dimethylindolin-1-yl)propanoic acid (**D4**) (0.5 g, 1.41 mmol) was dissolved in ethanol (10 ml) and heated to reflux. Tetrabutylammonium hydroxide solution (1 ml, 40 %) was added and the solution was allowed to reflux for 1 h. After cooling the solvent was removed *in vacuo* and the resulting mixture was purified by column chromatography (SiO_2) with dichloromethane and methanol (90:10) as eluent. The solution was then concentrated, and pure product was crashed out after ethanol was added. (Yield 0.04 g, 5.00 %)

^{1}H NMR (500 MHz, DMSO) δ 7.23 (1 H, d, -Ph-**H**, J 7.2), 7.14 (1 H, t, -Ph-**H**, J 7.5), 6.84 (2 H, dd, **H**-Ph-**H**, J 15.7, 7.9), 5.50 (1 H, s, -C-**CH**-C-), 3.99 – 3.92 (2 H, m, -**CH$_2$**-CH$_2$), 2.45 (2 H, m, -CH$_2$-**CH$_2$**), 1.55 (6 H, s, -**CH$_3$**-C-**CH$_3$**-).

^{13}C NMR (101 MHz, DMSO) δ 195.84, 179.17, 157.83, 144.00, 140.32, 127.77, 122.06, 120.09, 107.19, 84.78, 57.99, 49.06, 46.20, 28.00, 23.53, 19.68, 13.96.

MS (FTMS$^-$) [M$^-$] calculated = 326.10, [M$^-$] observed = 326.10.04, m/e

FT-IR (ATR) ν/cm^{-1} 2960 (m), 2932 (w), 2874 (m), 1752 (vs), 1733 (m), 1546 (s), 1310 (vs).

UV-visible λmax 423 nm (42,671 M^{-1} cm^{-1} ± 824 M^{-1} cm^{-1}) in ethanol.

Preparation of 3-(dicyanomethylene)-2-((3-dodecylbenzthiazol-2-ylidene)methyl)-4-oxocyclobut-1-en-1-olate (D7)

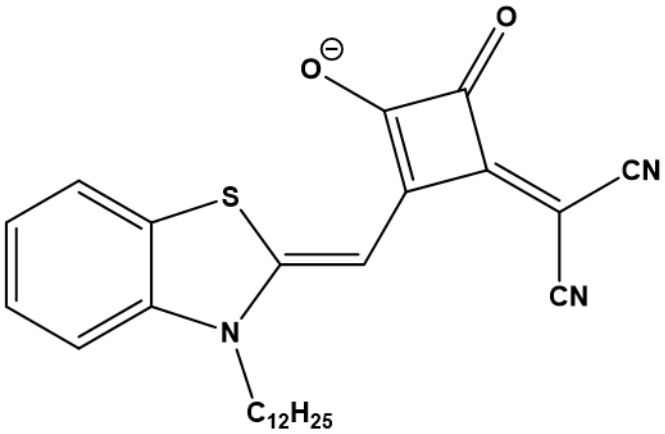

A mixture of 3-((3-dodecylbenzothiazol-2-ylidene)methyl)-4-ethoxycyclobut-3-ene-1,2-dione (**6**) (0.5 g, 1.13 mmol) and malononitrile (85 mg, 1.25 mmol) were dissolved in ethanol (15 ml). Triethylamine (0.20 ml, 1.47 mmol) was added dropwise to the solution and it was allowed to stir for 2 h at room temperature. After the reaction had completed the solvent was removed *in vacuo* and the product was obtained as an orange solid after purification by column chromatography (SiO_2), first with ethyl acetate and petroleum ether as eluent to remove impurities. Pure product can then be run off the column with a dichloromethane: methanol mix (80:20). Yield (0.20 g, 38.46 %)

^{1}H NMR (500 MHz, DMSO) δ 7.64 (1 H, dd, -Ph-**H**, *J* 7.8, 0.6), 7.28 (2 H, ddd, **H**-Ph-**H**, *J* 20.9, 11.0, 4.2), 7.11 – 7.00 (1 H, m, -Ph-**H**), 5.89 (1 H, s, -C-**CH**-C-), 3.90 (2 H, t, -**CH$_2$**-CH$_2$- *J* 7.6), 1.70 – 1.58 (2H, m), 1.40 – 1.33 (3 H, m), 1.33 – 1.28 (3 H, m), 1.23 (13 H, s, alkyl chain), 0.85 (3 H, t, -CH$_2$-**CH$_3$**- *J* 6.9).

^{13}C NMR (126 MHz, DMSO) δ 190.96, 186.34, 174.44, 168.48, 153.89, 141.82, 127.05, 126.44, 122.62, 122.29, 119.86, 118.95, 111.01, 81.88, 68.86, 46.20, 45.32, 35.51, 31.78, 29.48, 29.34, 29.18, 26.50, 22.58, 16.18, 14.42, 9.08

MS (TOF MS ES $^-$) $[M]^-$ calculated = 460.21, $[M]^-$ observed = 460.21, m/e

FT-IR (ATR) ν/cm^{-1} 3448 (br), 2920 (s), 2852 (s), 2196 (s), 2180 (s), 1744 (m), 1624 (m), 1486 (s), 1356 (s), 738 (s)

UV-visible λ_{max} = 480 nm (28,148 M^{-1} cm^{-1} ± 881 M^{-1} cm^{-1}) in ethanol.

Preparation of 2-(2-((1-dodecyl-3,3-dimethylindolin-2-ylidene)methyl)-3-hydroxy-4-oxocyclobut-2-en-1-ylidene)malononitrile (D8)

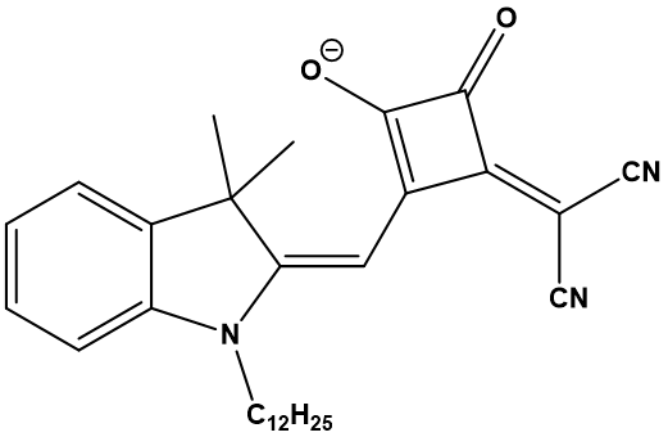

A mixture of 3-((1-dodecyl-3,3-dimethylindolin-2-ylidene)methyl)-4-ethoxycyclobut-3-ene-1,2-dione (**7**) (0.50 g, 1.11 mmol) and malononitrile (95 mg, 1.44 mmol) were dissolved in ethanol (15 ml). Triethylamine (0.2 ml, 1.44 mmol) was added dropwise to the solution and it was allowed to stir for 2 h at room temperature. After cooling the solvent was removed *in vacuo* and the product was obtained as a orange solid after purification by column chromatography (SiO_2), first with ethyl acetate as eluent to remove impurities and then with dichloromethane: methanol (80:20) to obtain the pure product. Yield (0.28 g, 53.85 %)

^{1}H NMR (500 MHz, DMSO) δ 7.32 (1H, dd, -Ph-**H,** J 7.3, 0.9), 7.20 (1H, td, -Ph-**H,** J 7.7, 1.2), 6.97 (1H, d, -Ph-**H,** J 7.9), 6.94 (1H, td, -Ph-**H,** J 7.5, 0.6), 5.92 (1H, s, -C-**CH**-C-), 3.73 (2H, t, -**CH$_2$**-CH$_2$-, J 7.5), 1.62 (2H, dd, -**CH$_2$**-CH$_2$-, J 14.5, 7.2), 1.56 (6H, s, **CH$_3$**-C-**CH$_3$**), 1.38-1.26 (5H, m), 1.22 (14H, s, alkyl chain), 0.85 (3H, t, -CH$_2$-**CH$_3$**-, J 6.9)

13C NMR (126 MHz, DMSO) δ 192.24, 185.73, 177.64, 167.90, 163.06, 143.52, 140.60, 127.96, 122.18, 121.34, 119.64, 118.64, 108.20, 84.70, 46.79, 42.49, 36.20, 31.75, 29.44, 29.31, 29.27, 29.18, 29.14, 28.41, 27.54, 26.39, 26.35, 22.55, 14.42.

MS (TOF-MS-ES $^-$) $[M]^-$ calculated = 470.28, $[M]^-$ observed = 470.28, m/e

FT-IR (ATR) ν/cm^{-1} 3382 (br), 2921 (s), 2852 (s), 2198 (s), 1738 (s), 1644 (m), 1484 (m), 1316 (s)

UV-visible λmax 460 nm (10,835 M^{-1} cm^{-1} ± 52 M^{-1} cm^{-1}) in ethanol.

Preparation of 2-((3-(2-carboxyethyl)benzothiazol-2-ylidene)methyl)-3-(dicyanomethylene)-4-oxocyclobut-1-en-1-olate (D9)

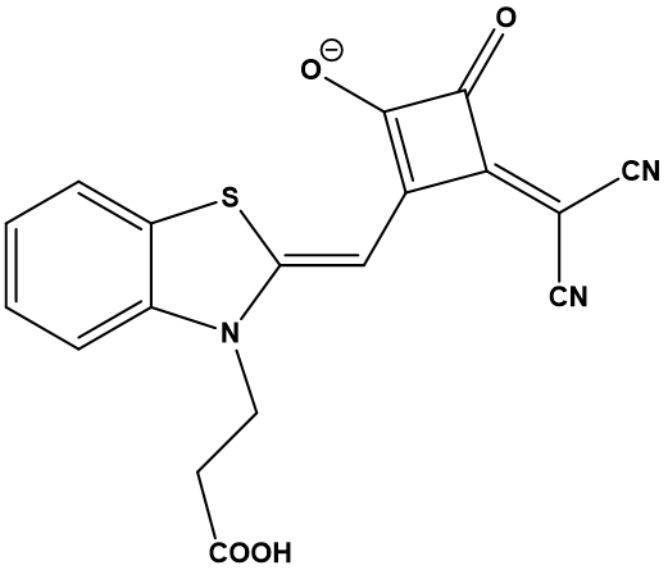

A mixture of 3-(2-((2-ethoxy-3,4-dioxocyclobut-1-en-1-yl)methylene)benzothiazol-3-yl)propanoic acid (**D3**) (0.50 g, 1.45 mmol) and malononitrile (106 mg, 1.6 mmol) were dissolved in ethanol (15 ml). Triethylamine (0.22 ml, 1.10 mmol) was added dropwise to the solution and it was allowed to stir for 2 h at room temperature. After cooling the solvent was removed *in vacuo* and the product was obtained as an orange solid after purification by column chromatography (SiO_2) with dichloromethane and methanol (80:20) as eluent to obtain the pure product. (Yield 0.25 g, 47.17 %)

^{1}H NMR (500 MHz, DMSO) δ 7.63 (1 H, d, -Ph-**H**, J 7.7), 7.35 – 7.24 (2 H, m, **H**-Ph-**H**), 7.07 (1 H, t, -Ph-**H**, J 7.2), 5.85 (1 H, s, -C-**CH**-C-), 4.15 (2 H, t, -**CH$_2$**-CH_2-, J 7.1), 2.64 (2 H, t, -**CH$_2$**-CH_2-, J 7.0).

^{13}C NMR (101 MHz, DMSO) δ 190.77, 185.86, 174.21, 167.88, 153.05, 141.13, 126.49, 125.87, 122.22, 121.79, 120.16, 119.32, 118.37, 110.85, 81.53, 9.03.

MS (FTMS $^{+}$) $[M+H]^{+}$ calculated = 366.05, $[M+H]^{+}$ observed = 366.05, m/e

FT-IR (ATR) ν/cm^{-1} 3056 (br, w), 2198 (s), 2178 (s), 1749 (m), 1737 (m), 1716 (s), 1663 (s), 1500 (s), 1411 (s), 1359 (s), 1308 (s), 1164 (s)

UV-visible λ_{max} 478 nm (35,374 M^{-1} cm^{-1} ± 386 M^{-1} cm^{-1}) in ethanol.

Preparation of 2-((1-(2-carboxyethyl)-3,3-dimethylindolin-2-ylidene)methyl)-3-(dicyanomethylene)-4-oxocyclobut-1-en-1-olate (D10)

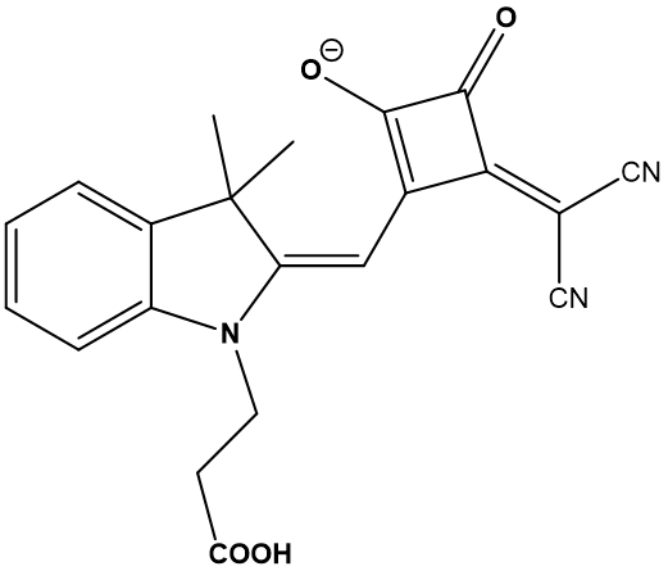

A mixture of 3-(2-((2-ethoxy-3,4-dioxocyclobut-1-en-1-yl)methylene)-3,3-dimethylindolin-1-yl)propanoic acid (**D4**) (0.5 g, 1.41 mmol) and malononitrile (102 mg, 1.55 mmol) were dissolved in ethanol (15 ml). Triethylamine (0.22 ml, 1.10 mmol) was added dropwise to the solution and it was allowed to stir for 2 h at room temperature. After cooling the solvent was removed *in vacuo* and the pure product was obtained after column chromatography (SiO_2) with dichloromethane and methanol (80:20) as eluent. (Yield 0.12 g, 22.64 %).

^{1}H NMR (500 MHz, DMSO) δ 7.31 (1 H, d, -Ph-**H**, J 7.2), 7.19 (1 H, t, -Ph-**H**, J 7.6), 7.02 (1 H, d, -Ph-**H**, J 7.8), 6.93 (1 H, t, -Ph-**H**, J 7.2), 5.84 (1 H, s, -C-**CH**-C-), 3.97 (2 H, t, -**CH$_2$**-CH$_2$-, J 6.5), 2.93 (2 H, dd, -CH$_2$-**CH$_2$**-, J 14.0, 6.8), 1.56 (6 H, s, -**CH$_3$**-C-**CH$_3$**-).

^{13}C NMR (126 MHz, DMSO) δ 185.73, 177.82, 167.87, 162.84, 143.23, 140.48, 133.47, 127.93, 122.11, 121.40, 119.61, 118.57, 108.57, 84.82, 46.75, 45.74, 27.49, 9.38.

MS (FTMS $^{+}$) $[M]^{-}$ calculated = 374.11, $[M]^{-}$ observed = 374.11, m/e

FT-IR (ATR) ν/cm-1 3412 (br, w), 3056 (br, w), 2198 (m), 1742 (m), 1544 (w), 1486 (m), 1312 (vs), 742 (s)

UV-visible λmax 456 nm (22,544 M^{-1} cm^{-1} ± 491 M^{-1} cm^{-1}) in ethanol.

Preparation of 4-bromobenzoic anhydride[211]

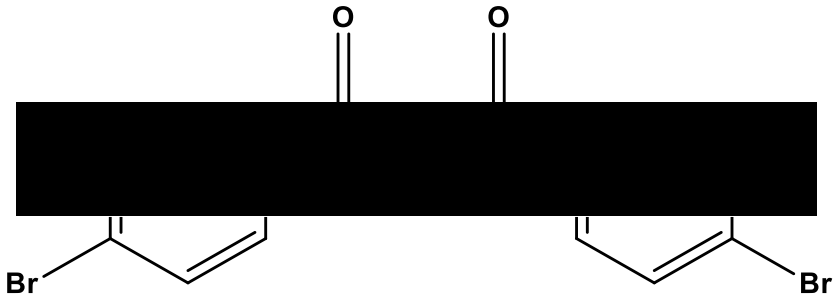

A solution of triethylamine (0.86 g, 8.51 mmol) in anhydrous tetrahydrofuran (5 ml) was added dropwise to a tetrahydrofuran (anhydrous) solution (10 ml) containing 4-bromobenzoic acid (1.00 g, 4.97 mmol) and methanesulfonyl chloride (0.31 g, 2.74 mmol) at 0 ^{o}C. The resulting mixture was stirred for 1 h and concentrated under vacuum. The mixture was extracted with $NaHCO_{3(aq)}$ and ethyl acetate three times, and the combined organic phase was washed with brine, dried over $MgSO_4$, filtered and concentrated to obtain pure 4-bromobenzoic anhydride (Yield 0.75 g, 78.95 %) m.p. 189–191 ^{o}C

^{1}H NMR (400 MHz, $CDCl_3$) δ 8.00 (4H, d, J 8.6), 7.68 (4H, d, J 8.6).

^{13}C NMR (101 MHz, DMSO) δ 167.09, 132.16, 131.76, 130.58, 127.30.

MS (TOF MS $^{+}$) $[M]^{+}$ calculated = 382.87, $[M]^{+}$ observed = 382.87

FT-IR (ATR) ν/cm^{-1} 3095 (w), 2971 (br), 1926 (w), 1782 (s), 1718 (m), 1582 (vs), 1480 (s), 1427 (m), 1394 (s), 1284 (m), 1212 (s), 1168 (s), 830 (s), 736 (s)

Preparation of 4-(N,N-Diphenylamino)-benzaldehyde (YD1)[211,212]

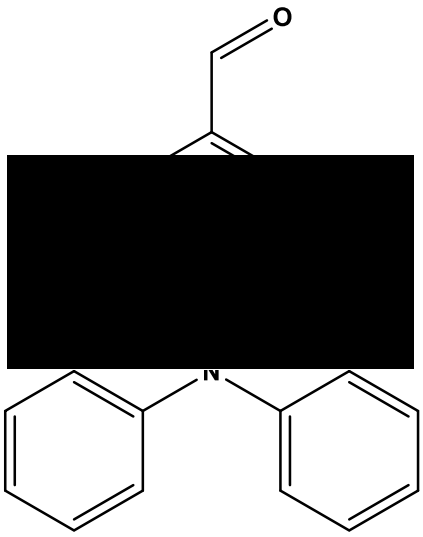

Phosphorous oxychloride (9.5 mL, 101.9 mmol) was added dropwise at 0 °C under N_2 to dimethylformamide (7.26 mL, 98.3 mmol) and the reaction mixture was stirred for 1 h. Triphenylamine (1.00 g, 4.08 mmol) was added, and the resulting mixture was stirred at 95 °C for 6 h. After cooling to r.t. the mixture was poured into ice-water (200 mL). and basified with 1 M NaOH. After extraction with CH_2Cl_2 (200 mL), the organic layer was washed with water (3 x 50 mL), dried ($MgSO_4$) and filtered. After evaporation of the solvent, the crude product was purified by column chromatography (CH_2Cl_2) to give a yellow solid. (Yield = 0.82 g, 73.61 %), mp 130-131 °C.

^{1}H NMR (500 MHz, CDCl3) δ 9.80 (1 H,**HC**-C=O, s), 7.67 (2 H, d,**HC**-Ph-**CH**, J 8.8), 7.33 (4 H, dd, **HC**-Ph-**CH**, J 8.6, 7.2), 7.19 – 7.14 (6 H, m), 7.01 (2 H, d, **HC**-Ph-**CH**, J 8.8).

^{13}C NMR (126 MHz, $CDCl_3$) δ 190.38, 153.32, 146.13, 131.27, 129.71, 129.09, 126.29, 125.09, 119.33.

FT-IR (ATR) ν/cm^{-1} 2829 (w), 2741 (w), 1682 (s), 1582 (s), 1486 (s), 1328 (m), 1286 (m), 1218 (s).

Preparation of N,N-diphenyl-4-vinylaniline (YD2)[165]

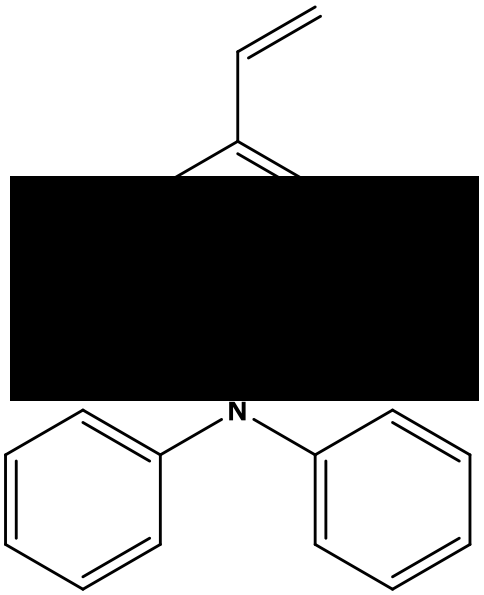

4-(N,N-Diphenylamino)-benzaldehyde (**YD-S1**) (7.50 g, 27.46 mmol) was dissolved in distilled tetrahydrofuran (20 ml) under nitrogen and added to a mixture of potassium *tert*-butoxide (4.62 g, 41.19 mmol) and methyl triphenyl phosphonium iodide (16.65 g, 41.19 mmol). This reaction mixture was stirred at room temperature for 24 h. The solution was then poured into distilled water: dichloromethane (1:1, v/v) and the organic layer separated in a separating funnel, dried over anhydrous magnesium sulphate and the solvent removed *in vacuo*. The product was purified by column chromatography (SiO_2) in petroleum ether/ dichloromethane (95:5, v/v). The pure product was identified by thin layer chromatography and precipitated in dichloromethane/methanol (1:20, v/v) to give a white solid. (Yield 4.55 g, 61.07 %), mp 92-93°C.

^{1}H NMR (500 MHz, DMSO) δ 7.38 (2H, d, =CH-Ph-N-, J 8.6), 7.30 (4H, dd, -NPh_2, J 8.4, 7.4), 7.05 (2H, t, -N-Ph_2, J 7.4), 7.01 (4H, dd, -N-Ph_2, J 8.5, 1.1), 6.93 (2H, d, =CH-Ph-N-, J 8.6), 6.66 (1H, dd, CH_2=CH-, J 17.6, 11.0), 5.69 (1H, dd, H-CH=CH-, J 17.6, 1.0), 5.16 (1H, dd, H-CH=CH-, J 10.9, 0.9).

^{13}C NMR (126 MHz, DMSO) 147.47, 147.41, 136.49, 131.97, 130.03, 127.74, 124.50, 123.65, 123.50, 113.09.

MS (FTMS +) $[M + H]^+$ calculated = 272.14, $[M + H]^+$ observed = 272.14

Preparation of 4-[2-(4-diphenylamino-phenyl)vinyl]benzoic acid ethyl ester (YD3)[165]

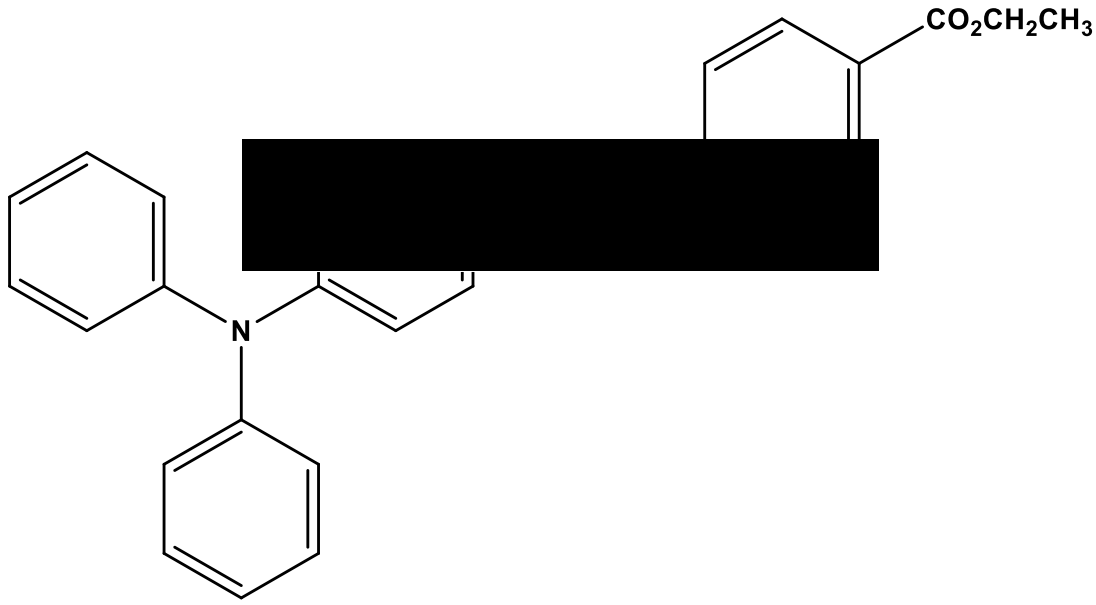

4-(N,N-Diphenylamino)-benzaldehyde (**YD2**) (1.03 g, 3.80 mmol) was dissolved in anhydrous N,N-dimethylacetamide (DMAC) (20 ml) with *trans*-di(m-acetato)bis [O-(di-o-tolylphosphoino)benzyl]dipalladium(II) (0.03 g, 0.03 mmol), ethyl-4-bromobenzoate (1.30 g, 5.68 mmol), Na_2CO_3 (0.80 g, 7.55 mmol) and 2,6 di-tert-butylcresol (0.08 g, 0.36 mmol) and the solution was stirred at 95 ^oC for 18 h. After cooling, the solution was poured into distilled water: dichloromethane (20 ml, 1:1 v/v) and the mixture separated using a separating funnel. The organic layer was dried over anhydrous magnesium sulphate and the solvent removed *in vacuo* before purification by column chromatography on silica gel with petroleum ether/ diethyl ether (95:5, v/v). The product was identified by thin layer chromatography and the solvent removed *in vacuo* followed by precipitation in methanol to give a yellow solid (**YD3**). Yield 0.32 g, 20%, mp 120–122 ^oC.

^1H NMR (500 MHz, DMSO) δ 7.93 (2 H, d, CH–Ph–CO–, *J* 8.4), 7.69 (2 H, d, –CO–Ph–CH, *J* 8.4), 7.54 (2 H, d, –Ph–N– Ph_2, *J* 8.6), 7.36 – 7.30 (5 H, m), 7.18 (1 H, d, CH–Ph–CH), *J* 16.4), 7.09 (2 H, t, –N–Ph2, *J* 7.4), 7.05 (4 H, d, –N–Ph_2, *J* 7.6), 6.95 (2 H, d, –Ph–N–Ph_2, *J* 8.6), 4.31 (2 H, q, Ph–COO–**CH_2**– CH_3, *J* 7.1), 1.33 (3 H, t, COO–CH_2–**CH_3**, *J* 7.1).

^{13}C NMR (500 MHz, DMSO) δ 165.97, 147.79, 147.29, 142.58, 131.23, 131.01, 130.10, 130.04, 128.57, 128.50, 126.75, 125.94, 124.87, 123.97, 122.96, 61.07, 14.67.

MS (TOF-MS-ASAP$^+$) $[M+H]^+$ calculated = 420.1964, $[M+H]^+$ observed = 420.1963, m/e

Preparation of 4-[2-(4-diphenylamino-phenyl)vinyl]benzoic acid (YD-Ac)[165]

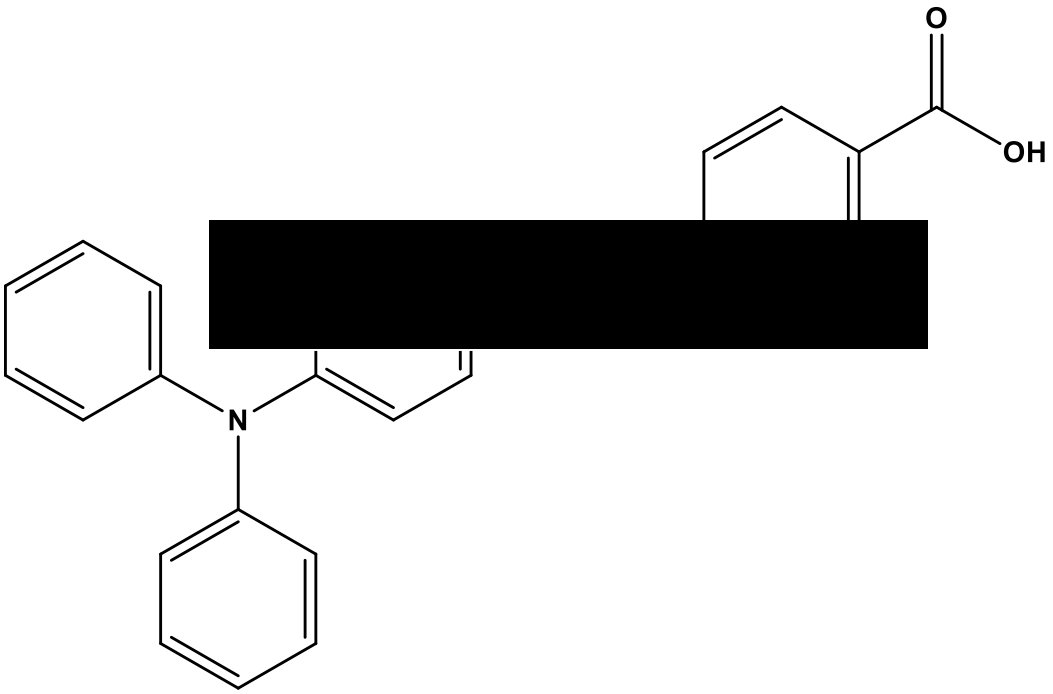

Compound (**YD3**) (0.35 g, 0.83 mmol) was dissolved in tetrahydrofuran–methanol–water (12 ml, 10:1:1, v/v/v) and LiOH 20 eq. (0.70 g, 0.83 mmol) was added. The mixture was stirred at 45 ^oC for 18 h. $HCl_{(aq)}$ (5%, 1.61 mol) was then added to adjust the pH to between 5 and 6. Ethyl acetate was added, and the organic layer was separated using a separating funnel, dried over anhydrous magnesium sulphate and the solvent removed *in vacuo* to give a yellow solid. Yield 0.25 g, 78 %, mp 214–216 ^oC.

^1H NMR (500 MHz, DMSO) δ 7.92 (2H, d, CH=Ph– CO, J 8.4), 7.67 (2H, d, CO–Ph–CH=, J 8.4), 7.54 (2H, d, –Ph–N–Ph_2, J 8.7), 7.33 (5H, dd, J 16.7, 9.3), 7.18 (1H, d, –CH=CH–Ph–, J 16.4), 7.08 (2H, t, –N–Ph_2, J 7.4), 7.05 (4H, d, –N–Ph_2, J 7.5), 6.96 (2H, d, –Ph–N–Ph_2, J 8.7).

^{13}C NMR (126 MHz, DMSO) δ 167.58, 147.73, 147.30, 142.19, 130.23, 130.08, 128.46, 126.63, 126.09, 124.82, 123.92, 123.05, 67.48, 25.59.

MS (FTMS$^-$) $[M - H]^-$ calculated = 390.15, $[M - H]^-$ observed = 390.15, m/e

Preparation of Yellow dye anhydride (YD-An)

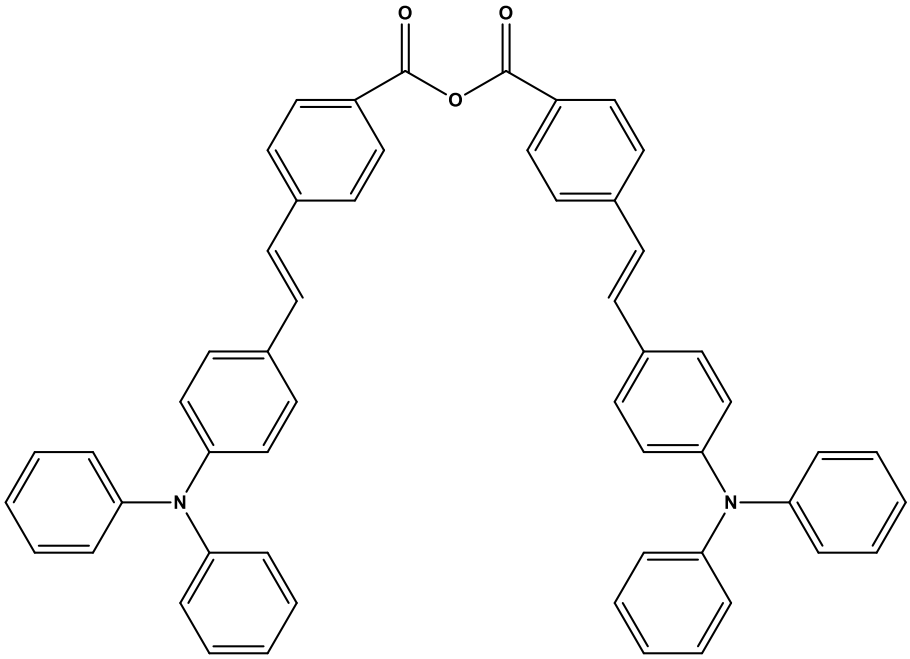

A solution of triethylamine (0.21 g 2.04 mmol) in anhydrous tetrahydrofuran (5 ml) was added dropwise to a tetrahydrofuran (anhydrous) solution (10 ml) **YD-Ac** (0.50 g, 1.19 mmol) and methanesulfonyl chloride (0.15 g, 1.31 mmol) at 0 ^{o}C. The resulting mixture was stirred for 1 h and concentrated under vacuum. The mixture was extracted with $NaHCO_{3(aq)}$ and ethyl acetate three times, and the combined organic phase was washed with brine, dried over $MgSO_4$, filtered and concentrated, before the crude residue was purified by column chromatography using silica gel and dichloromethane: petroleum ether: triethylamine in the ratio 1:1:0.01 (v/v) to afford pure product (Yield 70 mg, 15.23 %) M.P. = 121-123 ^{o}C.

^{1}H NMR (500 MHz, DMSO) δ 7.93 (2 H, d, CH=Ph– CO, J 8.4), 7.69 (2 H, d, CO–Ph–CH=, J 8.5), 7.54 (2 H, d, –Ph–N–Ph_2, J 8.7), 7.38 – 7.29 (5 H, m), 7.18 (1 H, d, –CH=CH–Ph–, J 16.4), 7.08 (2 H, t, –N–Ph_2, J 7.4), 7.04 (4 H, dd, –N–Ph_2, J 8.5, 1.0), 6.95 (2 H, d, –Ph–N–Ph_2, J 8.7).

^{13}C NMR (126 MHz, DMSO) δ 165.99, 147.79, 147.27, 142.57, 131.23, 130.99, 130.04, 128.51, 126.75, 125.93, 124.87, 123.98, 122.95, 67.28, 61.09, 46.24, 37.13, 31.99, 15.24, 14.66, 9.09.

FT-IR (ATR) ν/cm^{-1} 3029 (br, w), 2982 (br, w), 1709 (s), 1587 (s), 1505 (m), 1488 (s), 1269 (s), 1174 (s), 1104 (m).

UV-visible λ_{max} 383 nm in ethanol

2.5 DFT Modelling procedure

2.5.1 Computational details

The crystal structure of anatase TiO_2 available within Materials Studio[213] was used as the parent TiO_2 surface structure, whose lattice, atomic coordinates and electronic structure were optimised using the plane wave, pseudopotential code, CASTEP[214] within the formalism of density functional theory (DFT).[215–217] The exchange-correlation density functional was that of the generalised gradient approximation of Perdew, Burke and Ernzerhof (GGA-PBE)[218], and for all systems (including those containing the dye molecules) the electron-ion interactions were generated on-the-fly using the PBE functional to create consistent, norm-conserving pseudopotentials[219]. The corresponding valence electron wavefunctions were expanded by a plane wave basis set corresponding to a kinetic energy cut-off of 990 eV, which means that energy differences of more than 5 meV between same-molecule-plus-surface systems are more signifcant than 'computational noise'.

For optimisation of the unit cell of TiO_2, the Brillouin zone integrations were performed on a 7 x 7 x 9 Monkhorst-Pack[220] grid with 16 symmetry constraints, and for the surface-plus-molecule and gas-phase systems the single sampling point correpsonded to the gamma point. When modelling the TiO_2 surface, molecule, and surface-plus-molecule systems to account for long-range dispersions the pairwise, semi-empirical dispersion correction (SEDC) term of Tkatchenko and Scheffler[221] was used. Following the work of Martsinovich *et al.*[222] no Hubbard value was applied to Ti, which is further justified by our focus being the orientation of dye molecules on an anatase surface, rather than band gaps for example.

For all model systems (unless stated otherwise) the geometry was optimized using the method of Broyden–Fletcher–Goldfarb–Shanno (BFGS)[223] and the

self-consistent electronic minimisation method was density mixing. Further convergence details per BFGS iteration are as follows: electronic energy tolerance: 10^{-8} eV; energy change per ion: dE/ion 5×10^{-6} eV; maximum force: $|F|_{max}$ 0.01 eV/Å; change in displacement: $|dR|$ 5×10^{-4} Å. All calculations were non-spin polarised.

2.5.2 Anatase (1 0 1) TiO_2 Surface

The tetragonal unit cell of anatase TiO_2 available within Materials Studio has dimensions, a, b = 3.78 Å, c = 9.49 Å and following relaxation in accordance with the convergence criteria, the tetragonal dimensions became a, b = 3.81 Å, c = 9.71 Å. The expansion seen on relaxation is at most 2.4% which lies within the 1 to 5% expansion expected for the GGA-PBE density functional. The relaxed cell was cleaved (in Materials Studio) to build a series of *in vacuo* (101) surface slabs containing 2 to 5 layers. The energy differences per atom between layers were converged to less than 5 meV for the three-layered slab, which previosuly was shown to be sufficient to represent the relaxed atoms of the anatase surface.[222]

For the three-layered slab the vacuum space above the surface was tested, to determine the optimum c-length that would reduce potential artefactual electrostatic interactions between periodic images. A c-length of 15 Å was found to be well within the energy convergence criteria of 5 meV, although the cell was further increased to 20 Å to accommodate the dye molecules.

Finally, the optimum supercell size was determined whereby the three-layered slab of 20 Å (c-length), was increased both in the x- and y- directions. The dye molecule with the largest planar length (molecule **D9**) was placed on top of the surface of variously-sized slabs, and total energies were calculated without relaxation of the model system's atomic structure. Maximum forces were converged for 2X-4Y supercells producing a final, (1 0 1) anatase TiO_2 slab of dimensions: 20.86 Å x 15.23 Å x 29.02 Å.

2.5.2.1 Anatase (1 0 1) TiO_2 Surface-plus-dye

To generate the six half-squaraine dye molecules (see **Figure 2.13**), the crystal structures of structure **D3** (internal reference: 2916ncs0556za_NCS.cif) were manually modified to generate the starting geometry of **D1**, **D5** and **D9** and structure **D4** to generate the starting geometry of **D6**. These structures were then pre-optimised using the B3LYP hybrid functional[224–227] in combination with the def2-SVP basis set and the def2-SVP/J auxiliary basis sets[228,229] using the RIJCOSX[230,231] approximation as implemented in the ORCA package.[232]

To obtain a representative structure of a dye molecule on the surface, as many as possible configurations of the dye moelcule should be checked. However, this requires a fast methodology that can take the energy of the relative configurations into account. We decided to use 'AutoDock' (release 4.2.6)[233,234] as a cheap pre-screening methodology acknowledging its limited application to solid-state systems. Five or six different dyes configurations from the pre-screening results were chosen, which were placed on clean TiO_2 (1 0 1) surfaces and optimised using DFT. The surface-plus-dye configurations with the lowest energy (i.e. largest-in magnitude-adsorption energy) were identified as the most probable orientations of the dyes on the TiO_2 surface.

2.6 Dye-sensitised solar cell fabrication

2.6.1 Liquid dye-sensitised solar cells

2.6.1.1 Photoelectrode fabrication

To produce TiO_2 photoelectrodes, unless otherwise stated TEC 7(XOP Glass) fluorine-doped tin oxide coated conductive glass (TEC 8) was cut to 3.0 cm x 1.5 cm using a glass cutter. The electrode was then cleaned by sonication in various solvents: 1 x Hellmanex (1 % w/w), 1 x deionised water, 1 x isopropanol and 1 x acetone before being dried under nitrogen. Two strips of Scotch tape™ (3M Ltd) were placed along either side of the conductive side of FTO glass strip (lengthways), leaving approximately 10 mm gap of exposed FTO. A film of TiO_2 paste (Solaronix, Ti-Nanoxide T/SP) was deposited on the conductive side of the glass via doctor blading and the tape was removed. The thickness of the film is ca. 7.4 μm, as measured with

an Alpha-Step D-600 profiler. The TiO_2 film were sintered on a hotplate at 550 ^oC for 30 min (10 ^oC increments, see **Figure 2.38**).

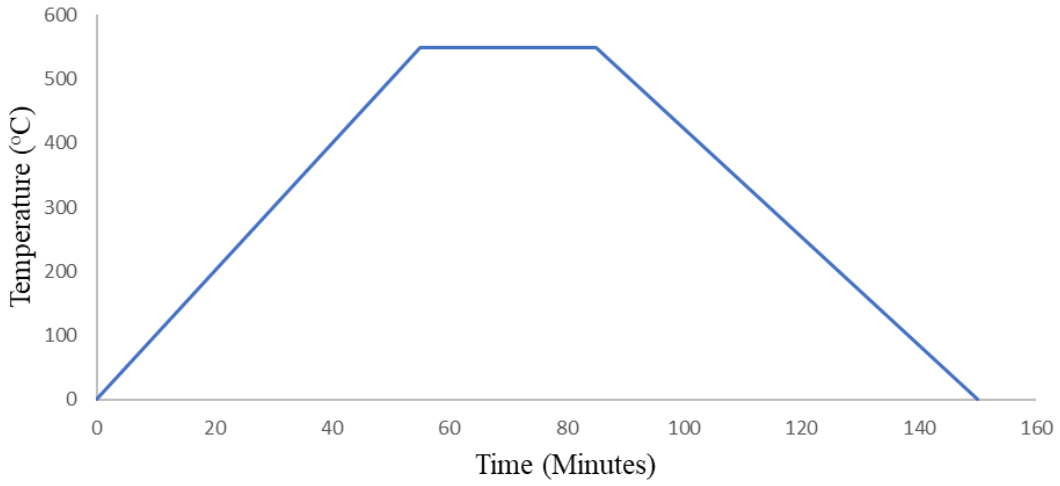

Figure 2.1 - Heating profile for the hotplate used to sinter TiO_2 photoelectrodes.

After sintering the films were allowed to cool to room temperature and then immersed in a 50 mmol aqueous $TiCl_4$ at 70 ^oC for 30 min. The film was then rinsed by deionized water and then annealed on a hotplate at 500 ^oC for 30 min. After cooling the edges of the TiO_2 electrode were shaped using a microscope slide to produce a 2 cm x 0.5 cm active area off centre (see **Figure 2.2**).

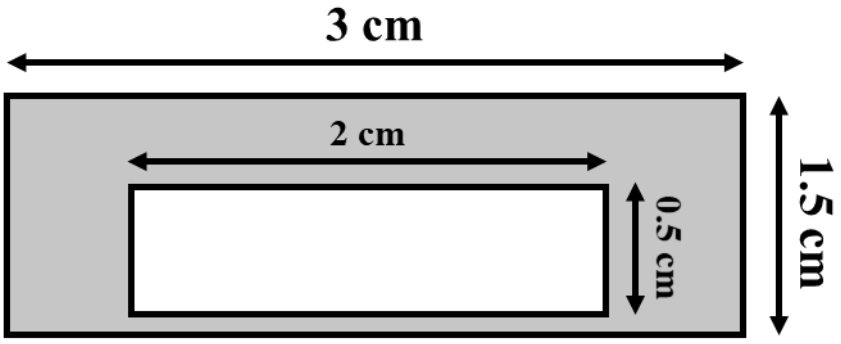

Figure 2.2 – Illustration of photoelectrode, grey rectangle represents the FTO glass while the white rectangle represents the TiO_2 active area.

2.6.1.2 Counter electrode fabrication

To produce TiO_2 counter electrodes, unless otherwise stated TEC 7(XOP Glass) fluorine-doped tin oxide coated conductive glass (TEC 8) was cut to 3.0 cm x 1.5 cm using a glass cutter. Two holes were then drilled into the electrode (non-conductive side up). Like the TiO_2 layer of the photoelectrode the holes were slightly off centre (0.5 cm from the top edges and 1 cm from the side). This would ensure that both holes are at either end of the TiO_2 active area after the two electrodes are sealed (see **Figure 2.3**).

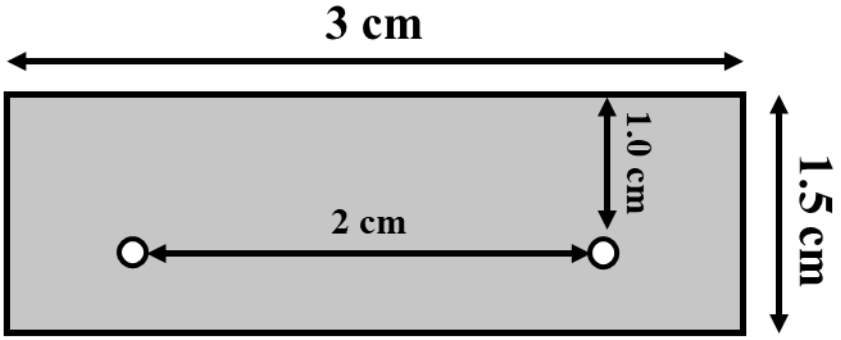

Figure 2.3 - Illustration of photoelectrode, grey rectangle represents the FTO glass while the white circles represent the drilled holes (~ 1mm diameter).

The electrodes were then cleaned by sonication in various solvents: 1 x Hellmanex (5 ml in 500 ml H_2O), 1 x deionised water (500 ml), 1 x isopropanol (500 ml) and 1 x acetone (500 ml) before being dried under nitrogen (same as the photoelectrode). After cleaning a layer platinum paste was deposited on the FTO side of the glass. This was done by dropping approximately 100 µl of Pt-1 paste (Solaronix) at the top of the electrode, the solution was then spread down the electrode using the thin end of a glass pipette. The electrodes were then placed on a hotplate and heated 10 ^oC per minute until it reached 400 ^oC after which the electrodes were allowed to cool to RT.

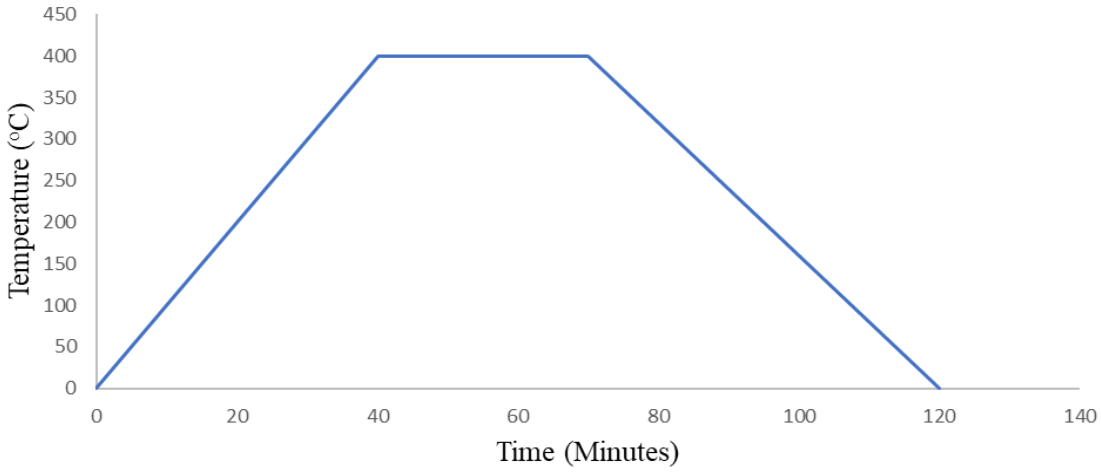

Figure 2.4 - Heating profile for the hotplate used to sinter platinum (Pt) counter-electrodes.

2.6.1.3 Sealing the DSC devices

The photo- and counter electrodes were sealed together using a 25 µm Surlyn™ thermoplastic (DuPont) which was heated in a heat press at 120 °C for 24 seconds on each side of the DSC device.

2.6.1.4 Pump dyeing the devices

Devices were dyed by passing 100 µl of dye solution (5 mg/ ml, in ethanol) through the device cavity 25 times. Next a 100 µl of ethanol was pumped through the device cavity to wash away any excess dye solution and finally the devices were allowed to dry naturally.

2.6.1.5 Adding the electrolyte

To make the electrolyte used for the ssDSC devices in this chapter I dissolved iodine (50 mmol), lithium iodide (50 mmol), guanidinium thiacyanate (50 mmol), 1-methyl-3-propyl-imidazolium iodide (800 mmol), benzimidazole (300 mmol) and tertbutyl pyridine (50 mmol) in acetonitrile. After which the solution was sonicated for ~ 2 minutes before being filtered through a 0.45 µm polytetrafluoroethylene (PTFE) filter (Sigma Aldrich). Approximately 20 µl of this solution was injected into the DSC devices using a syringe. The devices were then sealed by melting small squares of 25 µm Surlyn™ (0.5 cm^2) between the electrodes and small glass cover slips, taking care to minimise solvent evaporation. Finally, a silver paint (Agar fast drying suspension) was deposited onto the edge of the conductive side of each electrode using a small paintbrush. The paint was allowed to dry after which the devices were ready to be tested.

2.6.1.6 DSC device testing

Device performance was measured using I–V data using a Class AAA Solar Simulator at 100 mW cm^2 or 1 Sun between 0 and 1 V (Oriel Sol3A). Spectral response was measured in DC mode using a Keithley 2400 sourcemeter at a scan rate 0.1 V s^{-1}. Lamp calibrated to 1 Sun (100 mW cm^2) using a KG5 IR- filtered silicon cell (Newport Oriel 91150-KG5)

2.6.2 Solid state dye-sensitised solar cell (ssDSC) device manufacture

2.6.2.1 Etching of FTO glass substrates

To produce TiO_2 photoelectrodes, unless otherwise stated TEC 7(XOP Glass) fluoride-doped tin oxide coated conductive glass of 7 Ω/sq was cut to 2.8 cm x 1.5 cm using a glass cutter. To etch the FTO glass a single strip of Scotch tape™ (3M Ltd) was placed along the conductive side of FTO glass strip (lengthways), leaving approximately 4.5 mm of FTO glass exposed on either side. After which the exposed areas of FTO were coated in a thin layer of Zinc powder (Timstar laboratories) and a 4M solution of HCl was slowly pipetted onto the powder. After approximately 3 minutes the reaction is complete, and the glass slides were washed with deionised water and the Scotch tape™ was removed. The etched glass strip was then further cut to 2.8 cm^2 before being sonicated in various solvents: 1 x Hellmanex (5 ml in 500 ml H_2O), 1 x deionised water (500 ml), 1 x isopropanol (500 ml) and 1 x acetone (500 ml) before being dried under nitrogen. Finally, the glass slides were O_2 plasma cleaned and placed on a hotplate at 100^oC ready for a TiO_2 compact layer to be deposited.

2.6.2.2 Cleaning FTO glass substrates

. The substrates were carefully cleaned in ultrasonic baths of Hellmanex (5 ml in 500 ml H_2O), deionized water (500 ml), isopropanol (500 ml) and acetone (500 ml) successively. The electrodes were then dried under N_2 before being O_2 plasma cleaned.

2.6.2.3 Depositing the TiO_2 compact layer

The compact TiO_2 blocking layer was deposited onto the surface of a pre-cleaned FTO substrate by spray pyrolysis at 300 ^oC using an airbrush (~ 15 cm away from the electrodes). The solution used in the spray pyrolysis was Ti-isopropoxide in isopropanol (10 % by weight). 25 spray cycles were used as a standard parameter. After 25 sprays the electrodes were sintered at 450 ^oC for 30 minutes (increasing temperature 10^oC per minute from 300 ^oC to 450 ^oC). After which the electrodes were

allowed to cool to room temperature ready for the mesoporous TiO_2 layer to be deposited.

2.6.2.4 Depositing the TiO_2 scaffolding layer

Mesoporous TiO_2 films were coated on the compact TiO_2 layer by spin coating of a diluted TiO_2 paste (GreatCellSolar, DSL18-NRT) with ethanol (4:1, mass ratio). The thickness of the film was ca. 1.0 µm, as measured with an Alpha-Step D-600 profiler. The TiO_2 film were sintered on a hotplate at 500 ^oC for 30 min (10 ^oC increments). The heating profile of the sintering process can be seen in **Figure 4.21**.

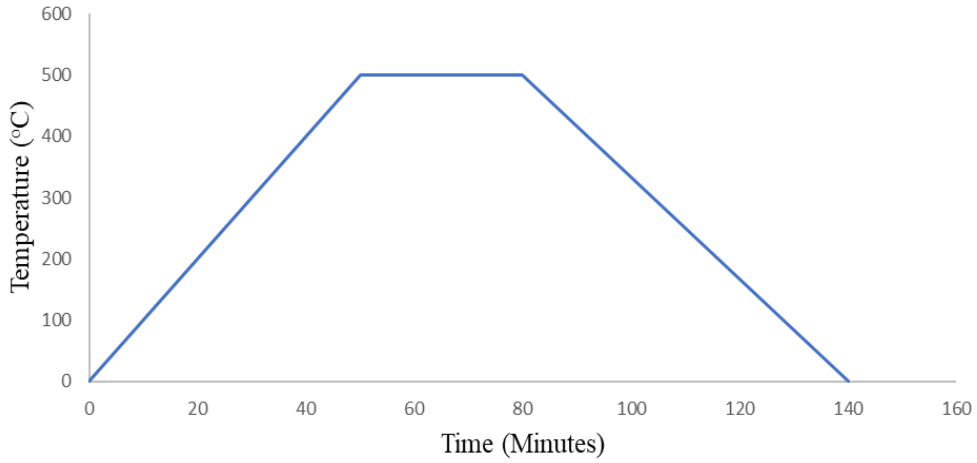

Figure 2.5 - Heating profile for the hotplate used to sinter TiO_2 photoelectrodes

After sintering the films were allowed to cool to room temperature and then immersed in a 0.02 M aqueous $TiCl_4$ at 70 ^oC for 30 min. The film was then rinsed by deionized water and then annealed on a hotplate at 500 ^oC for 30 min.

2.6.2.5 Dyeing the TiO_2 photoelectrodes

After cooling to 70 ^oC the film was immersed for 18-24 hours in 0.1 mM solution of LEG4 dye (dissolved in acetonitrile: t-butanol, 1:1), after which the sensitised electrodes were rinsed by ethanol and dried using an air gun.

2.6.2.6 Preparing/ depositing the HTM solution

Subsequently, the HTM solutions were prepared by dissolving spiro-OMeTAD in chlorobenzene at a concentration of 73 mM, with addition of LiTFSI (6.9 mM, from a stock solution in acetonitrile with concentration of 0.5 M) and t-BP (209 mM). The HTM solution was then doped with FK209 (2.5 mM, from a stock solution in acetonitrile 250 mM). 150 µl of HTM solution was deposited onto the electrode using a micro pipette. The solution was then spun for 30 s at 2000 rpm, 2000 rpm

acceleration. All the HTM solutions were prepared in glove box under nitrogen atmosphere.

2.6.2.7 Deposition of the counter electrode

Finally, a 30-40 nm thick (monitored by a Sigma SQM-160 thickness monitor) Au back contact was deposited onto the organic semiconductor by thermal evaporation in an Edwards E306 bell jar evaporator. An array of images to demonstrate the various ssDSC manufacturing steps can be seen in **Figure 2.6**.

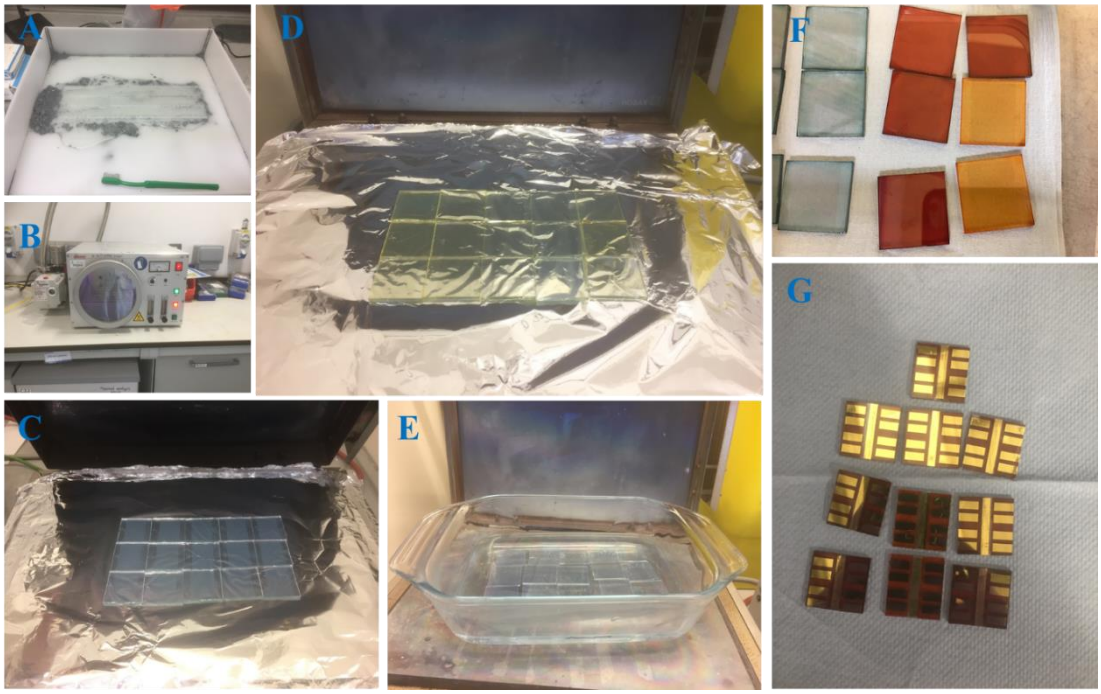

Figure 2.6 – Photographs demonstrating the various techniques for the preparation of ssDSC device. A = Etching of FTO, B = Plasma cleaning of photoelectrodes, C = TiO_2 compact layer on FTO glass, D = Mesoporous TiO_2 (before sintering), E = $TiCl_4$ treatment of photoelectrodes, F = Various dyed electrodes and G = Completed devices (after Au deposition)

2.6.3 Device testing

2.6.3.1 Testing set-up

Devices were designed in order to provide 8 pixels/ testing areas. Each device was etched down the middle and coated in Au using a bespoke 3D printed mask, this ensured that each pixel was separate from each other. An photograph of a ssDSC device with 8 pixels (made during this project) can be seen in **Figure 2.7**.

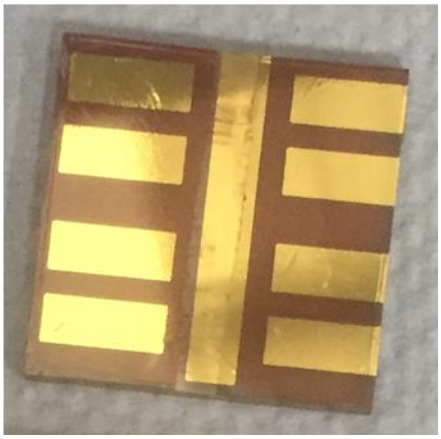

Figure 2.7 - Au coated ssDSC device with 8 pixels

The 3D printed mask also ensured that the devices perfectly fitted the testing rig, designed by Dr Daniel Burkett (SPECIFIC). **Figure 2.8** shows the 3D printed mask made by Dr Daniel Burkett. Making a PV device is often used to accurately define the area of illumination for the cell and therefore obtain more accurate data. However, it can also be used to artificially increase a device's performance by causing indirect illumination and reflecting internal light.

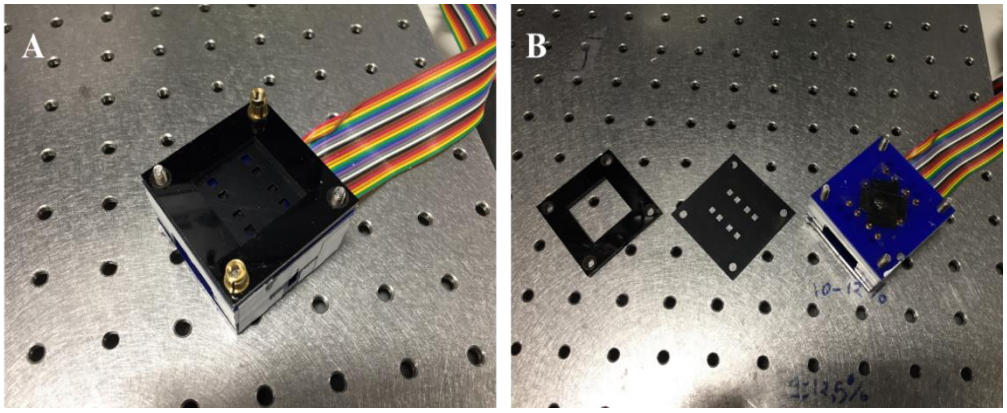

Figure 2.8 – ssDSC device 8-pixel testing rig.

2.6.3.2 Testing factors

2.6.3.3 Short-circuit current

Short-circuit current (I_{sc}) is the current passing through the DSC device when the voltage across the cell is zero. Short-circuit current is usually denoted as J_{sc} (short-circuit current density) to remove the dependence on the area of the solar cell.[235] The equation denoting short-circuit current density can been seen in equation 4.3 below. Where A represents the active area of the cell and is a function of the number and type

of photons available, the optical properties and the collection probability of the DSC device.[236]

$$J_{sc} = I_{sc} / A \qquad (mA/ cm^2) \qquad (2.1)$$

2.6.3.4 Open-circuit voltage (V_{oc})

Open-circuit voltage (V_{oc}) is the maximum voltage obtained from the DSC device at zero current.[237] The V_{oc} corresponds to the amount of forward bias on the DSC device due to the light-generated current.

2.6.3.5 Fill Factor

In simple terms, the fill factor (FF) of a solar cell is a measure of the quality of a solar cell. The FF determines the maximum power from the solar cell. The FF effectively represents the "squareness" of the I-V curve and is determined by the ratio of maximum power (P_{mp}) to the product of V_{oc} and I_{sc} of the DSC device (see equation 4.4).[237]

$$FF = P_{mp} / V_{oc} \times I_{sc} \qquad (2.2)$$

2.6.3.6 Efficiency

The efficiency of a solar cell is the most commonly used parameter to compare one solar cell to another and represents the maximum electrical energy output of the device compared to the energy input from the sun. The equation for a device's efficiency can been seen in equation 4.5.[235]

$$\eta = (V_{oc} \times I_{sc} \times FF) / P_{in} \qquad (2.3)$$

Where P_{in} is the power input from the sunlight. The efficiency (η) is usually expressed as a percentage (%). Besides the cell performance itself, the efficiency of a DSC device depends on the incident light spectrum and intensity as well as operating temperature. The internationally recognised standardised conditions of DSC devices is under the AM 1.5 global solar spectrum at a temperature of 300 K.[235,237]

2.6.3.7 External Quantum efficiency

External Quantum efficiency (EQE) sometimes referred to as Incident photon to charge carrier efficiency (IPCE) refers to the ratio of charge carriers collected compared to the number of photons of a given energy hitting the solar device.

$$IPCE (\lambda) = 1240 \times I_{sc} / \lambda \times \Phi \qquad (2.4)$$

Where, λ is the wavelength (nm), I_{sc} is the short-circuit current (mA/ cm^2) and Φ is the incident radiative light flux (W/ m^2).

For a DSC device, IPCE is defined as:

$$\mathbf{IPCE\ (\lambda) = LHE(\lambda)\ x\ \Phi(inj)\ x\ \eta(coll)} \qquad \mathbf{(2.5)}$$

Where, LHE (λ) represents the light harvesting efficiency for photons at wavelength λ, Φ(inj) is the quantum yield for the electron injection into the TiO_2 from the excited dyes and η(coll) is the number of injected charges that are able to reach the counter electrode.[238]

2.6.4 Experiment 1 (Doping with FK209)

Electrodes were prepared as described in section 4.3.2. However, Nanoporous TiO_2 films were coated on the compact TiO_2 layer via spin coating a diluted TiO_2 paste (GreatCellSolar DSL18NR-T) with ethanol (3:1, mass ratio). The thickness of the film is *ca*. 1.4 μm, as measured with an Alpha-Step D-600 profiler. The HTM recipe for the undoped devices was as follows: HTM solutions were prepared by dissolving the spiro-OMeTAD in chlorobenzene at a concentration of 150 mM, with addition of LiTFSI (20 mM, from a stock solution in acetonitrile with concentration of 0.5 M) and t-BP (200 mM), from a stock solution in chlorobenzene with concentration of 1.0 M). The HTM recipe for the doped devices were identical however, the solution was doped with FK209 (2.5 mM, from a stock solution in acetonitrile 250 mM).

2.6.5 Experiment 2 (Effect of the "blocking" layer)

Electrodes were prepared as described in section 4.3.2. The solution used in the spray pyrolysis was Ti-isopropoxide in isopropanol (10 % by weight), in isopropanol. The first set of devices used 25 spray cycles (used as standard parameter), whilst the second set of devices used 10 spray cycles (all at 300 ^oC). The BL for the third and final set of devices was deposited by spin coating 150 μl of Ti-Nanoxide BL/SC (Solaronix) at 5,000 rpm, 2,000 rpm acceleration for 30 seconds. All three sets of devices were sintered at 450 ^oC for 30 minutes

2.6.6 Experiment 3 (Optimisation of TiO_2 thickness)

Electrodes were prepared as described in section 4.3.2. However, several dilutions of DSL18NR-T and Ti-Nanoxide T/SP were prepared. TiO_2 pastes were diluted with

ethanol using the following ratio's (1:2, 1:3, 1:4 and 1:5, TiO_2: Ethanol) and were allowed to mix before being deposited as described in section 4.3.2

2.6.7 Experiment 4 (Effect of $TiCl_4$ treatment)

Electrodes were prepared as described in section 4.3.2. However, Nanoporous TiO_2 films were coated on the compact TiO_2 layer via spin coating a diluted TiO_2 paste (Ti-Nanoxide T/SP) with ethanol (2:1, mass ratio). The thickness of the film is *ca*. 0.69 μm, as measured with an Alpha-Step D-600 profiler. Also the set of ssDSC devices that did not undergo $TiCl_4$, were still allowed to heat 70^oC before being placed in the LEG4 dye bath to ensure all electrodes were at the same temperature for the sensitisation process.

2.6.8 Experiment 5 (Effect of dyeing time)

Electrodes were prepared as described in section 4.3.2. However, one set of ssDSC devices were restricted to ~ 2 hours dyeing time whilst the second set were allowed to dye according to section 4.3.2.

2.6.9 Experiment 6 (Effect of HTM thickness on ssDSC device performance)

Electrodes were prepared as described in section 4.3.2. However, the spin speed settings for spin coating were modified. Three different spin coating settings were used. The first set of ssDSC devices were spin coated as described in section 4.3.2, yet the second and third set were spin coated at 3,000 rpm, 3,000 rpm acceleration and 4,000 rpm and 4,000 rpm acceleration (respectively).

2.6.10 Experiment 7 (Testing of novel materials for ssDSC devices)

The LEG4 electrodes were prepared as described in section 4.3.2. However, Nanoporous TiO_2/ ZrO_2 films were coated on the compact TiO_2 layer via spin coating a diluted TiO_2 or ZrO_2 paste (Ti-Nanoxide T/SP or Zr-Nanoxide ZT/SP) with ethanol (2:1, mass ratio). The thickness of the film is *ca*. 0.69 and 0.65 μm respectively, as measured with an Alpha-Step D-600 profiler. After the sintering step of the $TiCl_4$ treatment, the films were allowed to cool to ~ 70 before being immersed for ~18 h in 0.1 mM solution of LEG4, JMS062 and JMS063 dissolved in ethanol, the sensitized electrodes were rinsed then rinsed by ethanol and dried under N_2.

2.6.11 Experiment 8 (Lifetime testing of ssDSC devices)

Electrodes were prepared as described in section 4.3.2 and tested at 0 and 48 hours after manufacture

2.7 Dye loading

To study dye loading, one layer of transparent paste (TiNanoxide T/SP, Solaronix) was doctor bladed onto a series of plain glass slides (1.0 cm x 5 cm). The TiO_2 layer was sintered at 500 ^oC for 30 min. After cooling, the TiO_2 coated slides were placed in dye solutions (0.5 mmol) for 18 hours. The slides were then rinsed with ethanol and dried under N_2 before the dyes were desorbed with tetrabutylammonium hydroxide solution (1.0 M in methanol). Solutions were then measured using UV-Vis spectroscopy.

3 Novel Benzothiazole Half-Squaraines: Model Chromophores to Study Dye-TiO_2 Interactions in Dye-Sensitized Solar Cells

3.1 Introduction

The work in this chapter has been published in Journal of Materials Chemistry A (October 2020).[239]

As described in Chapter 1, the surface orientation and self-assembly of DSC dyes on TiO_2 surfaces is still not well understood. The surface organisation and interactions between dyes is often commented about in the literature but there is very little proof to back up the theories regarding these processes.[4] However, it is well known that having different dyes and other molecular species on the photoelectrode can have a huge effect on performance. It has also been well documented that dye aggregation has huge implications for DSC devices and that CDCA can have a positive influence on aggregated dyes.[152,164,240] There have been many studies observing the electron injection of individual dyes experimentally.[241] However theoretical or experimental studies looking at the fundamental processes which occur are few and far between. This chapter attempts to address these issues using half-squaraine (HfSQ) dyes as a model chromophore. Holliman *et al.*[123] studied these dyes previously and found HfSQ dyes to be synthetically versatile and moderately efficient. Holliman was able to achieve $\eta = 5\ \%$[157] for a HfSQ with a single anchor and $\eta = 5.5\%$[123] for a HfSQ with two anchors. HfSQ dyes were proven to be effective when co-sensitised with squaraine dye SQ2 ($\eta = 6.1\ \%$)[157] and showed increased performance when sensitised with CDCA co-sorbent.[157] For this chapter, we synthesised two novel yet analogous sets of HfSQ dyes using benzyl indoles linked to squaric acid moieties. One group of the HfSQ dyes contains a sulphur heteroatom opposite the indole nitrogen (dyes (**D1**), (**D3**) (**D5**) (**D7**), (**D9**)) whilst the second group contains a dimethyl-derivatised carbon opposite the indole nitrogen (**D2**), (**D4**), (**D6**), (**D8**), (**D10**)). The sulphur has been incorporated into one set of these dyes in order to study its influence on dye energy levels and device performance. Sulphur can also be used as an atomic label for angle -resolved X-ray photoelectron spectroscopy (ARXPS). By identifying the sulphur heteroatom in X-ray photoelectron spectroscopy data, the aim has been to study how the dye-TiO_2 orientation varies with the position of the carboxylate linker on the dye periphery.

Figure 3.1 shows ten new half-squaraine dyes

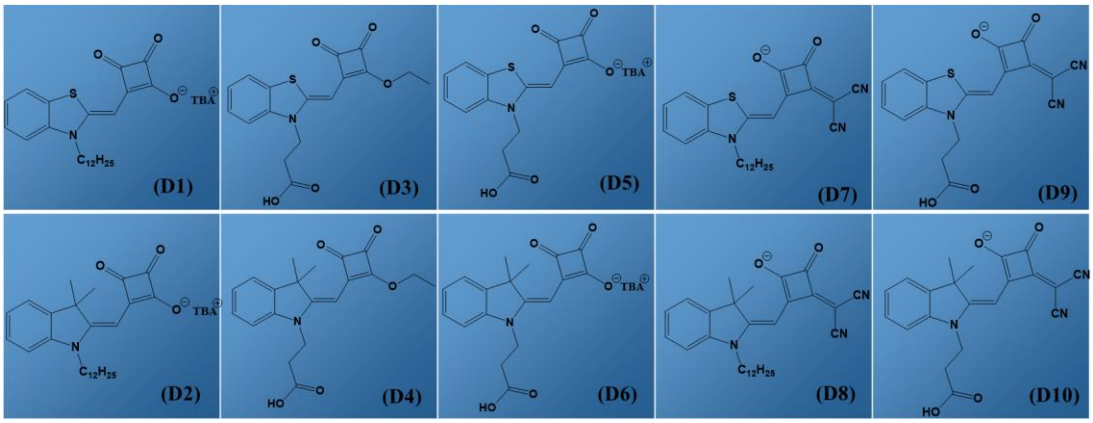

Figure 3.1 - Ten novel half-squaraine dyes synthesised in this chapter. The bottom five dyes contain a dimethyl-derivatised carbon opposite the indole nitrogen. The top five dyes are identical however, the dimethyl-derivatised carbon has been exchanged for a sulphur heteroatom

Dyes (**D3**), (**D4**), (**D5**), (**D6**), (**D9**) and (**D10**) all have been synthesised with a carboxylic acid anchoring group bound to the nitrogen of the indole. Theoretically these dyes should bind through the carboxylic acid unit, therefore the sulphur or dimethyl-derivatised carbon should be pointing away from the TiO_2 and towards the electrolyte. The other dyes (**D1**), (**D2**), (**D7**), and (**D8**) have been synthesised with a twelve-carbon chain bound to the nitrogen of the indole. Theoretically this should stop the dyes binding to the TiO_2 through this unit and force the dyes to bind through the squaric acid unit. According to previous papers this should cause the dyes to bind to the TiO_2 at a 90^o angle (compared to (**D3**), (**D4**), (**D5**), (**D6**), (**D9**) and (**D10**)). This position would ensure the sulphur or dimethyl-derivatised carbon atoms are close to the TiO_2 surface. By controlling where the sulphur atom lies (relative to the TiO_2 surface) the aim is to test if/how the sulphur affects DSC device performance. Several reports such as those by Berlinguette *et al.*[242] suggest sulphur atoms can aid device performance.[242,243] By incorporating sulphur into the dye, these workers reported a shift in the energy of the HOMO which should increase the V_{oc} by reducing the overpotential required for regeneration (see **Figure 3.2**). Hence, this shift lower should mean that the triiodide electrolyte is more easily able to transfer an electron to the oxidised dye resulting in increased efficiency.[194]

Whilst this looks promising, other papers such as those by O'Regan *et al.*[244] have reported that sulphur atoms can have a negative effect on device efficiency.[244,245] O'Regan suggests that by having a sulphur atom incorporated into the dye, it can

provide binding sites for oxidised species in the triiodide redox shuttle (I_2 or I_3^-). This interaction means there is an increased concentration of these species near the TiO_2 surface accelerating the recombination process.[244,245]

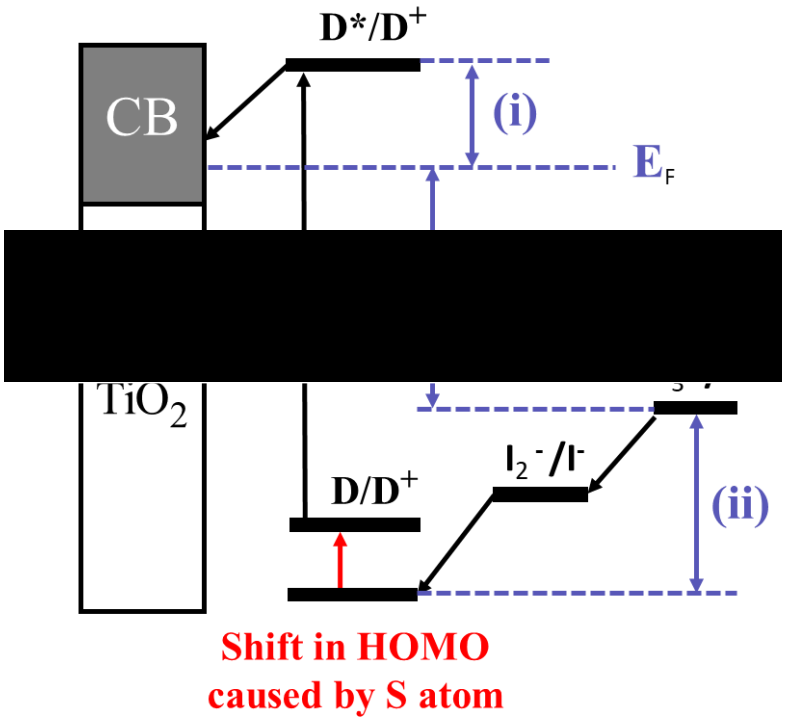

Figure 3.2 - Shift in HOMO caused by the addition of sulphur atom to half-squaraine sensitiser. E_F = Fermi level, (i) dye injection overpotential and (ii) dye regeneration overpotential. D = ground state dye, D* = excited state dye, D^+; = oxidised dye, CB = conduction band, hv = sunlight and V_{oc} = open circuit voltage[2]

It has also been reported that when bound to two other atoms such as carbon, sulphur atoms become sp^3 hybridised. This is particularly useful when incorporating a sulphur moiety into the chromophore of our dyes. Furthermore, because the d-orbitals of the sulphur atom should also be easily accessible they should be able form a charge transfer complex with triiodide electrolyte. This means that, if the sulphur is incorporated in the HOMO of the dye, then the charge transfer complex should allow for faster regeneration of the dye (theoretically the empty p-orbitals should point away from the TiO_2 surface). When the sulphur is in the LUMO of the dye the same interaction should occur. However, this time the sulphur will be close to the TiO_2 surface and therefore its orbitals should be much nearer the TiO_2 surface. The sulphur is likely to cause a build-up of oxidised electrolyte (I_3^-) near the titania surface. It's well documented that a build-up of I_3^- ions near the TiO_2 surface causes recombination by pulling injected electrons from the titania surface.[246,247] The work in this chapter

seeks to study this issue because a sulphur atom (or 'atomic tag') has been incorporated into a known chromophore (e.g. a half squaraine) to study dye-electrolyte interactions but also to investigate dye orientation at TiO_2 surfaces using a combination of theoretical and experimental data (i.e. DFT modelling, DSC device data and angle resolved X-ray photoelectron spectroscopy).

3.1.1 X-ray Photoelectron spectroscopy (XPS)

X-ray photoelectron spectroscopy (XPS) also known as electron spectroscopy for chemical analysis (ESCA) is a useful tool for analysing and characterising the surface chemistry for a range of materials.[248–250] By irradiating samples with a beam of X-rays, XPS can probe the substrate surface and then by measuring the kinetic energy (or indirectly their characteristic binding energy) of electrons emitted from the sample in order to determine elemental composition, empirical formula, chemical state and electronic state of the materials on the surface (see **Figure 3.3**).[251]

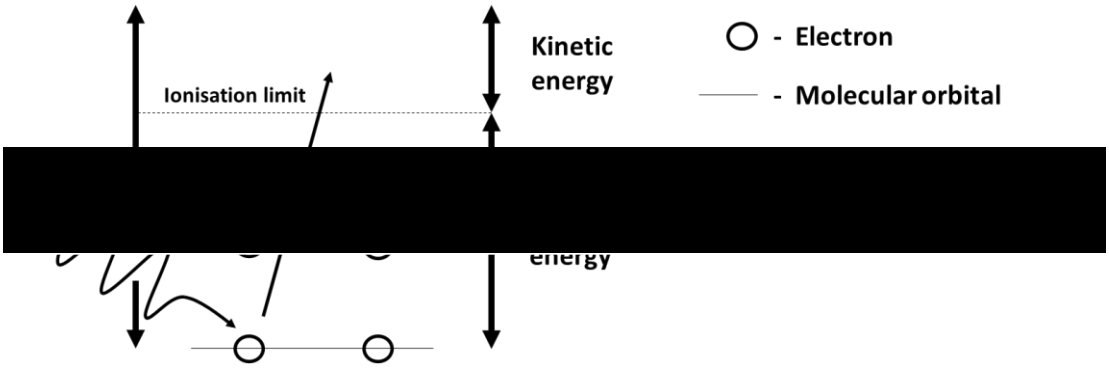

Figure 3.3 - The principle of photoelectron spectroscopy[216]

3.1.2 Angle resolved X-ray Photoelectron spectroscopy (ARXPS)

The main difference between ARXPS and XPS is the ability to tilt the sample in relation to the X-ray beam.[252] Rotating the sample relative to the X-ray beam provides additional information about the thickness and composition of the ultra-thin films in a non-destructive manor unlike sputtering techniques.[253] One advantage of ARXPS is that it can be applied to thin films because some films can either be too thin or be destroyed by conventional methods.[254]

Although XPS is a common technique to study DSC devices, it's use is usually centred around the surface analysis of both the photo-[255,256] and counter-electrodes.[257,258] In

reality most papers that use XPS to study DSC devices, use it as a confirmation technique to look at modification or doping of the electrode surface, rather than a techniques to understand what is happening at the surface.[259,260] Although there are some papers that use XPS to look at dyes. For example, Akbari *et al.*[261] and O'Shea *et al.*[262] used XPS alongside computational data to identify dye absorption modes for perylene and fluorescein dyes (binding through carboxylic anchors). Both papers have suggested binding orientations of the dyes yet, other than the binding groups little to no evidence is given.[261, 262]

To the best of my knowledge, only a single paper has used ARXPS to analyse the sensitisation of dyes onto TiO_2 for DSC devices. Pellegrino *et al*.[263] sensitised TiO_2 with a unsymmetrical phthalocyanine (ZnPc-II) dye. Pellegrino used various techniques including visible absorption, atomic force microscopy and angle-resolved X-ray photoelectron spectroscopy to study the sensitisation process of the ZnPc-II dye.[263] Pellegrino found that the surface orientation of the ZnPc-II was directly affected by the concentration of the sensitising solution.[263] At low dye concentrations, the aromatic rings interacted more with the TiO_2 (suggesting a flat or planar geometry). However, at higher dye concentrations, the dyes formed dendric clusters away from the surface (although this was determined by measuring the voltage, not by XPS measurements).[263]

3.2 Results and discussion

3.2.1 Dye synthesis

The synthetic routes to make all half-squaraines in this chapter are shown in **Scheme 3.1**.

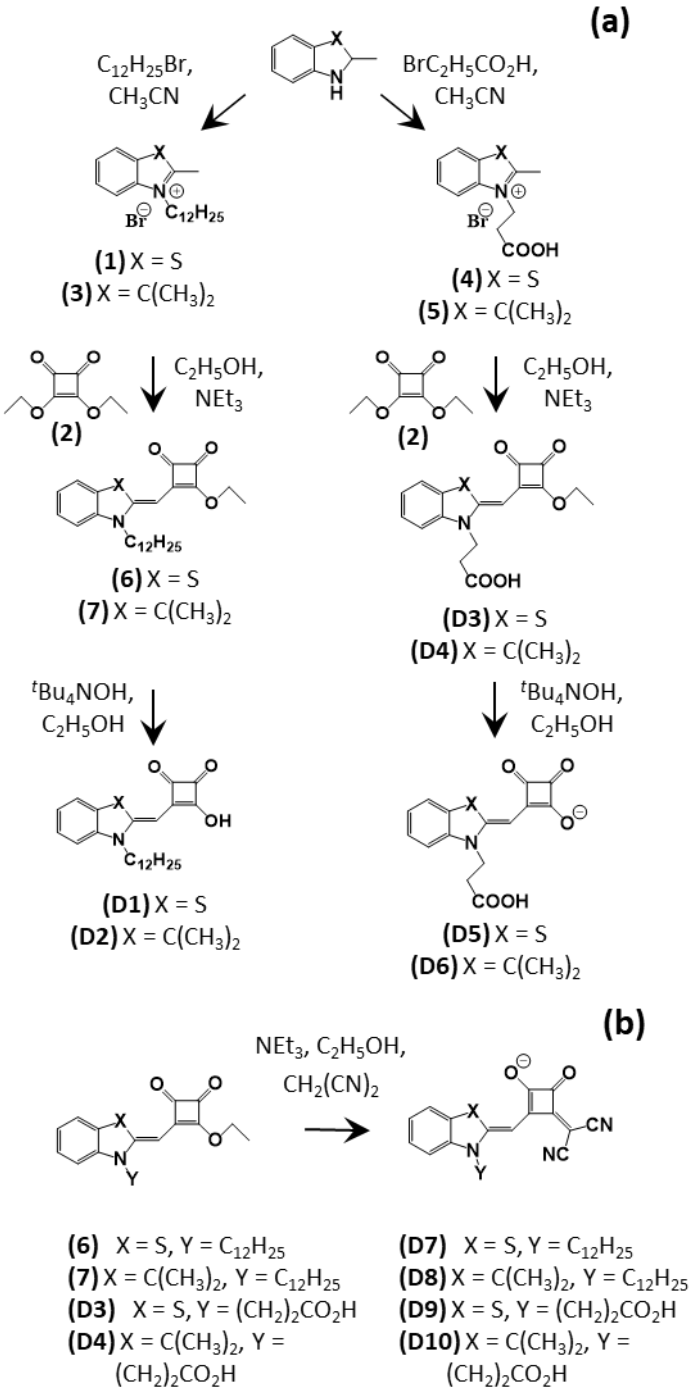

Scheme 3.1 - Synthetic pathways to (a) half-squaraine (HfSQ) dyes and (b) vinyl dicyano HfSQ dye derivatives

The synthetic routes used to produce the Hf-SQ used in this work are shown in **Scheme 3.1(a–b)**. The first step to synthesise these dyes is a Sn2 reaction between the indole (2,3,3-trimethylindolenine and 2-methylbenzothiazole) and the alkyl halide chains (1-bromododecane and 3-bromopropionic acid, see **Figure 3.4**). This a simple reflux reaction run under inert conditions (N_2) resulting in compounds (**1**), (**3**), (**4**) and (**5**). Compounds (**3**), (**4**) and (**5**) have been previously reported[207–210]. Compound (**1**) has been reported in the literature[206]. However, no analysis details were given. Therefore, in this work, it has been identified using multiple analytical techniques including ^{1}H/ ^{13}C NMR and mass spectrometry. The synthesis of compounds (**3**) and (**5**) resulted in moderate to high yields (65 - 73 %). However, the yield of indoles (**1**) and (**4**) were a lot smaller (< 10 % for **1**) on the first attempt. Initially, this was believed to be down to the long alkyl chain increasing indole solubility to point where it limited the amount of product that it was possible to recover. So, it was decided to reduce the ratio of 2-methylbenzothiazole to 1-bromododecane from 1:3 to 1:1. This only had a small negative effect on the yield, probably down to more unreacted benzothiazole. After both reactions, the resulting mixture was analysed by mass spectrometry and no product was observed. This eliminated the idea of 1-bromododecane changing the reaction solubility. Next, it was thought that the solubility of the starting materials could be a problem and therefore other solvents including toluene, dichloromethane, chlorobenzene and reagent alcohol (all anhydrous) were tried. The reaction in dichloromethane didn't work at all, this was put down to the low solvent boiling point not allowing the activation energy (E_A) of the reaction to be reached. Toluene and chlorobenzene had little effect on yield when compared to acetonitrile. However, using reagent alcohol did increase the reaction yield from 16.7 – 20%. Finally, when the reaction was given 48h rather than 24h to ensure all the starting material had reacted, this increased the yield further from 20 to > 24% yield. Although this was still low, it was almost double the initial reaction yield. Ultimately, this low yield is likely to be caused by the S atom causing a shift in electron density making the nitrogen atom less reactive to the haloalkane when compared to the indole containing a dimethyl-derivatised carbon (instead of sulphur) which showed a much higher yield. It is also worth noting that the yield of this reaction could also be increased by using 1-iododododecane instead of 1-bromododecane because iodide is a much better leaving

group and therefore far more reactive. Hence, it was possible to achieve yields greater than 30 % using 1-iododododecane.

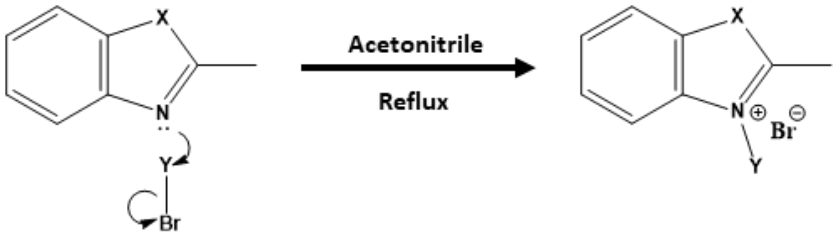

Figure 3.4 - General synthesis of HfSQ dyes step 1

However, it was decided to use 1-bromodecane due to its lower cost which when considered on a cost-benefit analysis proved to be a better choice. A cost benefit analysis of using 1-bromododecane and 1-iododododecane can be seen in **table 3.1**.

Table 3.3.1 – Cost benefit analysis of using 1-bromododecane over 1-iododododecane (costs of reagents taken from Sigma Aldrich)[10]

Reagent	Amount needed (g)	Cost (£)	Yield (%)	Cost per gram of product (£/g)
1-Bromododecane	16.7	5.69	25	1.72
1-Iododododecane	16.7	20.30	30	5.08

The opposite effect on yield was observed when these indoles were reacted with squaric acid to form dyes (**6**), (**7**), (**D3**) and (**D4**). The dyes produced from indoles containing sulphur had much higher yields (47% and 64% for dyes (**6)** and (**D3**), respectively) compared with the dyes made from indoles with the dimethyl moiety (42% and 35% for (**7)** and (**D4)**, respectively). The explanation for this was easily observed throughout the reaction on the TLC plate and purification column. Before purification, the dyes without sulphur appeared green in colour. This suggested that the reaction mixture had both half-squaraine product (red/orange) and full squaraine impurity (blue) which together made green. However, the reaction mixtures of the dyes containing sulphur were red in colour. This suggested that there was little to no full squaraine (blue) product (see **Figure 3.5**). As the sulphur dyes were less

susceptible to full squaraine conversion this meant a higher yield of half-squaraine was obtained.

Figure 3.5 - (left) column chromatography of $C(CH3)_2$-containing dye (**7**) showing green due to the combination of yellow/red half-squaraine along with a blue full-squaraine impurity and (right) the synthesis of sulphur-containing dye (**6**), which only shows the red/yellow colour of half-squaraine.

The reaction scheme for step two can be seen in **Figure 3.6**.

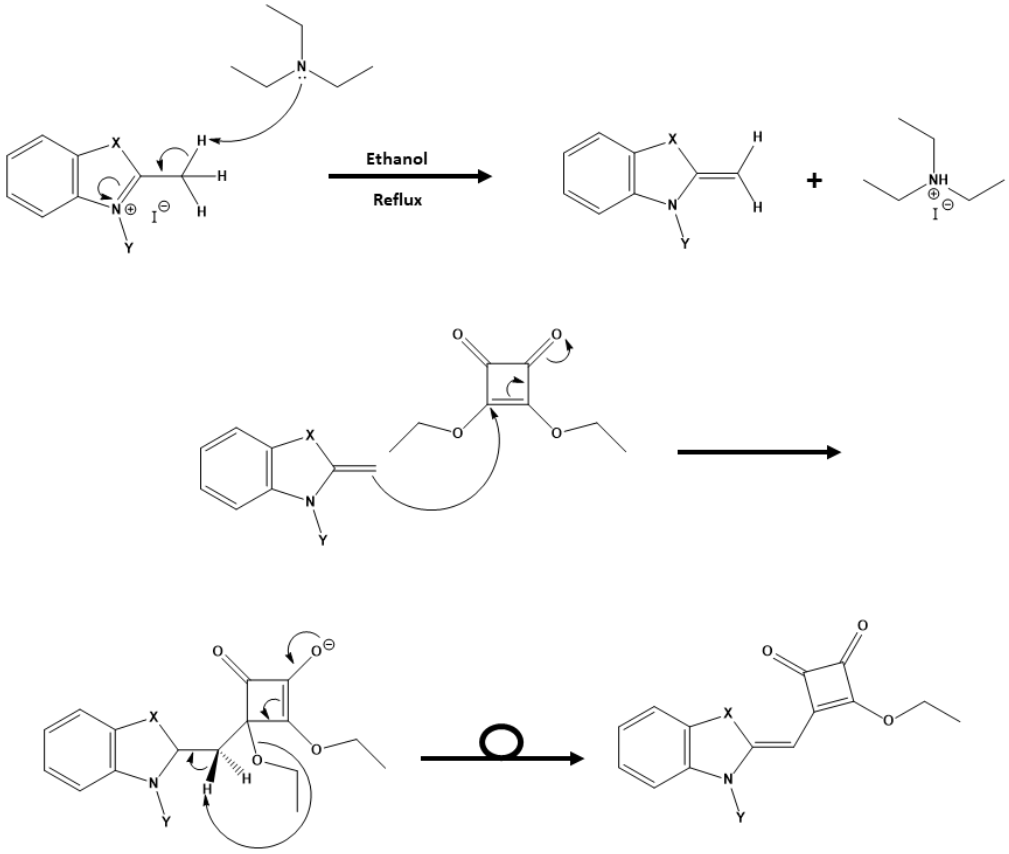

Figure 3.6 - General synthesis of HfSQ dyes step 2

The third reaction was de-esterification of the organic dyes (see **Figure 3.7**). For this type of reaction, previous literature normally reports the use of an inorganic base is used such as $NaOH_{(aq)}$.[210,264] However, the effect of Na^+ ions on the photoelectrode has been widely reported to have a negative effect on device performance in DSC devices.[265] Therefore, it was decided that an organic base such as tetrabutylammonium hydroxide should be used, as the tetrabutylammonium ion has been widely reported to have a positive influence on device performance.[266] The reason for using an organic base over an inorganic base such as NaOH is discussed in **section 3.2.2**.

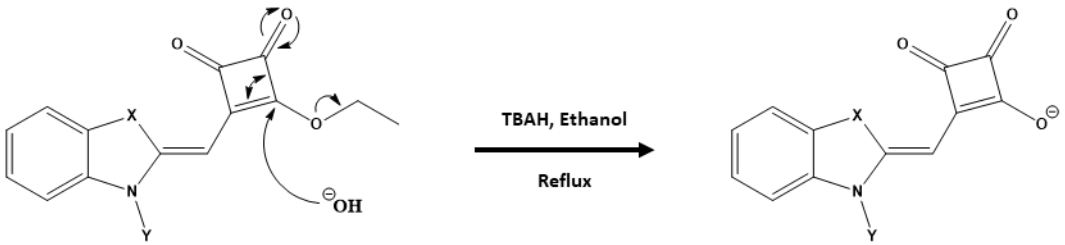

Figure 3.7 - General synthesis of HfSQ dyes step 3

Although the de-esterification reaction was relatively easy to perform (no inert atmosphere required), the purification of some of the dyes was particularly difficult. In the literature, it was reported that the reaction solutions were concentrated during work-up before cold ethanol was added and then the product precipitated.[123] However, despite several attempts, this technique did not work for the compounds reported here. The reasoning was that both the starting material and product were soluble in polar solvents (such as ethanol) and therefore when the ethanol was added everything would remain in solution rather than precipitate. Therefore, other methods were tried in order to obtain the product.

Dyes (**D1**) and (**D2**) were relatively easy to purify as the starting material was soluble in ethyl acetate so a column was run using a mixture of petroleum ether:ethyl acetate to remove any starting material. After this, the solvent system was changed to mixture of dichloromethane and methanol to obtain the product. In fact, compound (**D2**) has been synthesised before but using $NaOH_{(aq)}$ as a base rather than tetrabutylammonium hydroxide which suggests that the presence of the tetrabutylammonium ion may have increased the solubility of the product in ethanol[210]. For more discussion on why tetrabutylammonium hydroxide was used rather than NaOH, please see chapter 2.2.2. (counter ion effects on DSC performance). The synthesis of dyes (**D5**) and (**D6**) were not as simple because the starting material and the product had almost identical solubilities in all the solvent systems tried. It therefore was not possible to separate the materials by hand when using tetrabutylammonium hydroxide as the base. Therefore, the reaction was tried using $NaOH_{(aq)}$ to increase the yield of the product to make purification easier. Unfortunately, it still was not possible to purify the product using method either. Fortunately, towards the end of this work our research group purchased a flash chromatography system. Therefore, the initial de-esterification experiment was re-attempted and the product of this was purified with the flash chromatography

system in order to obtain greater control over the separation. This time, after the initial purification, the solution was concentrated, and the pure product did precipitate with cold ethanol however, the yields were low (< 10 %).

The final synthetic strategy was to convert the squaraine group of the four esterified dyes (i.e. the sulphur or methylene indoles along with N-indole alkyl/propionic acid dyes) into vinyl dicyano acyloin moieties ((**D7**), (**D8**), (**D9**), (**D10**)). To the best of my knowledge (**8**), (**12**), (**16**) and (**17**) have not previously been reported in the literature and are novel compounds. A proposed synthetic scheme for this reaction can be seen in **Figure 3.8**). These new dyes have been identified using several analytical techniques. The resonances identified in the 1 H NMR spectrum suggest that (**D7**), (**D8**), (**D9**) and (**D10**) have been isolated as the triethylamine salt. Four protons are identified in the aromatic region between 8.96 and 6.93 ppm with multiplicities including a doublet, triplets and multiplets. Resonances between 5.0 and 6.0 ppm have the correct multiplicities and integration to be identified as the methylene proton located near the squaric acid moiety, the ethyl group attached to the nitrogen of the indole and the methyl groups located at the 3 position of the indole unit, respectively. The ethyl group of the triethylamine cation has been identified by quintet and triplet peaks around 3.20 and 1.30 ppm, which integrate to six and nine protons, respectively. Furthermore, the coupling constants calculated for the protons in each environment are similar to those reported for previous half squaraine dyes synthesised by Holliman *et al.* [123] In addition, ^{13}C NMR data show a resonance at 108-111 ppm which is associated with the cyano (CN) functional group. In addition, resonances for the carbonyl group of the squaric acid and carboxylic acid moiety are also identified between 192 and 174 ppm. Analysis using high resolution mass spectrometry identifies the M^+ ion which corresponds to the target molecule in the non-salted form. Attenuated total reflectance infrared (ATR-IR) spectroscopy has been used to identify functional groups in the molecule including the nitrile and carbonyl groups.

Dyes (**D2**) and (**D8**) are new but similar to those synthesised during a recent report of a single linker Hf-SQ dyes.[123] Holliman *et al.* showed the effect of linker position on device performance[123] highlighting that the best performing dyes had the anchoring group bound to the acceptor unit of the dye.[123] This paper looked at having multiple anchors on the same chromophore and their effect upon device performance. Although dyes with more than one anchor group didn't show improved efficiency, device

stability did improve. This shows that dyes can bind to the TiO_2 surface through multiple sites if the anchor groups can get close enough to the surface, but it does not confirm if the dyes only inject their electrons through a single anchoring group. Holliman used various spectroscopic techniques (UV-Vis and ATR-IR) to demonstrate how half-squaraine dyes bind to the TiO_2 surface by understanding what bonding is taking place at the TiO_2 surface. Holliman also uses this information to postulate how these dyes may orientate themselves during the sensitisation process. Though there is plenty of data to back up their theories of dye binding little evidence is given on dye orientation leading to the work in this chapter.

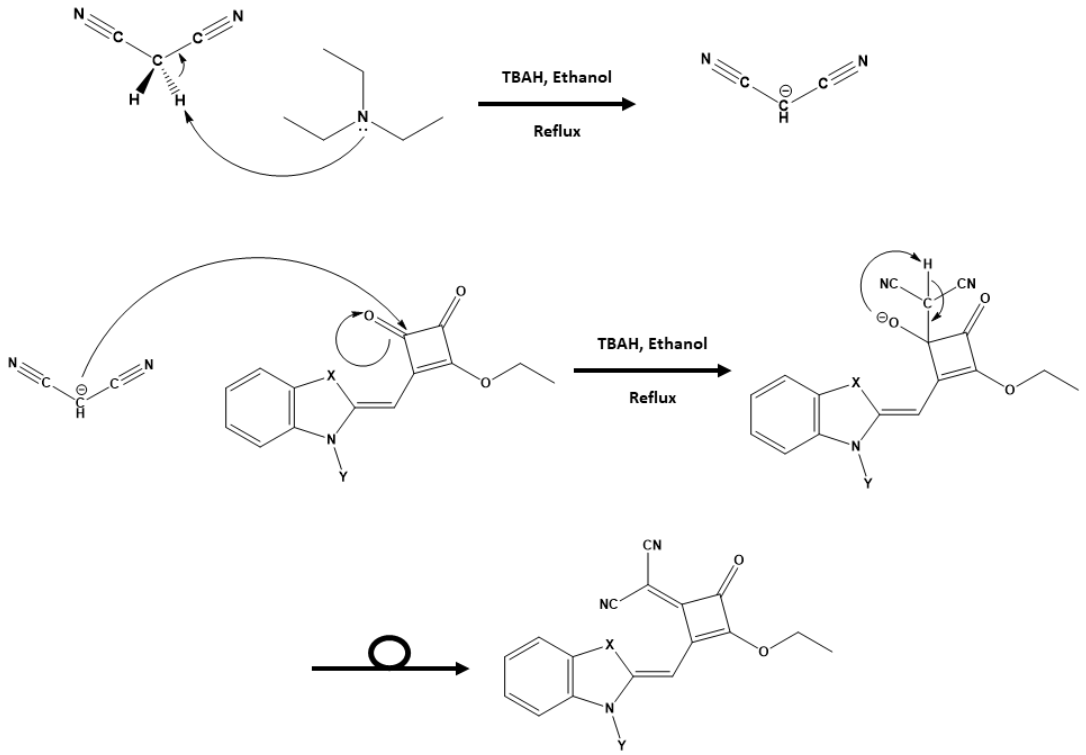

Figure 3.8 -Proposed synthesis of HfSQ dyes step 4

As the structure of the dyes can be quite complicated **Table 3.2** gives a general summary of the structure of each dye for easy comparison.

Table 3.2 – Summary of HfSQ dye structures synthesised in this chapter

Dye	S or $(CH_3)_2$	X =	Binding site
(**D1**)	S	$C_{12}H_{25}$	Aceloin
(**D2**)	$(CH_3)_2$	$C_{12}H_{25}$	Aceloin
(**D3**)	S	$(CH_2)_2CO_2H$	Carboxylic acid
(**D4**)	$(CH_3)_2$	$(CH_2)_2CO_2H$	Carboxylic acid
(**D5**)	S	$(CH_2)_2CO_2H$	Aceloin and Carboxylic acid
(**D6**)	$(CH_3)_2$	$(CH_2)_2CO_2H$	Aceloin and Carboxylic acid
(**D7**)	S	$C_{12}H_{25}$	Aceloin and/ or Dicyano
(**D8**)	$(CH_3)_2$	$C_{12}H_{25}$	Aceloin and/ or Dicyano
(**D9**)	S	$(CH_2)_2CO_2H$	Carboxylic acid, Aceloin and/ or Dicyano
(**D10**)	$(CH_3)_2$	$(CH_2)_2CO_2H$	Carboxylic acid, Aceloin and/ or Dicyano

3.2.2 Counter Ion effects on DSC performance

In the synthesis of compounds (**D1**), (**D2**), (**D5**) and (**D6**) I discussed using tetrabutylammonium hydroxide to remove the ester from the acceptor unit of the half-squaraine dyes rather than the more widely reported method of using aqueous sodium hydroxide ($NaOH_{(aq)}$). This is down to several papers including that of Wang *et al.*[265] reporting that DSC devices with Na^+ ions present showed a dramatically reduced overall conversion efficiency. Na^+ ions on the TiO_2 surface increased charge recombination.[265] When compared to titania nanosheets washed with H_2O, sheets washed with $NaOH_{(aq)}$ showed to have an increase in impurities and defects in the film. Using XPS the impurities were identified as Na^+ ions, the depth profile confirmed a large concentration of Na^+ on the TiO_2 surface, therefore proving Na^+ was responsible for the increased charge recombination. Therefore, we decided to look into alternatives to de-esterify acceptor unit of the half-squaraine dyes in particular tetrabutylammonium hydroxide.

3.2.2.1 Effects of Tetrabutylammonium ions on DSC device performance

Unlike Na^+ ions, $[CH_3(CH_2)_3]_4N^+$ ions have been proven beneficial for DSC devices. Nazeeruddin *et al.*[266] studied the effects of tetrabutylammonium hydroxide on Ru

sensitizers in DSC devices. By synthesising three analogous dyes (with varying amounts of $[CH_3(CH_2)_3]_4N^+$), Nazeeruddin was able to determine the effects of $[CH_3(CH_2)_3]_4N^+$ on DSC device performance.[266]

Nazeeruddin found that as you increased the number of $[CH_3(CH_2)_3]_4N^+$ counter ions in N3 dye, the PCE increased (N3 = 7.4 %, N3[TBA] = 7.7 %, N719 = 8.4 %, $N3[TBA]^3$ = 9.3 %). However, when all the H^+ ions were exchanged for TBA^+ ions, the performance dropped from 9.3 % for $N3[TBA]^3$ to 8.2 % for N712 (though it is worth noting that this is still 1 % higher than the efficiency of N3 without any tetrabutylammonium hydroxide ions). The chemical structures of N3, N719 and N712 can be seen in **Figure 3.9**.

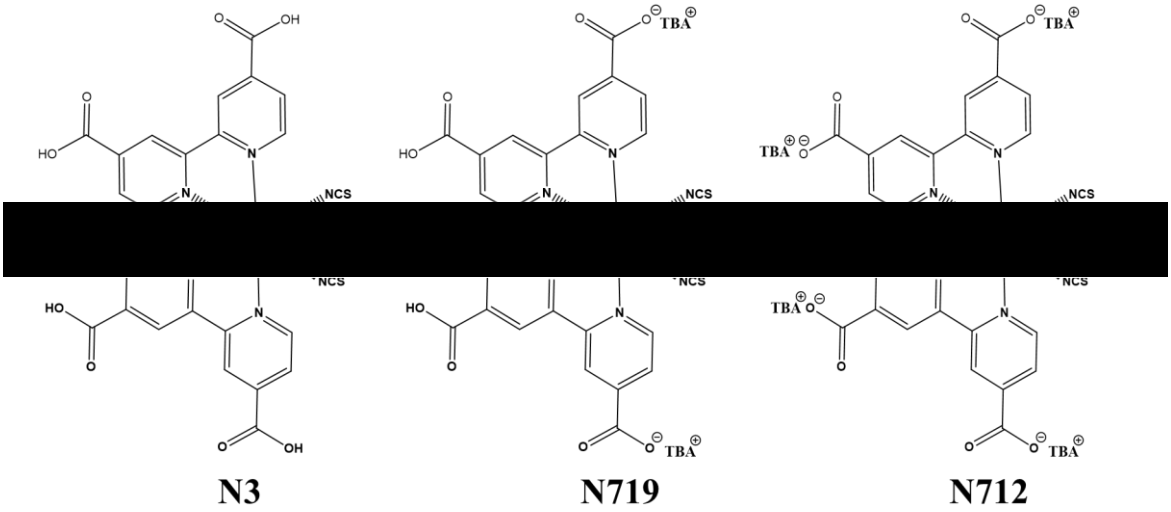

Figure 3.9 - Structures of N3, N719, N712. Synthesised by Nazeeruddin et al.[229]

The reason for this is that most n-type dyes for DSC devices are slightly acidic and therefore protonate the TiO_2 surface during the sensitisation process.[246] These protons lower the conduction band of the TiO_2 surface and give it slightly positive charge.[246] Although this allows for good e^- injection into the TiO_2 conduction band (increasing J_{sc}), it also reduces the energy difference between the TiO_2 conduction band and the redox potential of the electrolyte reducing V_{oc}. When H^+ is replaced by a less acidic ion such as a tetrabutylammonium hydroxide there is little effect on the energy of TiO_2 conduction band resulting in higher V_{oc}. However, this is slightly offset by less efficient electron injection into the TiO_2 (resulting in lower J_{sc}). As there is a larger positive effect on V_{oc} than negative effect on J_{sc} when using tetrabutylammonium hydroxide ions the device performance is generally improved. However, for the best performance the ratio of H^+ to tetrabutylammonium hydroxide need to be balanced in

order to optimise V_{oc} and J_{sc}.[246] As well as increasing V_{oc} tetrabutylammonium hydroxide ions are also known to reduce electron – electrolyte recombination.[247] The large size of $[CH_3(CH_2)_3]_4N^+$ ions disturb the approach of I_3^- and I_2 ions (through stearic hinderance) to the TiO_2 surface interrupting ionic species exchange.

3.2.3 Spectroscopic analysis

Figure 3.10 shows the UV-Vis spectra of HfSQ dyes in solution and after sorption onto TiO_2 electrodes. The spectra in solution show that modification of the of the squaric acid moiety by replacing a carbonyl group with a vinyl dicyano group causes the absorption of the spectra to exhibit a bathochromic shift in the spectra of (**D7**), (**D8**), (**D9**) and (**D10**) by comparison to the unmodified dyes (**D1**), (**D2**), (**D5**) and (**D6**) respectively. The dyes with the highest molar extinction coefficient (ε) is observed for the esterified squaraine (**D4**). Esterified dyes (**D3**) and (**D4**) generally showed the highest (ε), whilst the de-esterified dyes (**D1**), (**D2**), (**D5**) and (**D6**) generally showed lower (ε). Dyes with vinyl dicyano modified dyes (**D7**), (**D8**), (**D9**) and (**D10**) generally showed the lowest (ε). The spectra for dyes with sulphur (**D1**), (**D3**), (**D5**), (**D7**) and (**D9**) are quite different to the dyes without sulphur (**D2**), (**D4**), (**D6**), (**D8**) and (**D10**). De-esterified sulphur containing dyes all have lower (ε) compared to their dimethyl derivatised carbon counterparts. However, sulphur dyes with the diycano moiety (**D7**) and (**D9**) show much higher (ε) than the equivalent dyes without sulphur (**D8**) and (**D10**) respectively. This is very interesting as it shows the sulphur plays an important role in the HOMO and LUMO of these dyes.

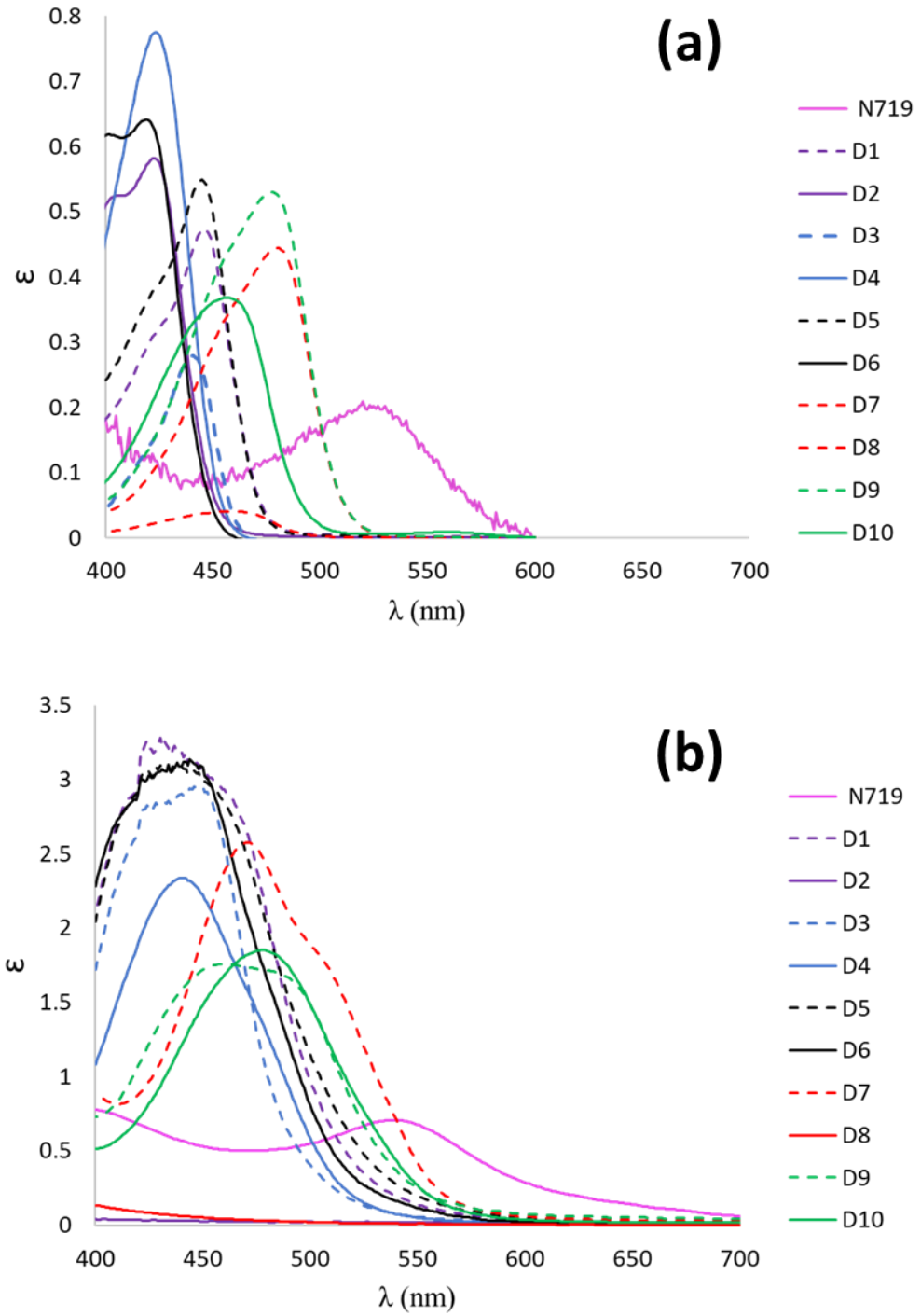

Figure 3.10 - UV-Vis spectra of HfSQ dyes in solution (a) and dyes adsorbed onto a transparent TiO_2 surface (b). For clarity, structurally related dyes have the same colour and $C(CH_3)_2$ dyes have solid lines, whilst S dyes have dashed lines.

Figure 3.10b Shows the absorption UV-Vis data when the dyes are absorbed onto transparent, mesoporous TiO_2 films (via passive dyeing). The data shows a broadening of the peaks as compared to dyes in solution. Interesting all dyes (other than (**D8**))

show much higher absorption for the HfSQ dyes compared to N719. This could be explained by higher ε however, dyes (**D3**) and (**D10**) show similar ε to N719 yet show much higher absorption peaks. This is most likely down to higher dye loading on the TiO_2 surface. The HfSQ dyes are much smaller and therefore there should be more space for them to absorb to the TiO_2 surface. Dye (**D8**) shows the lowest absorption of all the dyes, this is partly down to having the lowest (ε) of all the dyes (10,835 M^{-1} cm^{-1}). However, this is ~ half the absorption of other dyes such as (**D9**) yet the absorption of (**D8**) is less than a 10^{th} of (**D9**). This suggests lower dye absorption, which would make sense as dye (**D8**) only absorbs using the single linker of the acyloin moiety. Dye (**D9**) is able to chemisorb both through the squaric acid and/or from the propionic acid linker. The weaker bonding was also observed experimentally. During device manufacturing, the dyed TiO_2 was washed with ethanol (after pump dyeing). During washing dye (**D8**) was visibly seen to desorb from the TiO_2 surface (see **Figure 3.11**).

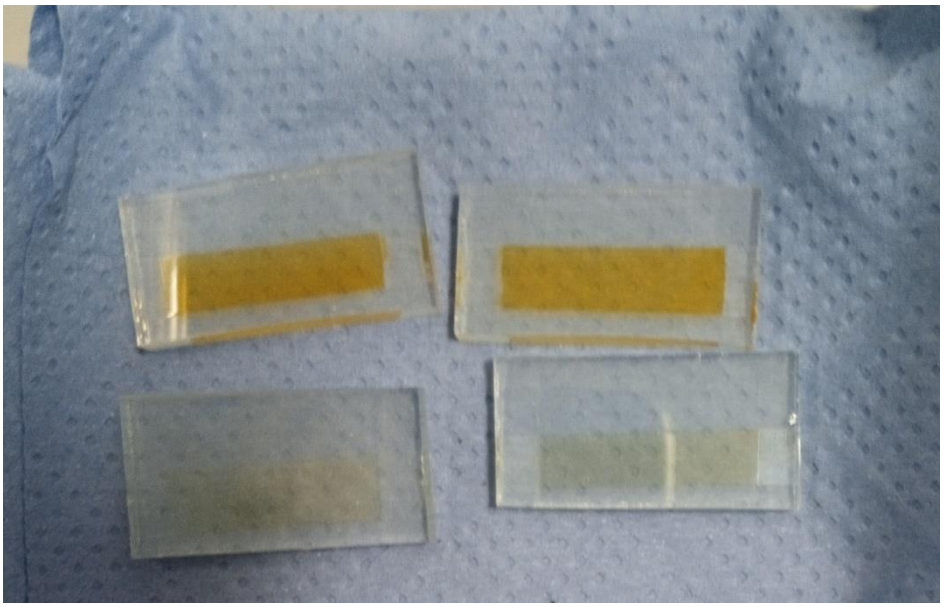

Figure 3.11 – Images of replicate TiO_2 electrodes which have been dyed with (**D2**) or (**D8**) and then washed with ethanol. The image shows that (**D2**) remains whilst (**D8**) desorbs.

To further investigate the interaction between the dyes and TiO_2, ATR-infrared spectroscopy has been used to compare adsorbed dye and dye powders (see appendix). Dyes (**D3**) and (**D4**) have been designed and synthesised to covalently link to TiO_2 through the carboxylic acid unit on the indole N. The ATR-IR data shows a reduction in signal for the C=O and O-H (> 3000 cm^{-1}) on sorption. This suggests the formation of an ester linkage between the carboxylic acid and the TiO_2 surface. A N-H peak is

also observed for the TiO_2-sorbed dyes. Considering there is only a single nitrogen atom the dyes structure it suggests that the dye sits flat and the N atom is interacting with the TiO_2 surface. Dyes (**D1**) and (**D2**) have been designed and synthesised to covalently link to TiO_2 through the carboxylic acid unit on the acyloin moiety. Like dyes (**D3**) and (**D4**), the ATR-IR data for dyes (**D1**) and (**D2**) show a reduction in signal for the C=O and O-H (> 3000 cm^{-1}) on sorption. Suggesting the formation of an ester linkage between the acyloin moiety and the TiO_2 surface. The ATR-IR data also shows a shift for the N-H peak, suggesting that (**D1**) and (**D2**) lie flat against the TiO_2 surface. However, the peak shift could also arise from the formation of tetrabutylammonium ions arranging themselves on the TiO_2 surface as one would expect (or both). Dyes (**D7**) and (**D8**) have been designed and synthesised to covalently link to TiO_2 through the acyloin moiety however it is unclear whether they absorb through the carboxylic acid unit or the vinyl dicyano unit. The ATR-IR data for dyes (**D7**) and (**D8**) show a reduction in signal for the C=O and O-H (> 3000 cm^{-1}) on sorption. The reduction of O-H and COOH bonds suggests the formation of an ester linkages between the acyloin moiety and the TiO_2 surface. The disappearance of the N-H peak suggests that the dye is binding through the carboxylic acid unit of the acyloin moiety and not the dicyano unit. Dyes (**D6**), (**D7**), (**D9**) and (**D10**) have been designed and synthesised to covalently link to TiO_2 through two linker groups; the acyloin moiety and the carboxylic acid unit on the indole N. For (**D5**) and (**D6**) the sharp, intense carbonyl (1750 – 1752 cm^{-1}) peaks of the dye powder shrink and shift compared to the dyed TiO_2 powder (1762-1764 cm^{-1}). A OH broad peak appears in the dyed TiO_2 powder, whilst the N-H bond reduces or disappears entirely. This suggests dye (**D5**) and (**D6**) are binding through the both the propionic acid and acyloin moiety forming ester bonds. Like dyes (**D5**) and (**6**), dyes (**D9**) and (**D10**) have also been designed and synthesised to covalently link to TiO_2 through two linker groups; the acyloin moiety and the carboxylic acid unit on the indole N. However, it is unclear whether it bonds through the vinyl dicyano unit or the carboxylic acid unit of the acyloin moiety. The ATR-IR data for dyes (**D9**) and (**D10**) show sharp, intense carbonyl (1742-1749 cm^{-1}) and dicyano (2198 cm^{-1}) peaks of the dye powder almost disappear entirely. A small O-H broad peak appears in the dyed TiO_2 powder, whilst the N-H bond shift (3056 cm^{-1}) compared to the dyed TiO_2 powder (2975-3003 cm^{-1}). This suggests dyes (**D9**) and (**D10**) bind to the TiO_2 through the carboxylic acid unit on the indole N. The disappearance of the vinyl dicyano unit and shift of the N-H bond

also suggests bonding to the TiO_2. However, the computer modelling data suggest that the dye is bound through the carboxylic acid unit of the acyloin moiety and the vinyl dicyano units are interacting with the TiO_2 surface or the S atom of the indole, which would explain the ATR-IR peaks.

3.2.4 Dye orientation studies (DFT modelling)

Using density functional theory (DFT) this work has gained an insight into the orientation and binding of single dye molecules on the (1 0 1) surface of anatase TiO_2, at zero kelvin (0 K). Six of the nine dyes were investigated: four benzothiazole – (**D1**), (**D3**), (**D5**), and (**D9**); two dimethyl-derivatised – (**D4**) and (**D6**) and found the dye molecules preferentially adsorb to lie near-planar and horizontal to the surface.

From a sub-section of orientations – including vertical and edge-on – we allowed the dye molecules to relax to their energy minima. Absolute adsorption energies were calculated and the lowest energy minima (i.e. preferentially adsorbed orientations) corresponded to molecules lying horizontally to the surface.

The DFT modelling of the six individual dyes as neutral gas phase molecules is in good agreement with the available crystal structure data (**section 3.2.7**) for all the dyes (**Figure 3.12**). The common surface-bonding motif to under-coordinated Ti sites (i.e. Ti5c) is via the linker groups: squaraine, carboxylic acid and the cyano group. Carboxylic acid and squaraine – when not directly bonded to the surface – can form hydrogen-bonds to 2-coordinated surface oxygen. These hydrogen bonds in a physical system are dynamic and are influenced by ambient energetics; the hydrogen will 'hop' between the surface and dye. The simulated hydrogen bonds range in length from 1.76 Å to 2.16 Å, implying they are relatively strong. These secondary bonding phenomena enhance stability of these dye configurations on the TiO_2 surface. All six dyes exhibit all or a selection of bonding features: linkers, hydrogen bonds and electrostatic interactions between the planar rings of the dye and the TiO_2 surface.

Table 3.3 – The dyes, their groups, the linkers to the surface, angle of inclination of the squaraine moiety and the planar rings to the surface; the estimated projected surface area of the molecules on the surface, based on their Van der Waals outline

Dye	Group opposite indole N	Number of (linking modes)[a]	Approx. angle to TiO_2 surface (degrees)		Projected surface area of dye on surface (Å^2)
			Squaraine moiety	Planar rings	
(D1)	S	2 x Sq (O) 1 x Sq (O)-Surf (HO)	40	10-15	72
(D3)	S	1 x Sq (O) 1 x COO 1 x Sq (O)-Surf (HO)	45	15-20	73
(D4)	$C(CH_3)_2$	2 x Sq (O) 1 x COOH-Surf (O)	35	15-20	119
(D5)	S	2 x Sq (O) 1 x Sq (OH)-Surf (O) 1 x COOH-Surf (O)	30	0-5	86
(D6)	$C(CH_3)_2$	2 x Sq (O) 1 x Sq (O)-Surf (HO) 1xCOOH-Surf (O)	30	0-5	83
(D9)	S	1 x Cyano (N) 1 x COOH-Surf (O)	5	5-10	109

[a] Sq (O): squaraine O bonds directly to Ti_{5c}; COO: carboxylic O bonds directly to Ti_{5c}; Sq (O)-Surf (HO): hydrogen bond between squaraine O and hydroxylated surface; Sq (OH)-Surf (O): hydrogen bond between hydroxylated squaraine and surface O; COOH-Surf (O): hydrogen bond between carboxylate group and surface; Cyano (N): cyano-N bonds directly to Ti_{5c}.

The images in **Figure 3.12** show the dyes in a plan view, which gives an indication of the surface area they occupy and what the electrolyte or hole transport material "sees". Through this work, an estimation of the surface area of TiO_2 covered by a single dye. The results demonstrate the dyes occupy a surface area between 72–119 Å^2. For dye (**4**) the surface area occupation in a physical system could be larger because it was truncated for modelling. If an average 10 mm thick mesoporous, anatase TiO_2 photoanode film has a density of 3.78 g cm^3, this represents 3.78 mg of TiO_2 per cm^2. If the TiO2 has a surface area of 50 m^2 g^{-1}, there should be enough surface area for 2.56 x 10^{17} molecules of (**D3**), 1.59 x 10^{17} molecules of (**D4**) and in between for (**D5**), (**D6**), (**D9**). The author emphasizes that these are crude approximations based on 0 K,

DFT-optimized geometries, allowing for complete occupation of the available surface area (**Table 3.2**).

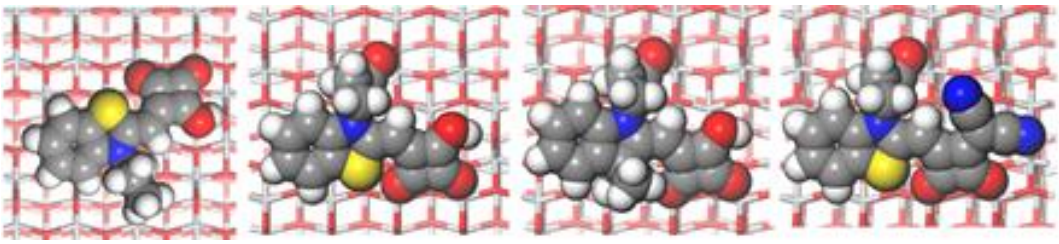

Figure 3.12 – Plan views of DFT modelling of the relaxed configurations of the most probable orientations of (from top to bottom) dyes (**D1**), (**D3**), (**D4**), (**D5**), (**D6**) and (**D9**) showing their Van der Waals outline mode on the TiO_2 surface.

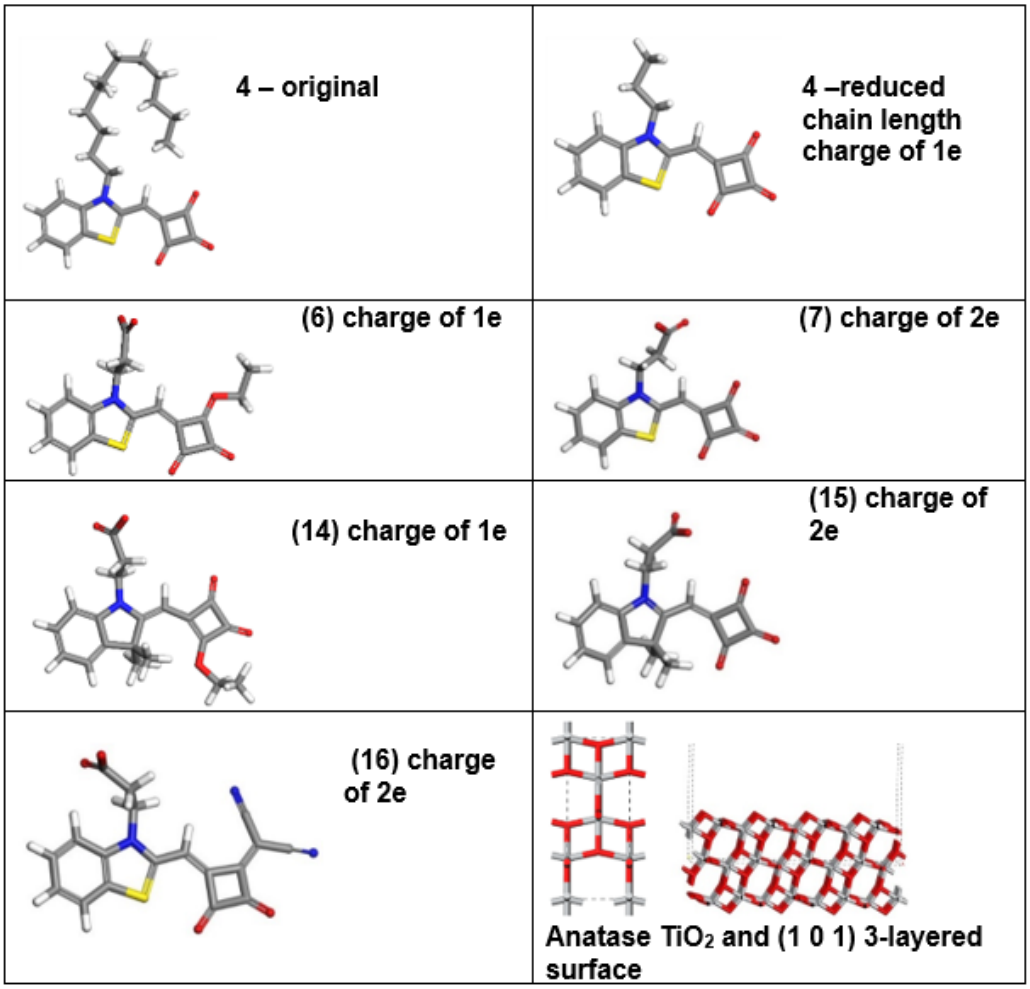

Figure 3.13 – Six half-squaraine dyes and the final TiO_2 model. Grey – carbon; white – hydrogen; red – oxygen; blue – nitrogen; yellow – sulphur; silver Ti. One or two hydrogens were added to the dyes in order to make them neutral for both gas-phase calculations and surface adsorption.

In addition, in order to reduce the computational time required to model the data, dyes (**D1**), (**D2**), (**D7**) and (**D8**) all had their 12–carbon (dodecyl) alkyl chains reduced to 2-carbon (ethyl) chains (see **Figure 3.13**). The computers modellers decided this would save a significant amount of time without compromising the data.

The difficulties with this modelling approach is that, to save computational time, it is done in a vacuum, whereas experimentally there is either a solvent or gas molecules present. For example, during the dyeing process used in this thesis, solvents such as ethanol, ter-butanol and acetonitrile were used to dissolve the dye before being passed over the TiO_2 to allow the dye to absorb. Though the solvent is quickly removed after dyeing, it will affect the process of how the dye adsorbs to the TiO_2 although the effect on the final dye orientation is less clear. DSC devices also often contain a liquid electrolyte which is constantly in contact with the photoelectrode during device operation. Therefore, this is very likely to have an effect on how the dyes orientate during device operation. It is possible to model excited states of dyes in solution using a polarizable continuum model (PCM)[267,268]. However, this model is not applicable to dyes adsorbed on surfaces.

3.2.5 Angle-resolved X-ray photoelectron spectroscopy (ARXPS)

3.2.5.1 Sample preparation

Usually when making DSC devices, as stated previously, the TiO_2 is dyed anywhere between 18 – 24 h. However, as the single crystals of TiO_2 used in this thesis are atomically flat, they have a much smaller surface area. Thus, as part of the experimental design for this section of work, this needed to be considered in terms of the dying times. The concern was that, if the TiO_2 was dyed for too long, then the dyes might not form a monolayer and might begin to aggregate affecting the data. If this were to occur, then the average dye orientation would be random and there would be no clear orientation observed by ARXPS. On the other hand, if there was insufficient dye on the surface then the signal to noise ratio on the data would be poorer, and the scan rate would need to be increased in order to improve this. So initial dyeing times were tested, and it was found that, after dyeing the TiO_2 for 2 and 6 h (in 0.5 mmol dye solutions) no substantial difference was observed in the ARXPS data. It was therefore determined that 2h dyeing time was enough time for these experiments. After dyeing, the samples were washed with ethanol and dried under nitrogen, after which the samples were placed on the XPS sample holder using carbon tap as an adhesive.

3.2.5.2 ARXPS troubleshooting

In order to run angle-resolved X-ray photoelectron spectroscopy, the synthesised half-squaraine dyes were sensitised to single crystals of TiO_2 (orientation (110)K(001), (0.5 x 0.5 cm^2). A single crystal of TiO_2 had to be used for these experiments because the mesoporous TiO_2 films which are normally used to make DSC devices possess very uneven and porous surfaces (e.g. with many peaks and troughs, **see Figure 3.14**). This uneven surface would mean that not all the dyes would orientate themselves the same way and therefore the results of the ARXPS would be inconclusive. Therefore, by using an atomically flat single crystal, all of the dye on the TiO_2 surface should self-assemble in the same orientation and therefore the dyes should all be orientated in the same way.

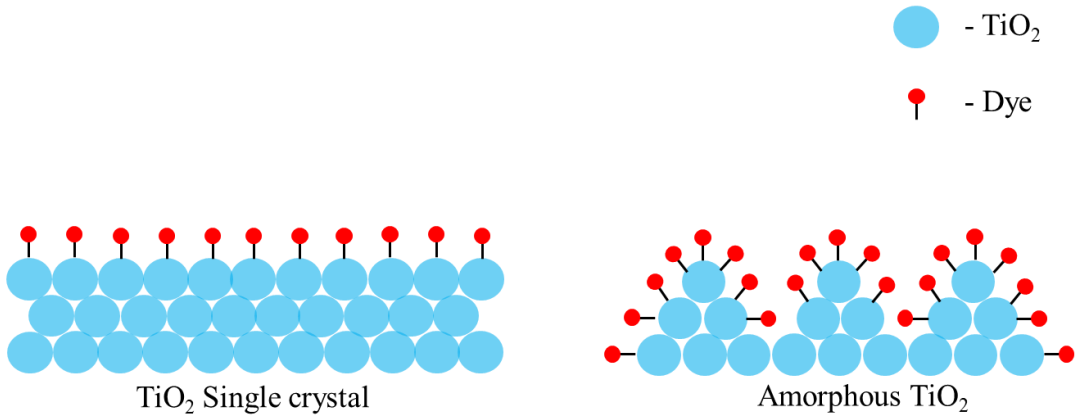

Figure 3.14 - Dye absorption of TiO_2, Single crystal of TiO_2 (Left) and Amorphous TiO_2 (Right)

The dye orientation was determined by comparing the intensities of the chemical peaks for atoms within the dye structure (S, C, O and N) compared to the peaks that belong to the TiO_2 surface (Ti and O) at varying angles. At higher angles (e.g. 90°), the X-rays penetrate through the dye and into the TiO_2. Therefore, at these angles we see small peaks for the atoms within the dye and larger peaks for the atoms in the TiO_2 substrate. As the angles get smaller (e.g. 45°) the X-rays penetrate less of the substrate and more of the dye. This means an increase in the intensity of the atoms within the dye is observed alongside a decrease in the intensity of the TiO_2 peaks. By comparing the ratios of the peaks of the dye atoms to those of the TiO_2 it is possible to accurately determine their positional relationship to one another and therefore determine dye orientation (see **Figure 3.15**).

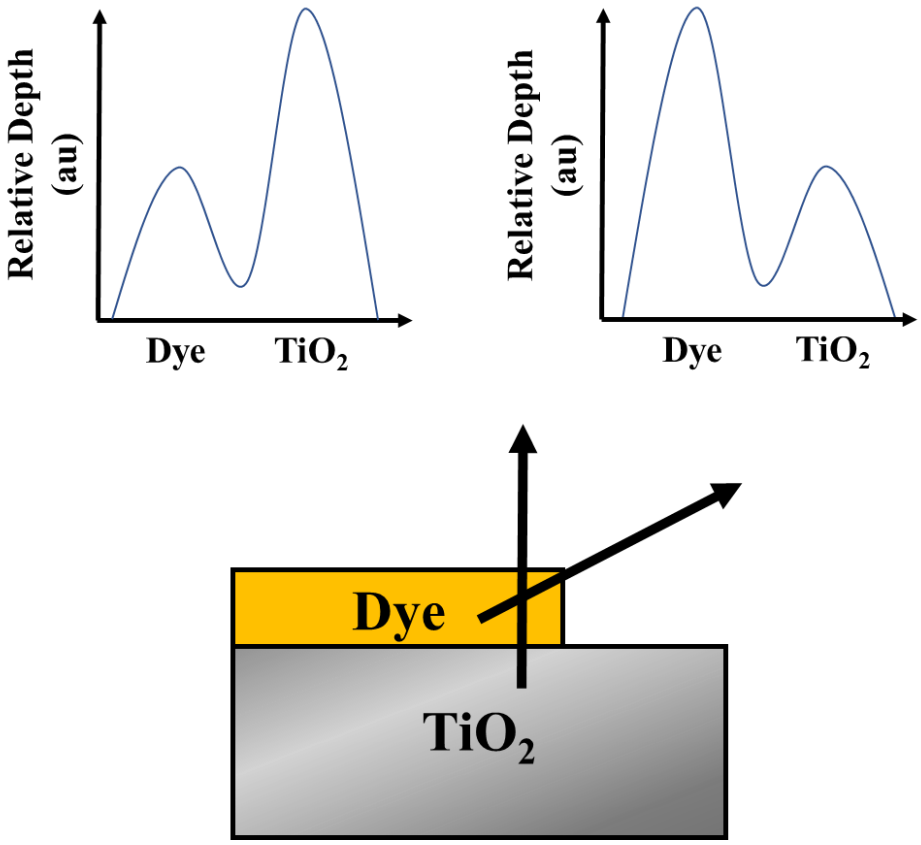

Figure 3.15 - Relative depth of X-rays at a bulk angle - 90° (left), and at a surface angle - 45° (right) during angle-resolved x-ray spectroscopy (ARXPS).

An unexpected problem was identified during the initial data measurements because it became apparent (under the XPS optical microscope) that the TiO_2 single crystals being used were only polished on one side. Upon visual inspection there was no difference between the polished and unpolished sides of the crystals. However, when the crystals were placed under the optical microscope attached to the XPS, the difference was very clear (see **Figure 3.16**). Therefore, the TiO_2 slides had to be removed from the XPS, cleaned and re-bound to the analysis tray. To ensure this never happened again, the procedure was altered, and each sample thereafter was analysed using a Keyence optical microscope to ensure the correct crystal orientation (polished side up) was used before the samples were prepared for full ARXPS analysis. This was a simple but very important step because, had the crystals been set up facing the wrong way up, the data were useless and, as some of the experiments took approximately 9 hours of instrument time, it could have meant wasting days of analysis.

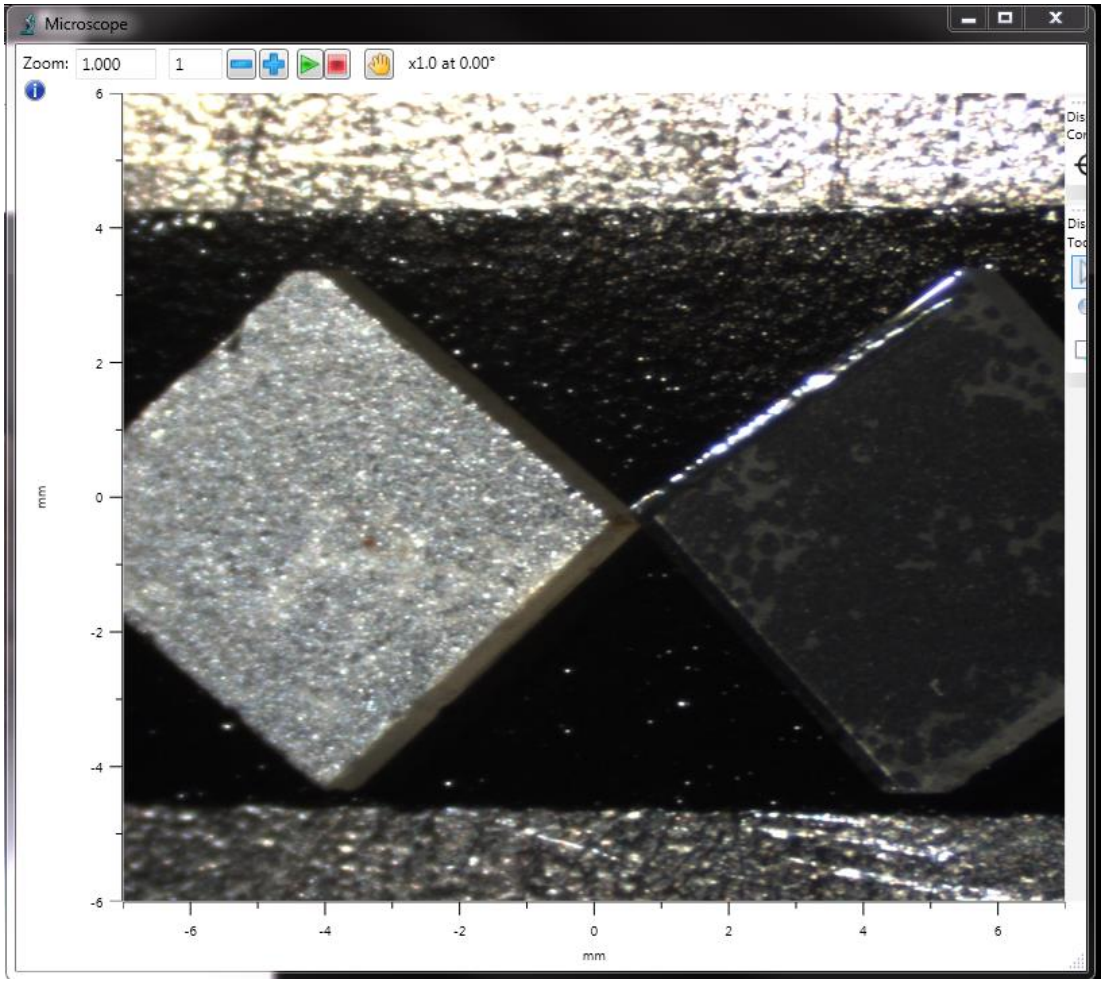

Figure 3.16 – TiO_2 single crystals under the optical microscope of the XPS. Unpolished crystal (left), polished crystal (right)

Another difficulty we came across when running XPS on such small samples was the signal to noise ratio which also affected the resolution of the data. Thus, with the samples at 90^o to the incident X-ray beam, the signal to noise ratio and the resolution of the data were extremely good. But as the angles became smaller the data became noisier and the resolution of the data decreased. We were able to improve this slightly by changing the position of the samples within the holder. Initially the samples were placed perpendicular on the sample holder. However, by rotating the sample by 45^o we could increase the surface area of our samples by 41.4 % (see **Figure 3.17**). Though this helped to improve the signal to noise ratio and resolution of the data, the number

of scans for some elements (such as S and N, increased to 20 and 8 scans respectively) had to be increased to make sure the data were of sufficient quality for our experiments.

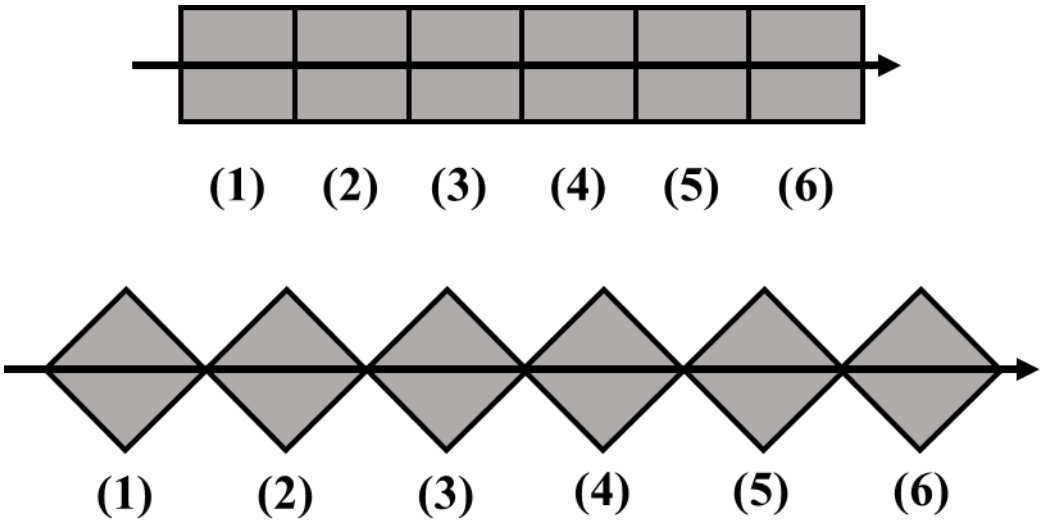

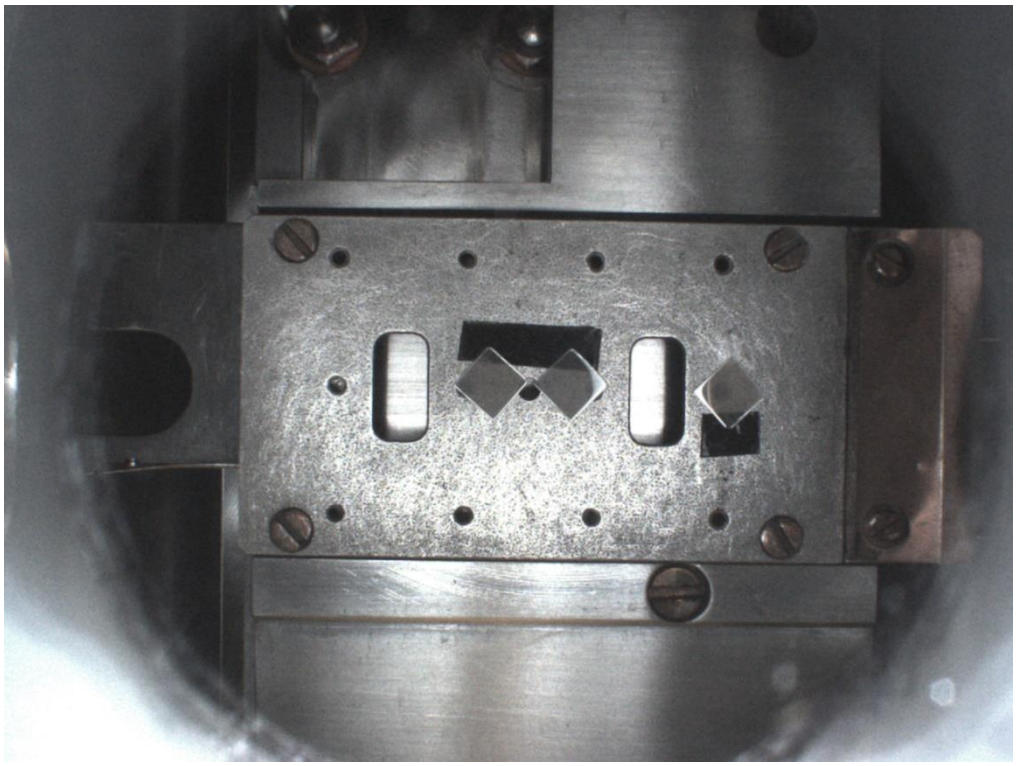

Figure 3.17 – TiO_2 single crystals loaded onto the XPS sample holder. Samples have been rotated by 45° to increase surface area for XPS analysis

Most of our ARXPS studies had to be run over a weekend due to the time-consuming nature of the experiments. Although XPS can be a relatively quick experiment, ARXPS is inherently time consuming as at each angle (5 angles per sample, 0^o, 40^o, 55^o, 63^o and 70^o) several scans must be taken. As a result, most of these ARXPS experiments ranged from three to nine hours, with the dyes containing sulphur moieties taking the longest time. Though sulphur is generally a good atomic probe for XPS (as it has lots of electron density), in our dyes sulphur was only present in small quantities (between 4 and 9 %). This quantity was okay for ARXPS at 90^o. However, as the measurement angles got smaller the signal to noise and the resolution of the data decreased. Therefore, if the peaks at each angle were too small, the error of the XPS baseline could interfere with the data. By increasing the scan rate (from 1 to 20), it was possible to ensure the accuracy and reliability of the data but only at the cost of time.

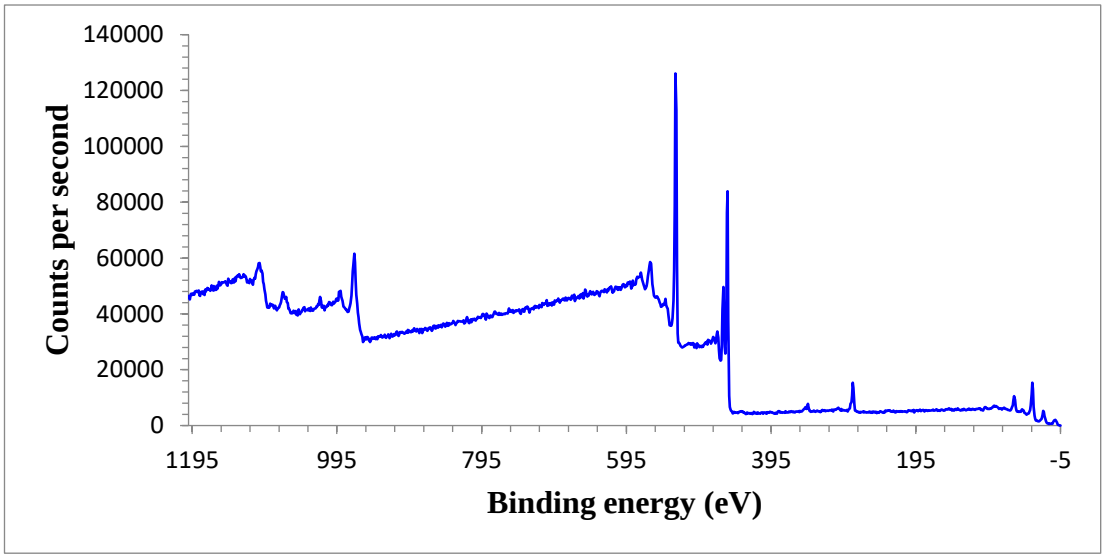

Figure 3.18 – XPS wide scan of a HfSQ dye. Two wide scans are run for each sample, one before XPS analysis and one after. Both spectra are compared to try to identify any signs of degradation during experimentation.

During a typical sample run, the measurement started by taking wide scan at the start of each experiment and then again at the end. A wide scan example of a half-squaraine dye can be seen in **Figure 3.18**). These wide scans were particularly useful for identifying important elements to look for. However, as organic dyes are known to break down under high energy radiation (X-rays) the wide scans were also used to see if the dyes began to break down under the X-ray beam. By comparing the peak

intensities at the start and end of each experiment it was possible to see any intensity changes which might indicate if any of the dyes had begun to break down. However, it was surprising and pleasing to see that all of the dyes were extremely stable and there were no signs that any degradation had occurred in any of the samples.

3.2.6 ARXPS analysis of dyes

3.2.6.1 Analysis of dyes (D1) and (D2)

The data for the different dyes have been grouped together into pairs of dyes which only differ based on whether there is a sulphur or a dimethyl moiety opposite the indole nitrogen. Otherwise, each pair of dyes were structurally similar. The first pair of dyes are (**D1**) and (**D2**) which both have a de-esterified squaraine unit and a dodecyl side group attached to the indole nitrogen.

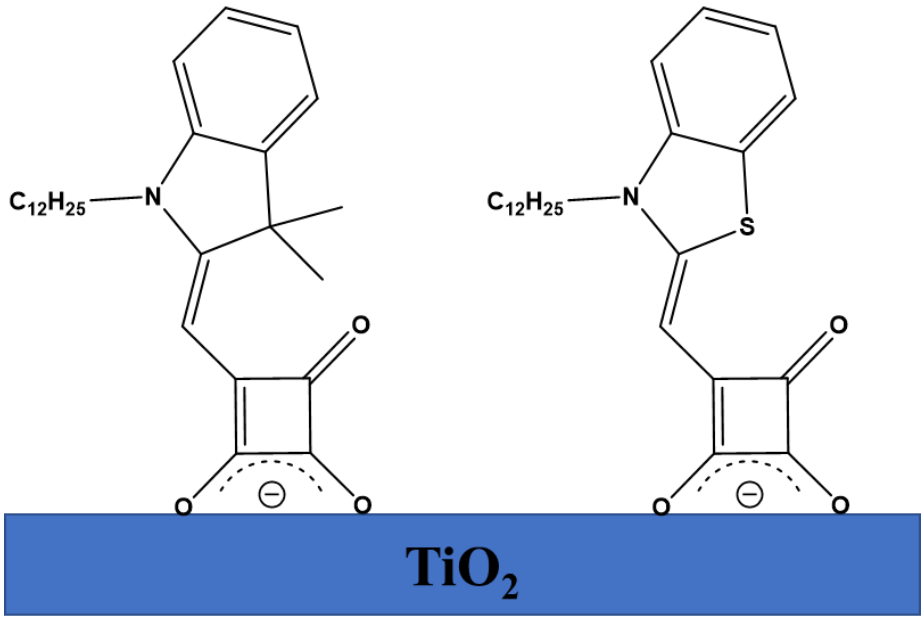

Figure 3.19 - Proposed orientation of dye (**D2** - left) and (**D1** - right) before being analysed by XPS and computer modelling

Figure 3.19 shows the proposed orientation of dye (**D1**) and (**D2**) before ARXPS and computer modelling took place. In the literature similar dyes were said to sensitise perpendicular to the TiO_2 surface through the acyloin moiety of the squaraine unit.[157] Sensitising at this angle would mean the alkyl chain and dimethyl-derivatised carbon/ sulphur moieties sit almost parallel to the TiO_2 whilst the benzene group sits at the very top surface perpendicular to the TiO_2.

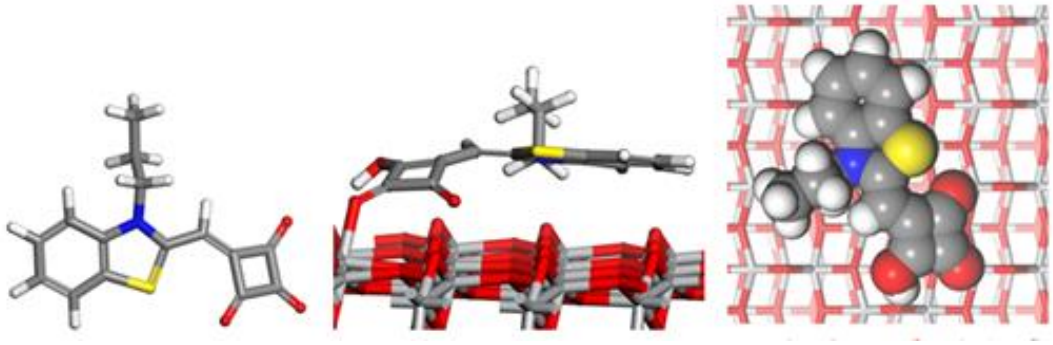

Figure 3.20 - DFT modelling of the relaxed configurations of the most probable orientations of dye (**D1**) (LHS without on an anatase (101) TiO_2 surface, where 'most probable' means largest (in magnitude) adsorption energy. The RHS image shows an aerial view of dye (**D1**) molecules on the TiO_2 surface where the dyes are depicted as 'space-filling'. They approximately cover a projected surface area (in $Å^2$ and to two significant figures) of (**D1**) – 96

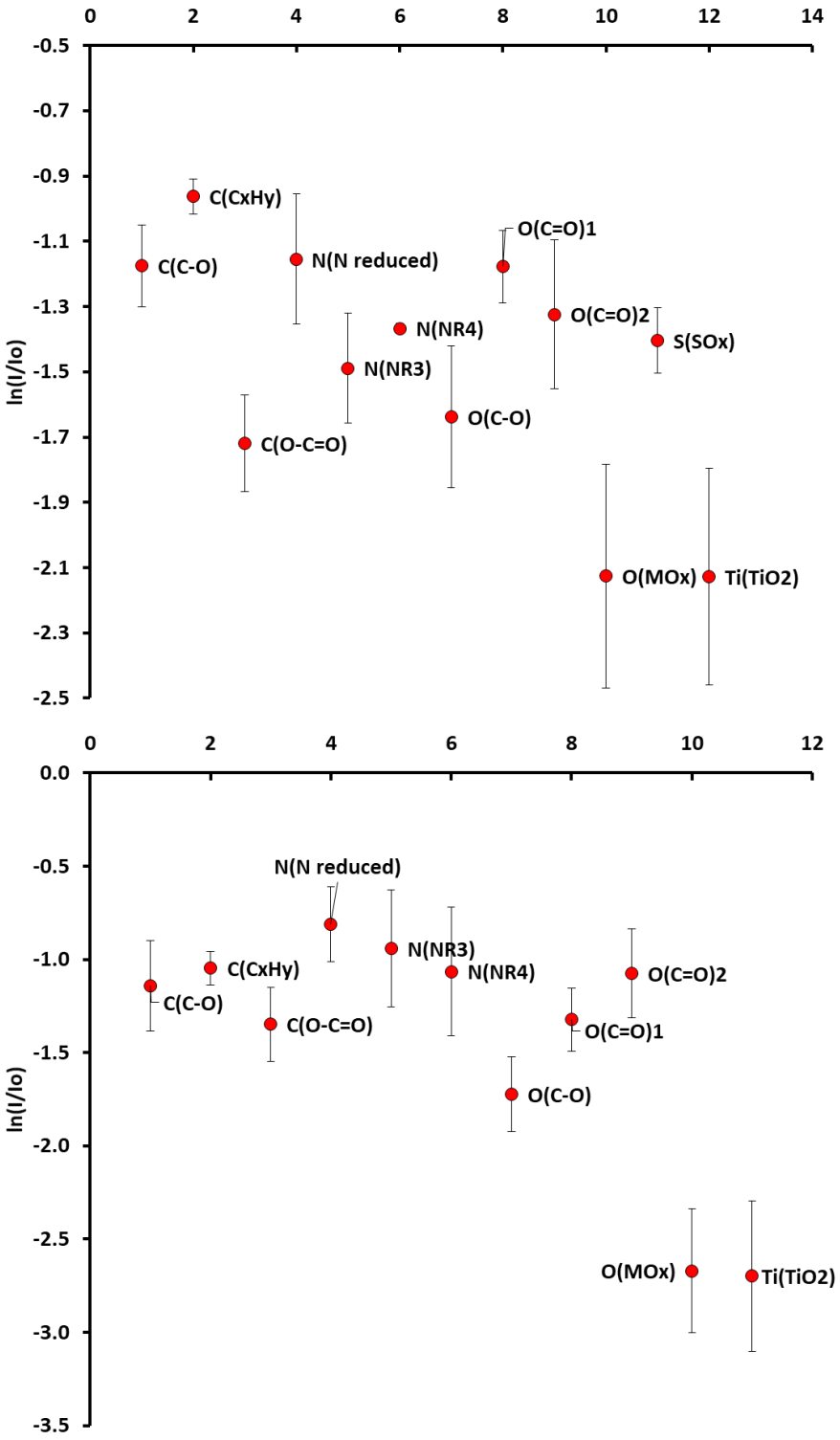

Figure 3.21 - Atomic positions in the z-axis (perpendicular to TiO_2 single crystal surface) of dye (**D1** - top) and dye (**D2** - bottom) – calculated from angle-resolved XPS data. The data are presented with the vertical axis $In(I/I_o)$ representing the vertical distance moving away from the surface.

Data for dyes (**D1**) and (**D2**) are shown in **Figures 3.20** and **3.21**. As suggested by Holliman *et al.*[157] dye (**D1**) and (**D2**) chemisorb to the TiO_2 through the acyloin moiety of the squaraine unit. Thus, as expected, the ARXPS experimental data shows that the acyloin group of the squaraine moiety (labelled COOX) is closest to the TiO_2 surface which suggests that this dye does adsorb through this unit. However, the computer modelling also showed that dye (**D2**) doesn't bind through two oxygen atoms as previous suggested but actually binds through a single oxygen atom (see **Figure 3.22**).

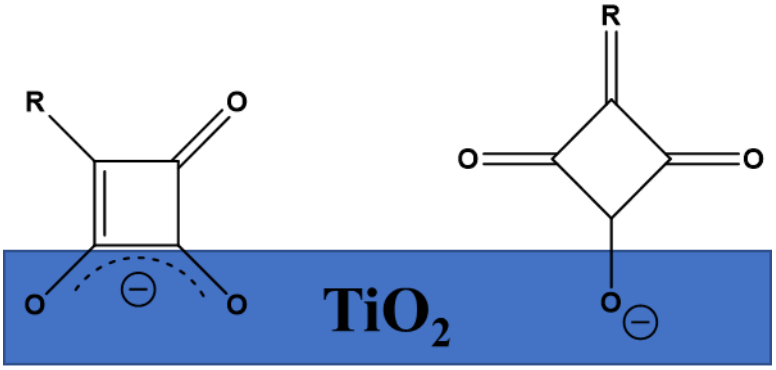

Figure 3.22 - Binding of acyloin group of dyes (**11**) and (**4**).
Predicted (left) versus modelled (right)

The data (ARXPS and computer modelling) also suggest that this dye does not adsorb perpendicular to the TiO_2 surface as initially thought but rather is orientated at quite a shallow angle with the nitrogen atom of the indole ring slightly closer to the TiO_2 surface than the oxygen atoms of the squaraine group. By comparison, dye **(D1)** is the analogous dye to **(D2)** except that it has a sulphur atom in place of the dimethyl-derivatised carbon of the indole. Here again the ARXPS data show that the acyloin moiety is closest to the TiO_2 surface as expected.

3.2.6.2 Analysis of dyes (D3) and (D4)

The next pair of dyes are (**D3**) and (**D4**) which both have an esterified squaraine unit and a propionic acid linker group attached to the indole nitrogen.

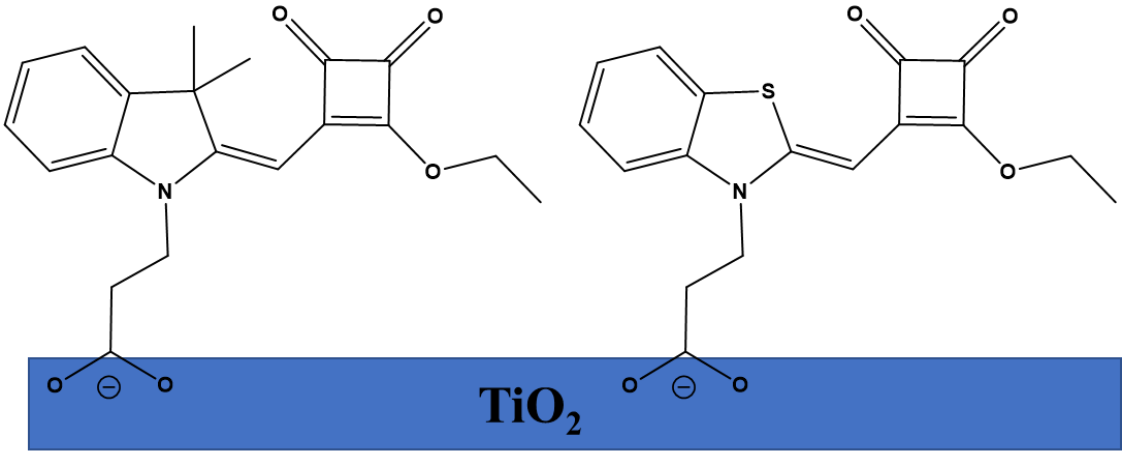

Figure 3.23 - Proposed orientation of dyes (**D4**) and (**D3**) before being analysed by XPS and computer modelling

Figure 3.23 shows the proposed orientation of dyes (**D3**) and (**D4**) before ARXPS and computer modelling took place. A similar orientation was suggested by Holliman *et al.*[157] when they synthesised an almost identical dye back in 2014. In this orientation dyes (**D3**) and (**D4**) have a single chemisorbing group bound to the TiO_2 through the carboxylic acid moiety coming from the nitrogen atom of the indole. As the dye is perpendicular to the TiO_2 surface the sulphur atom and carbonyl groups point in the opposite direction.

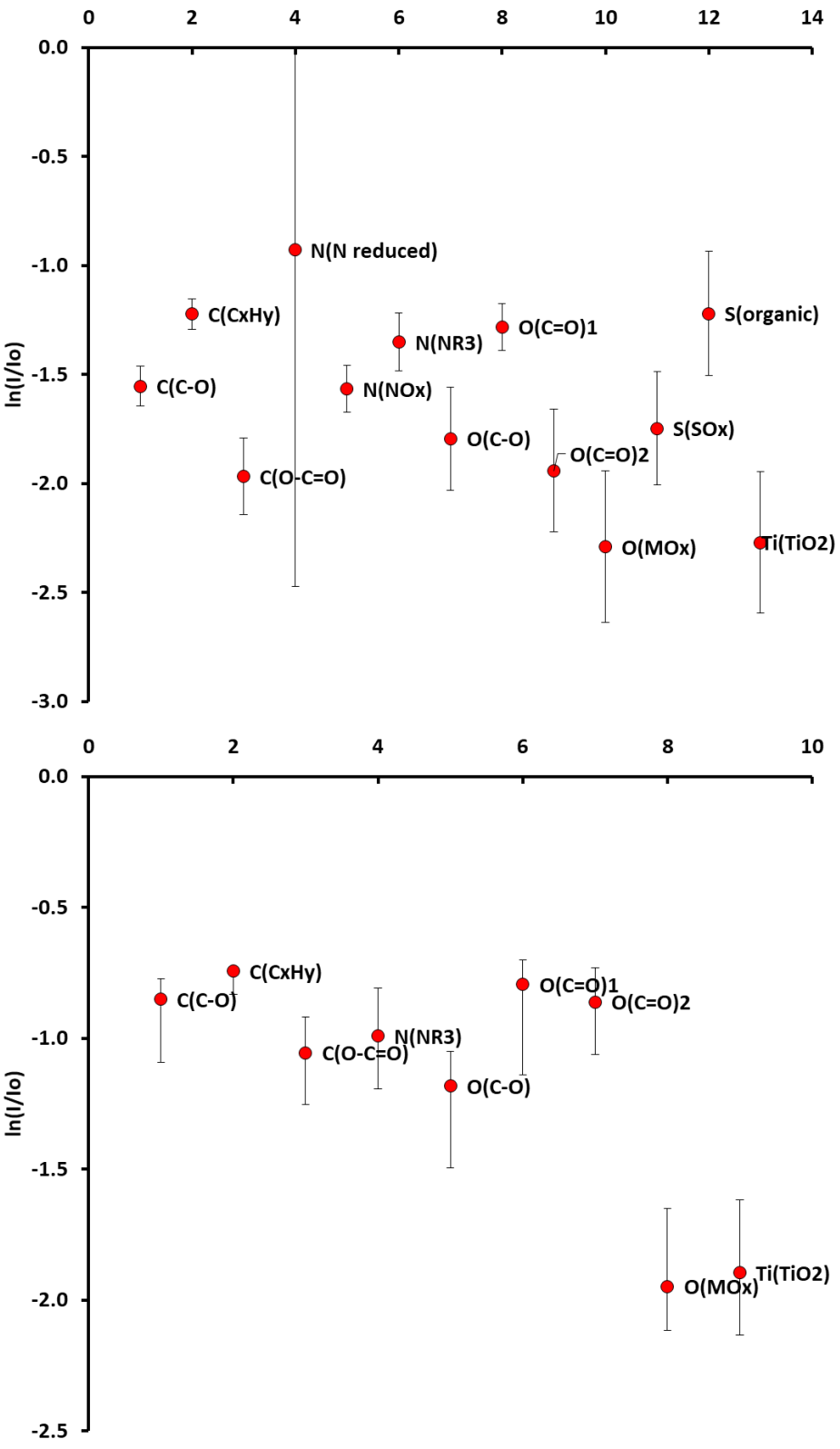

Figure 3.24 - Atomic positions in the z-axis (perpendicular to TiO_2 single crystal surface) of dye (**D3** - top) and dye (**D4** - bottom) – calculated from angle-resolved XPS data. The data are presented with the vertical axis $In(I/I_o)$ representing the vertical distance moving away from the surface.

Figures 3.24 show the ARXPS of dyes (**D3**) and (**D4**). The ARXPS and DFT modelling suggest that dyes (**D3**) and (**D4**) bind through a single carboxylic acid which agrees with the initial proposed binding orientation. However, the data suggests that the dyes do not absorb perpendicular to the surface but in fact orientated a shallow angle.

3.2.6.3 Analysis of dyes (D5) and (D6)

The next pair of dyes are (**D5**) and (**D6**) which both have a de-esterified squaraine unit and a propionic acid linker group attached to the indole nitrogen.

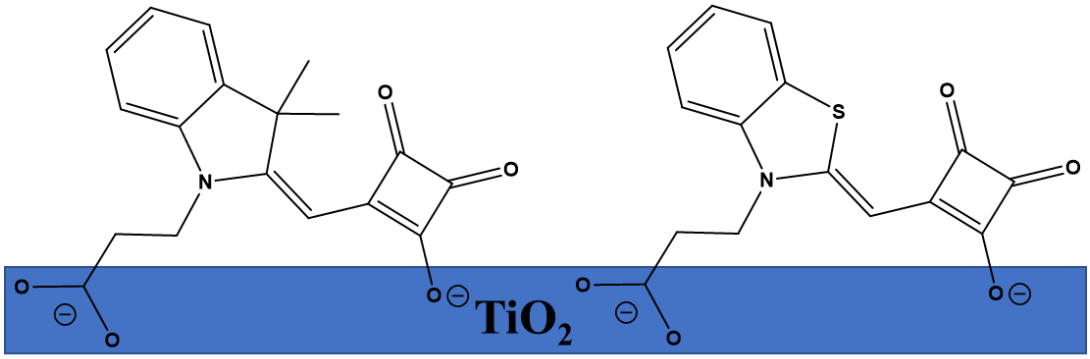

Figure 3.25 - Proposed orientation of dye (**D6** - left) and (**D5** - right) before being analysed by XPS and computer modelling

Figure 3.25 shows the proposed orientation of dyes (**D5**) and (**D6**) before ARXPS and computer modelling took place. In the same paper where Holliman *et al.*[157] suggested the orientation of dyes (**D3**) and (**D4**), it also suggests the orientation of dyes similar to (**D5**) and (**D6**). In this orientation dyes (**D5**) and (**D6**) have two chemisorbing groups bound to the TiO_2. One through the carboxylic acid moiety from the nitrogen atom of the indole and the other through the acyloin group of the squaraine moiety. In this orientation the dyes lie at a slight angle on the surface meaning that the benzene group sits at the very top of the dyes and the sulphur and dimethyl-derivatised carbon groups point away from the TiO_2 at an approximate 45^o angle.

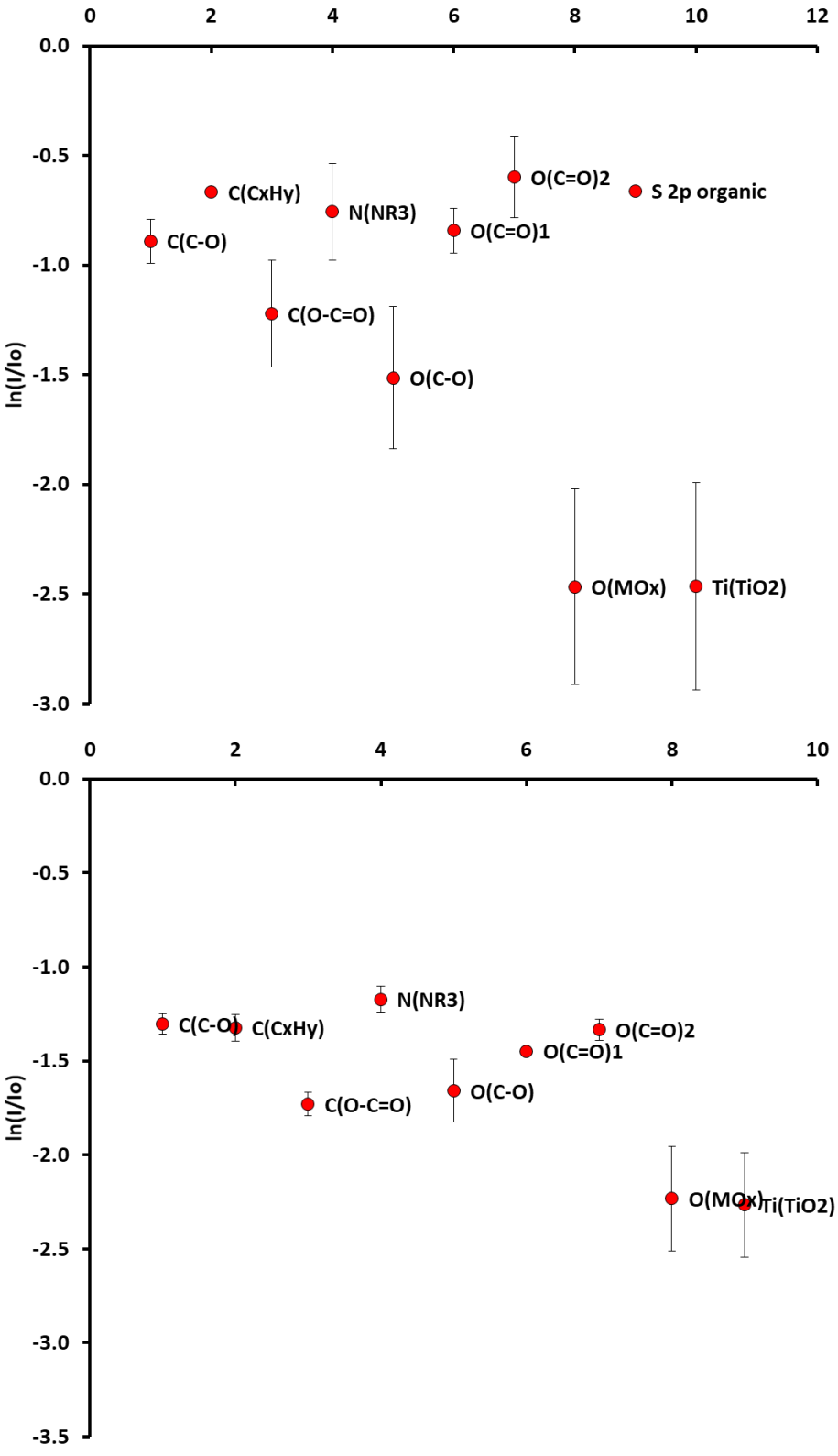

Figure 3.26 - Atomic positions in the z-axis (perpendicular to TiO_2 single crystal surface) of dye (**D5** - top) and dye (**D6** - bottom) – calculated from angle-resolved XPS data. The data are presented with the vertical axis $In(I/I_o)$ representing the vertical distance moving away from the surface.

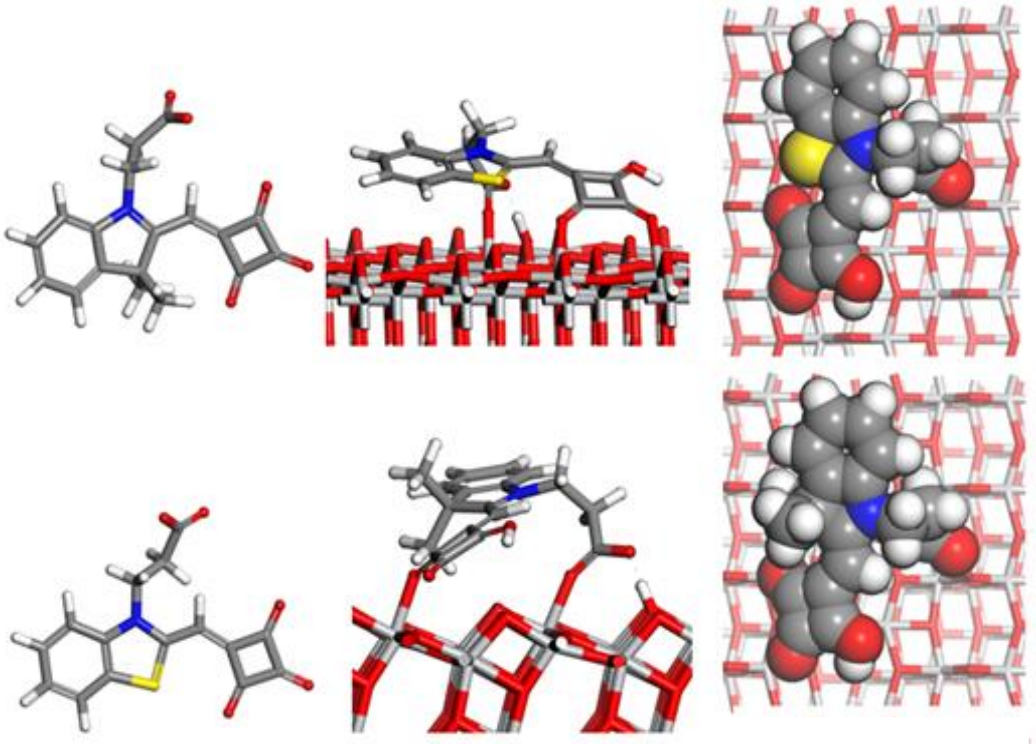

Figure 3.27 - DFT modelling of the relaxed configurations of the most probable orientations of dyes (**D6**) and (**D5**) (LHS without on an anatase (101) TiO_2 surface, where 'most probable' means largest (in magnitude) adsorption energy. The RHS image shows an aerial view of dye (**D6**) and (**D5**) molecules on the TiO_2 surface where the dyes are depicted as 'space-filling'. They approximately cover a projected surface area (in $Å^2$ and to two significant figures) of (**D5**) – 77 and (**D6**) – 82;

Figures 3.26 and 3.27 show the DFT modelling and ARXPS of dyes (**D5**) and (**D6**). Both the ARXPS and DFT modelling show that dyes (**D5**) and (**D6**) bind through two anchors as suggested earlier, one through the nitrogen of the indole and the other through the acyloin moiety of the squaraine. However, like dyes (**D3**) and (**D4**) the data suggests that the dyes are not perpendicular to the TiO_2 but are almost planar against the TiO_2 instead. This means that the sulphur and dimethyl-derivatised carbon no longer sit at the top of the dye but actually sit somewhere in the middle.

3.2.6.4 Analysis of dyes (D7) and (D8)

The next pair of dyes are (**D7**) and (**D8**) which both have a vinyl dicyano-derivatised, de-esterified squaraine unit and a dodecyl alkyl side group attached to the indole nitrogen**.** Dyes (**D7**) and (**D8**) are identical except for a sulfur atom in dye (**D7**) and a dimethyl-derivatised carbon in dye (**D8**), the "**X**" in **Figure 3.28** represents where the sulfur and dimethyl-derivatised carbon lie within the dyes structure.

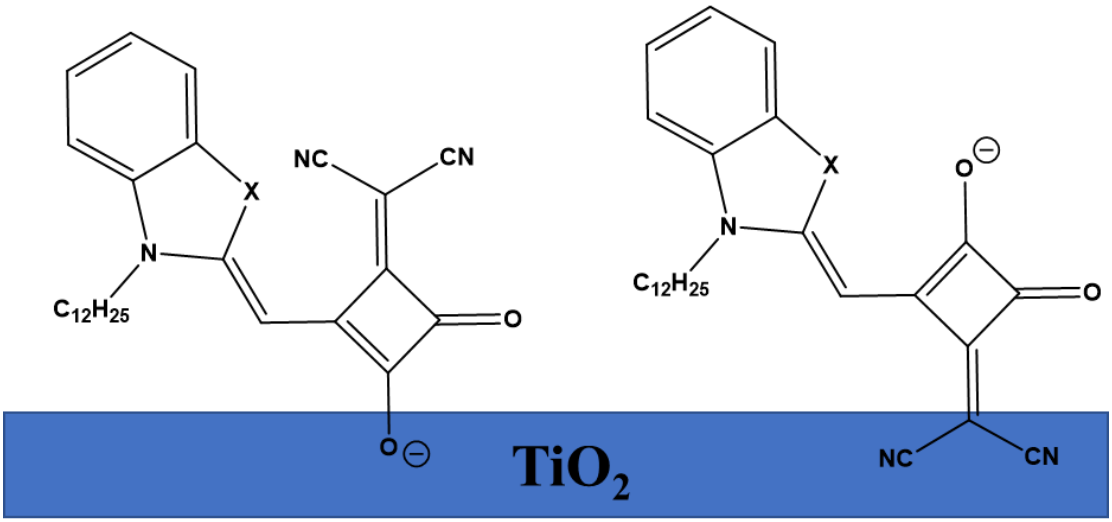

Figure 3.28 - Proposed orientation of dyes (**D7**) and (**D8**) before being analysed by XPS and computer modelling. X = S (**D7**) or $C(CH_3)_2$ (**D8**)

Figure 3.28 shows the proposed orientation of dyes (**D7**) and (**D8**) before ARXPS and computer modelling took place. Dyes (**D7**) and (**D8**) have a single chemisorbing anchor to the TiO_2 through the squaraine unit. Like dyes (**D9**) and (**D10**), there are two proposed orientations for theses dyes and it is not clear whether the dyes bind through the acyloin or the vinyl dicyano moiety of the squaraine unit. As (**D7**) and (**D8**) only have a single anchor, the way the dye binds to the TiO_2 has a large impact on the dye orientation. Both proposed orientations suggest the dyes sit perpendicular to the TiO_2 surface with the long alkyl chain sitting at a 45^o angle. The sulphur and dimethyl-derivatised carbon sits at the top of the dyes pointing away from the TiO_2. Binding through the acyloin of the squaraine unit would mean the vinyl dicyano moiety is pointing away from the TiO_2 surface and would have better electron injection resulting in higher efficiencies. Despite this, papers such as Holliman *et al.*[123] have used ATR-IR to show that there is bonding taking place between the vinyl dicyano moieties

and the TiO_2. This bonding is weaker than if the dye was bound through the acyloin moiety. For dyes (**D9**) and (**D10**) this is not as important as they have two anchors but as dyes (**D7**) and (**D8**) only have a single anchor a weaker bond will impact dye uptake and performance as it has been noted that dyes containing a vinyl dicyano unit more easily desorb from the TiO_2 surface in the presence of acetonitrile (the most common solvent for triiodide electrolytes).

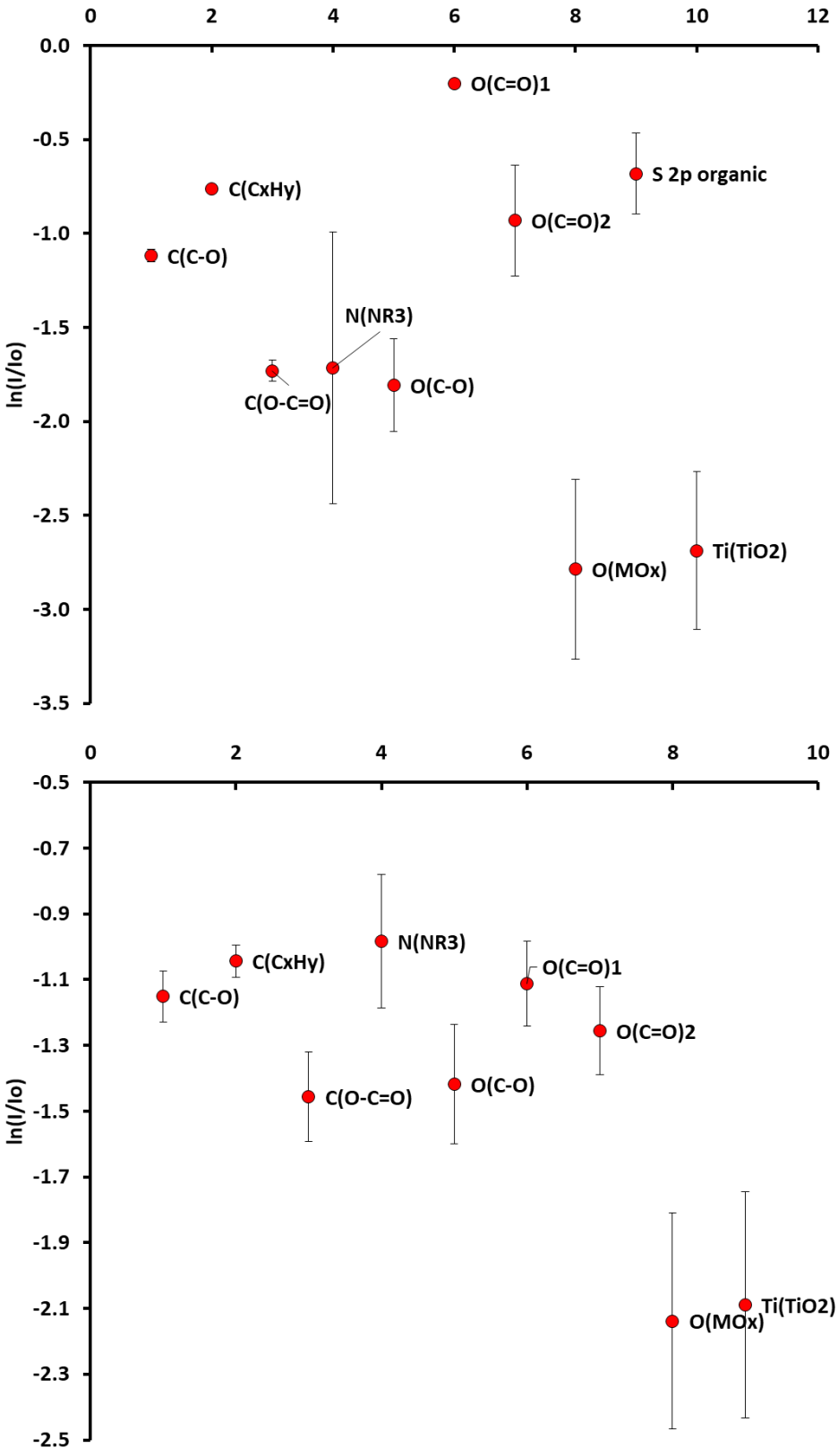

Figure 3.29 - Atomic positions in the z-axis (perpendicular to TiO_2 single crystal surface) of dye (**D7** - top) and dye (**D8** - bottom) – calculated from angle-resolved XPS data. The data are presented with the vertical axis $In(I/I_o)$ representing the vertical distance moving away from the surface.

Figures 3.29 show the ARXPS of dyes (**D7**) and (**D8**). The ARXPS show that dyes (**D7**) and (**D8**) bind through the propionic acid attached to the indole nitrogen. As with dyes (**D9**) and (**D10**) the bonding between the vinyl dicyano groups and the TiO_2 observed by Holliman *et al.*[123] could be down to the vinyl dicyano groups being very close to the TiO_2 surface. Though the vinyl dicyano groups are not chemically bonded to the TiO_2 they are in close enough proximity to interact with it which would explain the ATR-IR peaks. Like the previous dyes discussed, dyes (**D7**) and (**D8**) are not perpendicular to the TiO_2 as first thought but are in fact are orientated at a shallow angle to the TiO_2.

3.2.6.5 Analysis of dyes (D9) and (D10)

The next pair of dyes are (**D9**) and (**D10**) which both have a vinyl dicyano derivatised, de-esterified squaraine unit and a propionic acid linker group attached to the indole nitrogen (see **Figure 3.30**). Dyes (**D9**) and (**D10**) are identical except for a sulfur atom in dye (**D9**) and a dimethyl-derivatised carbon in dye (**D10**), the "**X**" in **Figure 3.30** represents where the sulfur and dimethyl-derivatised carbon lie within the dyes structure.

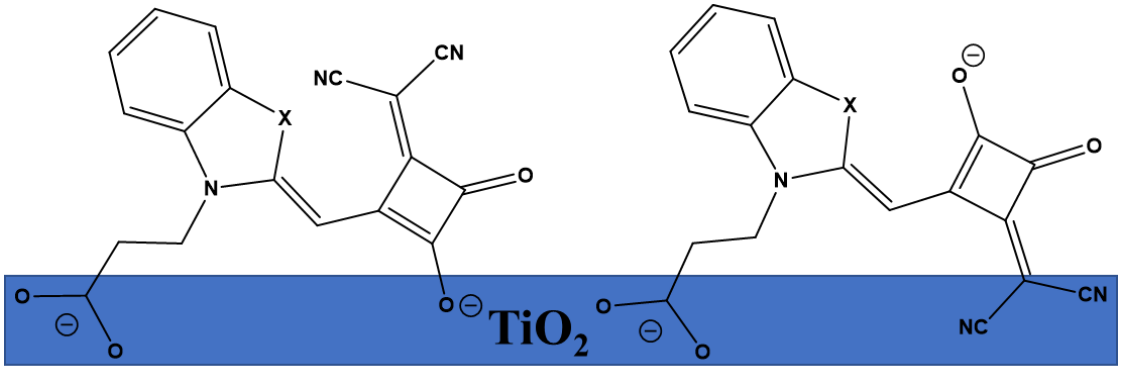

Figure 3.30 - Proposed orientation of dyes (**D9**) and (**D10**) before being analysed by XPS and computer modelling. X = S (**D9**) or $C(CH_3)_2$ (**D10**)

Figure 3.30 shows the proposed orientation of dyes (**D9**) and (**D10**) before ARXPS and computer modelling took place. Though it is generally agreed that dyes (**D9**) and (**D10**) bind to the TiO_2 through two sites (the carboxylic acid off of the N indole and through the acyloin moiety) the literature suggests two potential orientations, with evidence for both.[157,123] Both suggested orientations have the first chemisorbing group bound to the TiO_2 through the carboxylic acid moiety coming from the nitrogen atom of the indole. Yet it is not agreed whether the other anchor is through the acyloin or vinyl dicyano groups of the squaraine

moiety. Holliman *et al.*[123] used ATR-IR to determine that the nitrile groups of the vinyl dicyano unit themselves closer to the TiO_2. This result was surprising as this orientation would likely result in poorer electron injection compared to the other suggested orientation. It was also noted that the dyes that contained vinyl dicyano moiety easily desorbed from the TiO_2 surface which could be explained by the weaker bonding between TiO_2 and the nitrile groups.

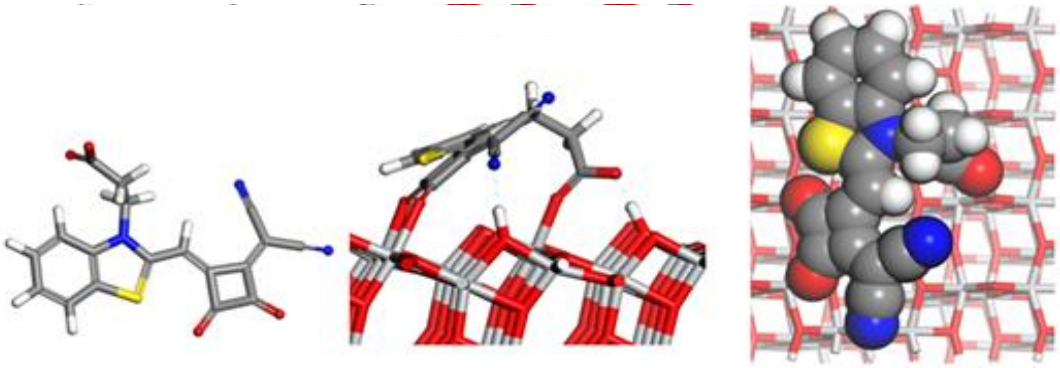

Figure 3.31 - DFT modelling of the relaxed configurations of the most probable orientations of dyes (**D9**) (LHS without on an anatase (101) TiO_2 surface, where 'most probable' means largest (in magnitude) adsorption energy. The RHS image shows an aerial view of dye (**D9**) molecules on the TiO_2 surface where the dyes are depicted as 'space-filling'. They approximately cover a projected surface area (in $Å^2$ and to two significant figures) of (**D10**) – 94.

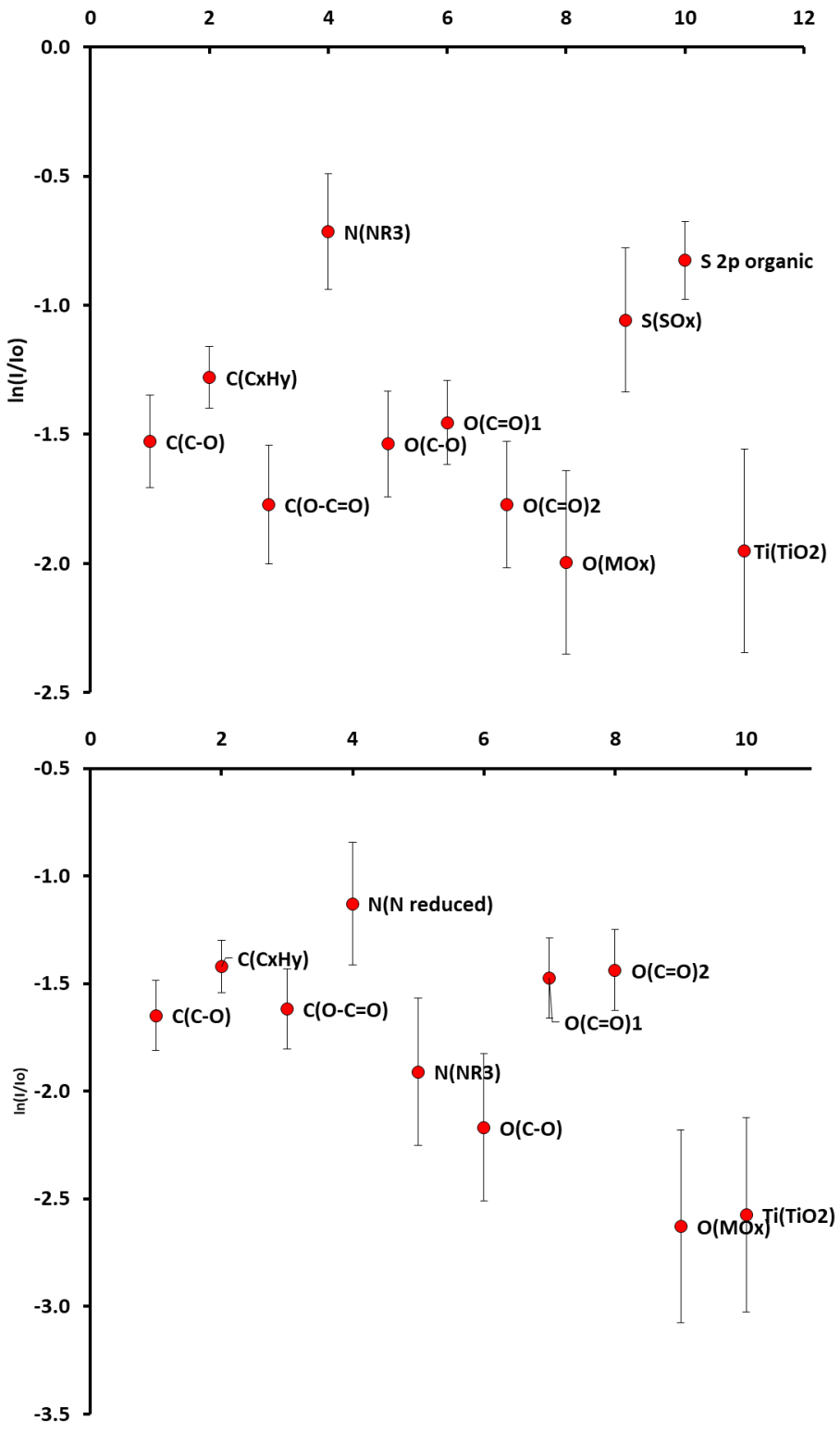

Figure 3.32 - Atomic positions in the z-axis (perpendicular to TiO_2 single crystal surface) of dye (**D9** - top) and dye (**D10** - bottom) – calculated from angle-resolved XPS data. The data are presented with the vertical axis $In(I/I_o)$ representing the vertical distance moving away from the surface.

Figures 3.31 and 3.32 show the DFT modelling and ARXPS of dyes (**D9**) and (**D10**). Both the ARXPS and DFT modelling show that dyes (**D9**) and (**D10**) bind through two anchors agreeing with the earlier predictions. The first anchor is the propionic acid attached to the indole nitrogen. Surprisingly the second anchor is the acyloin moiety and not the vinyl dicyano groups. The bonding between the vinyl dicyano groups and the TiO_2 noted by Holliman *et al*.[123] could be down to the vinyl dicyano groups being very close to the TiO_2 surface. Though not chemically bonded the groups do appear to be close enough to interact with the TiO_2 which could be enough to be seen by ATR-IR spectroscopy. Like the previous dyes discussed, dyes (**D9**) and (**D10**) are not perpendicular to the TiO_2 but are in fact are orientated at a shallow angle.

The TD-DFT and ARXPS experiments undertaken on the synthesised half-squaraine dyes in this chapter have given us more information and a better understanding regarding the chemical bonding. However, the orientation of these dyes was completely mis-understood. The initial predictions showed most of the dyes sit perpendicular to the TiO_2 but our experiments show that these dyes orientate themselves at a very shallow angle to the TiO_2. This will drastically change how we now design these dyes for a multitude of reasons. The first of these is dye loading. For the most part dyes, perpendicular to the TiO_2 will cover far less surface area then the same dyes lying planar to the surface. Few dye molecules on the surface will result in fewer photons absorbed and ultimately limit the efficiency of any devices made. The orientation of the dyes will also change what the TiO_2 and electrolyte/ HTM sees (see **Figure 3.33**). At a perpendicular angle, the HOMO of the half-squaraines sit at the very top of the dye away from the TiO_2 whilst the LUMO of the dyes sits at the bottom of the dye. In this orientation whatever atoms form the HOMO would be exposed to the electrolyte/ HTM and therefore determine how easily the dye is regenerated. As the LUMO sits next to the TiO_2 it would impact how much recombination takes place. These orientations are considered during the design phase of the dye and are therefore minimised. However, our experiments show that the dyes sit flat to the TiO_2 which means that dye design needs to be reconsidered. If the dyes are flat, then both the HOMO and LUMO sit on the on TiO_2 surface. Any atoms that were incorporated into

the HOMO to aid dye regeneration may in fact aid recombination of electrons from the TiO_2. On top of this the LUMO is now exposed to the electrolyte/ HTM and any modification (e.g. long alkyl chains) may in fact reduce the amount of electrolyte that can reach the dye and therefore reduce dye regeneration and limit performance. **Figure 3.33** illustrates the computer modelling and ARXPS results and how they show the orientation of dyes on TiO_2.

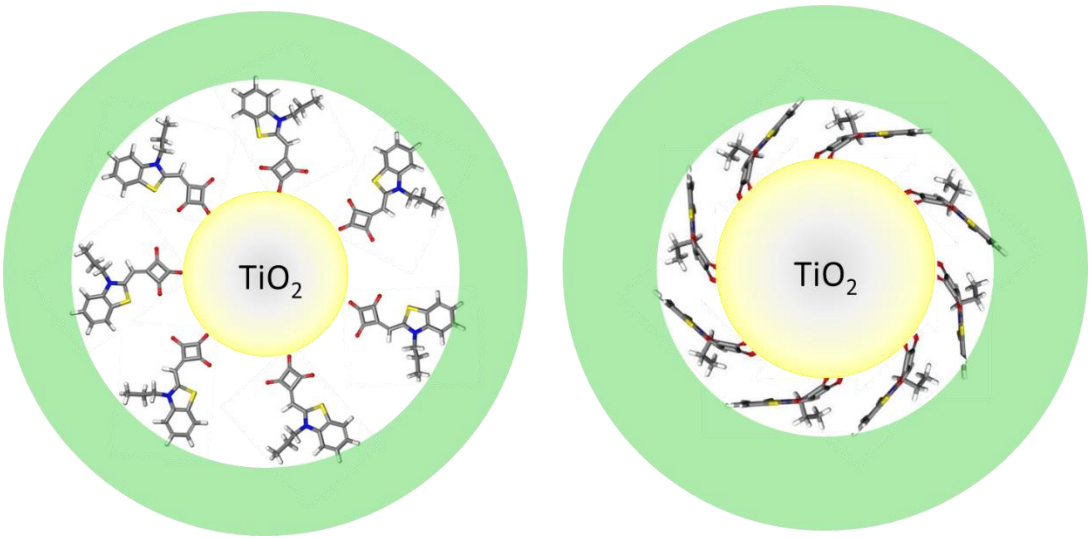

Figure 3.33 - Theoretical HfSQ dye orientation (left) vs proposed HfSQ dye orientation (right). The different colours represent the different atoms in the dyes. Grey = carbon, red = oxygen, white = hydrogen, blue = nitrogen and yellow = sulphur. The yellow cycle represents the TiO_2, whilst the green ring represents HTM. Depending on the orientation of the dyes the HTM will see different parts of the molecule.

3.2.7 X-ray crystallography

In each experiment a suitable crystal was selected and mounted on a MITIGEN holder in perfluoroether oil on a Rigaku FRE+ equipped with either HF Varimax confocal mirrors (**D3**) or VHF Varimax confocal mirrors (**4**, **5**, **7** and **D4**) and an AFC12 goniometer and HG Saturn 724+ detector (**4**, **5**, **7** and **D3**) or HyPix 6000 detector (**D4**). The crystal was kept at T = 100(2) K during data collection. Using Olex2[269] the structure was solved with the ShelXT[270] structure solution program, using the Intrinsic Phasing solution method. The model was refined with ShelXL[270] using Least Squares minimisation. All non-hydrogen atoms were refined anisotropically and all hydrogen atom positions were calculated geometrically except those bonded to heteroatoms which were located from the difference map and refined using a riding model. The solvent water molecule present in 6 was refined with rigid body constraints.

Compound (**4**) a = 14.2803(3) Å, b = 10.7176(2) Å, c = 16.7845(4) Å, α = 90°, β = 108.662(2)°, γ = 90°; V = 2433.81(9) Å^3, Monoclinic, C2/c, Z = 8, $D_{calc.}$/ g cm^{-3} = 1.906, μ/mm^{-1} = 2.788 T/K = 100(2), θ_{max} = 27.485°, 10576 measured reflections, 2789 independent reflections [R_{int} = 0.0203], 2606 reflections used, wR_2 (all data) = 0.0406, R1 = 0.0168 (I > 2(I)), CCDC 1908056 .

Compound (**5**) a = 7.3991(2) Å, b = 13.6384(4) Å, c = 29.8148(10) Å, α = 90°, β = 90°, γ = 90°; V = 3008.67(16) Å^3, Orthorhombic, Pbca, Z = 8, $D_{calc.}$/ g cm^{-3} = 1.586, μ/mm^{-1} = 2.124; T/K = 100(2), θ_{max} = 27.486°, 25790 measured reflections, 3452 independent reflections [R_{int} = 0.0760], 2583 reflections used, wR_2 (all data) = 0.0628, R1 = 0.0336 (I > 2(I)), CCDC 1908059.

Compound (**7**) a = 9.2092(4) Å, b = 10.9301(4) Å, c = 12.2653(5) Å, α = 100.390(3)°, β = 99.578(4)°, γ = 92.170(3)°; V = 1194.49(9) Å^3, Triclinic, P-1, Z = 2, $D_{calc.}$/ g cm^{-3} = 1.178, μ/mm^{-1} = 0.075; T/K = 100(2), θ_{max} = 27.485°, 15143 measured reflections, 5441 independent reflections [R_{int} = 0.0428], 3949 reflections used, wR_2 (all data) = 0.1478, R1 = 0.0486 (I > 2(I)) CCDC 1908058.

Compound (**D3**) a = 9.4467(7) Å, b = 9.8579(7) Å, c = 10.8912(8) Å, α = 114.208(7) °, β = 113.622(7)°, γ = 91.306(6)°; V = 826.02(12) Å^3, Triclinic, P-1, Z = 2, $D_{calc.}$/ g cm^{-3} = 1.461, μ/mm^{-1} = 0.231; T/K = 100(2), θ_{max} = 27.484°, 10889 measured reflections, 3776 independent reflections [R_{int} = 0.0429], 2693 reflections used, wR_2 (all data) = 0.1309, R1 = 0.0531 (I > 2(I)), CCDC 1908057.

Compound (**D4**) a = 12.5207(3) Å, b = 10.7016(2) Å, c = 26.8410(5) Å, α = 90°, β = 90°, γ = 90°; V = 3596.47(13) Å^3, Orthorhombic, $Pca2_1$, Z = 8, $D_{calc.}$/ g cm^{-3} = 1.313, μ/mm^{-1} = 0.095; T/K = 100(2), θ_{max} = 27.485°, 39507 measured reflections, 8244 independent reflections [R_{int} = 0.0257], 7642 reflections used, wR_2 (all data) = 0.0887, R1 = 0.0344 (I > 2(I)), CCDC 1908060.

Where a, b and c are the length of the cell edges and α, β and γ are the angles between them. Monoclinic, Triclinic and Orthorhombic refer to the crystal family. Z *is* the number of molecules in the unit cell. D_{calc} is the calculated density. V is the volume of the unit cell. P-1 and $Pca2_1$ are the space groups. The R value is the measure of the quality of the atomic model obtained. T/K is the temperature in kelvin. θ_{max} is the maximum angle measured. CCDC refers to each molecule in the Cambridge crystallographic data centre

Finally, the optimum supercell size was determined whereby the three-layered slab of 20 Å (*c*-length), was increased both in the *x*- and *y*- directions. The dye molecule with the largest planar length (molecule **D9**) was placed on top of the surface of variously-sized slabs, and total energies were calculated without relaxation of the model system's atomic structure. Maximum forces were

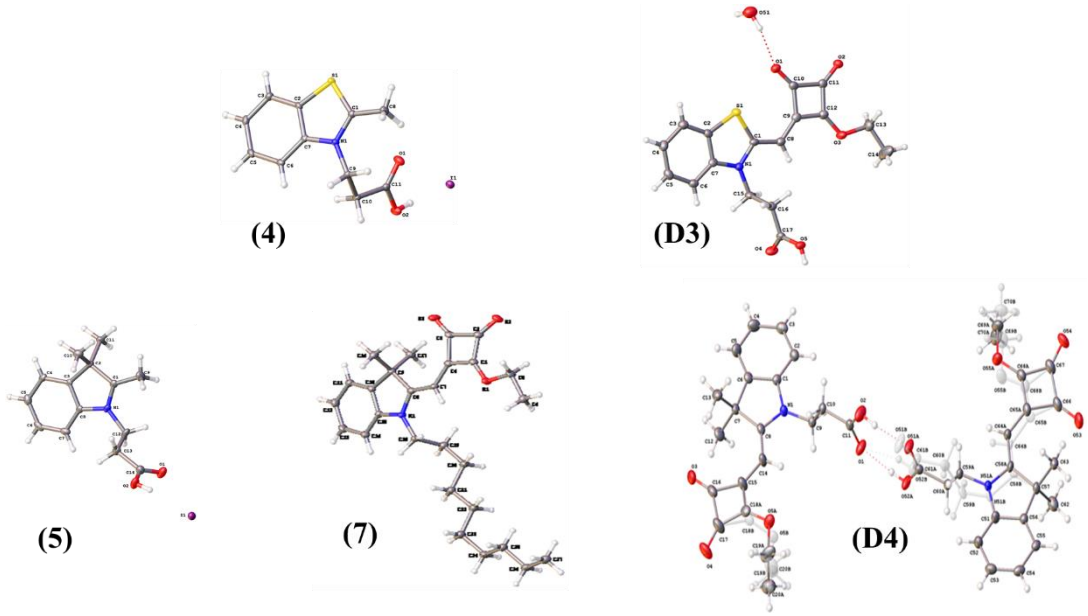

Figure 3.34 - X-ray crystal structures of (**4**), (**5**), (**7**), (**D3**) and (**D4**). Displacement ellipsoids are shown at 50% probability and minor disorder components are shown 'ghosted'

converged for 2X-4Y supercells producing a final, (101) anatase TiO_2 slab of dimensions: 20.86 Å x 15.23 Å x 29.02 Å (see **Figure 2.34**).

Obtaining crystal structures for small organic molecules is inherently difficult, particularly for those which have long alkyl chains (due to steric hindrance). Therefore, only some crystals structures were obtained for my materials.

3.2.8 Device data

Figure 3.35 and **Table 3.3** show I–V data for all sHfSQ devices. As stated above, the aim when designing these Hf-SQ dyes was to incorporate a sulphur atom in order to study its influence on dye energy levels and device performance.

Thus, dye (**D1**), (**D3**), (**D5**), (**D7**) and (**D9**) were designed and synthesized with a sulphur atom incorporated into the indolenine group, whilst dyes (**D2**), (**D4**), (**D6**),

(**D8**) and (**D10**) were identical however rather than a sulphur atom these dyes have been synthesised with a dimethyl derivatised carbon.

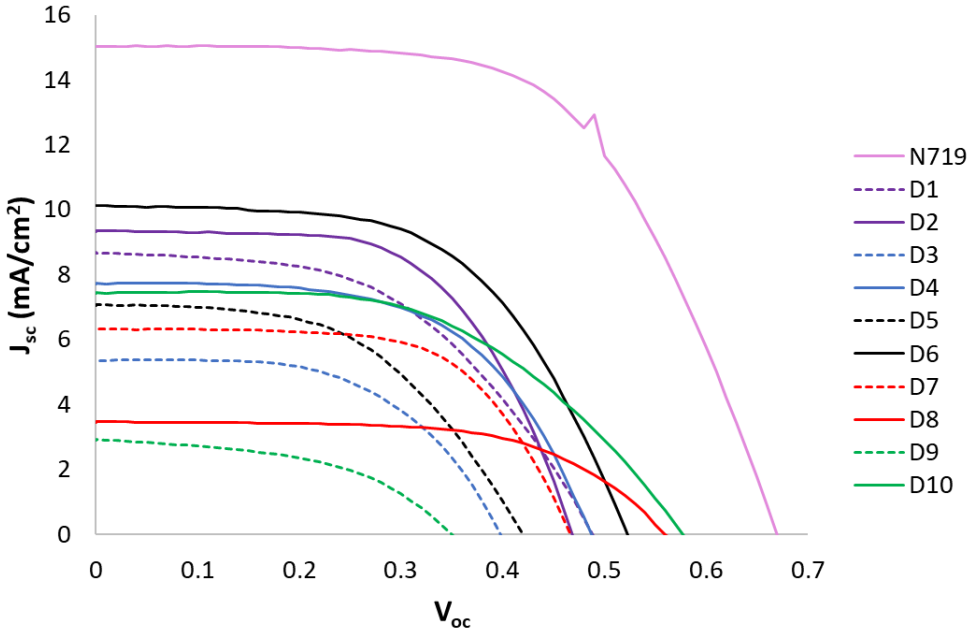

Figure 3.35 – I-V graphs for DSC devices made using the different dyes. For clarity, structurally related dyes have the same colour and $C(CH_3)_2$ dyes have solid lines, whilst S dyes have dashed lines.

Table 3.4 – I-V for liquid DSC devices prepared using sHfSQ dyes (data are the mean of 3 replicates with standard error +/- 0.1 %)

Dye	V_{oc}	J_{sc} (mA/cm^2)	FF (%)	η (%)	"Hero Cells" (η %)
(**D1**)	0.48	8.18	52	2.04	2.20
(**D2**)	0.48	8.60	59	2.42	2.60
(**D3**)	0.39	4.90	56	1.07	1.19
(**D4**)	0.49	6.90	58	1.96	2.19
(**D5**)	0.41	6.27	53	1.34	1.53
(**D6**)	0.52	8.66	57	2.59	3.00
(**D7**)	0.45	6.50	58	1.69	1.86
(**D8**)	0.52	3.84	58	1.16	1.18

(**D9**)	0.35	2.79	49	0.48	0.50
(**D10**)	0.57	7.16	53	2.16	2.26
N719	0.66	14.69	56	5.48	6.10

3.2.8.1 Dye spectral response versus device performance

The spectral response of the HfSQ dyes has also been tested (**Figure 3.36**) using N719 as a reference. The data shows that dye (**D10**) responds most strongly (EQE *ca*. 65 %) between 500 and 600 nm (where solar intensity is highest) this correlates to the dye having good efficiency (η = 2.16) and the also the vinyl dicyano modification shifting the absorption of the dye relative to (**D4**) and (**D6**). Dyes (**D7**), (**D8**) and (**D9**) have also been modified with a vinyl dicyano causing a bathochromic shift in their absorption. However, the EQE of dyes (**D7**), (**D8**) and (**D9**) all are lower (~ 57, 20 and 60 % respectively) than their unmodified counterparts (78, 49 and 69 % respectively) which corresponds to the UV-Vis absorption of the films and the lower molar extinction (ε) co-efficient of the dyes. This suggests that by modifying the dyes with a dicyano unit it negatively affects the bonding that takes place and therefore reduces the amount of dye adsorbed onto the TiO_2 surface. However, this doesn't translate into the device data, with dye (**D8**) having the lowest molar extinction (ε) coefficient and EQE of all the dyes yet it has a relatively good device performance (η = 1.77 %). Whilst dye (**D9**) has the second highest absorption of all the dicyano modified dyes it also has the lowest device performance (η = 0.48 %).

3.2.8.2 Effect of binding site on dye orientation and DSC device performance

Dyes (**D3**), (**D4**), (**D5**), (**D6**), (**D9**) and (**D10**) were designed and synthesised to bind to the TiO_2 through the carboxylate linker attached to the indole N. The power conversion efficiency (η) of devices made using (**D3**), (**D4**), (**D5**), (**D6**), (**D9**) and (**D10**) are η = 1.07 %, 1.96 %, 2.59 %, 1.34 %, 0.48 % and 2.16 % respectively. Dyes (**D1**), (**D2**), (**D7**) and (**D8**) were designed to bind to the TiO_2 through the acyloin moiety off the squaric acid unit. When compared to the dyes bound through the carboxylate linker, dyes bound through the acyloin unit have increased PCE's of η = 2.04 %, 2.42 %, 1.69 % and 1.77 % (for dyes (**D1**), (**D2**), (**D7**) and (**D8**) respectively). The increase in efficiency came in the form of increased of J_{sc}. The average J_{sc} for dyes bound through the carboxylate linker was 6.11 mA/cm^2 whereas the average J_{sc} for the dyes bound through the acyloin moiety was 7.35 mA/cm^2. This increase in J_{sc} could be attributed to higher dye uptake however, the UV-Vis data doesn't enough difference

in absorbance to confirm this. The increase of J_{sc} is more likely down to be better electron injection, due to the directionality of the dye. Dyes bound through the acyloin moiety follow the typical structure of organic dyes (Donor-π bridge-acceptor-anchor-TiO_2), whereas the dyes bound through the carboxylate linker follow a slightly different architecture with the linker group in the centre of the dye rather than on the end. This lack of directionality has proven to have a negative impact on device performance (see **section 1.4.2.3** for more details). Our experiments show that all the dyes tested lie relatively flat to the TiO_2 no matter the binding site position (though to varying degrees). Therefore, it is possible binding site has a small effect on device performance however, it's more likely that other functional groups within the dye will have a much greater contribution to performance. Functional groups such as long alkyl chains could potentially stop the dyes being completely horizontal and/or stop the dyes interacting with each other. Dopants (such as *t*BP) will also likely create a barrier between the dyes and the TiO_2 surface. Nevertheless, the full effect of these groups requires further research in order to determine their full impact on dye orientation.

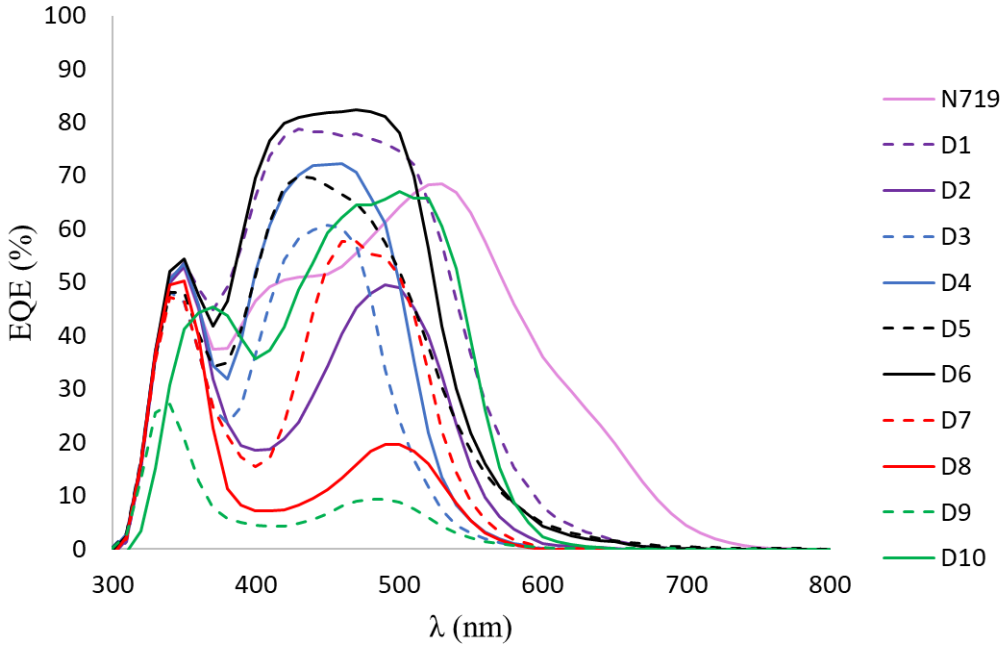

Figure 3.36 – EQE of DSC devices using HfSQ dyes. For clarity, structurally related dyes have the same colour and $C(CH_3)_2$ dyes have solid lines, whilst S dyes have dashed lines.

3.2.8.3 Effect of de-esterified dyes on DSC device performance

Dyes (**D1**), (**D2**), (**D5**) and (**D6**) were designed and synthesised by de-esterifying with tetrabutylammonium hydroxide. In the case of (**D1**) and (**D2**) the de-esterification was

used to give the dyes a linker to bind to the TiO_2. However, as the precursor dyes to (**D1**) and (**D2**) have no anchor groups they cannot inject electrons into the TiO_2 and therefore cannot produce working devices. Because of this they cannot be compared before and after de-esterification. Therefore, I will only compare (**D5**) and (**D6**) to their precursors (**D3**) and (**D4**). Dyes (**D5**) and (**D6**) were designed and synthesised to have two linker groups whereas their precursors (**D3**) and (**D4**) only contain a single linker. The first linker for dyes (**D3**), (**D4**), (**D5**) and (**D6**) binds to the TiO_2 through the carboxylate linker attached to the indole N and the second linker (only on (**D5**) and (**D6**)) is exposed on the acyloin moiety after de-esterification with tetrabutylammonium hydroxide. Dyes (**D5**) and (**D6**) showed higher efficiencies (η = 1.34 and 2.59 % respectively) compared to (**D3**) and (**D4**), achieving η = 1.07 and 1.96 % respectively. The increase in efficiency was down to an increase of J_{sc} (5.90 mA/cm^2 for (**D3**) and (**D4**) whereas 7.47 mA/cm^2). The increase of J_{sc} could be attributed to the absorption of more photons however only (**D5**) showed a higher molar extinction co-efficient over its counterpart, dye (**D6**) showed a decrease in molar extinction co-efficient. Similar dyes were synthesised Holliman *et al.*[123] Holliman use ATR-IR, UV and DSC device testing to show that increasing the number of linker groups for HfSQ dyes improves DSC device efficiency and stability.

3.2.8.4 Effect of Vinyl dicyano group on DSC device performance

Dyes (**D7**), (**D8**), (**D9**) and (**D10**) were designed and synthesised with a vinyl dicyano unit into the dyes core structure. The vinyl dicyano unit is known to extend spectral response in DSC dyes and improve device performance. However, the performance of all dyes were lower than equivalent dyes without a vinyl dicyano unit ((**D1**), (**D2**), (**D5**) and **D6**)). The largest drop in η was seen in dye (**D9**), which was 64.18 % lower than its not vinyl dicyano counterpart (**D5**). The average PCE for dyes with vinyl dicyano units was η = 1.32 % whereas the average PCE for the equivalent dyes without a vinyl dicyano unit was η = 1.52 %. This decrease in PCE was down to a lower J_{sc} value for dyes containing a vinyl dicyano unit (4.98 mA/cm^2 compared to 5.90 mA/cm^2). Dyes (**D7**), (**D8**), (**D9**) and (**D10**) all showed lower molar extinction (ε) co-efficient compared to (**D1**), (**D2**), (**D5**) and (**D6**). Therefore, although the absorption of dyes incorporating vinyl dicyano groups results in a bathochromic shift, the intensity of the absorption decreases. This means fewer photons are absorbed, decreasing J_{sc} resulting in a lower PCE.

3.2.8.5 Effect of sulphur on DSC device performance

The dyes in this chapter were designed and synthesised to study the effect of sulphur (and its position) on DSC performance. To this end dyes (**D1**), (**D3**), (**D5**), (**D7**) and (**D9**) were synthesised to incorporate a sulphur atom. Whereas dyes (**D2**), (**D4**), (**D6**), (**D8**) and (**D10**) were structurally identical however, the sulphur atom was replaced with a dimethyl derivatised carbon (for comparison). The sulphur atom in dyes (**D3**), (**D5**) and (**D9**) was designed to sit at the very top of the dye away from the TiO_2 surface. In theory the sulphur atom would have a positive interaction with the triiodide electrolyte increasing the speed of dye regeneration and therefore improving DSC device performance. For dyes (**D1**) and (**D7**) the sulphur should sit much closer to the TiO_2 surface. The sulphur atom should still interact positively with the triiodide electrolyte however, it will likely increase the concentration of Iodide near the TiO_2 surface, increasing recombination by pulling injected electrons out of the TiO_2.

DSC device data showed that performance decreased for all dyes that contained sulphur. The average PCE for dyes containing sulphur was η = 1.32 % however, the average PCE for the same dyes without sulphur was η = 2.18 %. (**D6**) which had no sulphur was the highest performing dye achieving η = 3.00 %, whereas the worst performing dye was the sulphur containing (**D9**) achieving η = 0.50 %. Both a drop in V_{oc} and J_{sc} contributed to the decreased performance of the sulphur containing dyes. With the average V_{oc} and J_{sc} of the sulphur dyes 0.42 V and 5.73 mA/cm^2. Whereas the non-sulphur containing dyes were able to achieve and average V_{oc} and J_{sc} of 0.51 V and 7.49 mA/cm^2. Preliminary electron injection kinetics measurements were made to determine if the dyes containing sulphur were less efficient at injecting electrons. The results of which can be seen in appendix (**Table 8.7).**

The preliminary data shows no correlation between electron injection kinetics and sulphur atoms within the dye structure. The poor performance of the sulphur dyes is more likely down to recombination of injected electrons from the TiO_2. The dyes synthesised in this chapter were initially designed under the belief that they would adsorb perpendicular to the TiO_2 surface. However, our experiments show that the dyes sit almost flat to the TiO_2 surface. If the dyes lie flat, then the sulphur atom within these dyes would be very close to the TiO_2 surface. The sulphur atom will cause a build-up of I_3^- near the TiO_2 surface. Electrons that have been injected in to the TiO_2

conduction band are more likely to recombine to the I_3^- to form $3I^-$ and therefore reduce the PCE of the DSC device.

A comparison of dark current between two dimethyl derivatised carbon dyes and their sulphur equivalents were investigated in order to understand the recombination processes taking place at the TiO_2 surface. By measuring the difference in dark current between each pair of dyes an approximation of the amount of recombination can be made.[271–273] The dark current of dyes **D1** and **D2** can be seen in **Figure 3.37**.

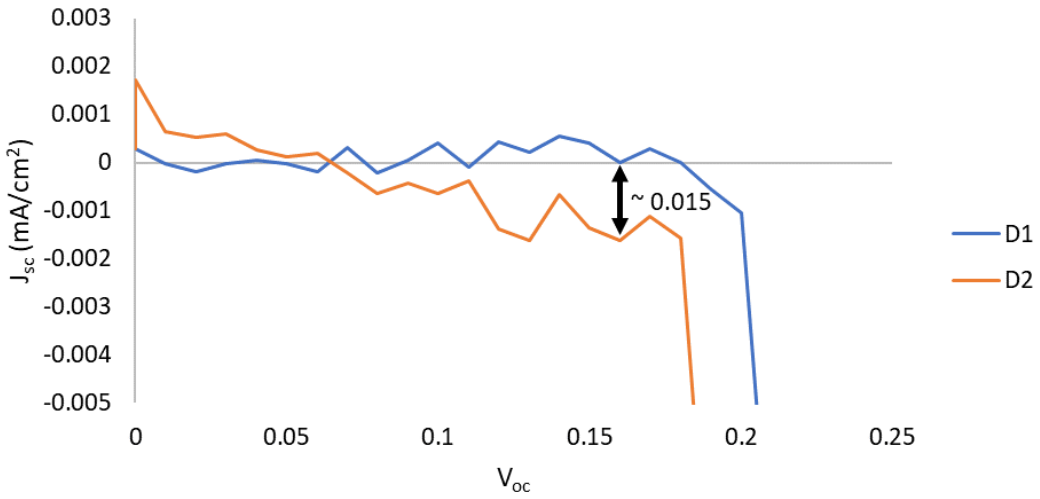

Figure 3.37 – Dark current measurement of dyes **D1** (blue) and **D2** (orange).

From **Figure 3.37** it is observed that **D2** has a lower dark current compared to **D1** (~ 0.015 mA/ cm^2. This suggests that **D2** has increased recombination from the TiO_2 to the triiodide electrolyte. This is interesting as its **D1** that contains the sulphur moiety. In order to investigate further the dark current of dyes **D3** and **D4** were also compared (see **Figure 3.38**).

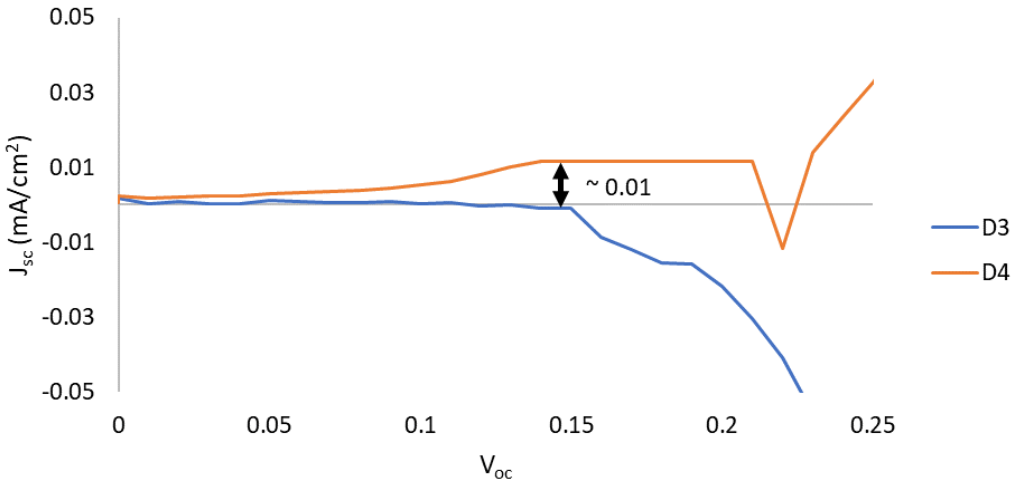

Figure 3.38 - Dark current measurement of dyes **D3** (blue) and **D4** (orange).

Figure 3.38 shows the opposite effect and the dye with the sulphur moiety (**D3**) has a higher dark current (~ 0.01 mA/cm^2) than its carbon counterpart (**D4**). These results are therefore inconclusive and further investigation is required. The comparison of the dyes dark current suggest sulphur plays an important role within the dyes structure. However, it relies on the assumption that all dyes give an even coverage on the TiO_2 surface. Nevertheless, we know understand from our experiments and computer modelling the coverage between the different dyes is vastly different (see **Table 3.3**).

4 Developing solid state dye-sensitised solar cell (ssDSC) devices for the testing of novel dyes and other materials

4.1 Introduction

Earlier chapters in this thesis have shown dye-sensitised solar cells to be a promising form of renewable energy. DSC devices are low-cost, easy to scale up and show good performance under diffuse light.[99] Whilst DSC devices typically absorb light at wavelengths < 700 nm, DSC technology also offers the ability to make efficient solar cells that are able to absorb wavelengths all across the AM 1.5 solar spectrum even with the potential of being transparent. However, a big disadvantage of DSC devices is the need for a liquid based electrolyte which is not only corrosive, susceptible to leakage but due to its various steps it limits V_{oc} diminishing the devices overall performance. To address this ssDSC devices have been developed that utilise a solid hole-transport material (HTM) rather than a liquid electrolyte. The most common HTM is 2,2',7,7'-Tetrakis[N,N-di(4-methoxyphenyl)amino]-9,9'-spirobifluorene (spiro-OMeTAD).[274] Though spiro-OMeTAD is the most common organic HTM ,it's worth noting that it is relatively expensive (1 g = £454)[170] and there are many others published in the literature, these include (but not limited to X60[275], triazotruxene(TAT)[2] and P3HT[276]. The chemical structures of spiro-OMeTAD and X60 can be seen below.

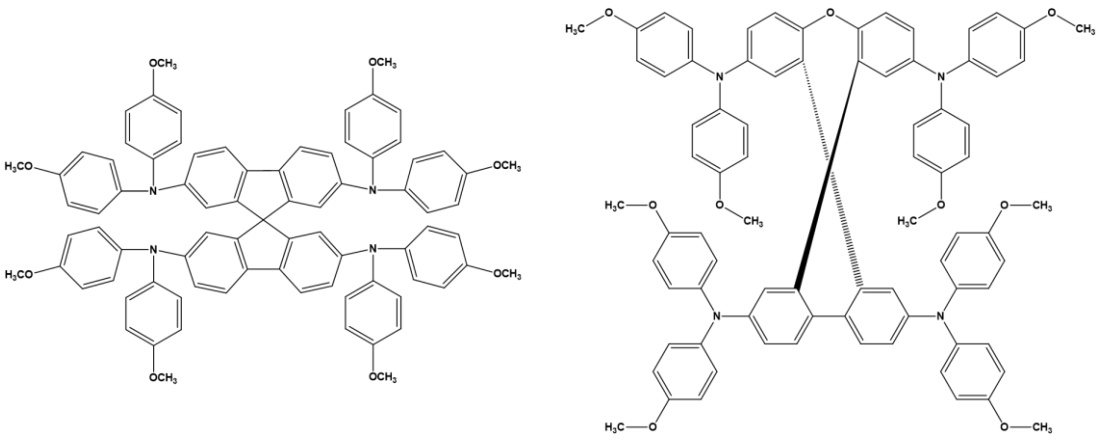

Figure 4.1 - Chemical structures of spiro-OMeTAD(left) and X60(right).

Replacing a liquid system such as triiodide redox couple with a solid organic HTM can potentially increase the device V_{oc}.

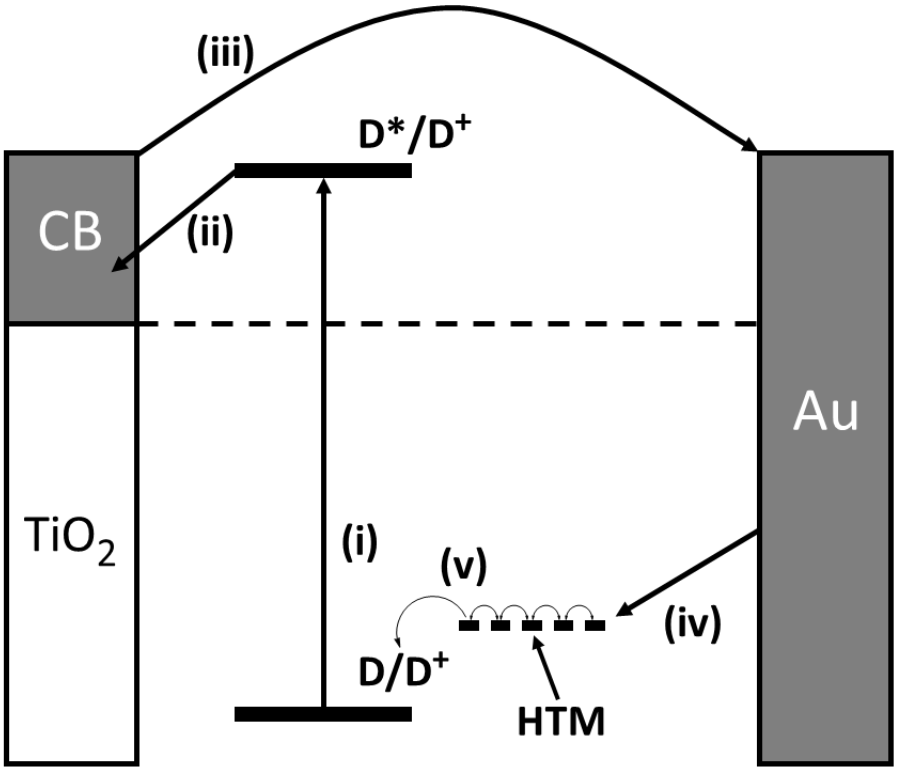

Figure 4.2 - Schematic of ssDSC device showing where a HTM operates within the device

By reducing the overpotential required for dye regeneration much higher V_{oc} can be achieved by using organic HTM's (see **Figure 4.2**).[4] Despite this increase, the change from a liquid to solid system comes with inherent difficulties new device design and operation. The biggest loss mechanism in ssDSC devices is interfacial charge recombination from the electrode/ HTM interface.[277]

4.1.1 Aim of this chapter

So far ssDSC utilising organic HTM's have only achieved $\eta = 7.3$ %[278] (inorganic HTM's have achieved $\eta = 11$ %)[205], somewhat below the $\eta = 14.7$ % achieved by a ssDSC utilising a cobalt redox shuttle. This shows ssDSC devices are still not yet fully

understood and therefore further research is required in order to fully explore the potential of these devices.

Like liquid DSC's ssDSC devices are made up of several unique parts that need to be optimised (TCO, TiO_2, dye, back contact, HTM). Optimising each aspect of such a device can take several months if not years, therefore the focus of this work was to create a well-balanced "control" device that could be made relatively easily with consistent results. After manufacturing such a device, bespoke pastes, dyes and HTM materials have been studied in order to test their impact in a ssDSC device.

To the best of the author's knowledge this chapter reports the first ssDSC manufacture from any Swansea university staff or students. Though Swansea University has a large research focus on photovoltaics its various research groups primarily focus on liquid DSC, perovskite and OPV devices. This chapter discusses my work breaking into a relatively new research area by developing ssDSC devices here in Swansea, so that myself and my colleagues are able to test bespoke materials synthesised by the CEMEG (chemistry, engineering, materials, environment group) and our collaborators.

4.2 Results and discussion

In order to advance ssDSC technology it is essential to discover and develop new strategies to supress recombination at the TiO_2/Dye/HTM interface. One such strategy is to deposit a compact TiO_2 blocking layer.

4.2.1 Deposition of TiO_2 "blocking layer"

This "blocking" layer of TiO_2 is designed to prevent the HTM reaching the electrode (FTO) surface. In the literature this layer is deposited in various ways however, the two most common are sputtering[279] and spray pyrolysis[280]. ssDSC devices with a "blocking" layer generally show much higher short-circuit current density than devices without.[281] Sometimes inorganic dyes such as ruthenium based sensitisers are able to combat this effect naturally in liquid dye cells. However, a blocking layer is absolutely necessary when using planar organic dyes (such as LEG4 and D35).[282] A cheap and easy way of depositing the blocking layer is through hydrolysis of $TiCl_4$.

4.2.2 $TiCl_4$ Treatment

$TiCl_4$ treatment causes further growth of TiO_2 on top of the main TiO_2 semiconductor layer. $TiCl_4$ is most often seen in the manufacture of liquid DSC's but has been more

recently employed in ssDSC devices in order to improve efficiency. $TiCl_4$ causes surface epitaxial growth of the TiO_2, decreasing average pore diameter, resulting in increased "inter-particle necking".[235] The treatment increases surface roughness and light absorbance whilst also decreasing electron transport resistance, reducing the chances of recombination occurring.[283] At the same $TiCl_4$ treatment deposits a layer of high purity TiO_2 on top of a relatively impure TiO_2 semiconductor layer, improving the injection efficiency and the "blocking" characteristics of the semiconductor at the semiconductor-electrolyte junction.[284]

4.2.3 Mesoporous TiO_2 semi-conductors in ssDSC devices

In DSC devices, TiO_2 is used a structured surface to adsorb dye molecules. Mesoporous scaffolds such as TiO_2 allow dye to penetrate through, allowing more dye to be absorbed but it's still only a single layer so all the dyes can inject their electrons into the conduction band of the TiO_2.The advantages of mesoporous TiO_2 was demonstrated by Grätzel and O'Regan.[99]

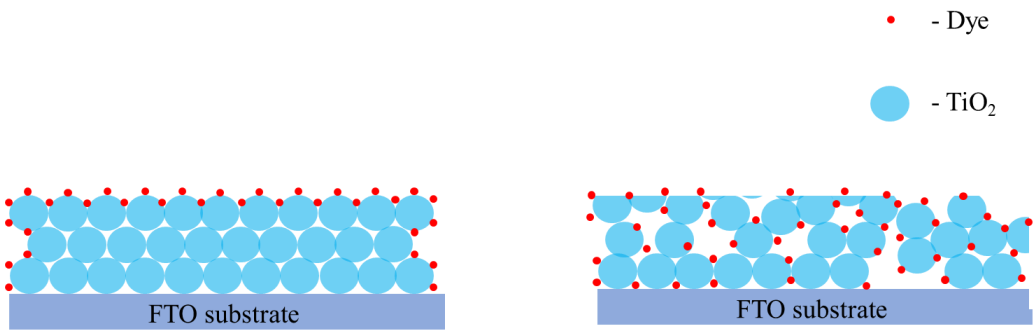

Figure 4.3 – Compact TiO_2 (left), Mesoporous TiO_2 right

The role of TiO_2 in ssDSC devices is identical to those in liquid DSC devices. The main difference between liquid and solid DSC scaffolding layers is the thickness. The thickness of the TiO_2 layer has a huge impact on device performance as it directly controls how much dye is absorbed and therefore how many photons can be absorbed. The TiO_2 is mesoporous and therefore by definition is full of pores or holes. The solid HTM in ssDSC devices are less able to penetrate the TiO_2 pores than electrolytes such as the triiodide redox couple commonly seen in liquid electrolytes. Because of this, ssDSC devices require a much thinner layer of TiO_2 (< 2.5 µm) in order to overcome the short diffusion length for optimum performance.[275]

Having no previous experience manufacturing ssDSC devices, the first set of devices were made using a recipe published by Xu *et al*[275]. Xu *et al.* designed a new HTM (X60) and were able to achieve 7.30 % in a ssDSC device. The first set of devices made for this chapter were identical to Xu's except for a few small modifications.

4.2.4 Manufacturing ssDSC devices

The first variable tested was in the form of TEC glass. Xu *et al.*[275] used TEC 15 glass for their devices however TEC 7 was used in the devices in this work. This choice was down to the higher conductance of TEC 7. TEC 7 is also easily available as it is commonly used in the manufacture of other PV devices (such as liquid DSC's and PSC's and has the lowest resistivity of the TEC glass range. However, TEC 7 glass is slightly hazier (< 1.5 %) than TEC 15 (< 0.8 %). The "haziness" of the glass will affect how much light is able to reach the dye. Therefore, the less hazy your glass the more light is absorbed and the greater the device performance. TEC 7 glass also has a rougher FTO surface that TEC 15. A rough surface is more able to adhere to TiO_2 which makes processing easier. However, a rough surface also requires a thicker BL to stop the HTM interacting with the FTO.

The second change was the HTM used, Xu used a HTM referred to as X60. However, spiro-OMeTAD was used as it is the reference hole-transport material for solid-state DSCs and PSC's and would therefore create a good baseline to compare against other devices. Both HTM's have very similar structures and therefore in the same class of "spiro" HTM's however, spiro-OMeTAD is generally more expensive than X60.[170]

Table 4.1 – Electronic property comparison between spiro-OMeTAD and X60 HTM's[101]

Name	HOMO (eV)	LUMO (eV)	Mobility ($cm^2\ V^{-1}\ s^{-1}$)	λ_{abs} (nm)	Mw g/mol
spiro-OMeTAD	-5.13	-2.06	8.1×10^{-5}	388	1225.43
X60	-5.15	-2.10	1.9×10^{-4}	387	1241.45

It is unclear what size the ssDSC electrodes were that Xu made however, the ones in this chapter are 2.8 cm^2. This size is much larger than most lab ssDSC devices but as masks and testing units were already available for this size device (used previously for PSC's) it made sense to create ssDSC devices this size. Finally, it was decided to allow the devices to oxidise overnight rather than doping with 1,1,2,2-tetrachloroethane. Other than these three changes the devices were identical to those in Xu's paper.

Unfortunately, the devices made following this method were completely inactive. The most likely reason for this was the thickness of the HTM layer. The thicker the HTM layer the longer it requires to oxidise. Therefore, in order to get these devices working they would have needed to be left for longer in an oxygen rich environment or be doped. This was later proven by remaking the same devices and doping with FK09.

It's well known HTM's like spiro-OMeTAD need to be left in an oxygen rich atmosphere or be doped with materials such as FK209 in order to be conductive.[285] In the literature spiro-OMeTAD HTM solutions usually contain between 2.5 and 35 % spiro-OMeTAD (in chlorobenzene).[286–290] Most of the papers that use concentrations higher than 10 % spiro-OMeTAD also use a dopant. There a couple papers using > 10 % spiro-OMeTAD who don't mention using a dopant however, considering the recipe we followed from Xu *et al.* only used 16.5 % spiro-OMeTAD and failed to oxidise in 24 hours. Any other papers using an equal or thicker layer must have left their devices for longer than 24 hours to fully oxidise.

In order to test whether or not the HTM layers in our devices were too thick to sufficiently oxidise overnight, the experiment was repeated but this time added dopant tris(2-(1H-pyrazol-1-yl)-4-tert-butylpyridine)cobalt(III) tri[bis(trifluoromethane)sulfonimide] (FK209) in order to force the spiro-OMeTAD to oxidise.

The performances can be seen below:

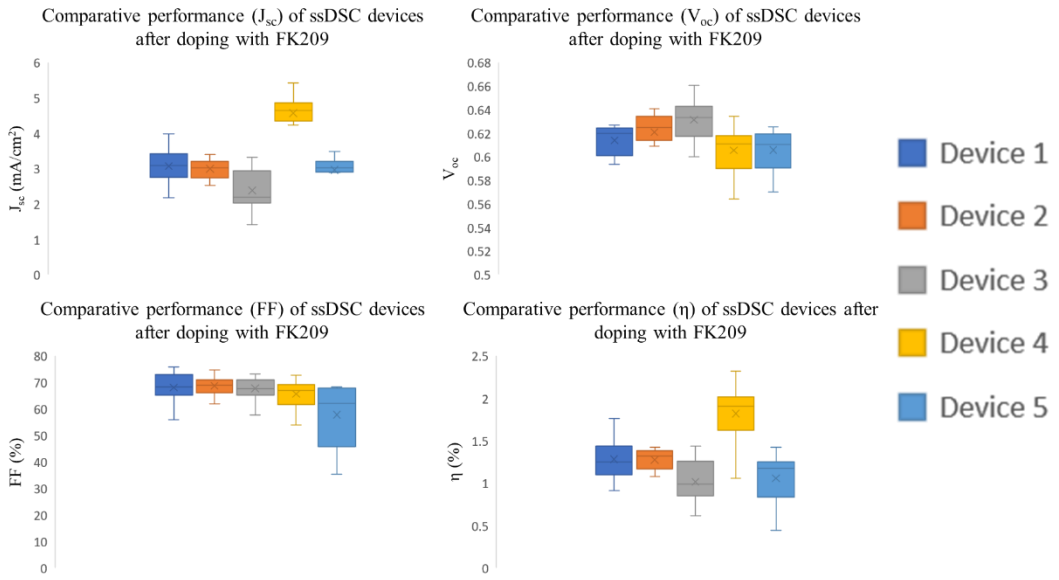

Figure 4.4 - Performance of ssDSC devices doped with FK209. J_{sc} (top left), V_{oc} (top right), FF (bottom left) and η (bottom right)

Table 4.2 - Summary of ssDSC device performance after doping with FK209

Device N^{o}	V_{oc}	J_{sc} (mA/cm^2)	FF (%)	η (%)	"Hero" cells η (%)
1	0.61	3.07	68	1.28	1.76
2	0.62	2.99	69	1.27	1.43
3	0.63	2.38	68	1.02	1.44
4	0.61	4.56	66	1.82	2.32
5	0.58	2.56	53	0.91	1.42

[a]Data are averages of 8 data points

The addition of the dopant (FK209) was enough to switch the ssDSC devices on (see **Figure 4.4** and **Table 4.2**). Though the performances are much lower than the paper it is a good starting point and showed that the devices work. However, the V_{oc} and J_{sc} of these devices is much lower than those seen in the literature. The V_{oc} of these devices is ~ 0.61 V and the J_{sc} is ~ 3.1 mA/cm^2, in the literature LEG4 should be able to reach ~ 1 V and > 11 mA/cm^2. Therefore, if these areas can be addressed the largest increase in performance should be observed. Low V_{oc} suggests more recombination or possible device shorting, whereas low J_{sc} suggests poor dye uptake.

4.2.5 Developing the ssDSC devices

Now working ssDSC devices have been made we needed to determine the effect of the various stages of the ssDSC development in order to see what steps impact V_{oc} and J_{sc} the most. The areas of development looked at were the effects of the "blocking" layer, thickness of mesoporous TiO_2, effect of $TiCl_4$ treatment, dyeing times and finally HTM thickness.

4.2.5.1 Effect of the "blocking" layer (BL)

The effect of the "blocking" layer has been widely studied in both PSC and ssDSC devices[291] (please see **chapter 4.2.1** for more detail). Because of this, many techniques have been developed to deposit the BL (spray pyrolysis, spin coating, atomic layer deposition etc)[291]. Spray pyrolysis is the most common method. However, unless sprayed by a machine it is subject to human error and the amount of BL with vary from person to person depending on their technique. The perfect BL should be just thick enough to avoid any FTO being exposed whilst not being too thick as this would mean injected electrons have a thicker TiO_2 layer to pass through. Therefore, it was important to develop the most efficient deposition method. By comparing two different methods; spin coating (using Ti-Nanoxide BL/SP paste supplied by solaronix) and spray pyrolysis (10 and 25 sprays using 10 % TiAcAc solution, supplied by Sigma Aldrich). A set of devices without any blocking layer were also made (as a comparison). **Figure 4.5** and **Table 4.3** show the performances of the ssDSC devices made with various blocking layers.

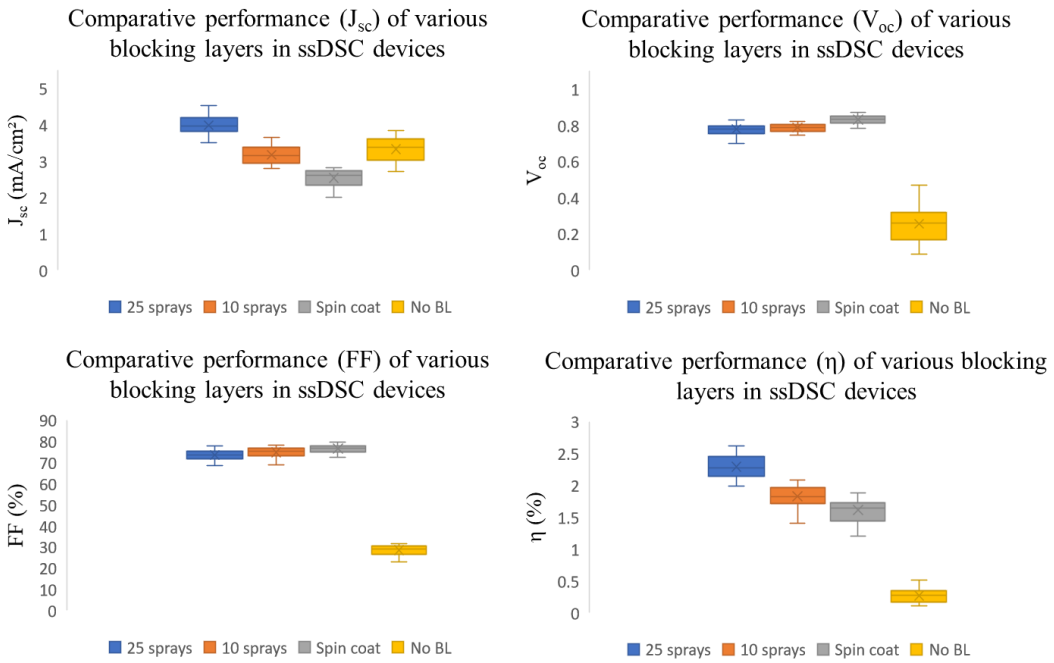

Figure 4.5 - Performance of ssDSC devices with various blocking layers. J_{sc} (top left), V_{oc} (top right), FF (bottom left) and η (bottom right).

Table 4.3 - Summary of ssDSC performance with various BL compositions

BL used	V_{oc}	J_{sc} (mA/cm^2)	FF (%)	η (%)	"Hero" cells η (%)
No BL	0.27	3.37	29	0.27	0.51
Spin coating (Ti-Nanoxide BL/SP)	0.83	2.54	75	1.59	1.89
10 sprays (10 % TiAcAc in IPA)	0.78	3.17	73	1.81	2.09
25 sprays (10 % TiAcAc in IPA)	0.78	3.99	74	2.29	2.61

[a]Data are averages of 24 data points. Three different ssDSC devices with 8 pixels per device.

The data shows that a BL is necessary for high performing ssDSC devices as the devices with 25 sprays were over 2% better than those without. Although spin coating improved V_{oc} slightly, it drastically reduced J_{sc} reducing overall device efficiency when compared to spray coating. 25 sprays were better than 10 sprays increase J_{sc} around 0.82 mA/cm^2. This is likely due to 10 sprays not creating a conformal coating over the FTO layer. Exposed FTO could come into contact with the HTM and cause unwanted recombination. Both the FF and V_{oc} of the devices without a BL were significantly lower than those with yielding a lower efficiency. Surprisingly the J_{sc} of

the devices without a BL layer were the second highest of all the device types. This is likely due to more light reaching the dyes. These devices were illuminated from the FTO side. Therefore, devices without a BL would likely allow more light to pass through to the LEG4 dye increasing J_{sc}. However, this could also come from the lack of a BL. A BL can make it even more difficult for the HTM to penetrate the TiO_2 scaffold layer. Yet, the results of this experiment demonstrate that the positive effect of using a BL out ways the smaller negative effects. For this experiment the maximum number of sprays reached was 25 however, the efficiencies continued to rise. Therefore, it would be worth investigating the effect of a thicker BL. As the aim of this chapter was to create a "good" ssDSC to test novel materials the researchers decided to stop at 25 sprays.

4.2.5.2 Thickness of mesoporous TiO_2

The thickness of the mesoporous TiO_2 layer is crucial as it determines exactly how much dye is able to adsorb to the surface and therefore controls how many photons can be absorbed. However, there is a limit to how thick the layer can be as too much decreases the pore filling of the HTM reducing the performance of the device.[292] Xu *et al.* diluted their TiO_2 paste with terpineol (1:2, mass ratio) to achieved a TiO_2 thickness of approximately 2.5 µm. It was decided to replicate this process but instead used ethanol to dilute the TiO_2 paste. The dilutions were 1:2, 1:3, 1:4 and 1:5. Before device testing the TiO_2 solutions were spun down (in the same method as the previous devices) and measure the thicknesses using profilometry. The thicknesses of the TiO_2 layers can be seen in **Table 4.4**.

Table 4.4 - Dilution of TiO_2 paste and measured film thickness

Dilution TiO_2 paste: Ethanol	1:2	1:3	1:4	1:5
Thickness (µm)	2.6	1.4	1.0	0.9

After measuring profilometry ssDSC devices were made using the same pastes and the results can be seen in **Figure 4.6** and **Table 4.5**.

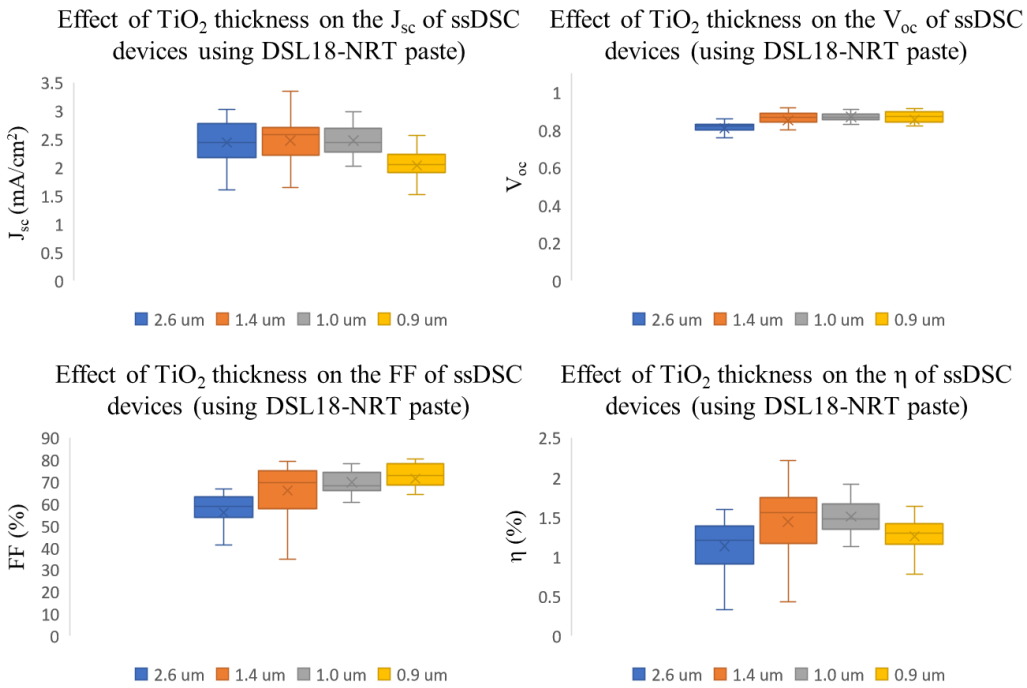

Figure 4.6 - Performance of ssDSC devices with various thicknesses of mesoporous TiO_2. J_{sc} (top left), V_{oc} (top right), FF (bottom left) and η (bottom right).

Table 4.5 - Summary of the effect of TiO_2 thickness on ssDSC device performance

TiO_2 Thickness (µm)	V_{oc}	J_{sc} (mA/cm^2)	FF (%)	η (%)	"Hero" cells η (%)
2.6	0.81	2.44	56	1.13	1.59
1.4	0.85	2.48	66	1.44	2.21
1	0.87	2.47	70	1.50	1.91
0.9	0.85	2.04	70	1.30	1.63

[a]Data are averages of 24 data points. Three different ssDSC devices with 8 pixels per device.

Of all the TiO_2 films, the best turned out to be ~1µm thick. This films likely optimises dye absorption and HTM pore filling yielding the best performance. Most of the films were very consistent however the 2.6 µm film had a much worse performance due to a 10 % drop in FF. The poor FF was attributed to poor coverage of the film. The

solution was so viscous that it was unable to spread evenly during spin coating and appeared more like a “paint splat” than the usual metal oxide film. See **Figure 4.7**.

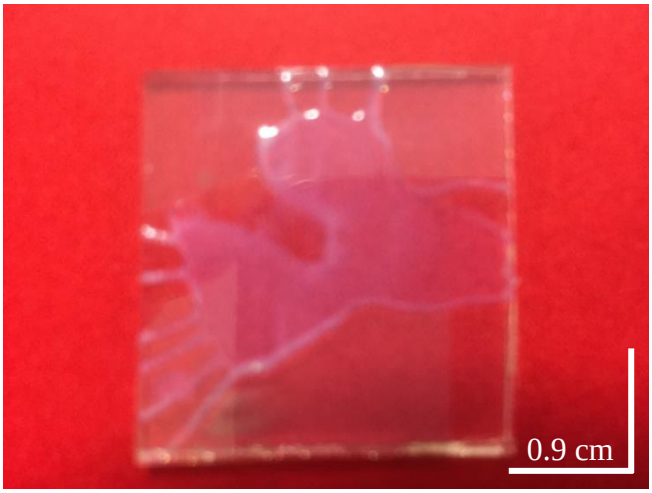

Figure 4.7 – Inconsistent film spreading of TiO_2 paste (1:2 with ethanol) after spin coating

To help combat this effect the films for the devices were spread using the tip of an Eppendorf pipette before spin coating. Though this made the films look better visually it still resulted in device performances recorded in **Table 4.5**.

Unfortunately, part of the way through this chapter GreatCellSolar (the company supplying the DSL18-NRT TiO_2 paste) stopped production. Because of this a decision was made to use paste supplied by Solaronix (Ti-Nanoxide T/SP) as according to the online specifications it was almost identical to the previous paste used. As the pastes had now been changed it was important to determine if the optimum thickness was the same as before.

Therefore, it was decided to replicate the earlier process using ethanol to dilute the TiO_2 paste into the same four concentrations (1:2, 1:3, 1:4 and 1:5, TiO_2: Ethanol). Before device testing the TiO_2 solutions were spun down and measure using profilometry giving the thicknesses as follows:

Table 4.6 - Dilution of solaronix (Ti-Nanoxide T/SP) TiO_2 paste and measured film thickness

Dilution TiO_2 paste: Ethanol	1:2	1:3	1:4	1:5
Thickness (µm)	0.62	0.40	0.26	0.18

The profilometry data shows the TiO_2 films made with Ti-Nanoxide T/SP are far thinner than the previous films made with DSL18-NRT (1:2 dilution gives thickness of 2.6 µm and 0.62 µm for DSL18-NRT and Ti-Nanoxide T/SP respectively). ssDSC devices were then made using the same TiO_2 solutions and the results can be seen in **Figure 4.8** and **Table 4.7**.

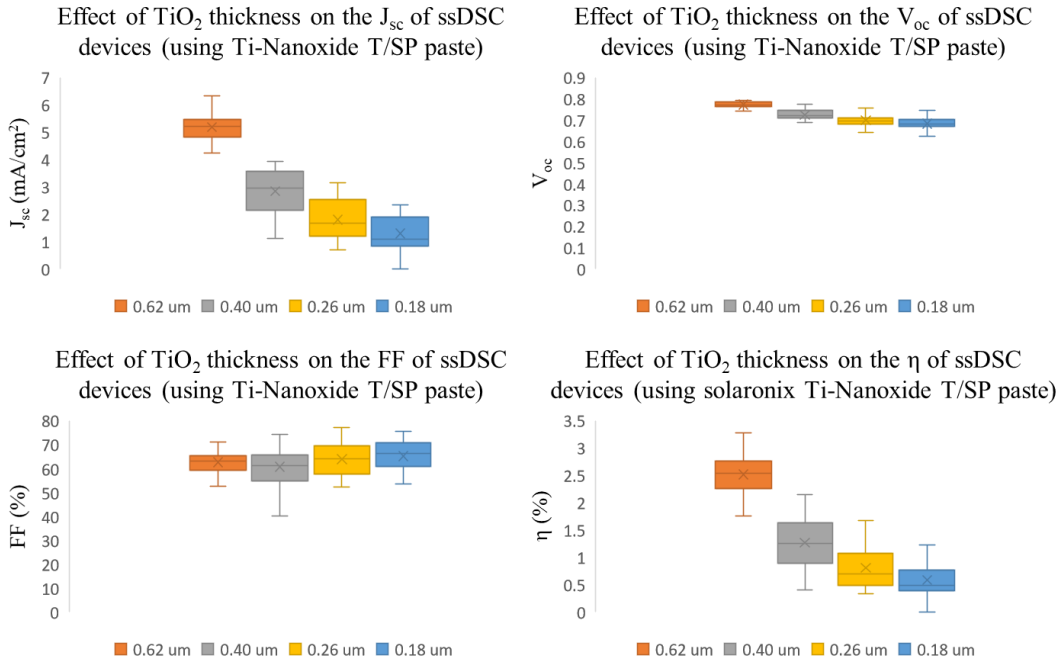

Figure 4.8 - Performance of ssDSC devices with various thicknesses of mesoporous TiO_2. J_{sc} (top left), V_{oc} (top right), FF (bottom left) and η (bottom right).

Table 4.7 - Effect of TiO_2 thickness on ssDSC device performance (using Ti-Nanoxide T/SP paste)

TiO_2 Thickness (µm)	V_{oc}	J_{sc} (mA/cm^2)	FF (%)	η (%)	"Hero" cells η (%)
0.62	0.77	5.19	63	2.52	3.29
0.40	0.75	2.85	61	1.27	2.06
0.26	0.70	1.80	64	0.81	1.62
0.18	0.68	1.30	65	0.59	1.24

[a]Data are averages of 24 data points. Three different ssDSC devices with 8 pixels per device.

Despite being the same architecture, devices using Ti-Nanoxide T/SP outperformed the same devices using DSL18-NRT. It yielded the highest performing device to date achieving 3.29 %. Devices using Ti-Nanoxide T/SP paste show huge increases J_{sc} and

a small decrease in V_{oc} compared to equivalent devices using DSL-18NRT yielding much higher efficiencies. Considering that the Ti-Nanoxide T/SP films were much thinner than the DSL18-NRT films it was surprising to see such an increase in efficiency. If the chemical properties of the films were identical then in theory the thicker films should adsorb more dye, absorbing more photons and therefore have a better performance. However, the Ti-Nanoxide T/SP films were darker in colour then the DSL18-NRT films, suggesting that they have adsorbed more dye, which would explain the higher performance (see **Figure 4.8**).

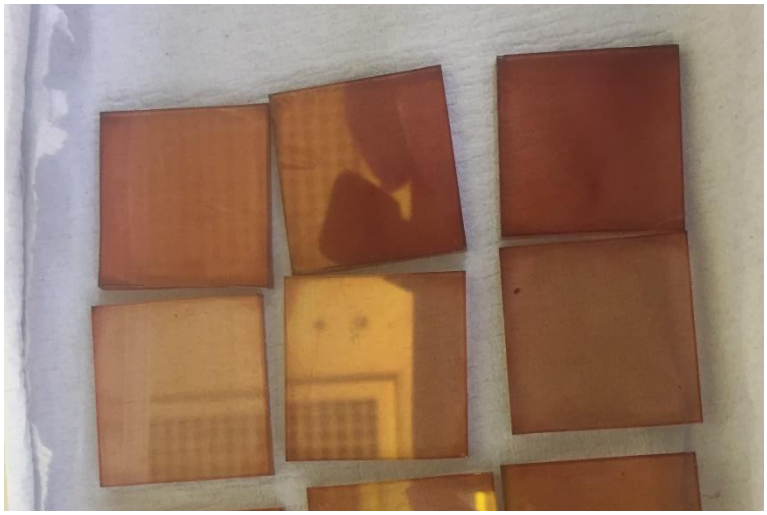

Figure 4.9 – ssDSC devices with Ti-Nanoxide T/SP films (top), ssDSC devices with DSL18-NRT films (bottom)

Even if the two manufactures prepare their TiO_2 pastes in the same way the pH, particle size and surfaces could vary drastically. For example TiO_2 nanoparticles prepared just by the sol-gel method can vary their pH from 3.2-6.8.[293,294] This could mean that the pastes used here could have drastically different pH values which would affect the point of zero charge (PZC). Therefore, it could simply be just the pH of the pastes that have caused drastically difference in dye uptake. However, this would require further investigation to know for sure. It is also worth noting that the optimum thickness for DSL18-NRT was 1.0 µm however for the new paste (Ti-Nanoxide T/SP) we have only investigated up to 0.62 µm and the performance has yet to drop again. Developing thicker films using the Ti-Nanoxide T/SP paste could yield even better performances. However due to time constraints this will be something that is investigated in the future. Following the TiO_2 thickness, the effect $TiCl_4$ treatment was studied.

4.2.5.3 Effect of $TiCl_4$ treatment

The chemical process of $TiCl_4$ treatment is explained in full in section 4.2.2. $TiCl_4$ treatment is a very common practice in liquid DSC devices and know used in ssDSC devices as a way of correcting for poor TiO_2 films.[295,296] In simple terms $TiCl_4$ treatment creates a new surface layer of TiO_2 on the mesoporous scaffold. It should have huge impact on poorly sintered films however if a film is already of good "quality" then the treatment has little to no effect.

In this section devices have been made with and without using $TiCl_4$ treatment. The results of this will give us information on 1) how well the TiO_2 films have been sintered and 2) what impact $TiCl_4$ has on ssDSC devices. The chemical equation for the formation of TiO_2 from $TiCl_4$ can be seen in **equation 4.1**.[297]

$$\mathbf{TiCl_4\ (aq) + 2H_2O\ (aq) \longrightarrow TiO_2(s) + 4HCl\ (aq)} \qquad \mathbf{(4.1)}$$

For liquid DSC devices normally 50-70 mmol of titanium(IV) chloride tetrahydrofuran is dissolved in deionised water and heated to 70 ^oC. The TiO_2 photoelectrodes are then submerged in the solution for 30 minutes. After the 30 minutes has passed the electrodes are removed, rinsed with deionised water and re-sintered at 500 ^oC. This

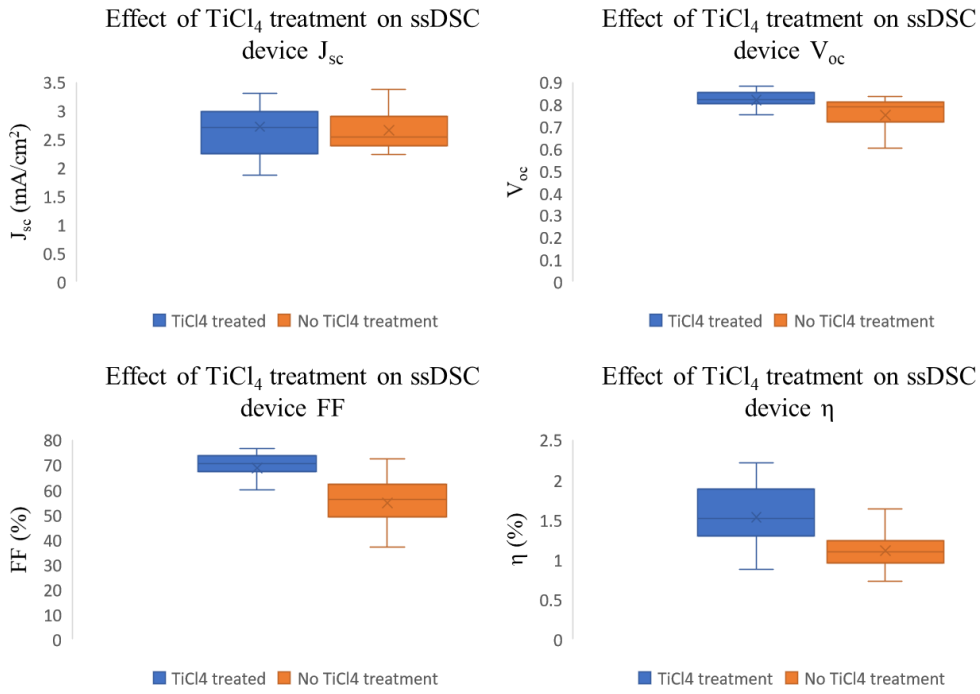

Figure 4.10 - Performance of ssDSC devices with and without $TiCl_4$ treatment. J_{sc} (top left), V_{oc} (top right), FF (bottom left) and η (bottom right).

process is identical for ssDSC devices. However, as the mesoporous TiO_2 layer was thinner in ssDSC devices the concentration of Titanium(IV) chloride tetrahydrofuran was reduced (usually to about 20 mmol). The performances of the ssDSC devices with and without $TiCl_4$ treatment can be seen in **Figure 4.10** and **Table 4.8**.

Table 4.8 – Effect of $TiCl_4$ treatment on the performance of ssDSC devices

$TiCl_4$ Treatment? (Y/N)	V_{oc}	J_{sc} (mA/cm^2)	FF (%)	η (%)	"Hero" Cells
N	0.75	2.66	55	1.11	1.85
Y	0.82	2.71	69	1.53	2.22

[a]Data are averages of 24 data points. Three different ssDSC devices with 8 pixels per device. TiO_2 thickness = 0.62 um.

Looking at the results using $TiCl_4$ treatment, there appears to be little difference between the two sets of devices in terms of J_{sc}. However, the V_{oc} increase ~ 70 mV suggesting less recombination is occurring. It seems to be that the biggest impact of $TiCl_4$ treatment is on the fill factor of the devices. This data suggests that $TiCl_4$ is necessary to achieve the very best performance out of ssDSC devices. After studying $TiCl_4$ treatment, electrode dyeing times were studied.

4.2.5.4 Dyeing times

There have been several methods developed in order to effectively dye liquid DSC devices the most common of these are passive dyeing and pump dyeing.[163] Depending on the dyeing method used the time scale can drastically change. Passive dyeing usually takes between 18-24 hours whilst pump dyeing can be as little as 5 minutes[164]. Unfortunately, as most ssDSC device architectures do not include an internal cavity pump dying is currently not an option therefore most ssDSC publications are limited to passive dying. However, some papers report dying ssDSC devices for 18-24 hours like liquid DSC devices, whilst other publications passive dye for just a couple of hours. In an optimised system the mesoporous TiO_2 must be sensitised with just a single monolayer of dye.[298] Dyeing for too long will cause dye aggregation on the TiO_2 surface increasing recombination. Dyeing for too little time will mean not all the TiO_2 is covered with dye, this will mean fewer photons absorbed and therefore a reduction in performance. To test this, devices have been dyed for 2 hours and compared against

devices that have been dyed overnight (~18 hours) and the results can be seen in **Figure 4.11** and **Table 4.9**.

Table 4.9 – Effect of dyeing time on ssDSC device performance

Dyeing time (hours)	V_{oc}	J_{sc} (mA/cm^2)	FF (%)	η (%)
2	0.81	2.78	69	1.56
~18	0.82	2.72	69	1.53

[a]Data are averages of 24 data points. Three different ssDSC devices with 8 pixels per device.

Both sets of devices were almost identical. Although 2 hours showed a small increase in efficiency (0.03 %) though this is negligible and could be down to experimental error. The data show the TiO_2 has become fully sensitised after just two hours.

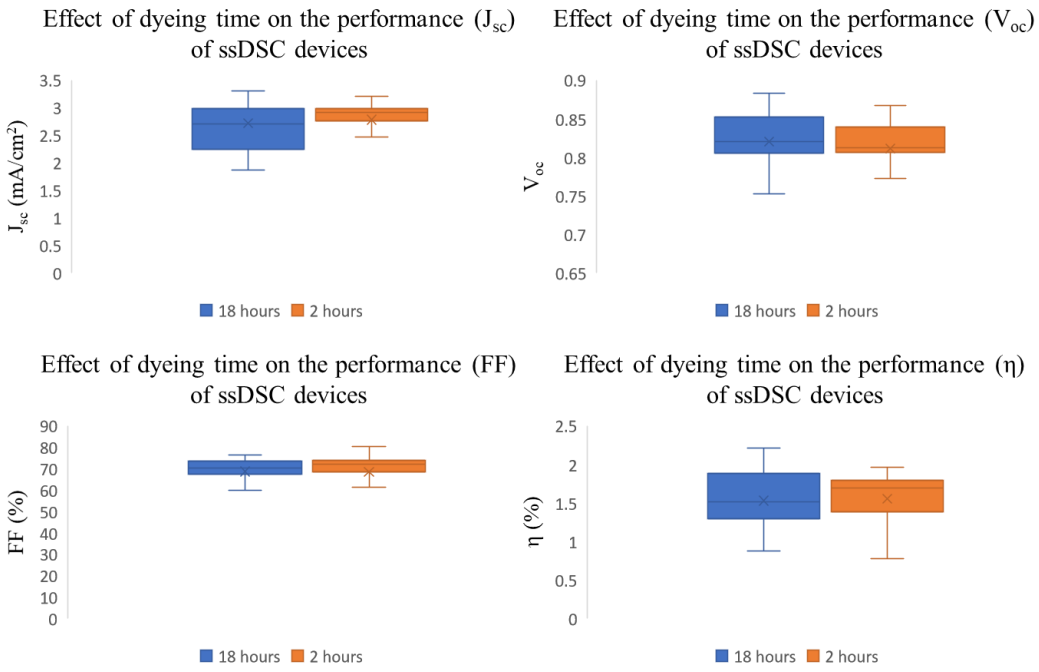

Figure 4.11 - Performance of ssDSC devices after dyeing with LEG4 dye for 18 hours (blue) and 2 hours (orange). J_{sc} (top left), V_{oc} (top right), FF (bottom left) and η (bottom right).

However, there is no evidence that the dyes undergo aggregation even after 18 hours. Further tests need to be carried out to see if dye aggregation occurs after 18 hours but these results show that it is up to the researcher on how long they dye ssDSC photoelectrodes as any dyeing time between 2 and 18 hours should have no impact on how the device performs. In order to maximise the efficiency of a DSC devices the dye must be easily regenerated. In the case of a ssDSC the HTM plays this role. Therefore, the HTM was investigated.

4.2.5.5 HTM thickness on device performance

The HTM layer is responsible for carrying charge from the counter electrode in order to regenerate the oxidised dye.[299] The thickness of the HTM layer is crucial aspect of the ssDSC device.[300] If the layer is too thick then an increase of series resistance will be observed. However, if the HTM layer is too thin then pinholes could appear, allowing the metal counter electrode to come into contact with the mesoporous TiO_2 layer, shunting the device.[292] Therefore, it is important to optimise this layer to get the best performance from the ssDSC devices. In this next section the thickness of the HTM layer has been varied and its effect upon device performance tested.

There are two ways that the HTM layer thickness can be altered. The HTM solution can be diluted/ concentrated or the spin speed of the spin coater can be changed. Either method should alter the thickness of the HTM layer. Rather than creating several solutions with varying concentration it was decided that the best method would be to create a single solution and gradually increase the speed of the spin coater. It was decided to spin three devices at 2,000 rpm, three devices at 3,000 rpm and finally three devices at 4,000 rpm.

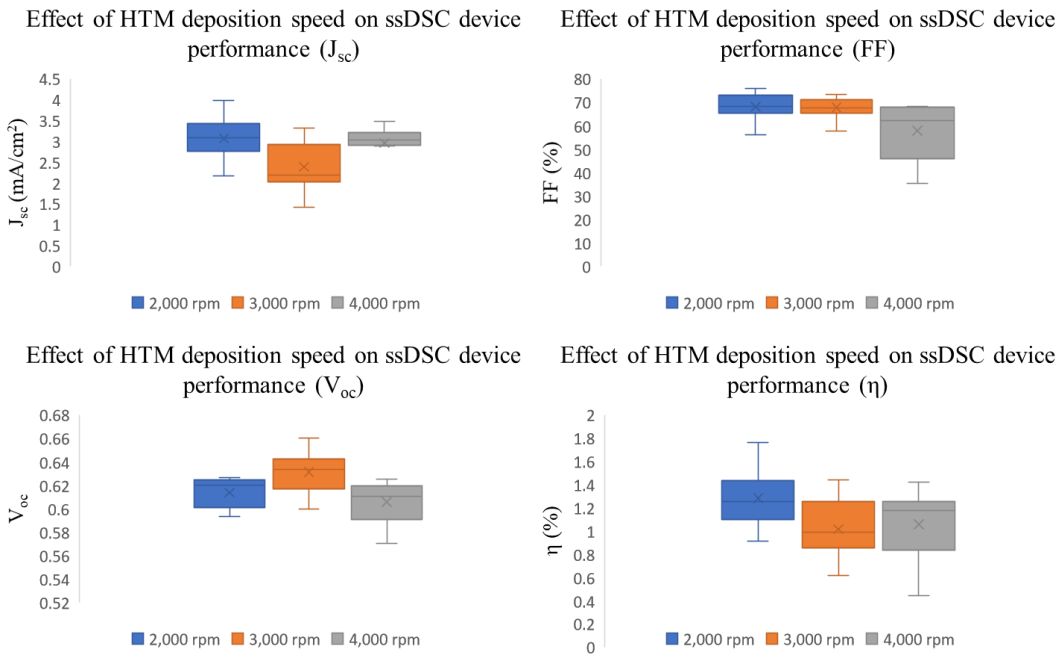

Figure 4.12 - Performance of ssDSC devices after varying the spin coater speed for HTM deposition. J_{sc} (top left), V_{oc} (top right), FF (bottom left) and η (bottom right).

Table 4.10 – Effect of HTM thickness on ssDSC device performance

Spin speed	V_{oc}	J_{sc} (mA/cm^2)	FF (%)	η (%)	"Hero" cells η (%)
2,000 rpm	0.61	3.07	68	1.28	1.76
3,000 rpm	0.63	2.38	68	1.02	1.44
4,000 rpm	0.58	2.56	53	0.91	1.42

[a]Data are averages of 24 data points. Three different ssDSC devices with 8 pixels per device.

Of the three speeds tested clearly the standard settings of 2,000 rpm at 2,000 rpm acceleration is the best. The V_{oc} is relatively unchanged between the three settings. However, both FF and J_{sc} drop slightly as the HTM film gets thinner. This could be down to pinholes appearing resulting in the Au counter electrode comes into contact with the mesoporous TiO_2 and shunting the device. It's worth noting that the V_{oc} of these devices is lower than the previous set. These devices were prepared out of the clean room and our studies have shown that ssDSC devices are extremely sensitive to dust leading to the decrease in V_{oc}.

The data here shows that controlling the HTM layer is crucial to achieve the highest performing ssDSC devices. However, a larger change may be observed by changing the HTM recipe itself. Almost all HTM recipes for ssDSC devices containing spiro-OMeTAD also contain *t*BP, LiTFSI and a dopant (such as FK209, TeCA etc). Each element has a specific role and just like in liquid DSC electrolytes, the concentrations of these materials need to be optimised for each device architecture. If the HTM layer is too thick than distance becomes a hindrance for the dopants. If the HTM layer is too thin, then dopants cause charge traps to occur. However, if the HTM thickness and dopants can be optimised then the charge is able to move quickly between the Au electrode and the oxidised dye (through the HTM layer). To optimise this system, it is very important to understand the dopants that are used and their role in ssDSC device performance.

*4.2.5.5.1 Role of 4-tertbutyl pyridine (t*BP*)*

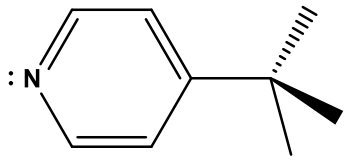

Figure 4.13 – Chemical structure of *t*BP

4-tertbutyl pyridine(*t*BP) is commonly used in ssDSC and PSC devices to improve photovoltaic performance.[301,302] The chemical structure of *t*BP can be seen in **Figure 4.13**. By using tBP in various concentrations Yang *et al*[309] showed that tBP as an additive was able to improve ssDSC device performance. The I-V data from Yang's work can be seen in **Table 4.11**.

Table 4.11 – Data of I-V characteristics for ssDSC devices with different *t*-BP concentrations[309]

ssDSC (mmol)	V_{oc} (mV)	J_{sc} (mA cm^{-2})	FF (%)	η (%)
0	560 +/- 28	5.5 +/- 0.3	53 +/- 3	1.66 +/- 0.08
60	915 +/- 46	6.7 +/- 0.3	68 +/- 3	4.12 +/- 0.21
120	930 +/- 47	10.0 +/- 0.3	63 +/- 3	5.85 +/- 0.29
240	950 +/- 48	9.8 +/- 0.3	62 +/- 3	5.81 +/- 0.29

Johansson *et al.*[301] used HAXPES and density functional theory to determine the role of *t*BP in ssDSC devices. By altering the concentration of *t*BP Johansson was able to show a shift in the CB of the TiO_2 caused by an interaction between the *t*BP and TiO_2.[301] Johansson also demonstrated that adsorbed *t*BP on the TiO_2 surface inhibits charge recombination, increasing photovoltaic performance.[301] Other studies including those done by Qi *et al.*[303] showed that *t*BP also prevents phase aggregation of LiTFSI and spiro-OMeTAD resulting in a homogeneous hole transport layer (HTL) which is vital for increased charge transport at the dye/HTL and HTL/electrode. *t*BP isn't the only dopant used in ssDSC devices, often LiTFSI is used to increase device performance.

4.2.5.5.2 Role of Bis(trifluoromethane)sulfonimide lithium salt (LiTFSI)

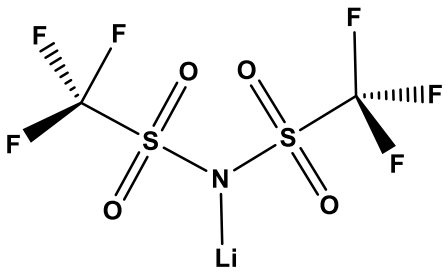

Figure 4.14 - Chemical structure of LiTFSI

LiTFSI is most commonly used as a dopant in ssDSC and PSC devices to increase conductivity and hole mobility of spiro-OMeTAD.[304] The chemical structure of LiTFSI can be seen in **Figure 4.14**. Li^+ ions are able to penetrate the pores of the TiO_2. This causes the conduction band of the TiO_2 to move down resulting in a higher photocurrent. As well as shifting the conduction band, the Li^+ ions are also able to react with oxygen and spiro-OMeTAD facilitating the oxidation process, see equations 4.1 and 4.2.

$$\text{spiro-OMeTAD} + O_2 \rightleftharpoons \text{spiro-OMeTAD}^{\bullet+}O_2^{\bullet-} \quad \textbf{(4.1)}$$

$$\text{spiro-OMeTAD}^{\bullet+}O_2^{\bullet-} + \text{LiTFSI} \longrightarrow \text{spiro-OMeTAD}^{\bullet+}\text{TFSI}^- + Li_xO_y \quad \textbf{(4.2)}$$

These two opposing systems (one that requires LiTFSI and the other that consumes LiTFSI) pose a difficult issue for ssDSC devices. Therefore there have been several papers aiming to remove limit the use LiTFSI from the HTM solution.[305] Although this is an important issue for ssDSC devices it isn't one that will be addressed in this thesis.

4.2.5.5.3 Role of other dopants in ssDSC devices

As discussed in section 1.3.1.1 doping is an important way to control the type and density of charge carriers in organic and inorganic semiconductors.[285,306] There are several different materials (FK102[306], FK269[306] and TeCA[275]) that are able to efficiently dope spiro-OMeTAD without the need for LiTFSI. However, the main dopant used in this thesis is tris(2-(1H-pyrazol-1-yl)-4-tert-butylpyridine)cobalt(III) tri[bis(trifluoromethane)sulfonimide] (FK209). The structure of FK209, FK269 and TeCA can be seen in **Figure 4.15**.

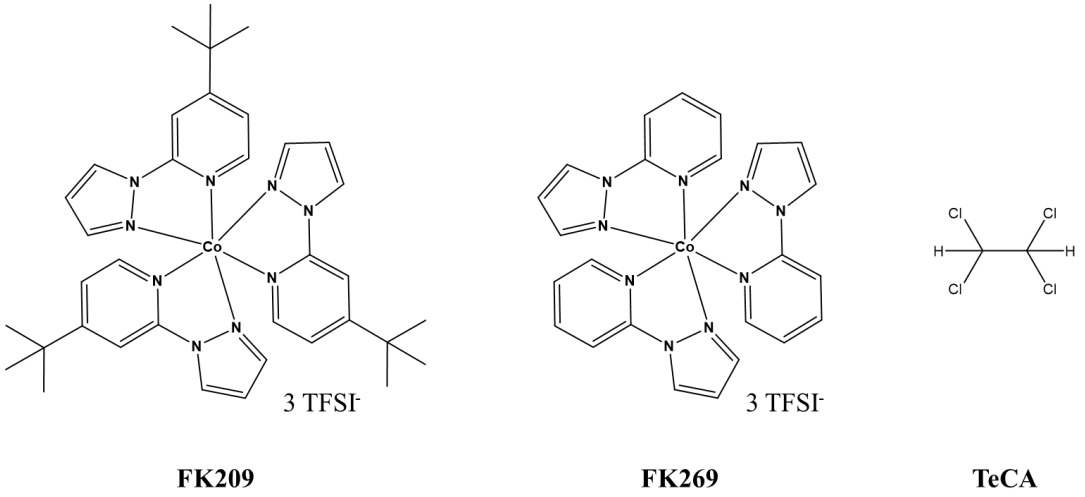

FK209 **FK269** **TeCA**

Figure 4.15 - Chemical structure of FK209 (left), FK269 (centre) and TeCA (right).

Dopants like FK209 are added to HTM solutions in order to successfully oxidise triaryl based HTM's such as spiro-OMeTAD without the need for LiTFSI and oxygen. Doping materials like spiro-OMeTAD in this way increases the reproducibility of device performances.[285]

4.2.5.6 Testing of novel materials for ssDSC devices

Ultimately the aim of this chapter was to design and make ssDSC devices using the equipment here at Swansea university and then use these devices to test novel materials made from our group and our collaborators. To this end we have tested bespoke BODIPY dyes (JMS063 and JMS069) synthesised by Glasgow University as well as triphenylamine dye D35 (supplied by Dyenamo). Devices have also been made with a mesoporous ziroconia layer rather than TiO_2 as well as attempted to be the first to design a spiro-OMeTAD based ssDSC sensitised with two co-sensitised dyes.

4.2.5.6.1 Testing bespoke BODIPY dyes (JMS062 and JMS069)

"Bodipy" dyes an abbreviation of boron-dipyrromethene have emerged as promising sensitisers for DSC devices due to their easy structural modification, strong light

absorption and photostability.[307] There are many variations of Bodipy dyes[307–310] however they all share the same core structure/chromophore see **Figure 4.16**

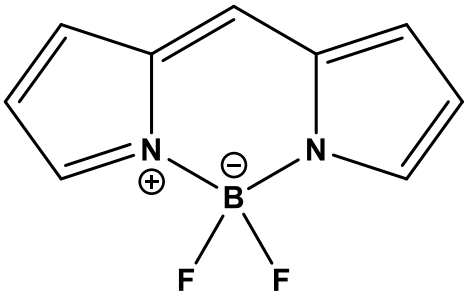

Figure 4.16 – Structure of the Bodipy fluoropldiaza-s-indacene

Most Bodipy dyes have strong absorptions between 500 and 600 nm. However, the performances of Bodipy dyes leave a lot to be desired with most failing to break the 2 % barrier.[308,309] This is most likely down to poor electron injection and high recombination as the high molar absorption co-efficient should give rise to much better performances in DSC devices.[311,312] Therefore, there has been much research devoted to designing new BODIPY dyes in order to reduce aggregation[311,312] and increase directionality[313,314] without compromising on their high molar absorption co-efficient. Despite this there have been a couple of high performing Bodipy dyes with the highest recorded performance with η = 6.06 % reported by Kubo *et al.*[315] This increase in performance was attributed to strong light harvesting originating from thienyl-cyanoacrylic acid anchors and the absence of strong donor units (such as triarylamine and carbazole) giving rise to a high J_{sc} (19.02 mA/cm^{-2}).

After studying this paper, the Cooke group at Glasgow University decided to synthesise two Bodipy dyes (JMS062 and JMS069), one with triarylamine and the other with 10-(2-ethylhexyl)-10H-phenothiazine group to study the effects of donor group at the α-position of Bodipy dyes. The chemical structures of JMS062 and JMS069 can be seen in **Figure 4.17**.

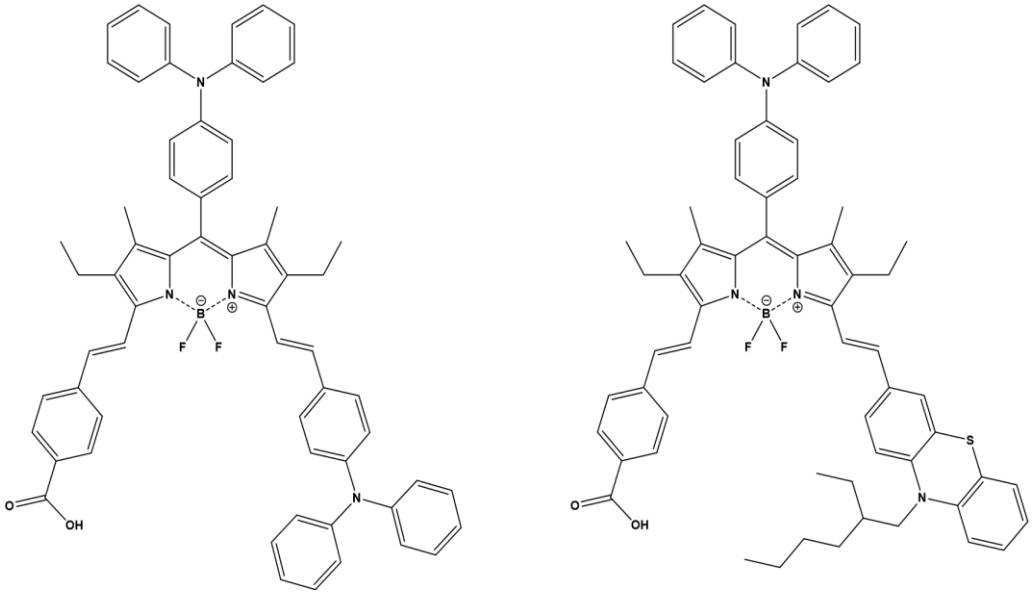

Figure 4.18 - Chemical structures of BODIPY dyes tested in this thesis JMS062 (left) and JMS069 (right)

The dyes were first tested in liquid DSC devices achieving η = 0.96 % and η = 1.41 % for JMS062 and JMS069 respectively. After which this these dyes were tested in the ssDSC devices developed in this chapter. The performances of these devices can be seen in **Figure 4.18** and **Table 4.11**.

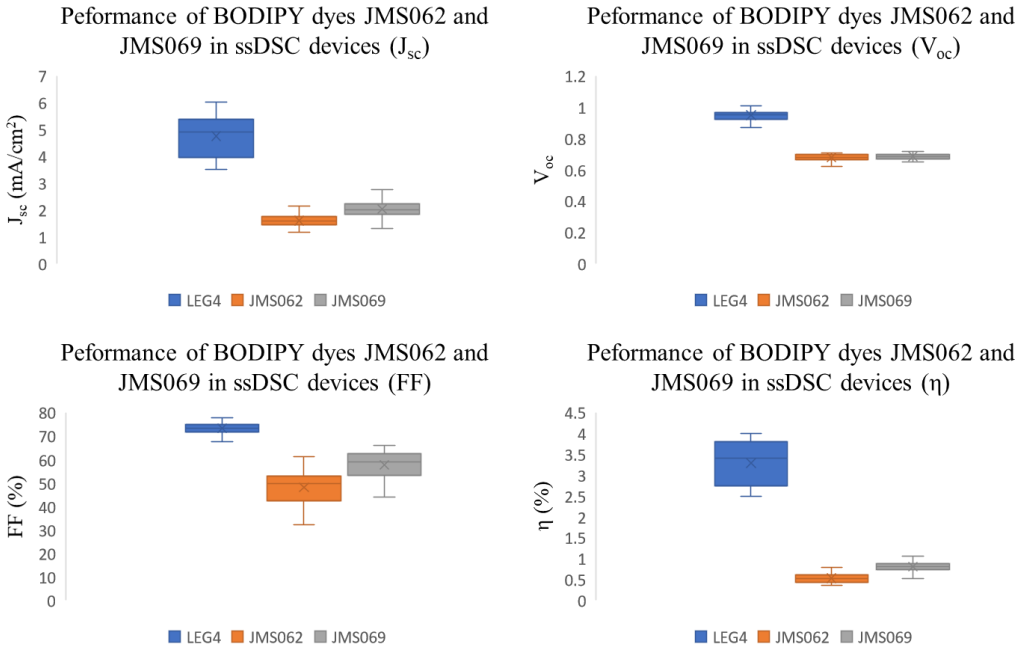

Figure 4.17 - Performance of ssDSC devices made using LEG4, JMS062 and JMS069. J_{sc} (top left), V_{oc} (top right), FF (bottom left) and η (bottom right).

Table 4.12 – Performance of novel BODIPY dyes in ssDSC devices

Dye	V_{oc}	J_{sc} (mA/cm^2)	FF (%)	η (%)	"Hero" cells
LEG4 (ssDSC)	0.95	4.75	73	3.30	4.00
JMS062 (ssDSC)	0.68	1.61	48	0.53	0.74
JMS069 (ssDSC)	0.69	2.03	58	0.81	1.17
JMS062 (DSC)	0.64	2.32	65	0.96	
JMS069 (DSC)	0.38	7.40	50	1.41	

[a]Data are averages of 24 data points. Three different ssDSC devices with 8 pixels per device.

Bodipy dyes JMS062 and JMS069 achieved η = 0.74 % and 1.2 % respectively. These performances are extremely promising as they are only slightly lower than those achieved in the liquid DSC devices. The V_{oc} of JMS062 and JMS069 were much higher than the equivalent liquid devices (0.68 and 0.69 V compared to 0.64 and 0.38 V) which was what was hoped for by better alignment of the energy levels in the devices. However, the J_{sc} of the ssDSC devices were significantly lower than those of the liquid devices (1.61 and 2.03 mA/cm^2 compared to 2.32 and 7.40 mA/cm^2). This drop in J_{sc} can be most likely attributed to dye loading. The liquid devices were prepared by pumping the Bodipy dyes through the device cavity. Pump dyeing can increase dye loading by forming the kinetic dye loading product rather than the thermodynamic product. Unfortunately, the architecture of the ssDSC devices doesn't allow for pump dyeing as there is no cavity, therefore it is limited to just passive dyeing which just forms the thermodynamic product.

During the ssDSC manufacturing it was also noticed that some of the dye desorbed during the HTM deposition step. Though this is mildly seen in other dyes such as LEG4 and D35, it was far more drastic in the devices made with JMS062 and JMS069. This loss of dye would also reduce the number of electrons injected into the TiO_2 and therefore have a direct impact on J_{sc}. The effect of dye desorption during HTM deposition can be seen in **Figure 4.19.**

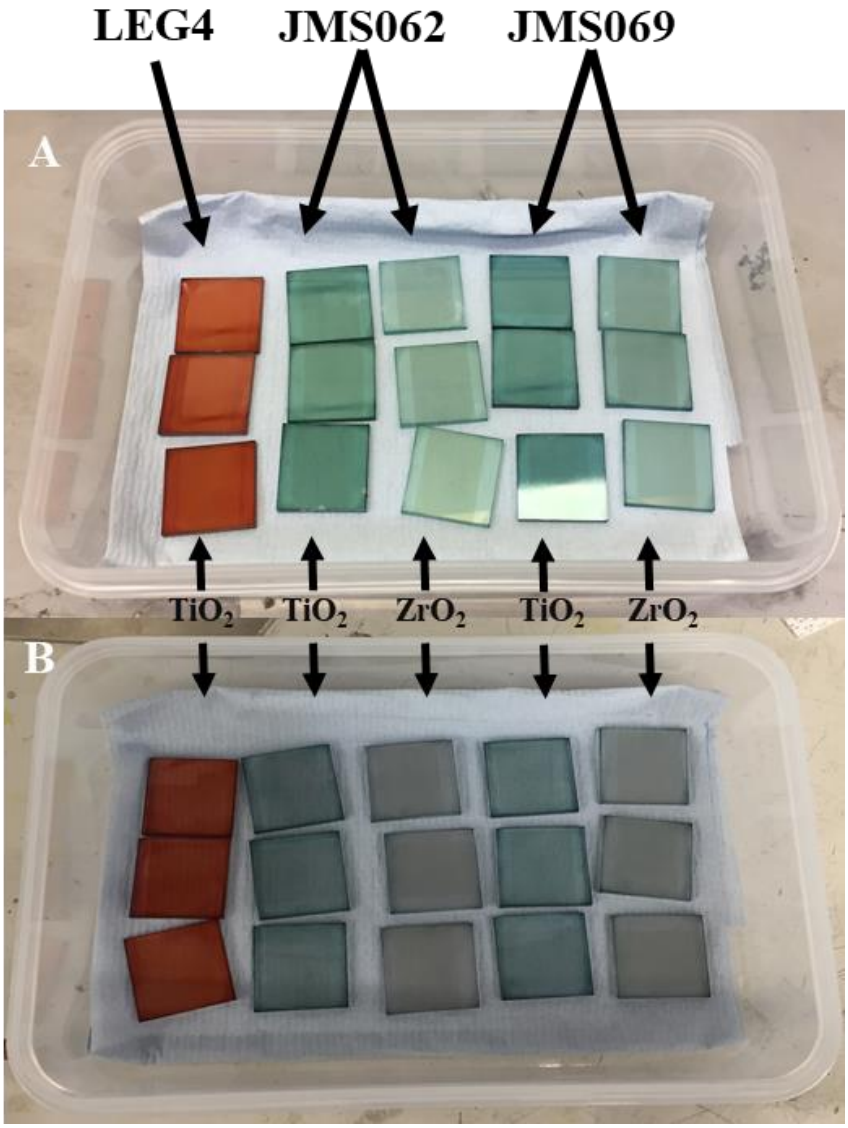

Figure 4.19 - ssDSC devices dyed with LEG4 and Bodipy dyes before (A) and after (B) HTM deposition

The dye desorption is likely down to poor adsorption of the Bodipy dyes or the basic pH of the HTM solution. Due to the fact this is not observed as much with devices made with other it is likely a combination of both. After seeing the dye desorption effect on TiO_2, ZrO_2 was investigated to see if the same thing happened.

4.2.5.6.2 *Testing mesoporous Zirconia as a dye absorbing layer*

Zirconia (ZrO_2) is a promising alternative to TiO_2 as a wide band-gap semiconductor for use in DSC devices.[316] ZrO_2 has not been as extensively investigated as TiO_2 in DSC devices due to its lower performance. However, it has several unique properties such as a high refractive index (n = 2.17)[317], wide optical band-gap (~ 6 eV)[318], low absorption and dispersion in the visible and NIR spectral region which make it a viable alternative to TiO_2.[316]

The researchers in the Cooke group at Glasgow University used TiO_2 and ZrO_2 photoelectrodes to measure the electron injection of dyes JMS062 and JMS069 (not yet published). The initial experiment used ZrO_2 as an insulator to measure against TiO_2. However, they found JMS062 actually injected electrons better into ZrO_2 than TiO_2. Therefore, it was decided to test if this translated into better ssDSC device performance.

In order to test this ssDSC devices were made using JMS062 and JMS069 deposited on TiO_2 and ZrO_2 and their performances were compared. The results of this experiment can be seen in **Figure 4.20** and **Table 4.12**

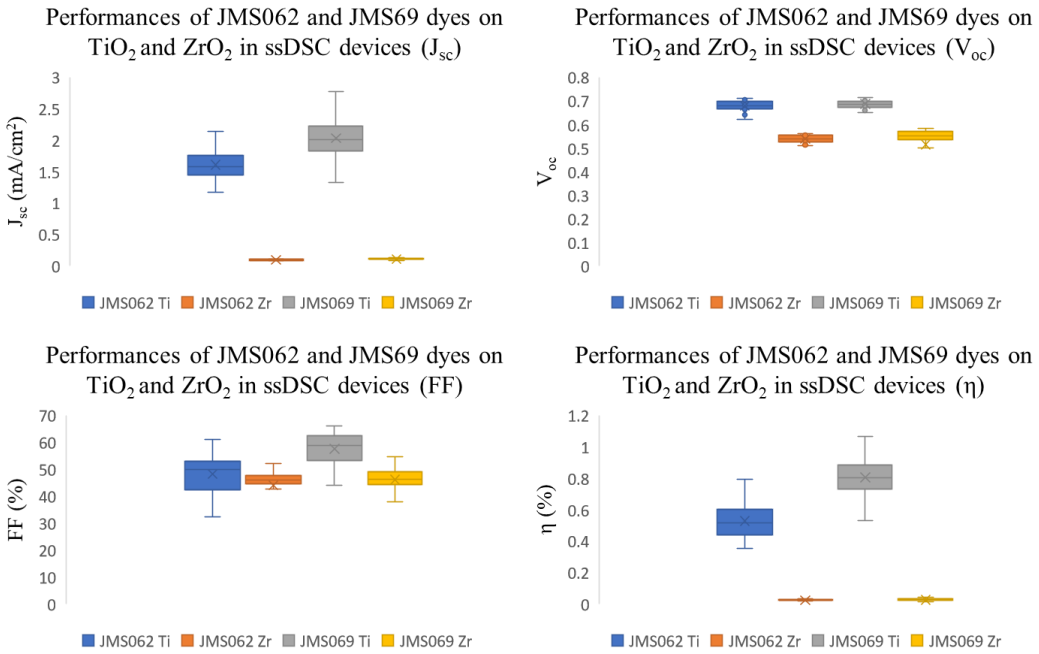

Figure 4.20 - Performance of ssDSC devices made using JMS062 and JMS069 on both TiO_2 and ZrO_2. J_{sc} (top left), V_{oc} (top right), FF (bottom left) and η (bottom right).

Table 4.13 - Performance of novel BODIPY dyes on TiO_2 and ZrO_2 in ssDSC devices

Dye/ Ti or Zr	V_{oc}	J_{sc} (mA/cm^2)	FF (%)	η (%)	"Hero" cells η (%)
JMS062/ Ti	0.68	1.61	48	0.53	0.74
JMS062/ Zr	0.54	0.10	48	0.02	0.03
JMS069/ Ti	0.69	2.03	58	0.81	1.17
JMS069/ Zr	0.51	0.11	44	0.03	0.04

[a]Data are averages of 24 data points. Three different ssDSC devices with 8 pixels per device.

Unfortunately using ZrO_2 did not create better performing devices. In fact, the ZrO_2 devices failed to work at all. During the HTM deposition Bodipy dyes JMS062 and JMS069 were almost entirely desorbed from the surface and therefore the J_{sc} dropped from 1.61 and 2.03 mA/cm^2 in the TiO_2 devices to 0.10 and 0.11 mA/cm^2 for the ZrO_2 devices. The effect of dye desorption during HTM deposition can be seen in **Figure 4.19**.

4.2.5.7 Lifetime testing of ssDSC devices

It's well known liquid DSC devices generally give better performances a couple of days after manufacture. When the devices are first dyed the dyes organise themselves into a kinetically driven snapshot. Overtime the dyes can rearrange themselves into the thermodynamically lowest energy conformation which is better for J_{sc} and therefore better for performance. ssDSC devices were made, tested and then tested again after 48 hours to observe any change in performance. The results of this experiment can be seen in **Figure 4.21** and **Table 4.13**.

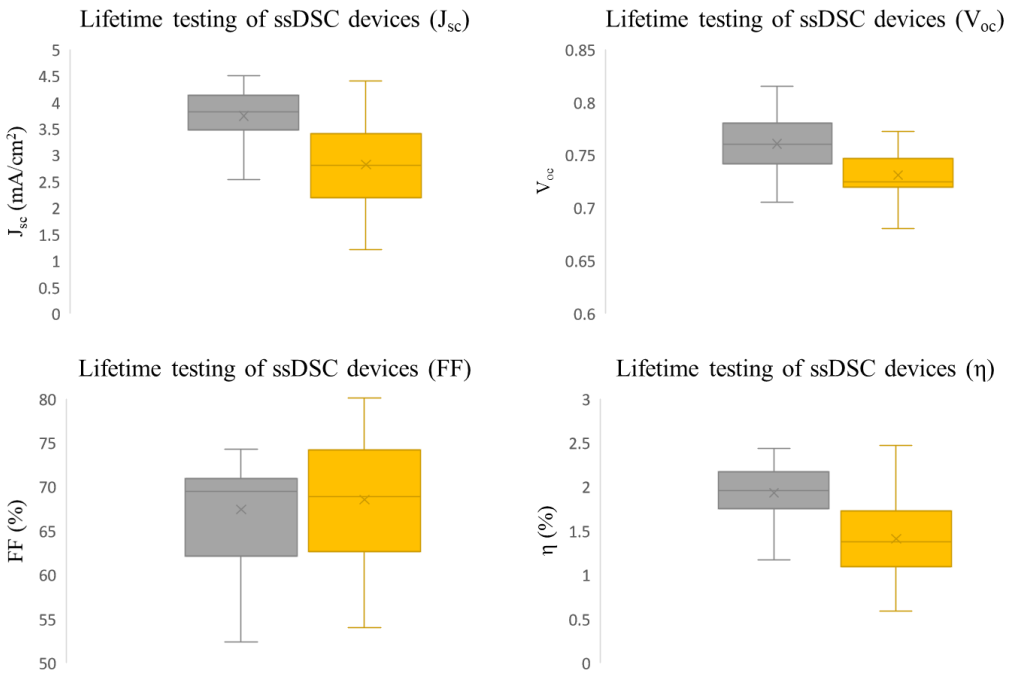

Figure 4.21 - Performance of ssDSC device Nº 3 at 0 (grey) and 48 hours (yellow) after manufacture. J_{sc} (top left), V_{oc} (top right), FF (bottom left) and η (bottom right).

Table 4.14 - Performance of ssDSC device 0 and 48 hours after manufacture

Device (n^o)	V_{oc}	J_{sc} (mA/cm^2)	FF (%)	η (%)	"Hero" cells η (%)
1 (0 h)	0.76	3.57	67	1.83	2.34
1 (48 h)	0.73	3.30	69	1.67	2.30
2 (0 h)	0.76	3.74	67	1.93	2.43
2 (48 h)	0.73	2.82	69	1.41	2.47
3 (0 h)	0.75	3.17	66	1.57	1.97
3 (48 h)	0.72	2.43	67	1.16	1.91

[a]Data are averages of 24 data points. Three different ssDSC devices with 8 pixels per device.

Looking at the data, it appears that the increase in performance observed in liquid DSC devices after 48 hours is not observed in ssDSC devices. Only one pixel of 1 device (N^o 2) increased in performance after 24 hours. Therefore, this is likely an anomaly. The only consistent factor to increase was the FF. However, this is offset by a small decrease in V_{oc} (~ 30 mV) and a large decrease in J_{sc} (20 – 92 mA/ cm^2). This decrease in J_{sc} is most likely down to degradation of the dye through aging. A similar effect will likely happen in liquid DSC devices. However, the liquid electrolyte in DSC devices will absorb and desorb dye molecules allowing for the thermodynamic product to form. The large increase of this effect will probably offset the losses from dye degradation. ssDSC devices do not have a liquid electrolyte and therefore the dye molecules are unable to rearrange themselves on the TiO_2 surface, so only the kinetic product can be formed.

5 Anhydrides

5.1 Introduction

The need to control dye uptake has been a major research focus in the area of DSC technology; especially the need to extend spectral response by co-sensitisation which requires even greater control of the sorption of multiple dyes. The overall aim here is to control additional dye uptake because this means more light harvested, more electrons injected into the conduction band of the TiO_2 and higher J_{sc} which directly relates to the efficiency of a device. However, this is not without its difficulties. As discussed previously, having more dye is advantageous if it is bonded directly to the TiO_2, but more dye often means that the top layer of dye absorbs light but is unable to make use of the energy as there is nowhere to inject the electron. In this scenario, device efficiencies are often reduced as there is less light available for the dye on the TiO_2 surface.

Attempts to solve this have led to breakthroughs such as co-sensitising two or more dyes.[165] Since most dyes use an acid linker, they all bind on the same sites. Therefore, having multiple dyes just means they are competing for the same amount of space. If all sites are occupied, then in theory a device with a single dye will not absorb more photons than a device with multiple dyes. Despite this, most co-sensitised devices do see an improvement in efficiency. It is likely that not all absorption sites are taken during the initial dyeing process, so when a new dye is added it does not have to compete for space.

To increase light absorption, there is a need to find a way to bind more dye directly to the TiO_2. Most current dyes use an acid moiety to bind to TiO_2. The acid moiety is negative and therefore needs to bind to a positive site, this could be the titanium atoms however there are also OH bonds present at the TiO_2 surface which could also act as a potential binding site (to form an ester). This means most of the negative sites (such as oxygen atoms) are theoretically free and unused. Considering there are twice as many oxygen atoms as titanium atoms in TiO_2 this is a huge waste (see **Figure 5.1**).

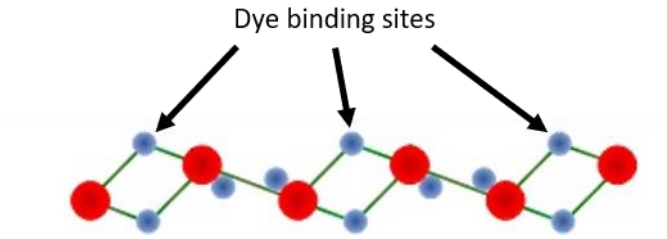

Figure 5.1 - TiO_2, The red spheres denote oxygen and blue spheres denote titanium atoms.

In reality a lot of the negative sites will be taken up with counter ions from the dyes themselves such as protons and tetrabutylammonium ions. However, as the ionic bonds between these ions and the surface are relatively weak, they could be replaced with more strongly bound dyes (bound through covalent bonding). Other sites will be taken up with co-adsorbents in the electrolyte (for instance tertbutylpyridine, Li^+). Despite this it is still very likely to have many free negative sites like it has free positive sites. Just like a negatively charged dye is needed to bind to positive sites, a dye with a positively charged anchor is required to bind to negative sites.

To the best of my knowledge there has only ever been a handful of dye synthesised with a positive anchor.[319,320] The lack of publications for positively charged dyes is most likely down to their low J_{sc} values due to unfavourable dye sorption kinetics. Despite decreased performances, positively charged dyes absorb to the TiO_2 surface through different sites compared to their negatively charged counterparts. Therefore, positively and negatively charged dyes could be used in tandem to co-sensitise DSC devices whilst minimising absorption competition. Positively charged dyes show comparable external quantum efficiencies to cyanoacrylic acid containing dyes (> 80 %) and exhibit significant robustness which would improve the overall stability of the device.[319,320]

This work reports a new approach to chemisorbing carboxylate-anchored dyes onto TiO_2 surfaces using anhydride precursor dyes, to adsorb a negatively charged and positively charged dyes simultaneously.

5.1.1 Anhydrides

Acid anhydrides are molecules with the general formula RC(=O)OC(=O)R or acyl-O-acyl see **Figure 5.2**.

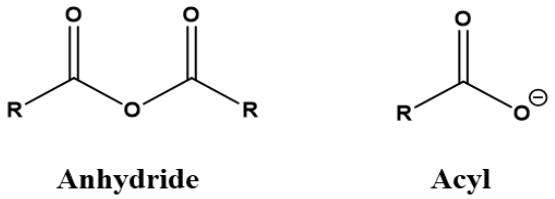

Figure 5.2 - General structure for Anhydrides (left) and Acyl groups (right)

The name anhydride means "without water" and comes from the very literal interpretation on how these molecules are formed, when the two acids react water is removed from the anhydride structure and is formed as a by-product (see **Figure 5.3**).

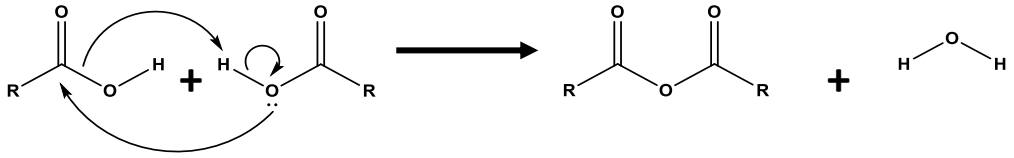

Figure 5.3 - General scheme for the formation of acid anhydrides

The bonds that bind oxygen to the two carbonyls is extremely weak (13.4 kcal for hydrolysis of dimethyl-maleic anhydride)[321] and easily polarisable. Anhydrides are naturally found in the human body as adenosine triphosphate (ATP). The body stores and releases energy by forming and breaking phosphoanhydride bonds. A lot of medicines also utilise poly(anhydride)s in drug delivery.[322] Initially the long chain polymer is insoluble in water however, after the anhydride bond is cleaved the monomers become water soluble and can therefore be absorbed into the body.[322] This chapter employs the anhydride bond to co-sensitise DSC devices in a single process.

5.1.2 Co-sensitisation

Like in a single dye system there is a need to understand how the dyes can self-assemble at the metal oxide surface in a co-sensitised system. Understanding dye loading and surface organisation are absolute essential in a multi-dye system (See **Figure 5.4**).[163]

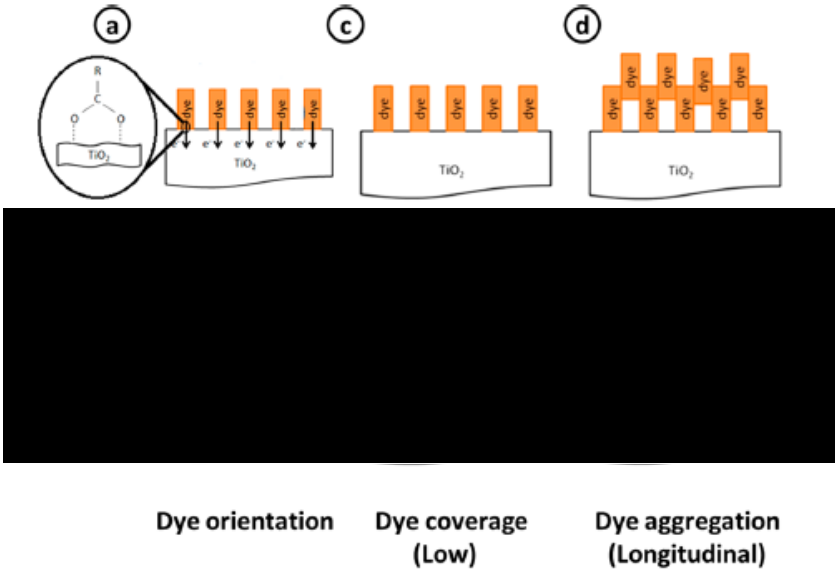

Figure 5.4 - Characteristics of the dye-TiO_2 interfacial structure, demonstrating various outcomes of dye loading that influence the function of a DSC working electrode.[163]

At the moment the largest challenges with co-sensitisation are dye loading (undesirable dye/ dye interaction and electrons quenching)[323–326] and dye processing.

For example, co-sensitisation of different dyes can be difficult, as partition coefficient (K_d) and molar extinction coefficient (ε) can vary enormously between dyes. So, you can have a highly adsorbing dye with a low ε and a less adsorbing dye with a high ε; how do you get the exact dye ratio on the surface that you want?

Siegers *et al.*[327,328] recently demonstrated the use of Förster resonance energy transfer between attached dye molecules (with an excitation transfer efficiency > 85 %). Siegers showed that when two dyes are spatially close, and their optical absorption and emission spectra overlap and electron transfer can occur. Though in Siegers case this electron transfer had a positive on device performance, it sometimes can be detrimental and therefore needs to be carefully controlled.[327,328]

In a co-sensitised system one dye is going to bind preferentially over the other (depending on their functional groups) making it very difficult to increase the loading of the lower K_d dye.

Optimising the spectral response of the dyes during the co-sensitisation process is not as simple as mixing two or more dyes together and expecting an increase in J_{sc}. For

instance if a Ru-bipy dye was co-sensitised with any of the half-squaraines synthesised by Holliman *et al.* [123] only a small improvement would be observed. Both the Ru-bipy and the half-squaraine dyes absorb between 400 and 650 nm and would therefore compete for the same photons. Whereas if a Ru-bipy dye was co-sensitised with a full squaraine dye the efficiency of the resulting device should be higher than a device with just a single dye. This was proven by Singh *et al.*[329] Singh co-sensitised squaraines dyes SPSQ1 and SPSQ2 with ruthenium-based dye N3. As the spectral response of the dyes complemented each other they gave the same effect as a single panchromatic dye, allowing for the absorption of more photons and producing a higher J_{sc} and therefore a higher η.

The third factor to consider when co-sensitising (after self-assembly and absorbance) is the molecular orbitals of the dyes. The HOMO/LUMO energy levels (of the different dyes) need to differ sufficiently (> 0.2 eV).[323–325,330] This difference should inhibit electronic interactions between the dyes, reducing recombination. Although, some papers claim that this interaction can have a positive influence on device efficiency.[331,332] Arakawa *et al.*[331] synthesised a series of benzothiazole merocyanine dyes with various alkyl chain lengths. The dyes synthesised with longer chain lengths showed increased electronic interaction (aggregation), while those with shorter chains showed a decrease in electronic interaction. The electronic interaction between the dyes broadened their absorption and increased IPCE.[331]

Dye orientation is also important for co-sensitisation. Qin *et al.*[333] showed this for squaraine dyes. Qin changed the trans-squaraine SQ1 dye into the cis-squaraine HSQ1 dye and then tested the dyes in two separated co-sensitised devices (device 1 = N3/HSQ1, device 2 = N3/SQ1). Qin *et al.* observed a significant improvement in device efficiency for the N3/HSQ1 (η = 8.14 %) combination over that of N3/SQ1(η = 5.90 %). This increase in performance for the cis-squaraine over the trans-squaraine shows that dye orientation is important. By converting SQ1 into HSQ1 Qin introduced bulky groups to the dye. The bulky groups of the cis-squaraine help decrease inter-molecular interactions between the dye molecules and reduce aggregation.[149] Qin also observed a red shift in the dye absorbance however this is more likely attributed to the vinyl dicyano unit[150] (See **Figure 5.5**)[4].

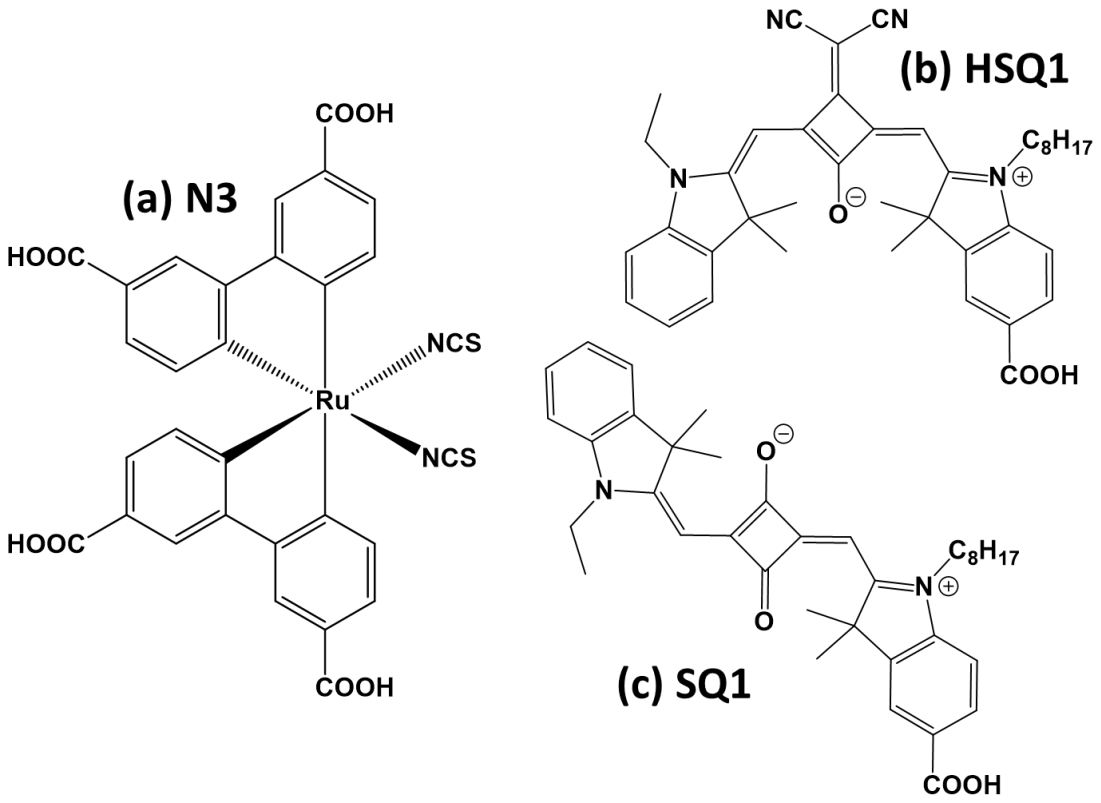

Figure 5.5 - Molecular structures of (a) N3, (b) HSQ1 and (c) SQ1. Reproduced with permission from [4]

For the first time two dyes have been bound through an anhydride bond as a novel method to co-sensitise DSC devices in a single process. Though the two dyes are chemically bonded through the anhydride unit, the bond breaks as it reaches the acidic TiO_2 surface to produce two oppositely charged units (see **Figure 5.6**).

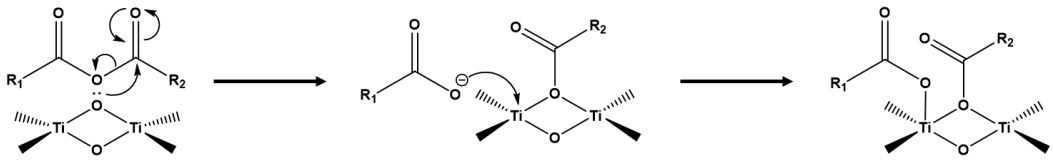

Figure 5.6 - General scheme to demonstrate the breakdown of an acid anhydride on a titania surface

This novel method of dye loading allows two dyes to chemisorb to TiO_2 through a single sorption process. This provides an alternative approach to control dye sorption kinetics, dye loading and surface organisation.

5.2 Results and discussion

5.2.1 Dye synthesis

The synthetic route used to produce the "yellow dye (**YD-Ac**) and the "yellow dye anhydride (**YD-An**)" used in this chapter are shown in **Scheme 5.1.**

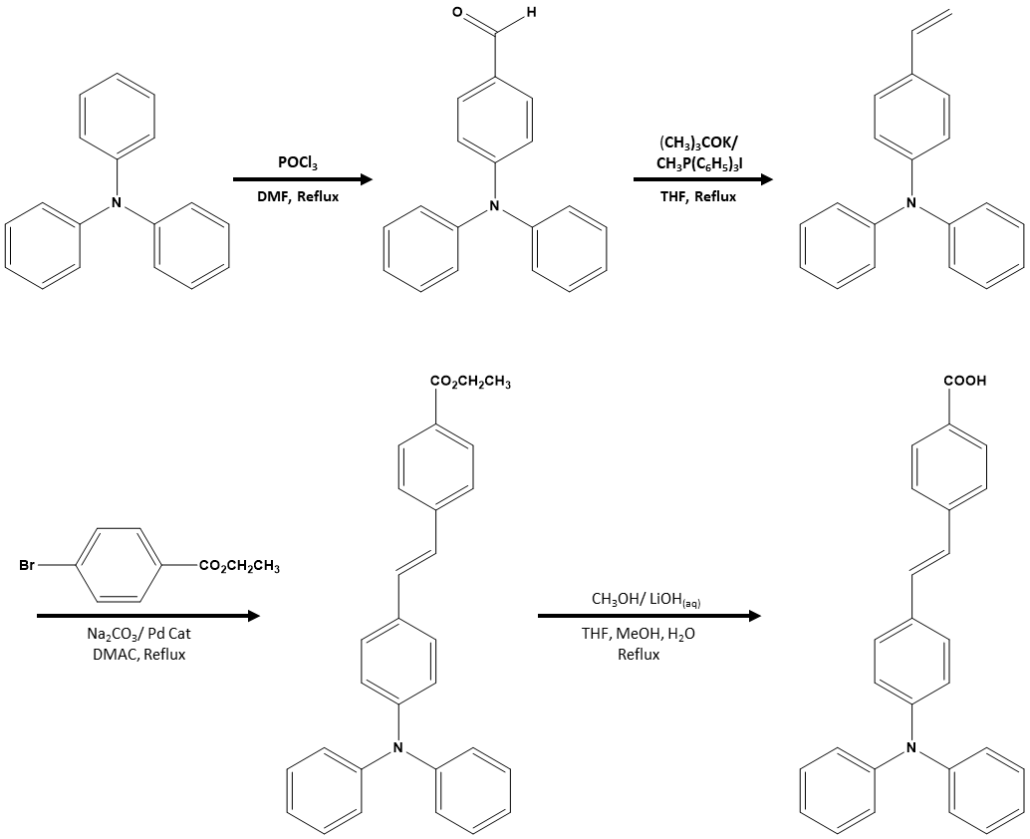

Scheme 5.1 - Synthetic scheme to produce "yellow dye" (**YD-Ac**)

Yellow dye has been previously synthesised by *Holliman et al.*[165] The first step is to convert triarylamine into (**YD-S1**) using phosphorous oxychloride and dimethylformamide (Vilsmeier-Haack formylation). To convert triarylamine into (**YD-S1**) a formylating agent is formed *in situ* from dimethylformamide and phosphorous oxychloride. An electrophilic substitution between phosphorous oxychloride and dimethylformamide forms a α-chloro amine, which is rapidly hydrolysed during work up to give the final aldehyde. The mechanism for this reaction can be seen in **Figure 5.7**.

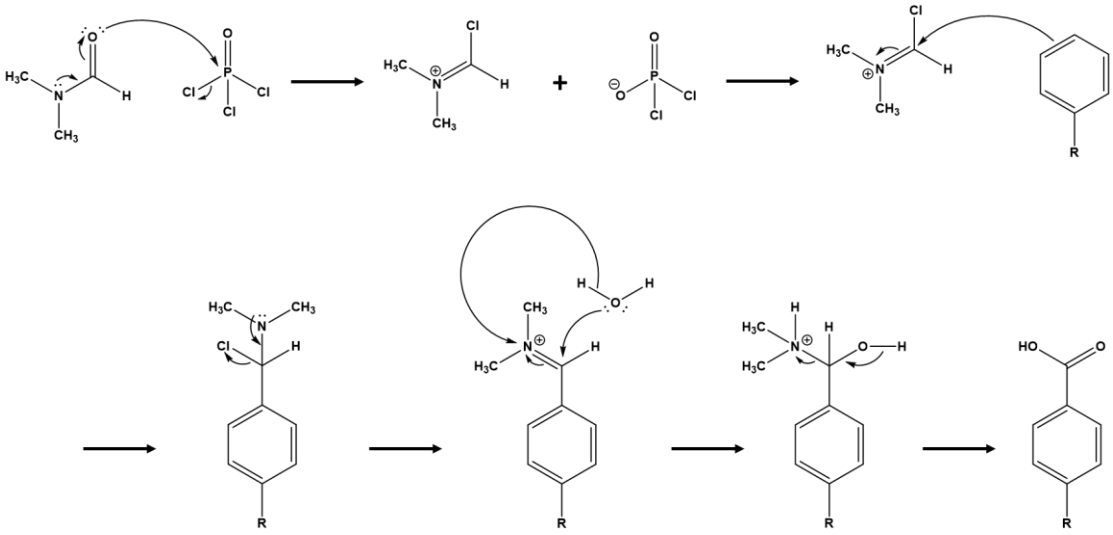

Figure 5.7 - Vilsmeier-Haack formylation mechanism

The next step in the synthesis of yellow dye is to convert the aldehyde group of 4-(N,N-diphenylamino)-benzaldehyde into an alkene via a Wittig reaction (see **Figure 5.8**).

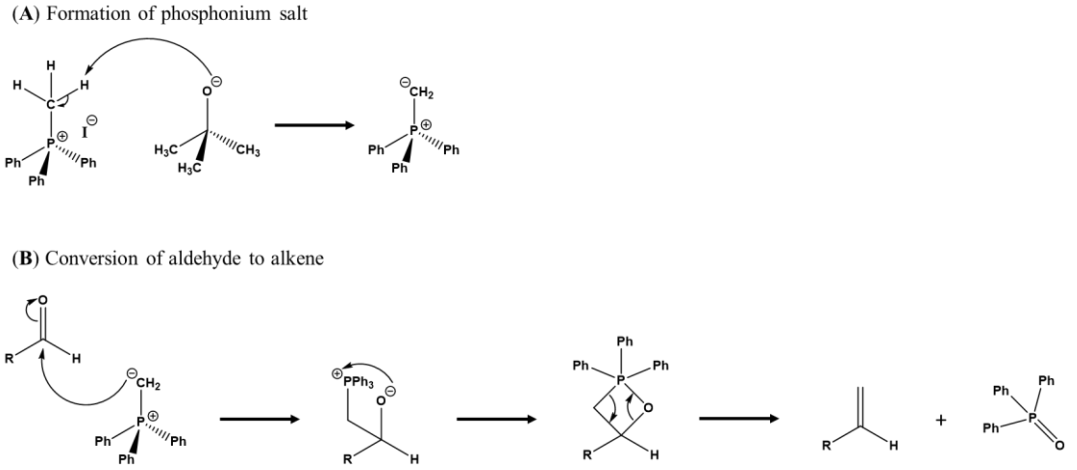

Figure 5.8 - Wittig reaction mechanism. (A): Formation of phosphonium salt, (B): Conversion of aldehyde to alkene

The Wittig reaction is a simple two pot synthesis reaction run under inert conditions (N_2) resulting in a relatively high yield (61.07 %). The first step is to form a phosphonium salt reacting methyltriphenylphosphonium iodide and potassium tert-butoxide. The second step using the phosphonium salt to convert 4-(N,N-diphenylamino)-benzaldehyde into an alkene (**YD2**). After the reaction the crude product can be purified by column chromatography to yield a white solid.

The following synthetic step involved coupling ethyl-4-bromobenzoate to diphenyl(4-vinyl)amine to produce the benzoic acid ester. In the first attempt to synthesise the

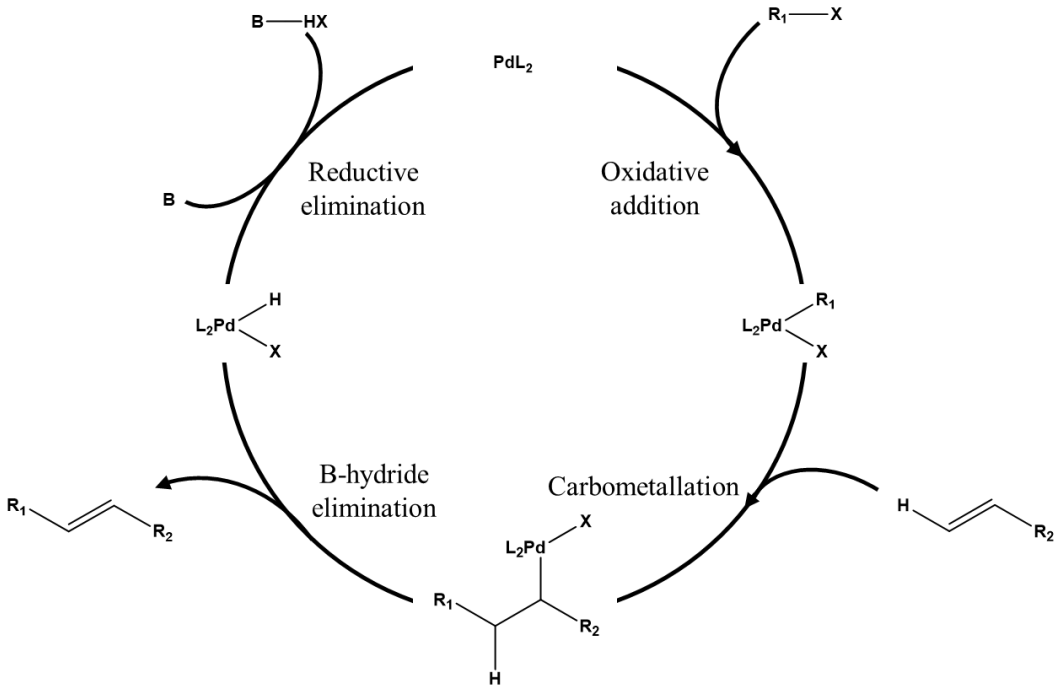

Figure 5.9 – Palladium-catalysed addition of vinyl group to organic halide or "Heck coupling"

product I directly followed the procedure given by *Holliman et al.*[165] Despite several attempts no product was obtained however, I was able to recover a large percentage of the diphenyl(4-vinyl)amine (between 30-50%). The large amount of unreacted diphenyl(4-vinyl)amine suggested that the quantities of the reagents mustn't have been correct. Therefore, I decided to modify the recipe given in the paper and use a procedure of my own, using the same ingredients but in different quantities.

After looking at the mechanism (**Figure 5.9**) for this reaction, I realised the only reason diphenyl(4-vinyl)amine wouldn't react would either be a lack of Pd catalyst or ethyl-4-bromobenzoate. Although I increased the amount of a couple of the materials the largest increase I made was to 4-bromobenzoate as the original recipe seemed extremely low for optimum reaction conditions. Holliman *et al.*[165] only used a molar ratio of 2.23:1, of diphenyl(4-vinyl)amine: 4-bromobenzoate. I decided this needed to be increased to a ratio of 1:1.5 to ensure all the diphenyl(4-vinyl)amine had reacted. After making these changes I was able to obtain the product, and after purification by column chromatography a yield of 20 % was achieved.

The final synthetic step to make yellow dye (**YD-Ac**) involved de-esterifying compound (**YD3**) using LiOH. HCl was then added to neutralise the solution and protonate the carboxylic acid unit. The mechanism to form (YD-Ac) can be seen in **Figure 5.10**.

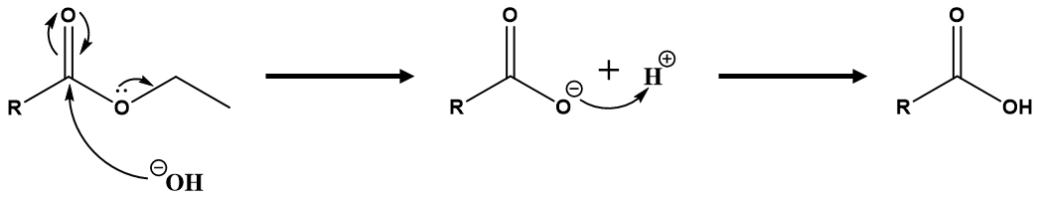

Figure 5.10 – Mechanism demonstrating the de-esterification of (**YD3**) to form (**YD-Ac**)

After removal of the solvent the pure product formed without need for further purification to yield 78 %.

After successfully synthesising yellow dye (**YD-Ac**) the next step was to chemically link two yellow dye molecules together through an anhydride bond. As yellow dye (**YD-Ac**) took a long time to synthesise, 4-bromobenzoic acid was used to practice the anhydride reaction as it was cheap to buy and readily available. Therefore two 4-bromobenzoic acid units were reacted together to form 4-bromobenzoic anhydride. The reaction scheme to form 4-bromobenzoic anhydride can be seen in **Figure 5.11**.

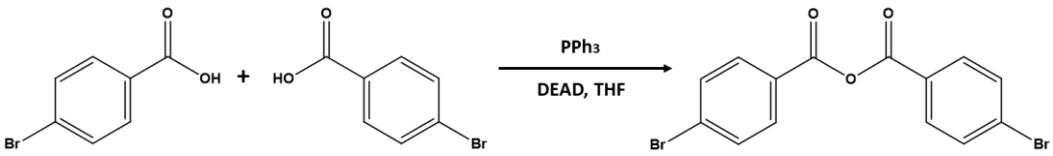

Figure 5.11 – Reaction scheme showing the synthesis of 4-bromobenzoic anhydride

4-bromobenzoic anhydride was initially synthesised following the Mitsunobu reaction. The Mitsunobu reaction is a two-pot synthesis utilising PPh_3 (triphenylphosphine) and DEAD (diethyl azodicarboxylate) over five steps, to form an anhydride bond between two acids (forming H_2O as a by-product). The Mitsunobu reaction mechanism can be seen in **Figure 5.12**.

1) Creating the Base

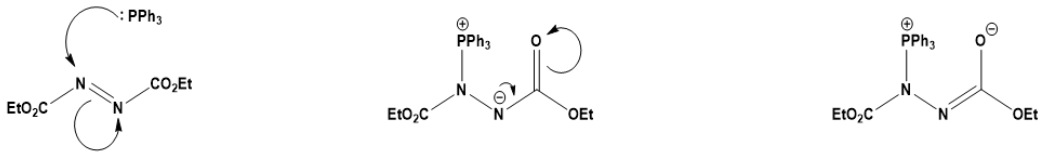

2) Deprotonation of Alcohol/Acid

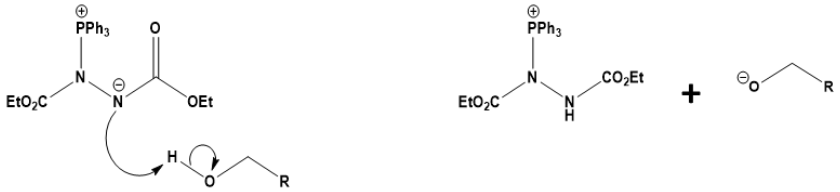

3) Oxygens affinity to Phosphorous

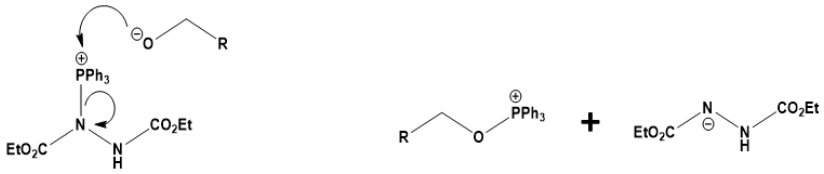

4) Deprotonation of the Nucleophile

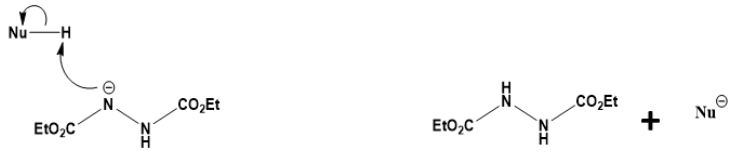

5) Forming the product

Figure 5.12 – Mistsunobu reaction mechanism.

After the reaction, the crude product underwent an aqueous work-up before being purified by column chromatography to yield a white solid (0.51 g, 53.12 %). This reaction had to be run under N_2 at 0 ^{o}C (using an ice bath). Though possible, these reaction conditions were difficult to achieve as I had recently moved labs with limited

N_2 access. Therefore, it was decided to search for an alternative reaction that did not require N_2. After searching through the literature, a new synthetic method was found utilising methanesulfonyl chloride and triethylamine which could be run without the use N_2. A proposed mechanism for the new reaction can be seen in **Figure 5.13**

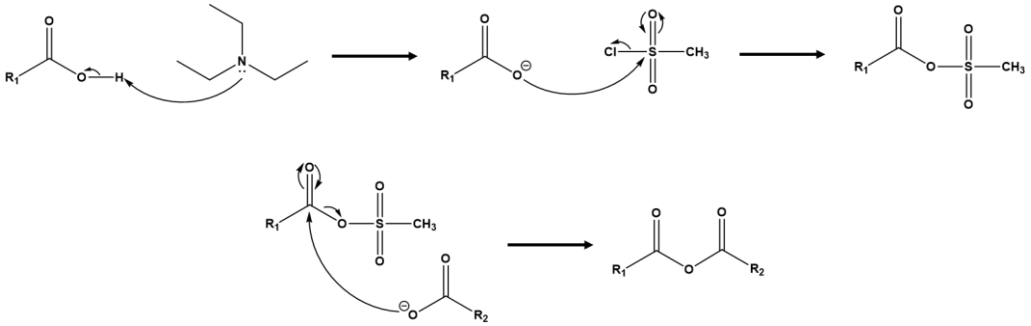

Figure 5.13 – Proposed mechanism to form anhydride bond using organic acid, methanesulfonyl chloride and triethylamine

Not only does this new synthesis not require an inert atmosphere (such as N_2) it also didn't require column chromatography afterwards improving the yield from 53.12 % (for the Mitsunobu method) to 78.95 % (for the new method). Both products were compared by ^{1}H NMR and although the second method showed a little impurity (< 0.1 %), it was much easier to synthesise and purify compared to the Mitsunobu method.

After optimising the reaction for 4-bromobenzoic acid, the new synthetic method was applied to (**YD-Ac**) to form yellow dye anhydride (**YD-An**). The thin layer chromatography (TLC) and NMR showed two products, therefore the crude material was purified using column chromatography (dichloromethane: petroleum ether, 1:1). Unfortunately, after the first synthesis the yield was extremely low (< 5 %) most likely down to the product breaking down on the silica column (due to the slight acidity of silica gel). Two common solutions for this are either to use a basic alumina column or to run a base down the column with the solvent mixture. It was decided to dissolve triethyl amine in the solvent system at a ratio of (1:1:0.01, dichloromethane: petroleum ether: triethylamine, v/v). From this method a yield of 15.23 % was achieved.

5.2.1.1 Analysis of yellow dye Vs yellow dye anhydride

As yellow dye (YD-Ac) and yellow dye anhydride (YD-An) are almost identical structurally (due to the symmetry of the molecules) and are therefore very difficult to tell apart. In order to confirm the product NMR (^{1}H and ^{13}C), ATR-IR, UV-Vis and mass spectrometry were run on both YD-Ac and YD-An.

5.2.1.1.1 ^{1}H and ^{13}C NMR analysis

As NMR is unable to differentiate between symmetrical protons and carbons both spectra are almost identical. In fact, the only difference is that YD-Ac has an additional proton bound to the carboxylic acid unit. However, this type of proton can't always be detected by NMR analysis. Because of this both NMR spectra look identical however, when the two spectra are overlaid a small shift is observed for YD-An (see **Figure 5.14**)

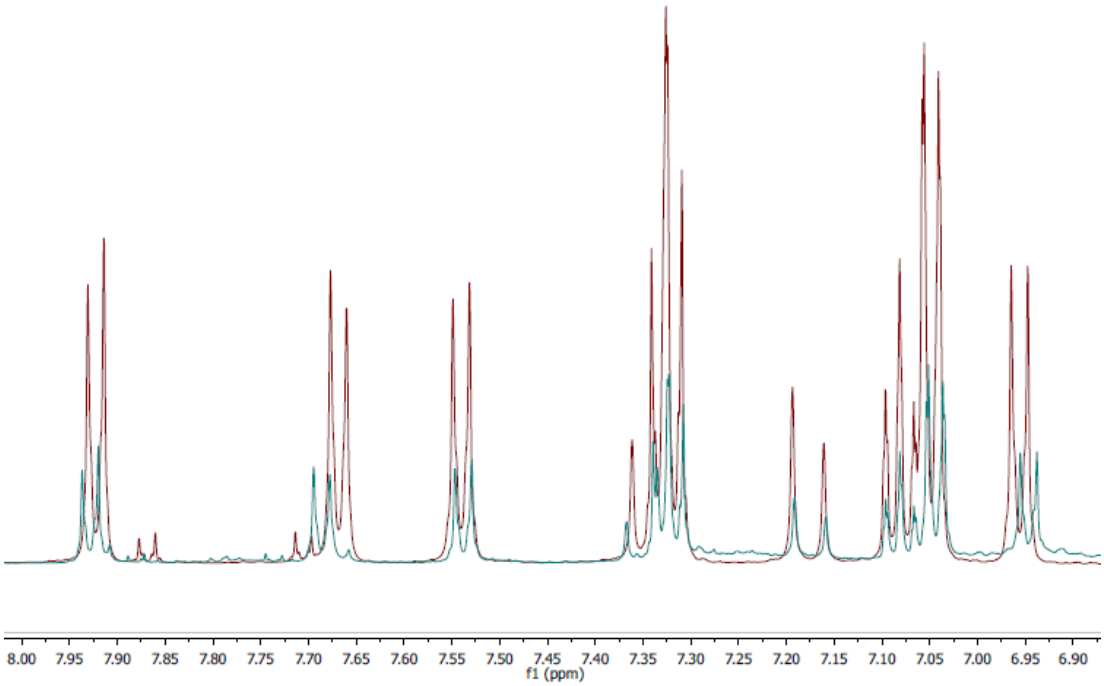

Figure 5.14 – Super imposed ^{1}H NMR spectra of YD-Ac (red) and YD-An (cyan)

5.2.1.1.2 ATR-IR

The overlaid ATR-IR spectra for **YD-Ac** and **YD-An** can be seen in **Figure 5.15**

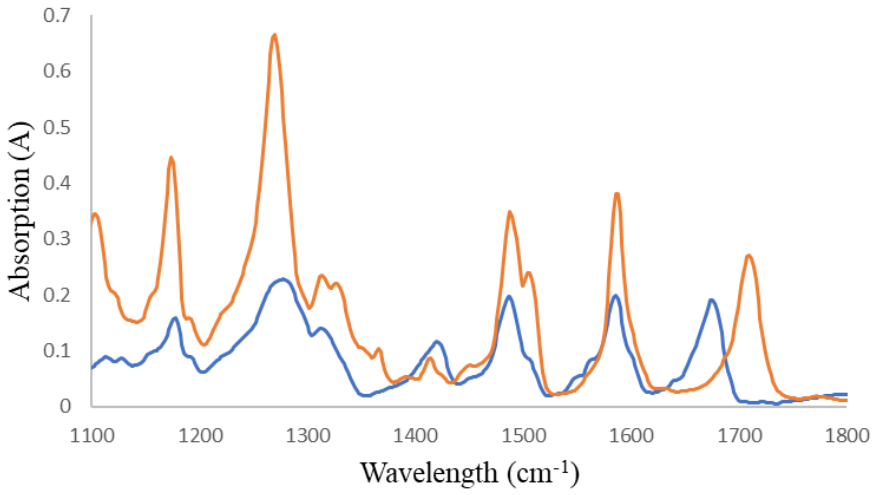

Figure 5.15 - ATR-IR spectra of YD-Ac (blue) and YD-An (orange) as a neat solid

The ATR-IR spectra show both YD-Ac and YD-An exhibit common bands at 1176 cm^{-1} (υOCO), 1274 cm^{-1} (υsym, COO), 1488 cm^{-1} (υasym, COO) and 1586 cm^{-1} (υC=C). These peaks are expected as all the functional groups are common to YD-Ac and YD-An. YD-Ac also shows a band at 1674 cm^{-1} (υHOC=O), YD-An also shows a similar peak however it is shifted to 1710 cm^{-1} (υ-OCOCO-).

5.2.1.1.3 UV-Vis

The overlaid UV-Vis spectra for YD-Ac and YD-An can be seen in **Figure 5.16**

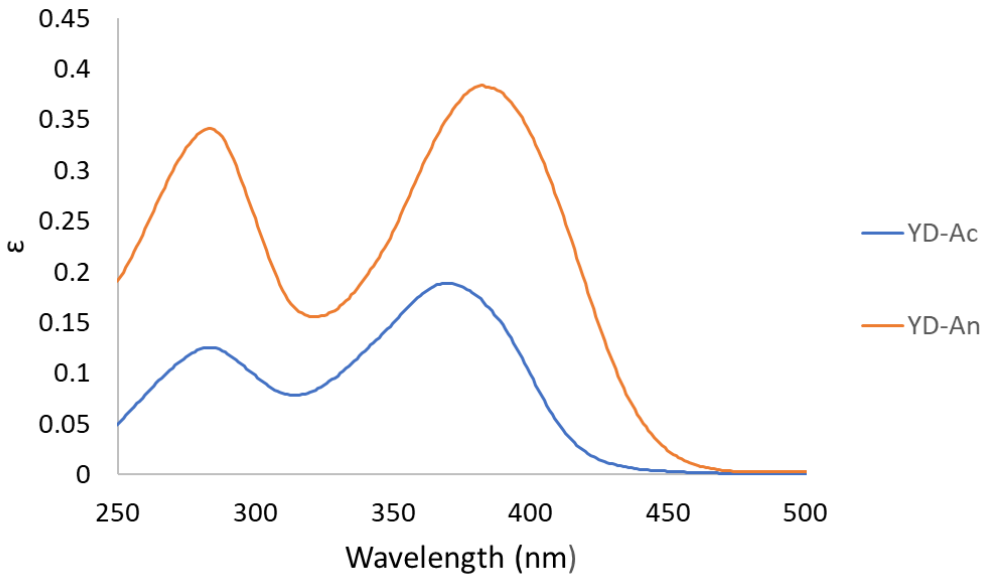

Figure 5.16 - UV-Vis spectra of YD-Ac (blue) and YD-An (orange). Concentration of dyes ~ 9 x 10^{-6} moldm^{-3}

The UV-vis data also show that the molar extinction coefficient of **YD-An** is ca. two times higher than **YD-1**. This is also observed in Chapter 1 for the esterified half-squaraine dyes where the free carboxylic acid is less coloured than the analogous ester. Thus, having another group bonded to the dye carboxylate (in this case another yellow dye) increases the probability of light absorption for what is otherwise a similar chromophore. The absorption of **YD-An** is red shifted c.a. 13 nm compared to **YD-Ac**.

5.2.2 Device testing

Table 5.1 - Summary of ssDSC device performance using YD-Ac and YD-An

Dye	V_{oc}	J_{sc} (mA/cm^2)	FF (%)	η (%)	"Hero" Cells (η %)
LEG4	0.95	4.76	73	3.29	4.00
YD-Ac	0.43	0.56	65	0.16	0.24
YD-An	0.47	0.09	60	0.02	0.03

[a]Data are averages of 24 data points. Three different ssDSC devices with 8 pixels per device.

Table 5.1 shows I-V data for ssDSC devices manufactured using **YD-Ac** and **YD-An**. Similar FF and V_{oc} are observed, though YD-An is ~ 40 mV higher. The largest

difference between the two dyes is J_{sc}. Both **YD-Ac** and **YD-An** show low J_{sc} values (0.56 and 0.09 respectively). These values and the colour of the electrodes after dying suggest poor dye uptake for both dyes however, this needs to be investigated further. YD-An uptake is likely lower than that of YD-Ac due the requirement that the anhydride bond break before absorption can take place. A potential way to overcome this poor dye uptake is to pump dye the ssDSC devices. Unfortunately, the architecture of ssDSC means they are currently limited to passive dying (see **chapter 6.2** for more details). However, liquid DSC devices could be made, and pump dyed to overcome the poor dye uptake. Holliman *et al.*[165] has done exactly this and shown its possible to achieve > 2 % efficiency with YD-Ac. Another way to overcome this could be to treat the TiO_2 with an acid, this would aid the breakage of the anhydride bond as it comes into contact with the TiO_2.

6 Conclusions and Future work

6.1 Chapter 3

Chapter 3 has shown that including S atoms within HfSQ dyes reduces DSC device efficiency. However, it is not for the reasons first thought. Initially it was believed that these dyes sit perpendicular to the TiO_2 surface. In this orientation having a sulphur in the HOMO of the dye would positively interact with the triiodide electrolyte and increase V_{oc} by reducing the overpotential required for dye regeneration. Having a sulphur atom in the LUMO would also interact with triiodide electrolyte. However, as it would lie close to the TiO_2 surface this would cause a greater number of oxidised electrolyte species near the TiO_2 surface increasing recombination.

ARXPS and computer modelling experiments have shown that these dyes do not sit perpendicular to the TiO_2 surface, but actually sit almost flat against the TiO_2 surface. This means no matter where the sulphur atom is in the dye structure it will be in close proximity to the TiO_2 surface and provide binding sites for oxidised species in the triiodide redox shuttle (I_2 or I_3^-). This increases the number of these species at the TiO_2 surface, increasing the amount of recombination leading to lower efficiencies.

As the HfSQ dyes lie flat not only could they increase recombination, but they will also take up more space on the TiO_2 surface. This will minimise the amount of dye that can absorb, reducing J_{sc} and therefore reducing the efficiency. However, what is not understood is how these dyes interact when new species of dyes enter the system. There have been several reports of co-sensitisation where the electrode is considered to be fully sensitised. However, when a new dye is introduced to the system it is able to still absorb.[161,165] This can often be put down to competition between the dyes. However, it could also be that the first dye in the system sits flat and then when a new dye is introduced it interacts with the flat dye causing it to move, freeing up space for the new dye (see **Figure 6.1**).

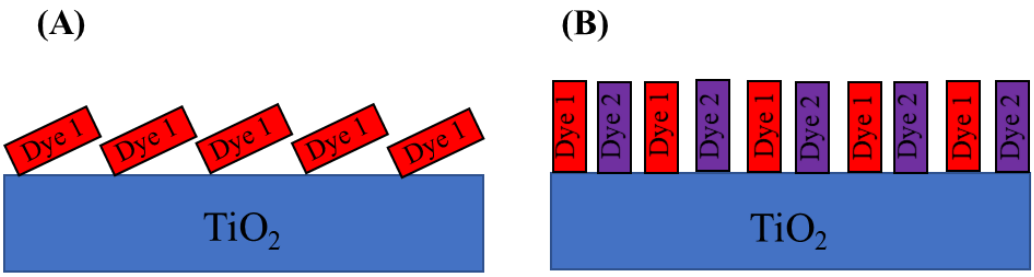

Figure 6.1 – TiO_2 sensitised with a single dye (A), Co-sensitised TiO_2 (B)

Nevertheless, this requires further investigation. Our team has previous published work on imaging dyes in DSC devices.[334] By applying this technique (alongside UV-Vis data) to analyse both the DSC device and the dye run-off (from pump dyeing), we should be able to determine if the dyes are competing for space or whether the dyes are "standing up" freeing up space for the new dye to sensitise to the TiO_2 surface.

6.2 Chapter 4

Chapter 4 demonstrates the development of ssDSC devices. By studying the effects of the "blocking" layer, thickness of mesoporous TiO_2, effect of $TiCl_4$ treatment, dyeing times and finally HTM thickness. These have all been assessed and optimised and η = 4.0 % has been achieved with LEG4 dye. The ssDSC have been used to assess novel dyes and various semi-conductor layers. A standard operating procedure (SOP) has been written and tested with staff and students so ssDSC research can continue to be developed here at Swansea University by myself and other researchers opening up a new avenue of research. This work has designed a method to reliably produce ssDSC devices here at Swansea University. The blocking layer, thickness/ properties of TiO_2, the effect of $TiCl_4$ treatment, dyeing time, HTM thickness and components have all been investigated. This data has then been used to manufacture ssDSC devices that are able achieve (η = 4.00 %). Novel dyes and pastes have been incorporated into these ssDSC devices and their performances tested.

Despite this there are still many other factors that need to be assessed in order to manufacture ssDSC devices that can compete with the very best published in the literature. The ssDSC devices in this chapter achieved 0.9 V. However, in the literature ssDSC devices made with LEG4 dye should be able to achieve 1.0 V. Optimising the HTM recipe should help to bridge this gap. Also, J_{sc} values in excess of 6.3 mA/cm^2 have been achieved. However, in the literature 10.8 mA/cm^2 have been reported. Higher J_{sc} devices can be achieved by co-sensitisation with other dyes. Pump dyeing

is a proven way to successfully co-sensitise DSC devices and increase performance. At the moment co-sensitisation in ssDSC devices is limited to passive dyeing the electrodes. If we could pump dye ssDSC devices, we could not only increase dye absorption but co-sensitise with two or more dyes to improve J_{sc}. As a result, from these data a pump dyeing tool is being designed that will create a cavity over the ssDSC devices to allow for pump dying. The first set of design schematics and testing of this tool can be seen in **Figure 6.2**. Using this new ssDSC pump dyeing system.

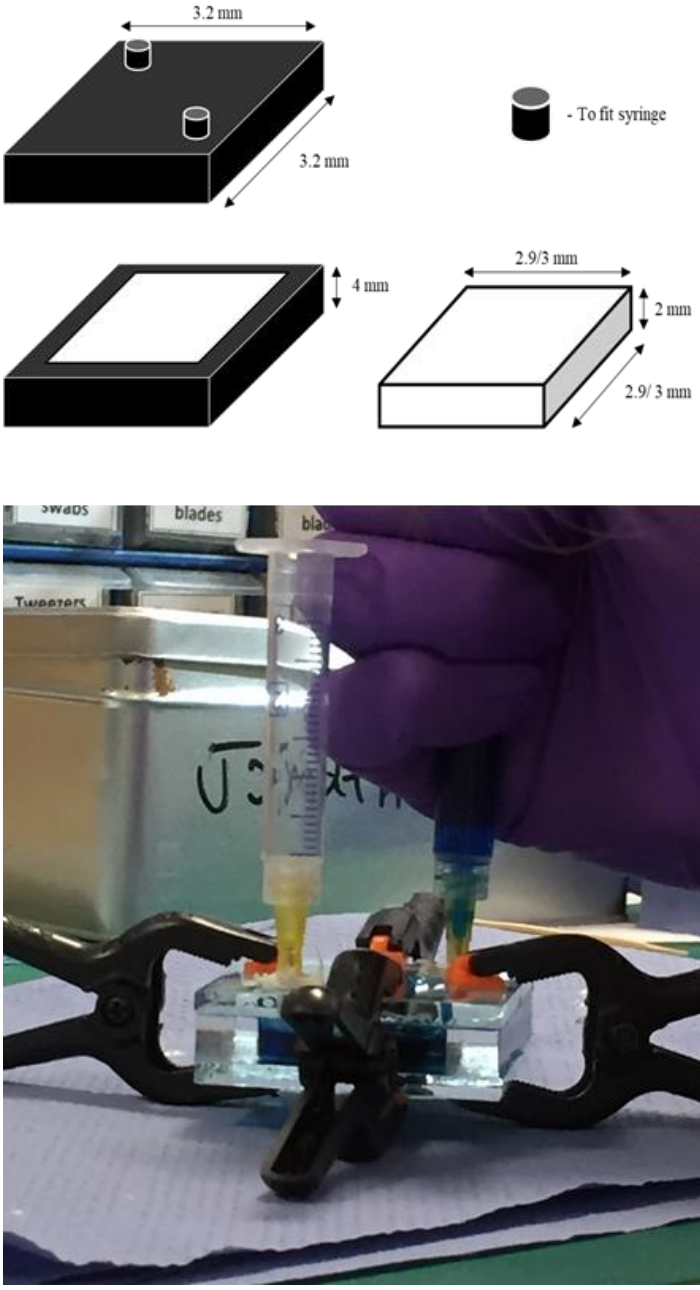

Figure 6.2 - ssDSC adaptor for pump dyeing. Schematic (top), actual (bottom).

6.3 Chapter 5

This chapter has reported a new approach to chemisorbing carboxylate-anchored dyes onto TiO_2 surfaces using anhydride precursor dyes. Both "yellow dye" (YD-Ac) and its anhydride (YD-An) have been synthesised, fully analysed and tested in ssDSC devices. Though efficiencies of the devices are currently low (0.16 and 0.02, YD-Ac and YD-An respectively). This is down to poor dye uptake as Holliman *et al.*[165] has proven its possible to achieve > 2 % efficiency with YD-Ac when pumped dyed. Pump dyeing has proven to have increased performance over identical devices that have been passively dyed. Where passive dyeing allows the dyes to self-assemble and form the kinetic product, the extra energy given to the system through pump dyeing allows dye molecules to form both kinetic and thermodynamic product

Using this method, it could be possible to link two different dyes/ adsorbents through an anhydride bond, co-sensitising a DSC device in a single process. An attempt has already been made at combining squaraine dye (SQ2) with Chenodeoxycholic acid (CDCA). Although mass spectrometry and TLC analysis suggested the product was synthesised it was incredibly difficult to separate by column chromatography. By synthesising two different molecules we vastly increase the number of potential impurities, see **Figure 6.3**

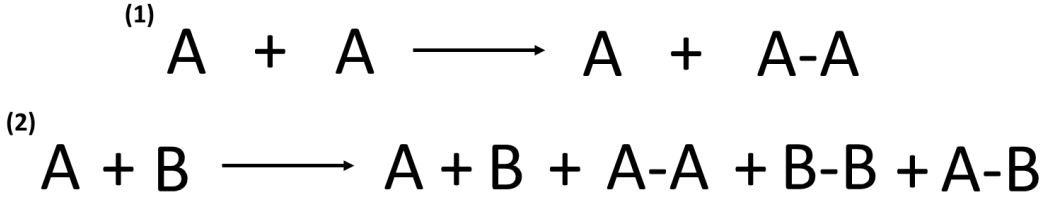

Figure 6.3 - Figure showing how the number of starting materials affects the number of products, (1): Two identical SM's can give up to two different products. (2): Two different SM's can give up to five different products

Not only does the number of impurities make the purification difficult but the solubility of the products also affects the difficulty of the purification. Both SQ2 and CDCA have very similar functional groups and therefore these two materials and any by-products will also have very similar solubilities. Rather than continuing with this difficult process it was decided to react SQ2 with stearic acid rather than CDCA.

Stearic acid is a carboxylic acid with an 18-carbon chain. The structures of SQ2-CDCA and SQ2-Stearic acid can be seen in **Figure 6.4**.

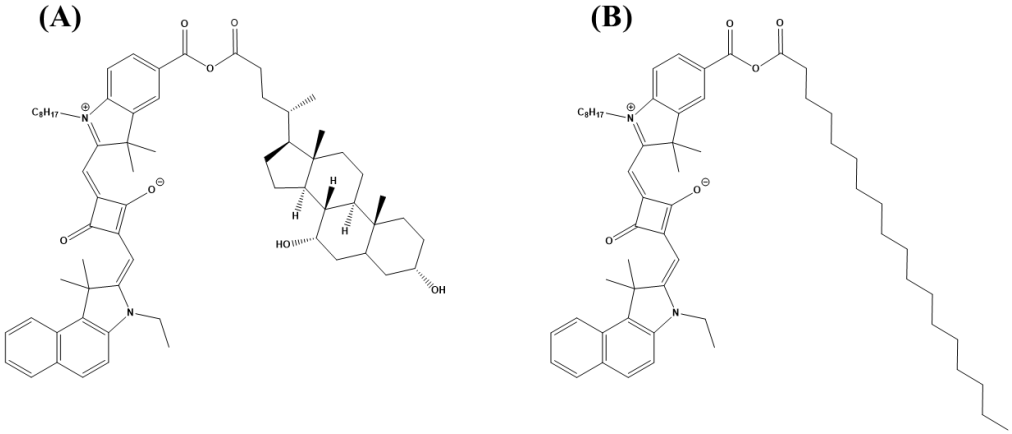

Figure 6.4 – Chemical structures of SQ2-CDCA (a) and SQ2-Stearic acid (B)

The vast difference in molecular structure between SQ2 and stearic acid should make the purification of the product much easier. The TLC plate for the crude product of SQ2-stearic can be seen in **Figure 6.5**

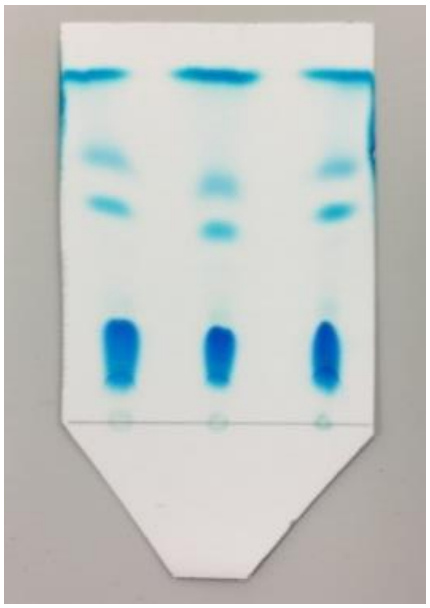

Figure 6.5 - TLC plate for the SQ2-stearic acid crude product (5 % MeOH in DCM)

Figure 6.5 shows the SQ2 containing products separated on a TLC plate from the reaction between SQ2 and stearic acid. The TLC was run in 5 % methanol (in dichloromethane. This mixture would likely move polar materials up to the top of the plate whilst the less polar materials stay nearer the bottom. Through a comparison TLC plate with the starting material, the bottom spot was identified as SQ2 dye. It's believed that one or both dots in the middle are the desired product (SQ2-stearic acid) and the very top spot would be (SQ2-SQ2). However, this is yet to be determined and further

analysis (high performance liquid chromatography and NMR) need to takes place before this can be confirmed.

7 References

1 K. Kakiage, Y. Aoyama, T. Yano, K. Oya, J. I. Fujisawa and M. Hanaya, *Chem. Commun.*, 2015, **51**, 15894–15897.

2 A. Connell, Z. Wang, Y.-H. Lin, P. C. Greenwood, A. A. Wiles, E. W. Jones, L. Furnell, R. Anthony, C. P. Kershaw, G. Cooke, H. J. Snaith and P. J. Holliman, *J. Mater. Chem. C*, , DOI:10.1039/C8TC04231D.

3 A. Hagfeldt, *Ambio*, 2012, **41**, 151–155.

4 P. J. Holliman, C. Kershaw, A. Connell, E. W. Jones, R. Hobbs, R. Anthony, L. Furnell, J. McGettrick, D. Geatches and S. Metz, *Sci. Technol. Adv. Mater.*, 2018, **19**, 599–612.

5 GCell by G24 Power, https://gcell.com/ (accessed 21st December 2020).

6 Exeger, https://exeger.com/, (accessed 21st December 2020).

7 greatcellsolar, http://www.greatcellsolar.com/, (accessed 21st December 2020).

8 Solaronix, https://www.solaronix.com/, (accessed 21st December 2020).

9 J. Rebek, *Proc. Natl. Acad. Sci.*, 2009, **106**, 10423–10424.

10 Sigma Aldrich, https://www.sigmaaldrich.com/united-kingdom.html, (accessed 21st December 2020) .

11 P. Gründler, *Chemical sensors: An introduction for scientists and engineers*, 2007.

12 M. Gratzel, *J. Photochem. Photobiol. C Photochem. Rev.*, 2003, **4**, 145–153.

13 G. A. Ozin, K. Hou, B. V. Lotsch, L. Cademartiri, D. P. Puzzo, F. Scotognella, A. Ghadimi and J. Thomson, *Mater. Today*, 2009, **12**, 12–23.

14 F. Scotognella, D. P. Puzzo, A. Monguzzi, D. S. Wiersma, D. Maschke, R. Tubino and G. A. Ozin, *Small*, 2009, **5**, 2048–2052.

15 L. Zhang and J. M. Cole, *J. Mater. Chem. A*, 2017, **5**, 19541–19559.

16 NREL, NREL Best Research-Cell Efficiences, https://www.nrel.gov/phttps://www.nrel.gov/pv/assets/pdfs/best-research-cell-efficiencies.20200925.pdf.

17 M. W. Penny, A. Tarat, R. A. Brown, T. G. G. Maffeis, K. E. Meissner, R. Majitha, D. T. J. Bryant, C. J. Nettle and D. R. Jones, *Nanoscale Res. Lett.*, 2014, **9**, 11.

18 K.-M. Huang, Y. Q. Wong, M.-C. Lin, C.-H. Chen, C.-H. Liao, J.-Y. Chen, Y.-H. Huang, Y.-F. Chang, P.-T. Tsai, S.-H. Chen, C.-T. Liao, Y.-C. Lee, L. Hong, C.-Y. Chang, H.-F. Meng, Z. Ge, H.-W. Zan, S.-F. Horng, Y.-C. Chao and H. Y. Wong, *Prog. Photovoltaics Res. Appl.*, 2019, **27**, 264–274.

19 M. A. Green, E. D. Dunlop, J. Hohl-Ebinger, M. Yoshita, N. Kopidakis and X. Hao, *Prog. Photovoltaics Res. Appl.*, 2020, **28**, 629–638.

20 T. Wang, Consumption of electricity worldwide from 1980 to 2016,

https://www.statista.com/statistics/280704/world-power-consumption/.

21 A. Hagfeldt, G. Boschloo, L. Sun, L. Kloo and H. Pettersson, *Chem. Rev.*, 2010, **110**, 6595–6663.

22 R. Lippmann, S. Babben, A. Menger, C. Delker and M. Quint, *Curr. Biol.*, 2019, **29**, R1326–R1338.

23 P. Gaüzère, L. Barbaro, F. Calatayud, K. Princé, V. Devictor, L. Raison, C. Sirami and G. Balent, *Agric. Ecosyst. Environ.*, 2020, **289**, 106722.

24 C. Y. Wright, M. Norval, T. Kapwata, D. J. du Preez, B. Wernecke, B. M. Tod and W. I. Visser, *Atmosphere (Basel).*, 2019, **10**, 634.

25 D. Abbott, *Proc. IEEE*, 2010, **98**, 42–66.

26 L. Waters and National Statistics., *Energy Policy*, 2019, **62**, 82–93.

27 UK energy: how much, what type and where from?, https://www.ons.gov.uk/economy/environmentalaccounts/articles/ukenergyhowmuchwhattypeandwherefrom/2016-08-15.

28 BEIS, *Off. Natl. Stat.*, 2020, 176 pp.

29 J. J. MacKenzie, *Nonrenewable Resour.*, 1998, **7**, 97–100.

30 J. Vincent, Fossil fuels: UK to 'run out of oil, gas and coal' in five years, https://www.independent.co.uk/news/uk/uk-to-run-out-of-fossil-fuels-in-five-years-9385415.html, (accessed 11 March 2018).

31 P. Voosen, How Long Can a Nuclear Reactor Last?, https://www.scientificamerican.com/article/nuclear-power-plant-aging-reactor-replacement-/.

32 Q. Schiermeier, J. Tollefson, T. Scully, A. Witze and O. Morton, *Nature*, 2008, **454**, 816–823.

33 Levelized Cost and Levelized Avoided Cost of New Generation and R. in the A. E. O. 2019, *Annu. Energy Outlook 2019*, 2019, 25.

34 H. Al-Shabibi, What is Levelized Cost of Energy (LCOE), and why should you care?, https://www.solarpowerrocks.com/affordable-solar/levelized-cost-of-energy/, (accessed 14 August 2019).

35 Levelized Cost of Energy and Levelized Cost of Storage – 2020, https://www.lazard.com/perspective/lcoe2020, (accessed 16 December 2020).

36 C. Maurer, C. Cappel and T. E. Kuhn, *Sol. Energy*, 2017, **154**, 158–186.

37 Z. Ma, H. Bao and A. P. Roskilly, *Sol. Energy*, 2018, **162**, 489–499.

38 S. Kurtz, J. Olson, J. Geisz, M. Wanlass, B. Mcmahon, D. Friedman, S. Ward, A. Duda, C. Kramer, M. Young, A. Kibbler, A. Ptak, J. Carapella, S. Feldman and C. Honsberg, *APS March Meet.*

39 S. Yang, W. Fu, Z. Zhang, H. Chen and C. Z. Li, *J. Mater. Chem. A*, 2017, **5**, 11462–11482.

40 E. Becquerel, *Comptes Rendus l'Academie des Sci.*, 1839, **9**, 561–567.

41 C. Honsberg and S. Bowden, First photovoltaic Devices, https://www.pveducation.org/pvcdrom/manufacturing/first-photovoltaic-devices, (accessed 10 March 2019).

42 W. G. Adams and R. E. Day, *Proc. R. Soc. London*, 1877, **25**, 113–117.

43 W. Shockley and H. J. Queisser, *J. Appl. Phys.*, 1961, **32**, 510–519.

44 S. Rühle, *Sol. Energy*, 2016, **130**, 139–147.

45 J. N. Munday, *J. Appl. Phys.*, , DOI:10.1063/1.4742983.

46 B. B. Ridge, I. L. Dubuque, I. A. Madison, W. I. New, Y. San and F. St, *Concepts Mod. Phys.*, 2008, **6**, 57–58.

47 A. Belghachi, in *Solar Cells - New Approaches and Reviews*, InTech, 2015, pp. 127–135.

48 Viridian Solar, .

49 J. Wu, Z. Lan, J. Lin, M. Huang, Y. Huang, L. Fan and G. Luo, *Chem. Rev.*, 2015, **115**, 2136–2173.

50 M. Grätzel, *MRS Bull.*, 2005, **30**, 23–27.

51 C.-P. Lee, R. Y.-Y. Lin, L.-Y. Lin, C.-T. Li, T.-C. Chu, S.-S. Sun, J. T. Lin and K.-C. Ho, *RSC Adv.*, 2015, **5**, 23810–23825.

52 F. H. Alharbi and S. Kais, *Renew. Sustain. Energy Rev.*, 2015, **43**, 1073–1089.

53 R. R. R. King, D. C. C. Law, C. M. M. Fetzer, R. A. A. Sherif, K. M. M. Edmondson, S. Kurtz, G. S. S. Kinsey, H. L. L. Cotal, D. D. D. Krut, J. H. H. Ermer and N. H. H. Karam, *Proc. 20th Eur. Photovolt. Sol. Energy Conf.*, 2005, 118.

54 L. El Chaar, L. A. Lamont and N. El Zein, *Renew. Sustain. Energy Rev.*, 2011, **15**, 2165–2175.

55 The perovskite-silicon tandem, https://www.oxfordpv.com/news/oxford-pv-perovskite-solar-cell-achieves-28-efficiency, (accessed 9 August 2019).

56 P. R. I. F. O. R. S. E. S. ISE, .

57 F. Bittau, C. Potamialis, M. Togay, A. Abbas, P. J. M. Isherwood, J. W. Bowers and J. M. Walls, *Sol. Energy Mater. Sol. Cells*, 2018, **187**, 15–22.

58 D. Ledinek, O. Donzel-Gargand, M. Sköld, J. Keller and M. Edoff, *Sol. Energy Mater. Sol. Cells*, 2018, **187**, 160–169.

59 S. Moon, K. Kim, Y. Kim, J. Heo and J. Lee, *Sci. Rep.*, 2016, **6**, 1–6.

60 L. C. Andreani, A. Bozzola, P. Kowalczewski, M. Liscidini and L. Redorici, *Adv. Phys. X*, 2019, **4**, 1548305.

61 Y. S. Peng and S. F. Gong, *J. Phys. D. Appl. Phys.*, 2020, **53**, 495107.

62 T. Ava, A. Al Mamun, S. Marsillac and G. Namkoong, *Appl. Sci.*, 2019, **9**, 188.

63 L. Duan, N. K. Elumalai, Y. Zhang and A. Uddin, *Sol. Energy Mater. Sol. Cells*,

2019, **193**, 22–65.

64 M. Urbani, M.-E. Ragoussi, M. K. Nazeeruddin and T. Torres, *Coord. Chem. Rev.*, 2019, **381**, 1–64.

65 P. Vincent, S. C. Shin, J. S. Goo, Y. J. You, B. Cho, S. Lee, D. W. Lee, S. R. Kwon, K. B. Chung, J. J. Lee, J. H. Bae, J. W. Shim and H. Kim, *Dye. Pigment.*, 2018, **159**, 306–313.

66 R. Sharma, *Heliyon*, 2019, **5**, e01965.

67 C.-P. Lee, C.-A. Lin, T.-C. Wei, M.-L. Tsai, Y. Meng, C.-T. Li, K.-C. Ho, C.-I. Wu, S.-P. Lau and J.-H. He, *Nano Energy*, 2015, **18**, 109–117.

68 M. Parchine, T. Kohoutek, M. Bardosova and M. E. Pemble, *Sol. Energy Mater. Sol. Cells*, 2018, **185**, 158–165.

69 S. Sharma, K. K. Jain and A. Sharma, 2015, 1145–1155.

70 N. Z. Vagidov, K. H. Montgomery, G. K. Bradshaw and D. A. Wilt, *Sol. Energy Mater. Sol. Cells*, 2018, **182**, 136–141.

71 A. Smith, The Case for Solar Power From Space, https://space.nss.org/the-case-for-solar-power-from-space/, (accessed 13 December 2020).

72 A. Sproul, *Solar Cells: Resource for the Secondary Science Teacher*, 2003.

73 P. Laube, Fundamentals: Doping: n- and p-semiconductors.

74 Univeristy of Cambridge, Direct and Indirect Band Gap Semiconductors, https://www.doitpoms.ac.uk/tlplib/semiconductors/direct.php, (accessed 10 March 2018).

75 T. D. Lee and A. U. Ebong, *Renew. Sustain. Energy Rev.*, 2017, **70**, 1286–1297.

76 C. Roselund, Global PV module prices collapse, https://www.pv-magazine.com/2018/06/21/global-pv-module-prices-collapse/, (accessed 8 March 2019).

77 A. Hagfeldt, G. Boschloo, L. Sun, L. Kloo and H. Pettersson, *Chem. Rev.*, 2010, **110**, 6595–6663.

78 G. Kavlak, J. McNerney and J. E. Trancik, *Energy Policy*, 2018, **123**, 700–710.

79 T. Helmenstine, Abundance of Elements in Earth's Crust – Periodic Table and List, https://sciencenotes.org/abundance-of-elements-in-earths-crust-periodic-table-and-list/, (accessed 10 March 2019).

80 M. Tao, *Terawatt Solar Photovoltaics*, Springer London, London, 2014, vol. 28.

81 W. Qarony, M. I. Hossain, M. K. Hossain, M. J. Uddin, A. Haque, A. R. Saad and Y. H. Tsang, *Results Phys.*, 2017, **7**, 4287–4293.

82 M. Nakamura, K. Yamaguchi, Y. Kimoto, Y. Yasaki, T. Kato and H. Sugimoto, *IEEE J. Photovoltaics*, 2019, **9**, 1863–1867.

83 L. M. Peter, *Electrochem. commun.*, 2015, **50**, 88–92.

84 M. A. Green, *Phys. E Low-Dimensional Syst. Nanostructures*, 2002, **14**, 65–70.

85 M. A. Green, *Prog. Photovoltaics Res. Appl.*, 2001, **9**, 123–135.

86 L. Meng, Y. Zhang, X. Wan, C. Li, X. Zhang, Y. Wang, X. Ke, Z. Xiao, L. Ding, R. Xia, H.-L. Yip, Y. Cao and Y. Chen, *Science (80-.).*, 2018, **361**, 1094–1098.

87 L. Sun, X. Xu, S. Song, Y. Zhang, C. Miao, X. Liu, G. Xing and S. Zhang, *Macromol. Rapid Commun.*, 2019, **40**, 1900074.

88 O. A. Abdulrazzaq, V. Saini, S. Bourdo, E. Dervishi and A. S. Biris, *Part. Sci. Technol.*, 2013, **31**, 427–442.

89 Q. Ma, Z. Jia, L. Meng, J. Zhang, H. Zhang, W. Huang, J. Yuan, F. Gao, Y. Wan, Z. Zhang and Y. Li, *Nano Energy*, 2020, **78**, 105272.

90 U. Würfel, D. Neher, A. Spies and S. Albrecht, *Nat. Commun.*, 2015, **6**, 6951.

91 Q. Burlingame, C. Coburn, X. Che, A. Panda, Y. Qu and S. R. Forrest, *Nature*, 2018, **554**, 77–80.

92 N. Elumalai, M. Mahmud, D. Wang and A. Uddin, *Energies*, 2016, **9**, 861.

93 S. Yang, W. Fu, Z. Zhang, H. Chen and C. Z. Li, *J. Mater. Chem. A*, 2017, **5**, 11462–11482.

94 M. Abd Mutalib, N. Ahmad Ludin, N. A. A. Nik Ruzalman, V. Barrioz, S. Sepeai, M. A. Mat Teridi, M. S. Su'ait, M. A. Ibrahim and K. Sopian, *Mater. Renew. Sustain. Energy*, 2018, **7**, 7.

95 Bis, *Notes*, 2011, 38.

96 W. Liao, D. Zhao, Y. Yu, N. Shrestha, K. Ghimire, C. R. Grice, C. Wang, Y. Xiao, A. J. Cimaroli, R. J. Ellingson, N. J. Podraza, K. Zhu, R.-G. Xiong and Y. Yan, *J. Am. Chem. Soc.*, 2016, **138**, 12360–12363.

97 T. M. Koh, T. Krishnamoorthy, N. Yantara, C. Shi, W. L. Leong, P. P. Boix, A. C. Grimsdale, S. G. Mhaisalkar and N. Mathews, *J. Mater. Chem. A*, 2015, **3**, 14996–15000.

98 J. Rawson, Photovoltaic (PV) Solar Panels, https://www.cat.org.uk/info-resources/free-information-service/energy/solar-photovoltaic/#:~:text=The life expectancy of a PV panel is,panels should come with a 'power output warranty'.

99 B. O'Regan and M. Grätzel, *Nature*, 1991, **353**, 737–740.

100 H. J. Snaith, *Adv. Funct. Mater.*, 2010, **20**, 13–19.

101 Dyenamo, https://dyenamo.se/, (accessed 5 January 2020).

102 V. C. Fuertes, C. F. A. Negre, M. B. Oviedo, F. P. Bonafé, F. Y. Oliva and C. G. Sánchez, *J. Phys. Condens. Matter*, 2013, **25**, 115304.

103 H. Gerischer, M. E. Michel-Beyerle, F. Rebentrost and H. Tributsch, *Electrochim. Acta*, 1968, **13**, 1509–1515.

104 H. TSUBOMURA, M. MATSUMURA, Y. NOMURA and T. AMAMIYA, *Nature*, 1976, **261**, 402–403.

105 S. A. A. R. Sayyed, N. I Beedri, V. S. Kadam and H. M. Pathan, *Bull. Mater. Sci.*, 2016, **39**, 1381–1387.

106 S. Dayang, M. Irwanto, N. Gomesh and B. Ismail, 2017, p. 020245.

107 N. A. Ludin, A. M. Al-Alwani Mahmoud, A. Bakar Mohamad, A. A. H. Kadhum, K. Sopian and N. S. Abdul Karim, *Renew. Sustain. Energy Rev.*, 2014, **31**, 386–396.

108 J. Ramirez-Perez, C. Maria and C. P. Santacruz, *Renewables Wind. Water, Sol.*, 2019, **6**, 1.

109 X.-F. Wang, C.-H. Zhan, T. Maoka, Y. Wada and Y. Koyama, *Chem. Phys. Lett.*, 2007, **447**, 79–85.

110 Mounir Alhamed, Ahmad S. Issa and A. Wael Doubal, *J. Electron Devices*, 2012, **16**, 1370–1383.

111 T. P. J. Krüger and R. van Grondelle, *J. Phys. B At. Mol. Opt. Phys.*, 2017, **50**, 132001.

112 A. Kay and M. Graetzel, *J. Phys. Chem.*, 1993, **97**, 6272–6277.

113 X. F. Wang, R. Fujii, S. Ito, Y. Koyama, Y. Yamano, M. Ito, T. Kitamura and S. Yanagida, *Chem. Phys. Lett.*, 2005, **416**, 1–6.

114 Y. Cao, Y. Bai, Q. Yu, Y. Cheng, S. Liu, D. Shi, F. Gao and P. Wang, *J. Phys. Chem. C*, 2009, **113**, 6290–6297.

115 T. Bessho, E. Yoneda, J. Yum, M. Guglielmi, I. Tavernelli, H. Imai, U. Rothlisberger, M. K. Nazeeruddin and M. Grätzel, *J. Am. Chem. Soc.*, 2009, **131**, 5930–5934.

116 M. K. Nazeeruddin, F. De Angelis, S. Fantacci, A. Selloni, G. Viscardi, P. Liska, S. Ito, B. Takeru and M. Grätzel, *J. Am. Chem. Soc.*, 2005, **127**, 16835–16847.

117 S. Aghazada and M. Nazeeruddin, *Inorganics*, 2018, **6**, 52.

118 E. Dell'Orto, L. Raimondo, A. Sassella and A. Abbotto, *J. Mater. Chem.*, 2012, **22**, 11364–11369.

119 Y. Ren, Y.-Z. Zheng, J. Zhao, J.-F. Chen, W. Zhou and X. Tao, *Electrochem. commun.*, 2012, **16**, 57–60.

120 P. . Sommeling, M. Späth, H. J. . Smit, N. . Bakker and J. . Kroon, *J. Photochem. Photobiol. A Chem.*, 2004, **164**, 137–144.

121 A. Burrows, J. Holman, A. Parsons, G. Pilling and G. Price, *Chemistry3*, Oxford university press, 2009.

122 P. W. Atkins, *Physical chemistry*, Oxford university press, 1986.

123 A. Connell, P. J. Holliman, E. W. Jones, L. Furnell, C. Kershaw, M. L. Davies, C. D. Gwenin, M. B. Pitak, S. J. Coles and G. Cooke, *J. Mater. Chem. A*, 2015, **3**, 2883–2894.

124 E. Galoppini, *Coord. Chem. Rev.*, 2004, **248**, 1283–1297.

125 L. Zhang and J. M. Cole, *ACS Appl. Mater. Interfaces*, 2015, **7**, 3427–3455.

126 L.-B. Xiong, J.-L. Li, B. Yang and Y. Yu, *J. Nanomater.*, 2012, **2012**, 1–13.

127 C. Lambert, Y. Mao, Y. Zheng, X. Tao, P. Hu and M. Huang, *Can. J. Chem.*, 2016, **94**, 1109–1118.

128 S. Dheivamalar and K. B. Banu, *Heliyon*, 2019, **5**, e02903.

129 M. Bourass, A. T. Benjelloun, M. Benzakour, M. Mcharfi, M. Hamidi, S. M. Bouzzine and M. Bouachrine, *Chem. Cent. J.*, 2016, **10**, 67.

130 J. Maçaira, L. Andrade and A. Mendes, *RSC Adv.*, 2014, **4**, 2830–2844.

131 M. Mazloum-Ardakani and R. Arazi, *Heliyon*, 2019, **5**, e01444.

132 H.-P. Lu, C.-Y. Tsai, W.-N. Yen, C.-P. Hsieh, C.-W. Lee, C.-Y. Yeh and E. W.-G. Diau, *J. Phys. Chem. C*, 2009, **113**, 20990–20997.

133 R. M. Abdel Aal, M. A. Gitru and Z. M. Essam, *Chem. Int.*, 2017, **3**, 258–267.

134 F. Labat, T. Le Bahers, I. Ciofini and C. Adamo, *Acc. Chem. Res.*, 2012, **45**, 1268–1277.

135 S. Fantacci and F. De Angelis, *Eur. J. Inorg. Chem.*, 2019, **2019**, 743–750.

136 S. Namuangruk, R. Fukuda, M. Ehara, J. Meeprasert, T. Khanasa, S. Morada, T. Kaewin, S. Jungsuttiwong, T. Sudyoadsuk and V. Promarak, *J. Phys. Chem. C*, 2012, **116**, 25653–25663.

137 E. Hadji Oumar Gueye, *Am. J. Mod. Phys.*, 2017, **6**, 1.

138 J. N. Clifford, E. Palomares, M. K. Nazeeruddin, R. Thampi, M. Grätzel and J. R. Durrant, *J. Am. Chem. Soc.*, 2004, **126**, 5670–5671.

139 J. Patwari, S. Sardar, B. Liu, P. Lemmens and S. K. Pal, *Beilstein J. Nanotechnol.*, 2017, **8**, 1705–1713.

140 S. H. Hwang, N. K. Kim, K. N. Koh and S. H. Kim, *Dye. Pigment.*, 1998, **39**, 359–369.

141 M. Tian, M. Furuki, I. Iwasa, Y. Sato, L. S. Pu and S. Tatsuura, *J. Phys. Chem. B*, 2002, **106**, 4370–4376.

142 S. Tatsuura, M. Tian, M. Furuki, Y. Sato, I. Iwasa, L. S. Pu, H. Kawashima and H. Ishikawa, *Appl. Phys. Lett.*, 2002, **81**, 2704–2706.

143 G. J. Ashwell, J. Ewington and K. Moczko, *J. Mater. Chem.*, 2005, **15**, 1154.

144 P. T. Snee, R. C. Somers, G. Nair, J. P. Zimmer, M. G. Bawendi and D. G. Nocera, *J. Am. Chem. Soc.*, 2006, **128**, 13320–13321.

145 G. Chen, H. Sasabe, T. Igarashi, Z. Hong and J. Kido, *J. Mater. Chem. A*, 2015, **3**, 14517–14534.

146 J. Park, C. Barolo, F. Sauvage, N. Barbero, C. Benzi, P. Quagliotto, S. Coluccia, D. Di Censo, M. Grätzel, M. K. Nazeeruddin and G. Viscardi, *Chem. Commun.*, 2012, **48**, 2782.

147 R. Bisht, M. F. Mele Kavungathodi and J. Nithyanandhan, *Chem. - A Eur. J.*, 2018, **24**, 16368–16378.

148 H. S. El Khadem, M. A. Shalaby, B. Coxon and A. J. Fatiadi, *J. Chem. Soc. Perkin Trans. 1*, 1992, 1511.

149 A. M. Della Pelle, P. J. Homnick, Y. Bae, P. M. Lahti and S. Thayumanavan, *J. Phys. Chem. C*, 2014, **118**, 1793–1799.

150 Q. Xu, G. Yang, Y. Ren, F. Lu, N. Zhang, M. Qamar, M. Yang, B. Zhang and Y. Feng, *Phys. Chem. Chem. Phys.*, 2017, **19**, 28867–28875.

151 A. Burke, L. Schmidt-Mende, S. Ito and M. Grätzel, *Chem. Commun.*, 2007, 234–236.

152 T. Inoue, S. S. Pandey, N. Fujikawa, Y. Yamaguchi and S. Hayase, *J. Photochem. Photobiol. A Chem.*, 2010, **213**, 23–29.

153 G. D. Sharma, R. Kurchania, R. J. Ball, M. S. Roy and J. A. Mikroyannidis, *Int. J. Photoenergy*, 2012, **2012**, 1–7.

154 M. Matsui, H. Mase, J.-Y. Jin, K. Funabiki, T. Yoshida and H. Minoura, *Dye. Pigment.*, 2006, **70**, 48–53.

155 N. Shahzad, F. Risplendi, D. Pugliese, S. Bianco, A. Sacco, A. Lamberti, R. Gazia, E. Tresso and G. Cicero, *J. Phys. Chem. C*, 2013, **117**, 22778–22783.

156 G. Cicero, G. Musso, A. Lamberti, B. Camino, S. Bianco, D. Pugliese, F. Risplendi, A. Sacco, N. Shahzad, A. M. Ferrari, B. Ballarin, C. Barolo, E. Tresso and G. Caputo, *Phys. Chem. Chem. Phys.*, 2013, **15**, 7198–7203.

157 A. Connell, P. J. Holliman, M. L. Davies, C. D. Gwenin, S. Weiss, M. B. Pitak, P. N. Horton, S. J. Coles and G. Cooke, *J. Mater. Chem. A*, 2014, **2**, 4055–4066.

158 W. Li, A. Zhu, A. Stewart, Z. Liu, Y.-B. Cheng, Z. Zhao and H. He, *RSC Adv.*, 2016, **6**, 114037–114045.

159 T.-F. Lu, W. Li, F.-Q. Bai, R. Jia, J. Chen and H.-X. Zhang, *J. Mater. Chem. A*, 2017, **5**, 15567–15577.

160 A. K. Singh, in *Engineered Nanoparticles*, Elsevier, 2016, pp. 19–76.

161 P. J. Holliman, K. J. Al-Salihi, A. Connell, M. L. Davies, E. W. Jones and D. A. Worsley, *RSC Adv.*, 2014, **4**, 2515–2522.

162 D. Hill, P. J. Holliman, J. McGettrick, M. Appelman, P. Chatterjee, T. M. Watson and D. Worsley, *Tribol. Int.*, 2018, **119**, 337–344.

163 J. M. Cole, G. Pepe, O. K. Al Bahri and C. B. Cooper, *Chem. Rev.*, 2019, **119**, 7279–7327.

164 P. J. Holliman, M. L. Davies, A. Connell, B. V. Velasco and T. M. Watson, *Chem. Commun.*, 2010, **46**, 7256.

165 P. J. Holliman, M. Mohsen, A. Connell, M. L. Davies, K. Al-Salihi, M. B. Pitak, G. J. Tizzard, S. J. Coles, R. W. Harrington, W. Clegg, C. Serpa, O. H. Fontes, C. Charbonneau and M. J. Carnie, *J. Mater. Chem.*, 2012, **22**, 13318.

166 K. Gräf, M. A. Rahim, S. Das and M. Thelakkat, *Dye. Pigment.*, 2013, **99**, 1101–1106.

167 A. Islam, M. Akhtaruzzaman, T. H. Chowdhury, C. Qin, L. Han, I. M. Bedja, R. Stalder, K. S. Schanze and J. R. Reynolds, *ACS Appl. Mater. Interfaces*, 2016, **8**, 4616–4623.

168 J. Chang, C.-P. Lee, D. Kumar, P.-W. Chen, L.-Y. Lin, K. R. J. Thomas and K.-C. Ho, *J. Power Sources*, 2013, **240**, 779–785.

169 A. Islam, M. Akhtaruzzaman, T. H. Chowdhury, I. M. Bedja, L. Han, A. Mirloup and R. Ziessel, in *2016 4th International Conference on the Development in the in Renewable Energy Technology (ICDRET)*, IEEE, 2016, pp. 1–4.

170 V. A. El Bitar Nehme, M. A. El Bitar Nehme and T. H. Ghaddar, *Sol. Energy*, 2019, **187**, 108–114.

171 C. Dette, M. A. Pérez-Osorio, C. S. Kley, P. Punke, C. E. Patrick, P. Jacobson, F. Giustino, S. J. Jung and K. Kern, *Nano Lett.*, 2014, **14**, 6533–6538.

172 M. S. Silberberg, *McGraw-Hill High. Educ.*

173 K. Hongsith, N. Hongsith, D. Wongratanaphisan, A. Gardchareon, S. Phadungdhitidhada and S. Choopun, *Efficiency Enhancement of ZnO Dye-sensitized Solar Cells by Modifying Photoelectrode and Counterelectrode*, Elsevier B.V., 2015, vol. 79.

174 R. Vittal and K.-C. Ho, *Renew. Sustain. Energy Rev.*, 2017, **70**, 920–935.

175 S. N. F. Zainudin, H. Abdullah and M. Markom, *J. Mater. Sci. Mater. Electron.*, 2019, **30**, 5342–5356.

176 E. M. Kaidashev, M. Lorenz, H. von Wenckstern, A. Rahm, H.-C. Semmelhack, K.-H. Han, G. Benndorf, C. Bundesmann, H. Hochmuth and M. Grundmann, *Appl. Phys. Lett.*, 2003, **82**, 3901–3903.

177 R. G. Breckenridge and W. R. Hosler, *Phys. Rev.*, 1953, **91**, 793–802.

178 G. A. Parks, *Chem. Rev.*, 1965, **65**, 177–198.

179 K. Keis, J. Lindgren, S.-E. Lindquist and A. Hagfeldt, *Langmuir*, 2000, **16**, 4688–4694.

180 H. Horiuchi, R. Katoh, K. Hara, M. Yanagida, S. Murata, H. Arakawa and M. Tachiya, *J. Phys. Chem. B*, 2003, **107**, 2570–2574.

181 K. Tennakone, V. P. S. Perera, I. R. M. Kottegoda and G. R. R. A. Kumara, *J. Phys. D. Appl. Phys.*, 1999, **32**, 374–379.

182 K. G. Godinho, A. Walsh and G. W. Watson, *J. Phys. Chem. C*, 2009, **113**, 439–448.

183 A. P. Popov, A. V. Priezzhev, J. Lademann and R. Myllylä, *J. Phys. D. Appl. Phys.*, 2005, **38**, 2564–2570.

184 W. Li, Z. Wu, J. Wang, A. A. Elzatahry and D. Zhao, *Chem. Mater.*, 2014, **26**, 287–298.

185 L. Schmidt-Mende and M. Grätzel, *Thin Solid Films*, 2006, **500**, 296–301.

186 M. Ben Manaa, S. Benhattab, B. Schmaltz, N. Berton, J. Bouclé, A. Ben Lamine and F. T. Van, *Mediterr. J. Chem.*, 2016, **5**, 599–604.

187 U. Diebold, *Surf. Sci. Rep.*, 2003, **48**, 53–229.

188 S. Mo and W. Y. Ching, *Phys. Rev. B*, 1995, **51**, 23–32.

189 P. Jussieu, P. Cedex, L. De Dynamique and U. Pierre, *Phys. Rev. B*, 1993, **47**, 11717–11724.

190 D. Reyes-Coronado, G. Rodríguez-Gattorno, M. E. Espinosa-Pesqueira, C. Cab, R. De Coss and G. Oskam, *Nanotechnology*, , DOI:10.1088/0957-4484/19/14/145605.

191 A. Amtout and R. Leonelli, *Phys. Rev. B*, 1995, **51**, 6842–6851.

192 H. Gerischer, *J. Phys. Chem.*, 1991, **95**, 1356–1359.

193 J. L. Lan, T. C. Wei, S. P. Feng, C. C. Wan and G. Cao, *J. Phys. Chem. C*, 2012, **116**, 25727–25733.

194 J. Teuscher, A. Marchioro, J. Andrès, L. M. Roch, M. Xu, S. M. Zakeeruddin, P. Wang, M. Grätzel and J.-E. E. Moser, *J. Phys. Chem. C*, 2014, **118**, 17108–17115.

195 H. Nusbaumer, J. Moser, S. M. Zakeeruddin, M. K. Nazeeruddin and M. Grätzel, *J. Phys. Chem. B*, 2001, **105**, 10461–10464.

196 R. Jiang, A. Anderson, P. R. F. Barnes, L. Xiaoe, C. Law and B. C. O'Regan, *J. Mater. Chem. A*, 2014, **2**, 4751–4757.

197 F. Bella, S. Galliano, C. Gerbaldi and G. Viscardi, *Energies*, 2016, **9**, 1–22.

198 A. Yella, S. Mathew, S. Aghazada, P. Comte, M. Grätzel and M. K. Nazeeruddin, *J. Mater. Chem. C*, 2017, **5**, 2833–2843.

199 H. Iftikhar, G. G. Sonai, S. G. Hashmi, A. F. Nogueira and P. D. Lund, *Materials (Basel).*, 2019, **12**, 1998.

200 M. Liu, M. B. Johnston and H. J. Snaith, *Nature*, 2013, **501**, 395–398.

201 A. Connell, Z. Wang, Y.-H. Lin, P. C. Greenwood, A. A. Wiles, E. W. Jones, L. Furnell, R. Anthony, C. P. Kershaw, G. Cooke, H. J. Snaith and P. J. Holliman, *J. Mater. Chem. C*, , DOI:10.1039/C8TC04231D.

202 N. Arora, M. I. Dar, A. Hinderhofer, N. Pellet, F. Schreiber, S. M. Zakeeruddin and M. Grätzel, *Science (80-.).*, 2017, **358**, 768–771.

203 M. Saliba, J. P. Correa-Baena, C. M. Wolff, M. Stolterfoht, N. Phung, S. Albrecht, D. Neher and A. Abate, *Chem. Mater.*, 2018, **30**, 4193–4201.

204 K. Murakoshi, R. Kogure, Y. Wada and S. Yanagida, *Chem. Lett.*, 1997, **26**, 471–472.

205 Y. Cao, Y. Saygili, A. Ummadisingu, J. Teuscher, J. Luo, N. Pellet, F. Giordano, S. M. Zakeeruddin, J. E. Moser, M. Freitag, A. Hagfeldt and M. Grätzel, *Nat. Commun.*, 2017, **8**, 15390.

206 M. Fardioui, M. E. M. Mekhzoum, A. el K. Qaiss and R. Bouhfid, in *Nanoclay Reinforced Polymer Composites*, 2016, vol. 44, pp. 167–194.

207 D. P. Hagberg, J. H. Yum, H. J. Lee, F. De Angelis, T. Marinado, K. M. Karlsson, R. Humphry-Baker, L. Sun, A. Hagfeldt, M. Grätzel and M. K. Nazeeruddin, *J. Am. Chem. Soc.*, 2008, **130**, 6259–6266.

208 Y. Zhang, 2013, 197.

209 T. DENTANI, K. NAGASAKA, K. FUNABIKI, J. JIN, T. YOSHIDA, H. MINOURA and M. MATSUI, *Dye. Pigment.*, 2008, **77**, 59–69.

210 A. N. Kabanakis, M. Bidikoudi, M. M. Elsenety, G. C. Vougioukalakis and P. Falaras, *Dye. Pigment.*, 2019, **165**, 308–318.

211 S. Gaspa, I. Amura, A. Porcheddu and L. De Luca, *New J. Chem.*, 2017, **41**, 931–939.

212 G. TANG, J. ZHOU, W. ZHANG, J. HU, D. PENG, Q. XIE and C. ZHONG, *Bull. Mater. Sci.*, 2015, **38**, 467–474.

213 D. Geatches, I. Rosbottom, R. L. Marchese Robinson, P. Byrne, P. Hasnip, M. I. J. Probert, D. Jochym, A. Maloney and K. J. Roberts, *J. Chem. Phys.*, 2019, **151**, 044106.

214 S. J. Clark, M. D. Segall, C. J. Pickard, P. J. Hasnip, M. I. J. Probert, K. Refson and M. C. Payne, *Zeitschrift für Krist. - Cryst. Mater.*, 2005, **220**, 567–570.

215 E. Fetil, S. Ozkan, T. Ilknur, Y. Erdem, B. Lebe and A. T. Gunes, *Int. J. Dermatol.*, 2002, **41**, 892–893.

216 P. Hohenberg and W. Kohn, *Phys. Rev.*, 1964, **136**, B864–B871.

217 M. Payne, M. Teter, D. Allan, T. Arias and J. Joannopoulos, *Rev. Mod. Phys.*, 1992, **64**, 1045.

218 J. P. Perdew, K. Burke and M. Ernzerhof, *Phys. Rev. Lett.*, 1996, **77**, 3865–3868.

219 D. R. Hamann, M. Schlüter and C. Chiang, *Phys. Rev. Lett.*, 1979, **43**, 1494–1497.

220 J. D. Pack and H. J. Monkhorst, *Phys. Rev. B*, 1977, **16**, 1748–1749.

221 A. Tkatchenko and M. Scheffler, *Phys. Rev. Lett.*, 2009, **102**, 073005.

222 N. Martsinovich, D. R. Jones and A. Troisi, *J. Phys. Chem. C*, 2010, **114**, 22659–22670.

223 B. G. Pfrommer, M. Côté, S. G. Louie and M. L. Cohen, *J. Comput. Phys.*, 1997, **131**, 233–240.

224 A. D. Becke, *J. Chem. Phys.*, 1993, **98**, 5648–5652.

225 R. Ahlrichs, M. Bär, M. Häser, H. Horn and C. Kölmel, *Chem. Phys. Lett.*, 1989, **162**, 165–169.

226 S. H. Vosko, L. Wilk and M. Nusair, *Can. J. Phys.*, 1980, **58**, 1200–1211.

227 P. J. Stephens, F. J. Devlin, C. F. Chabalowski and M. J. Frisch, *J. Phys. Chem.*, 1994, **98**, 11623–11627.

228 A. Schäfer, C. Huber and R. Ahlrichs, *J. Chem. Phys.*, 1994, **100**, 5829–5835.

229 A. Schäfer, H. Horn and R. Ahlrichs, *J. Chem. Phys.*, 1992, **97**, 2571–2577.

230 F. Neese, F. Wennmohs, A. Hansen and U. Becker, *Chem. Phys.*, 2009, **356**, 98–109.

231 R. Izsák and F. Neese, *J. Chem. Phys.*, 2011, **135**, 144105.

232 F. Neese, *Wiley Interdiscip. Rev. Comput. Mol. Sci.*, 2012, **2**, 73–78.

233 G. M. Morris, R. Huey, W. Lindstrom, M. F. Sanner, R. K. Belew, D. S. Goodsell and A. J. Olson, *J. Comput. Chem.*, 2009, **30**, 2785–2791.

234 G. M. Morris, D. S. Goodsell, R. S. Halliday, R. Huey, W. E. Hart, R. K. Belew and A. J. Olson, *J. Comput. Chem.*, 1998, **19**, 1639–1662.

235 M. I. Khan, 2013.

236 S. Mori and S. Yanagida, in *Nanostructured Materials for Solar Energy Conversion*, Elsevier, 2006, pp. 193–225.

237 V. Benda, in *A Comprehensive Guide to Solar Energy Systems*, Elsevier, 2018, pp. 151–179.

238 M. Grätzel, *Acc. Chem. Res.*, 2009, **42**, 1788–1798.

239 P. J. Holliman, C. P. Kershaw, E. W. Jones, D. Meza-Rojas, A. Lewis, J. McGettrick, D. Geatches, K. Sen, S. Metz, G. J. Tizzard and S. J. Coles, *J. Mater. Chem. A*, 2020, **8**, 22191–22205.

240 S. M. Abdalhadi, A. Connell, X. Zhang, A. A. Wiles, M. L. Davies, P. J. Holliman and G. Cooke, *J. Mater. Chem. A*, 2016, **4**, 15655–15661.

241 A. Listorti, B. O'Regan and J. R. Durrant, *Chem. Mater.*, 2011, **23**, 3381–3399.

242 K. C. D. Robson, K. Hu, G. J. Meyer and C. P. Berlinguette, *J. Am. Chem. Soc.*, 2013, **135**, 1961–1971.

243 H. Rensmo, S. Södergren, L. Patthey, K. Westermark, L. Vayssieres, O. Kohle, P. A. Brühwiler, A. Hagfeldt and H. Siegbahn, *Chem. Phys. Lett.*, 1997, **274**, 51–57.

244 B. C. O'Regan, K. Walley, M. Juozapavicius, A. Anderson, F. Matar, T. Ghaddar, S. M. Zakeeruddin, C. Klein and J. R. Durrant, *J. Am. Chem. Soc.*, 2009, **131**, 3541–3548.

245 C. Anselmi, E. Mosconi, M. Pastore, E. Ronca and F. De Angelis, *Phys. Chem. Chem. Phys.*, 2012, **14**, 15963.

246 T.-D. Nguyen, C.-H. Lin, C.-L. Mai and C.-G. Wu, *ACS Omega*, 2019, **4**, 11414–11423.

247 S. Kuwahara, S. Taya, N. Osada, Q. Shen, T. Toyoda and K. Katayama, *Phys. Chem. Chem. Phys.*, 2014, **16**, 5242.

248 H. Guo, H. Hu, X. Yu, K. Naito and Q. Zhang, *J. Nanosci. Nanotechnol.*, 2019, **19**, 7574–7583.

249 H. Wang, S. Wen, G. Han and Q. Feng, *Sep. Purif. Technol.*, 2019, **228**, 115756.

250 Z.-G. Zhou, H.-M. Du, Z. Dai, Y. Mu, L.-L. Tong, Q.-J. Xing, S.-S. Liu, Z. Ao and J.-P. Zou, *Chem. Eng. J.*, 2019, **374**, 170–180.

251 A. O. T. Patrocínio, E. B. Paniago, R. M. Paniago and N. Y. M. Iha, *Appl. Surf. Sci.*, 2008, **254**, 1874–1879.

252 XPSSimplified, Angle-resolved XPS, https://xpssimplified.com/angle_resolve_xps.php, (accessed 27 August 2019).

253 W. A. M. Aarnink, A. Weishaupt and A. van Silfhout, *Appl. Surf. Sci.*, 1990, **45**, 37–48.

254 J. F. Watts and J. Wolstenholme, *An Introduction to Surface Analysis by XPS and AES*, John Wiley & Sons, Ltd, Chichester, UK, 2003.

255 S. Bin Humam, H. H. Nguyen, C. Regmi, G. Gyawali, B. Joshi and S. W. Lee, *Ceram. Int.*, 2019, **45**, 4230–4236.

256 V. . Manikandan, A. K. Palai, S. Mohanty and S. K. Nayak, *J. Alloys Compd.*, 2019, **793**, 400–409.

257 S. Cho, H. Kim and M. M. Sung, *J. Ind. Eng. Chem.*, 2019, **77**, 470–476.

258 F. M. Pesci, M. S. Sokolikova, C. Grotta, P. C. Sherrell, F. Reale, K. Sharda, N. Ni, P. Palczynski and C. Mattevi, *ACS Catal.*, 2017, **7**, 4990–4998.

259 I. Y. Bu, *Optik (Stuttg).*, 2019, **182**, 658–663.

260 M. U. Shahid, N. M. Mohamed, A. S. Muhsan, R. Bashiri, A. E. Shamsudin and S. N. A. Zaine, *Diam. Relat. Mater.*, 2019, **94**, 242–251.

261 A. Akbari, J. Hashemi, J. Niskanen, S. Huotari and M. Hakala, *Phys. Chem. Chem. Phys.*, 2015, **17**, 10849–10855.

262 J. N. O'Shea, J. Ben Taylor and E. F. Smith, *Surf. Sci.*, 2004, **548**, 317–323.

263 G. Pellegrino, A. Alberti, G. G. Condorelli, F. Giannazzo, A. La Magna, A. M. Paoletti, G. Pennesi, G. Rossi and G. Zanotti, *J. Phys. Chem. C*, 2013, **117**, 11176–11185.

264 M. Gratzel, J.-H. Yum, P. Walter, S. Huber, D. Rentsch, T. Geiger, F. Nüesch, F. De Angelis and M. K. Nazeeruddin, *J. Am. Chem. Soc.*, 2007, **129**, 10320–1.

265 X. Wu, G. (Max) Lu and L. Wang, *J. Colloid Interface Sci.*, 2013, **391**, 70–73.

266 M. K. Nazeeruddin, R. Humphry-Baker, P. Liska and M. Grätzel, *J. Phys. Chem. B*, 2003, **107**, 8981–8987.

267 M. Pastore, E. Mosconi, F. De Angelis and M. Grätzel, *J. Phys. Chem. C*, 2010, **114**, 7205–7212.

268 S. N. Kane, A. Mishra and A. K. Dutta, *J. Phys. Conf. Ser.*, 2016, **755**, 011001.

269 O. V. Dolomanov, L. J. Bourhis, R. J. Gildea, J. A. K. Howard and H.

Puschmann, *J. Appl. Crystallogr.*, 2009, **42**, 339–341.

270 G. M. Sheldrick, *Acta Crystallogr. Sect. C Struct. Chem.*, 2015, **71**, 3–8.

271 D. P. Hagberg, T. Marinado, K. M. Karlsson, K. Nonomura, P. Qin, G. Boschloo, T. Brinck, A. Hagfeldt and L. Sun, *J. Org. Chem.*, 2007, **72**, 9550–9556.

272 H. Yu, S. Zhang, H. Zhao, G. Will and P. Liu, *Electrochim. Acta*, 2009, **54**, 1319–1324.

273 A. E. Shalan, M. M. Rashad, Y. Yu, M. Lira-Cantú and M. S. A. Abdel-Mottaleb, *Electrochim. Acta*, 2013, **89**, 469–478.

274 F. De Angelis, *Acc. Chem. Res.*, 2014, **47**, 3349–3360.

275 B. Xu, D. Bi, Y. Hua, P. Liu, M. Cheng, M. Grätzel, L. Kloo, A. Hagfeldt and L. Sun, *Energy Environ. Sci.*, 2016, **9**, 873–877.

276 E. H. Jung, N. J. Jeon, E. Y. Park, C. S. Moon, T. J. Shin, T.-Y. Yang, J. H. Noh and J. Seo, *Nature*, 2019, **567**, 511–515.

277 S. Handa, H. Wietasch, M. Thelakkat, J. R. Durrant and S. A. Haque, *Chem. Commun.*, 2007, 1725–1727.

278 B. Xu, D. Bi, Y. Hua, P. Liu, M. Cheng, M. Grätzel, L. Kloo, A. Hagfeldt and L. Sun, *Energy Environ. Sci.*, 2016, **9**, 873–877.

279 L. Meng and C. Li, *Nanosci. Nanotechnol. Lett.*, 2011, **3**, 181–185.

280 P. J. Cameron and L. M. Peter, *J. Phys. Chem. B*, 2003, **107**, 14394–14400.

281 P. Lellig, M. Meister, J. W. Ochsmann, M. A. Niedermeier, M. Rawolle, F. Laquai, P. Müller-Buschbaum and J. S. Gutmann, *Springerplus*, 2015, **4**, 502.

282 A. Burke, S. Ito, H. Snaith, U. Bach, J. Kwiatkowski and M. Grätzel, *Nano Lett.*, 2008, **8**, 977–981.

283 S. Ito, T. N. Murakami, P. Comte, P. Liska, C. Grätzel, M. K. Nazeeruddin and M. Grätzel, *Thin Solid Films*, 2008, **516**, 4613–4619.

284 M. K. Nazeeruddin, A. Kay, I. Rodicio, R. Humphry-Baker, E. Mueller, P. Liska, N. Vlachopoulos and M. Graetzel, *J. Am. Chem. Soc.*, 1993, **115**, 6382–6390.

285 T. H. Schloemer, J. A. Christians, J. M. Luther and A. Sellinger, *Chem. Sci.*, 2019, **10**, 1904–1935.

286 N. O. V Plank, H. J. Snaith, C. Ducati, J. S. Bendall, L. Schmidt-Mende and M. E. Welland, *Nanotechnology*, 2008, **19**, 465603.

287 E. J. W. Crossland, N. Noel, V. Sivaram, T. Leijtens, J. A. Alexander-Webber and H. J. Snaith, *Nature*, 2013, **495**, 215–219.

288 P. Docampo, S. Guldin, M. Stefik, P. Tiwana, M. C. Orilall, S. Hüttner, H. Sai, U. Wiesner, U. Steiner and H. J. Snaith, *Adv. Funct. Mater.*, 2010, **20**, 1787–1796.

289 E. J. W. Crossland, M. Kamperman, M. Nedelcu, C. Ducati, U. Wiesner, D. M.

Smilgies, G. E. S. Toombes, M. A. Hillmyer, S. Ludwigs, U. Steiner and H. J. Snaith, *Nano Lett.*, 2009, **9**, 2807–2812.

290 P. Docampo and H. J. Snaith, *Nanotechnology*, 2011, **22**, 225403.

291 H. M. Yates, M. Afzaal, A. Walter, J. L. Hodgkinson, S.-J. Moon, D. Sacchetto, M. Bräuninger, B. Niesen, S. Nicolay, M. McCarthy, M. E. Pemble, I. M. Povey and C. Ballif, *J. Mater. Chem. C*, 2016, **4**, 11269–11277.

292 I. Benesperi, H. Michaels and M. Freitag, *J. Mater. Chem. C*, 2018, **6**, 11903–11942.

293 P. Pookmanee and S. Phanichphant, *J. Ceram. Process. Res.*, 2009, **10**, 167–170.

294 A. Karami, *J. Iran. Chem. Soc.*, 2010, **7**, S154–S160.

295 N. Fuke, R. Katoh, A. Islam, M. Kasuya, A. Furube, A. Fukui, Y. Chiba, R. Komiya, R. Yamanaka, L. Han and H. Harima, *Energy Environ. Sci.*, 2009, **2**, 1205.

296 H. Choi, C. Nahm, J. Kim, J. Moon, S. Nam, D.-R. Jung and B. Park, *Curr. Appl. Phys.*, 2012, **12**, 737–741.

297 T.-H. Wang, A. M. Navarrete-López, S. Li, D. A. Dixon and J. L. Gole, *J. Phys. Chem. A*, 2010, **114**, 7561–7570.

298 D. Wei, *Int. J. Mol. Sci.*, 2010, **11**, 1103–1113.

299 D. Moia, U. B. Cappel, T. Leijtens, X. Li, A. M. Telford, H. J. Snaith, B. C. O'Regan, J. Nelson and P. R. F. Barnes, *J. Phys. Chem. C*, 2015, **119**, 18975–18985.

300 P. Vivo, J. K. Salunke and A. Priimagi, *Materials (Basel).*, 2017, **10**, 1087.

301 L. Yang, R. Lindblad, E. Gabrielsson, G. Boschloo, H. Rensmo, L. Sun, A. Hagfeldt, T. Edvinsson and E. M. J. Johansson, *ACS Appl. Mater. Interfaces*, 2018, **10**, 11572–11579.

302 S. Wang, M. Sina, P. Parikh, T. Uekert, B. Shahbazian, A. Devaraj and Y. S. Meng, *Nano Lett.*, 2016, **16**, 5594–5600.

303 E. J. Juarez-Perez, M. R. Leyden, S. Wang, L. K. Ono, Z. Hawash and Y. Qi, *Chem. Mater.*, 2016, **28**, 5702–5709.

304 A. Abate, T. Leijtens, S. Pathak, J. Teuscher, R. Avolio, M. E. Errico, J. Kirkpatrik, J. M. Ball, P. Docampo, I. McPherson and H. J. Snaith, *Phys. Chem. Chem. Phys.*, 2013, **15**, 2572.

305 B. Tan, S. R. Raga, A. S. R. Chesman, S. O. Fürer, F. Zheng, D. P. McMeekin, L. Jiang, W. Mao, X. Lin, X. Wen, J. Lu, Y. Cheng and U. Bach, *Adv. Energy Mater.*, 2019, **9**, 1901519.

306 J. Burschka, F. Kessler, M. K. Nazeeruddin and M. Grätzel, *Chem. Mater.*, 2013, **25**, 2986–2990.

307 H. Klfout, A. Stewart, M. Elkhalifa and H. He, *ACS Appl. Mater. Interfaces*, 2017, **9**, 39873–39889.

308 N. Boens, V. Leen, W. Dehaen, L. Wang, K. Robeyns, W. Qin, X. Tang, D. Beljonne, C. Tonnelé, J. M. Paredes, M. J. Ruedas-Rama, A. Orte, L. Crovetto, E. M. Talavera and J. M. Alvarez-Pez, *J. Phys. Chem. A*, 2012, **116**, 9621–9631.

309 G. H. Summers, J.-F. Lefebvre, F. A. Black, E. Stephen Davies, E. A. Gibson, T. Pullerits, C. J. Wood and K. Zidek, *Phys. Chem. Chem. Phys.*, 2016, **18**, 1059–1070.

310 I. Gonzalez-Valls, A. Mirloup, T. Le Bahers, N. Keller, T. Cottineau, P. Sautet and V. Keller, *RSC Adv.*, 2016, **6**, 91529–91540.

311 A. B. Descalzo, P. Ashokkumar, Z. Shen and K. Rurack, *ChemPhotoChem*, 2019, **2000**, cptc.201900235.

312 K. Yuan, X. Wang, S. K. Mellerup, I. Kozin and S. Wang, *J. Org. Chem.*, 2017, **82**, 13481–13487.

313 H. Ünal, D. Gunceler and E. Mete, *J. Photochem. Photobiol. A Chem.*, 2014, **278**, 14–18.

314 S. Swavey, J. Quinn, M. Coladipietro, K. G. Cox and M. K. Brennaman, *RSC Adv.*, 2017, **7**, 173–179.

315 Y. Kubo, D. Eguchi, A. Matsumoto, R. Nishiyabu, H. Yakushiji, K. Shigaki and M. Kaneko, *J. Mater. Chem. A*, 2014, **2**, 5204–5211.

316 D. R. Shinde, P. S. Tambade, K. M. Gadave, K. S. Pawar, M. Naushad and H. M. Pathan, *J. Mater. Sci. Mater. Electron.*, 2017, **28**, 11311–11316.

317 I. Bodurov, T. Yovcheva and S. Sainov, *J. Phys. Conf. Ser.*, 2014, **558**, 012062.

318 J. C. Garcia, L. M. R. Scolfaro, A. T. Lino, V. N. Freire, G. A. Farias, C. C. Silva, H. W. L. Alves, S. C. P. Rodrigues and E. F. da Silva, *J. Appl. Phys.*, 2006, **100**, 104103.

319 J. Massin, L. Ducasse, T. Toupance and C. Olivier, *J. Phys. Chem. C*, 2014, **118**, 10677–10685.

320 H. Masui, M. M. Maitani, S. Fuse, A. Yamamura, Y. Ogomi, S. Hayase, T. Kaiho, H. Tanaka, Y. Wada and T. Takahashi, *Asian J. Org. Chem.*, 2018, **7**, 458–464.

321 J. Koskikallio, *Acta Chem. Scand.*, 1956, **10**, 822–830.

322 J. Tamada and R. Langer, *J. Biomater. Sci. Polym. Ed.*, 1992, **3**, 315–353.

323 J.-H. Yum, E. Baranoff, S. Wenger, M. K. Nazeeruddin and M. Grätzel, *Energy Environ. Sci.*, 2011, **4**, 842–857.

324 D. Zhang, W. Wang, Y. Liu, X. Xiao, W. Zhao, B. Zhang and Y. Cao, *J. Photochem. Photobiol. A Chem.*, 2000, **135**, 235–240.

325 D. Colonna, V. Capogna, A. Lembo, T. M. Brown, A. Reale and A. Di Carlo, *Appl. Phys. Express*, 2012, **5**, 022303.

326 A. Yella, H.-W. Lee, H. N. Tsao, C. Yi, A. K. Chandiran, M. K. Nazeeruddin, E. W.-G. Diau, C.-Y. Yeh, S. M. Zakeeruddin and M. Gratzel, *Science (80-.).*, 2011, **334**, 629–634.

327 C. Siegers, J. Hohl-Ebinger, B. Zimmermann, U. Würfel, R. Mülhaupt, A. Hinsch and R. Haag, *ChemPhysChem*, 2007, **8**, 1548–1556.

328 C. Siegers, B. Olàh, U. Würfel, J. Hohl-Ebinger, A. Hinsch and R. Haag, *Sol. Energy Mater. Sol. Cells*, 2009, **93**, 552–563.

329 G. H. Rao, A. Venkateswararao, L. Giribabu, L. Han, I. Bedja, R. K. Gupta, A. Islam and S. P. Singh, *Phys. Chem. Chem. Phys.*, 2016, **18**, 14279–14285.

330 Z. S. Wang, Y. Cui, Y. Dan-oh, C. Kasada, A. Shinpo and K. Hara, *J. Phys. Chem. C*, 2007, **111**, 7224–7230.

331 K. Sayama, S. Tsukagoshi, K. Hara, Y. Ohga, A. Shinpou, Y. Abe, S. Suga and H. Arakawa, *J. Phys. Chem. B*, 2002, **106**, 1363–1371.

332 A. Ehret, L. Stuhl and M. T. Spitler, *J. Phys. Chem. B*, 2001, **105**, 9960–9965.

333 C. Qin, Y. Numata, S. Zhang, A. Islam, X. Yang, K. Sodeyama, Y. Tateyama and L. Han, *Adv. Funct. Mater.*, 2013, **23**, 3782–3789.

334 L. Furnell, P. J. Holliman, A. Connell, E. W. Jones, R. Hobbs, C. P. Kershaw, R. Anthony, J. Searle, T. Watson and J. McGettrick, *Sustain. Energy Fuels*, 2017, **1**, 362–370.

8 Appendix

8.1 NMR Spectra

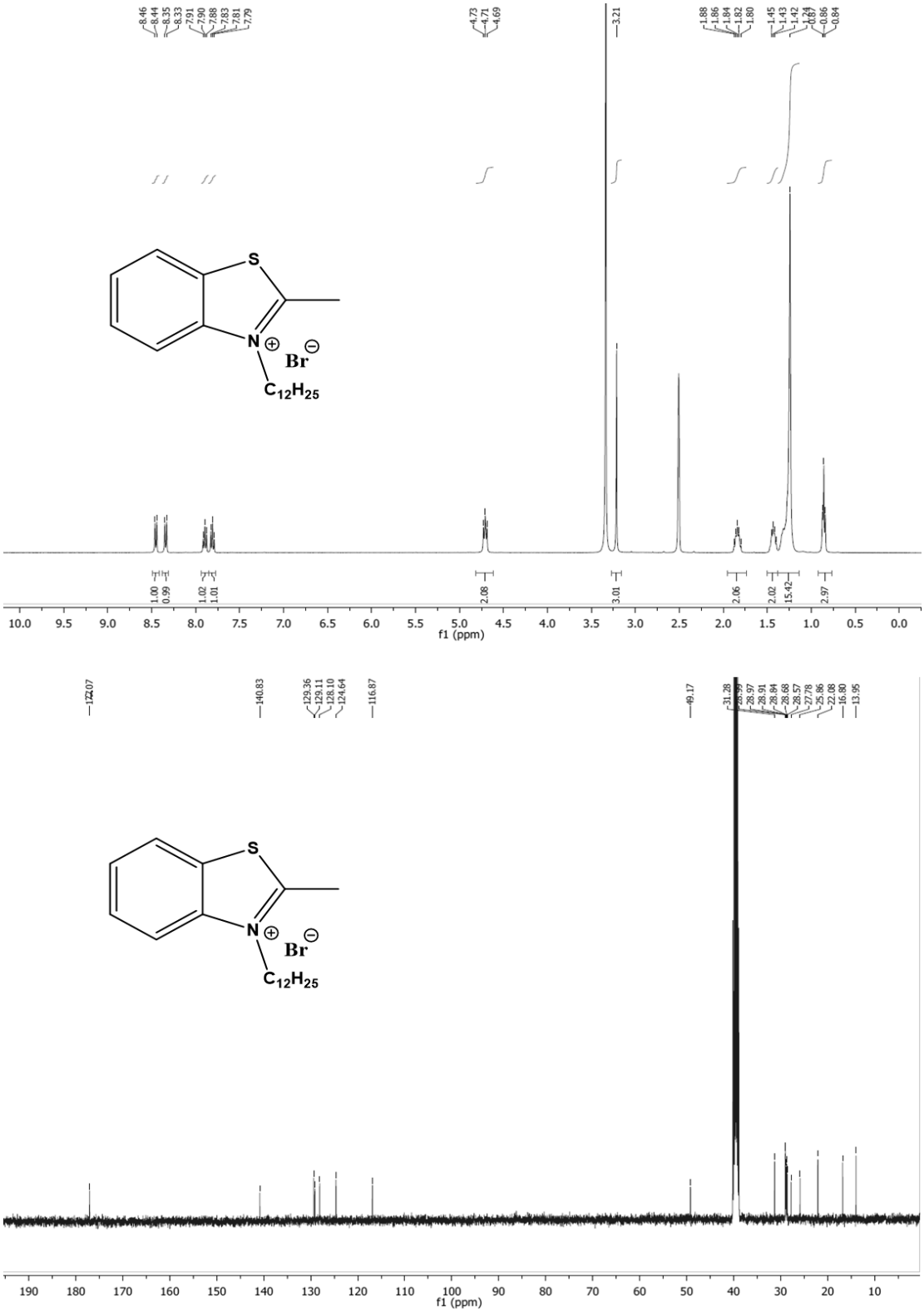

Figure 8.1 - ^{1}H (400 MHz) and ^{13}C (101 MHz) spectra of (**1**) in DMSO

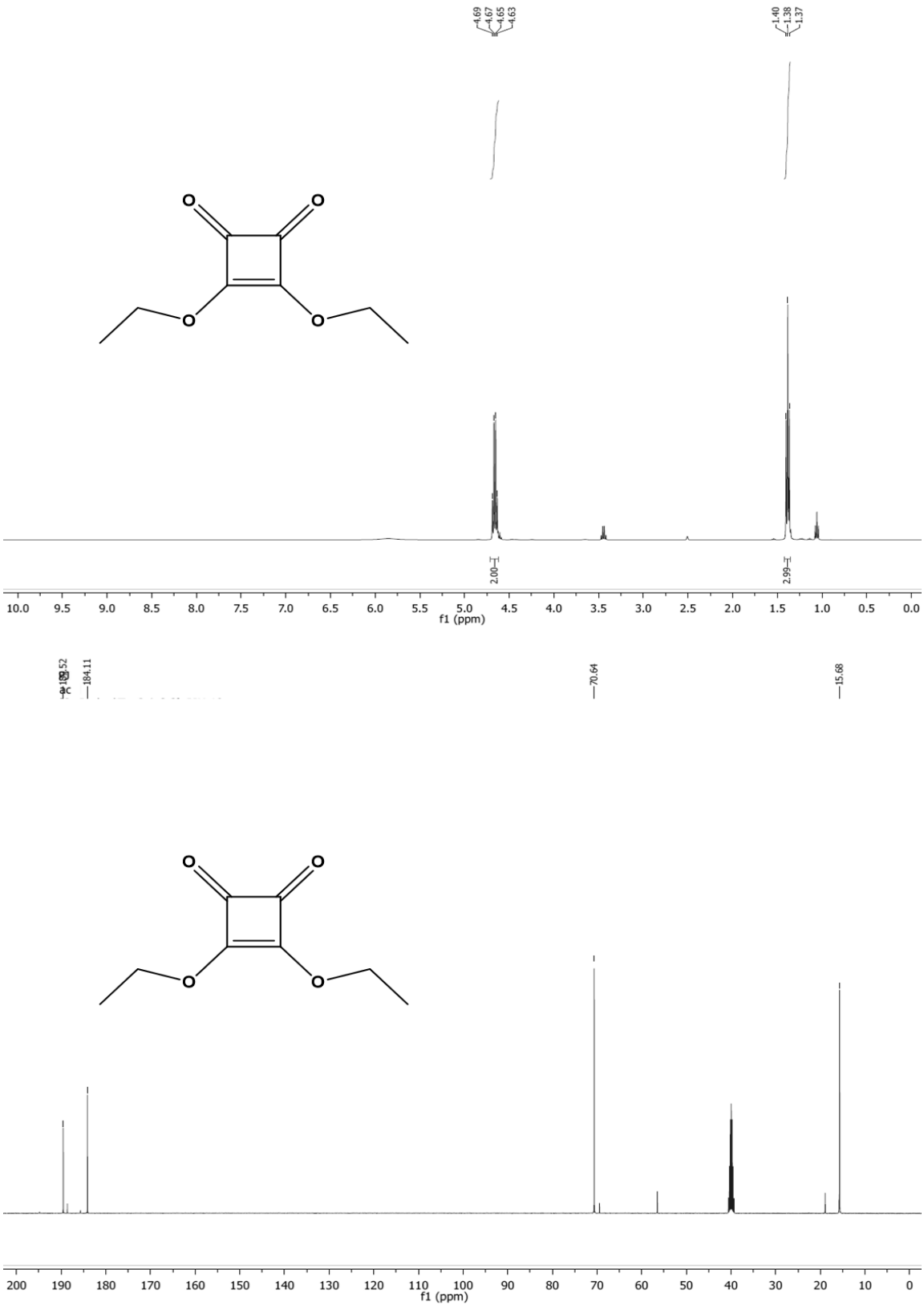

Figure 8.2 - ^{1}H (400 MHz) and ^{13}C (101 MHz) spectra of (**2**) in DMSO

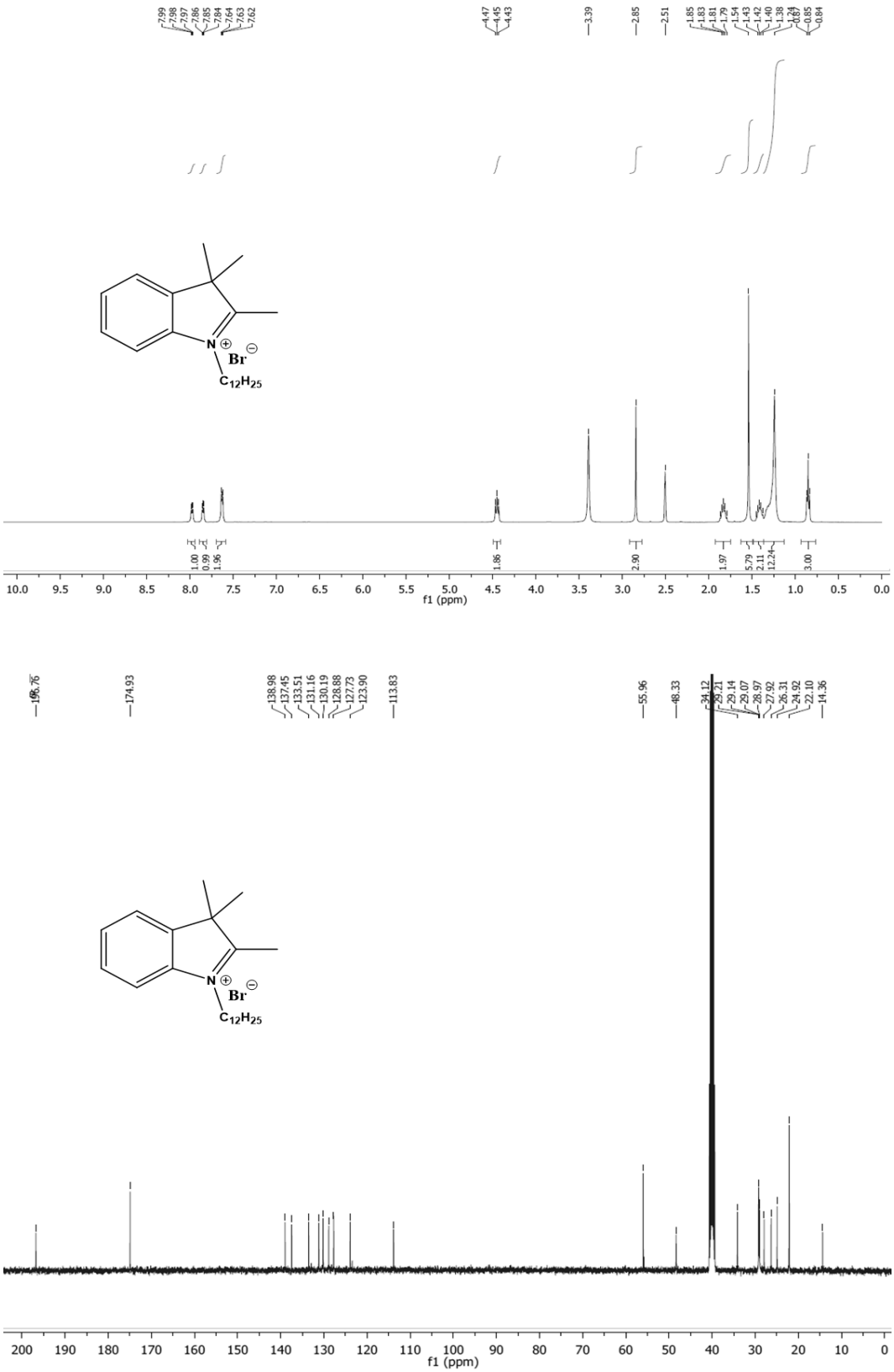

Figure 8.3 - ^{1}H (400 MHz) and ^{13}C (101 MHz) spectra of (**3**) in DMSO

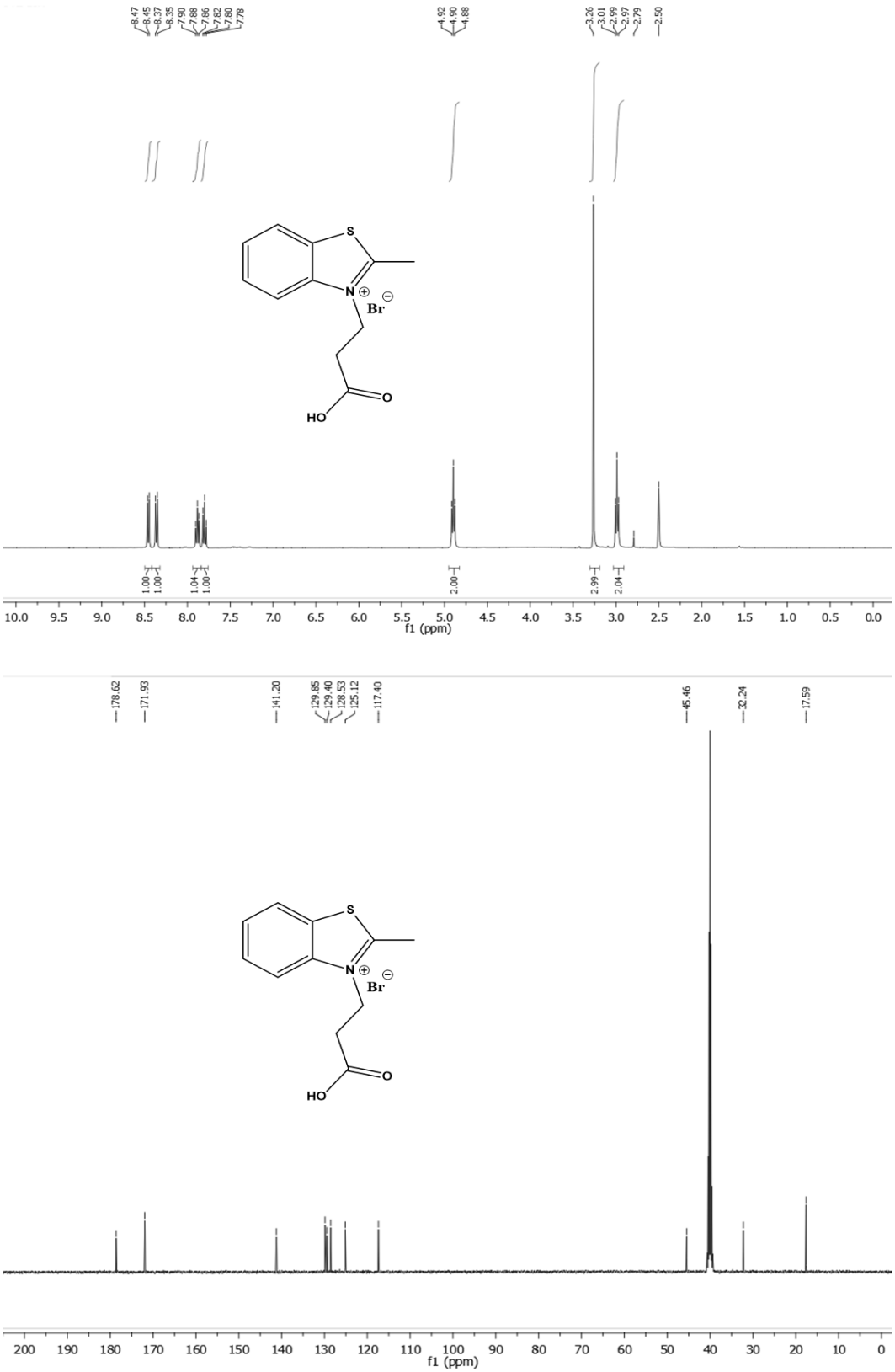

Figure 8.4 - ^{1}H (400 MHz) and ^{13}C (101 MHz) spectra of (**4**) in DMSO

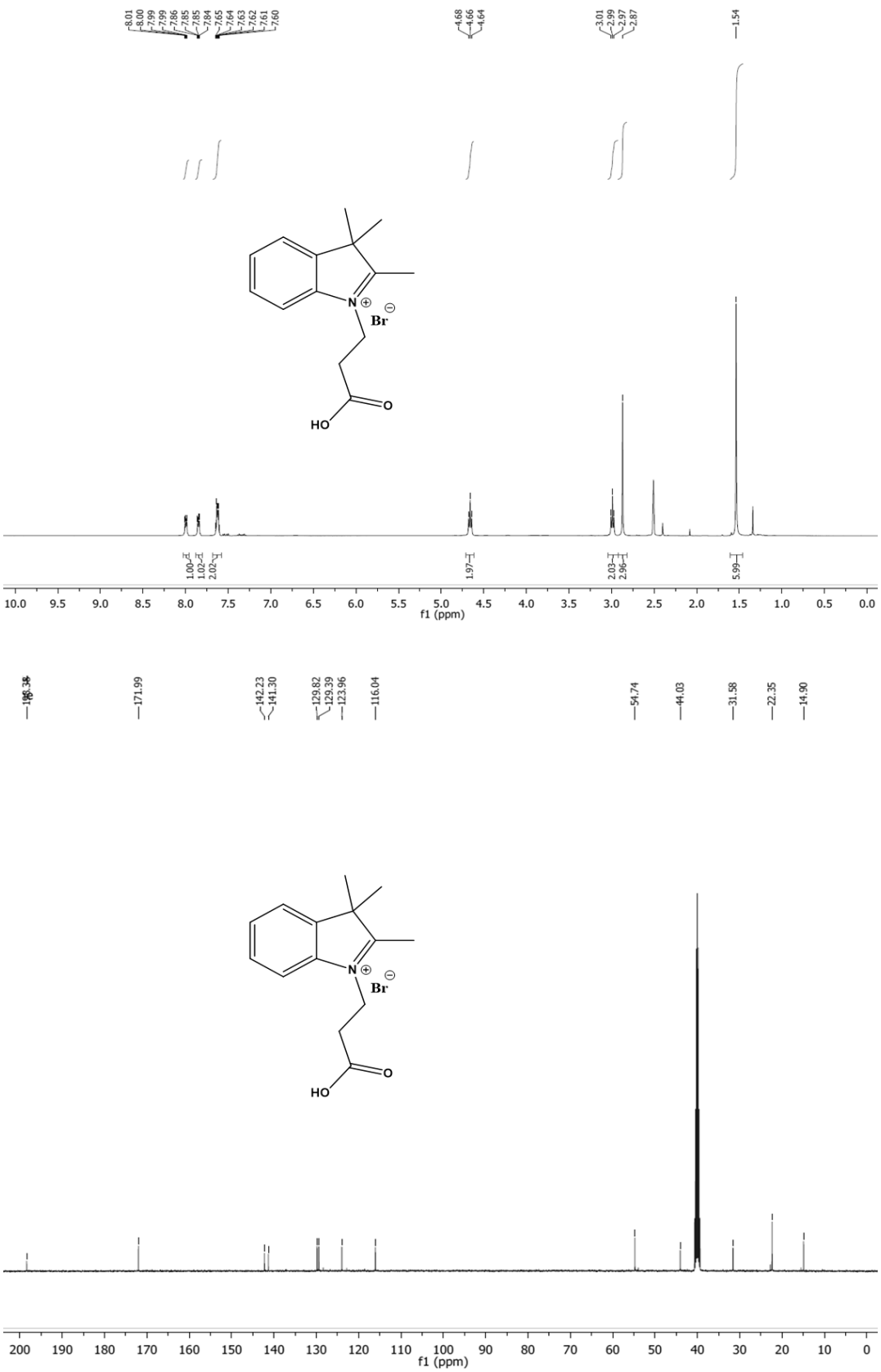

Figure 8.5 - ^{1}H (400 MHz) and ^{13}C (101 MHz) spectra of (**5**) in DMSO

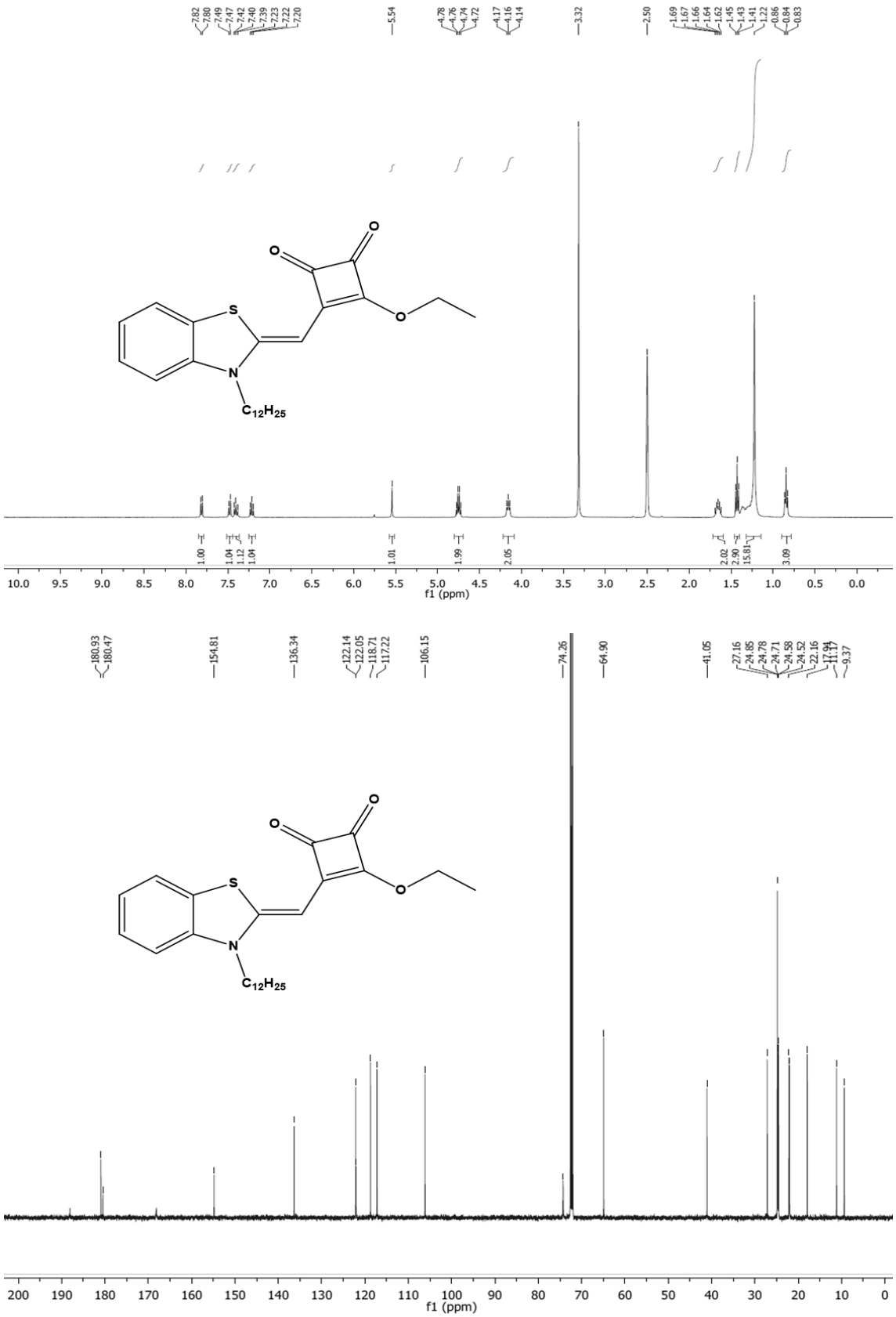

Figure 8.6 - ^{1}H (400 MHz) and ^{13}C (126 MHz) spectra of (**6**) in DMSO

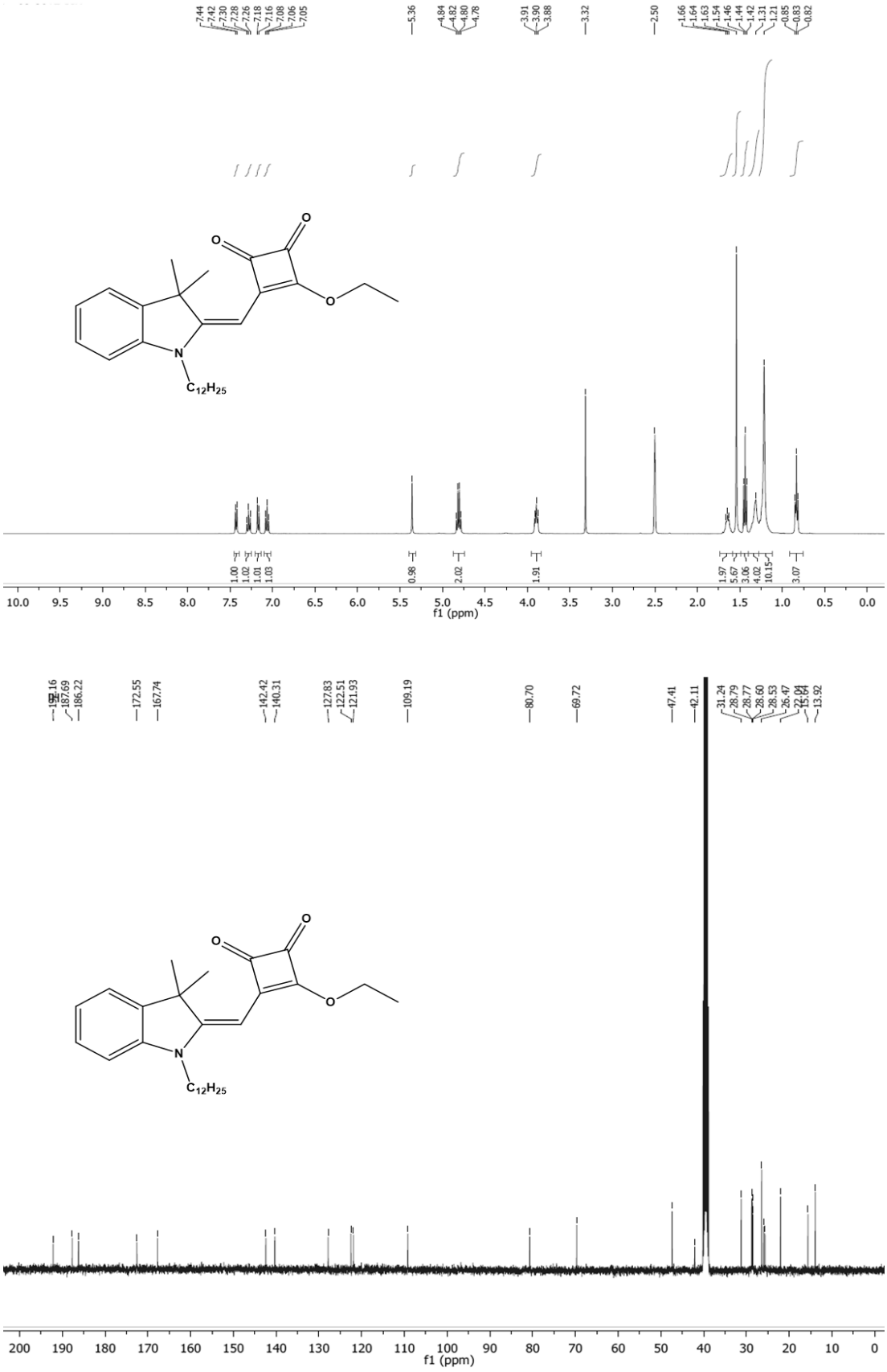

Figure 8.7 - ^{1}H (400 MHz) and ^{13}C (101 MHz) spectra of (**7**) in DMSO

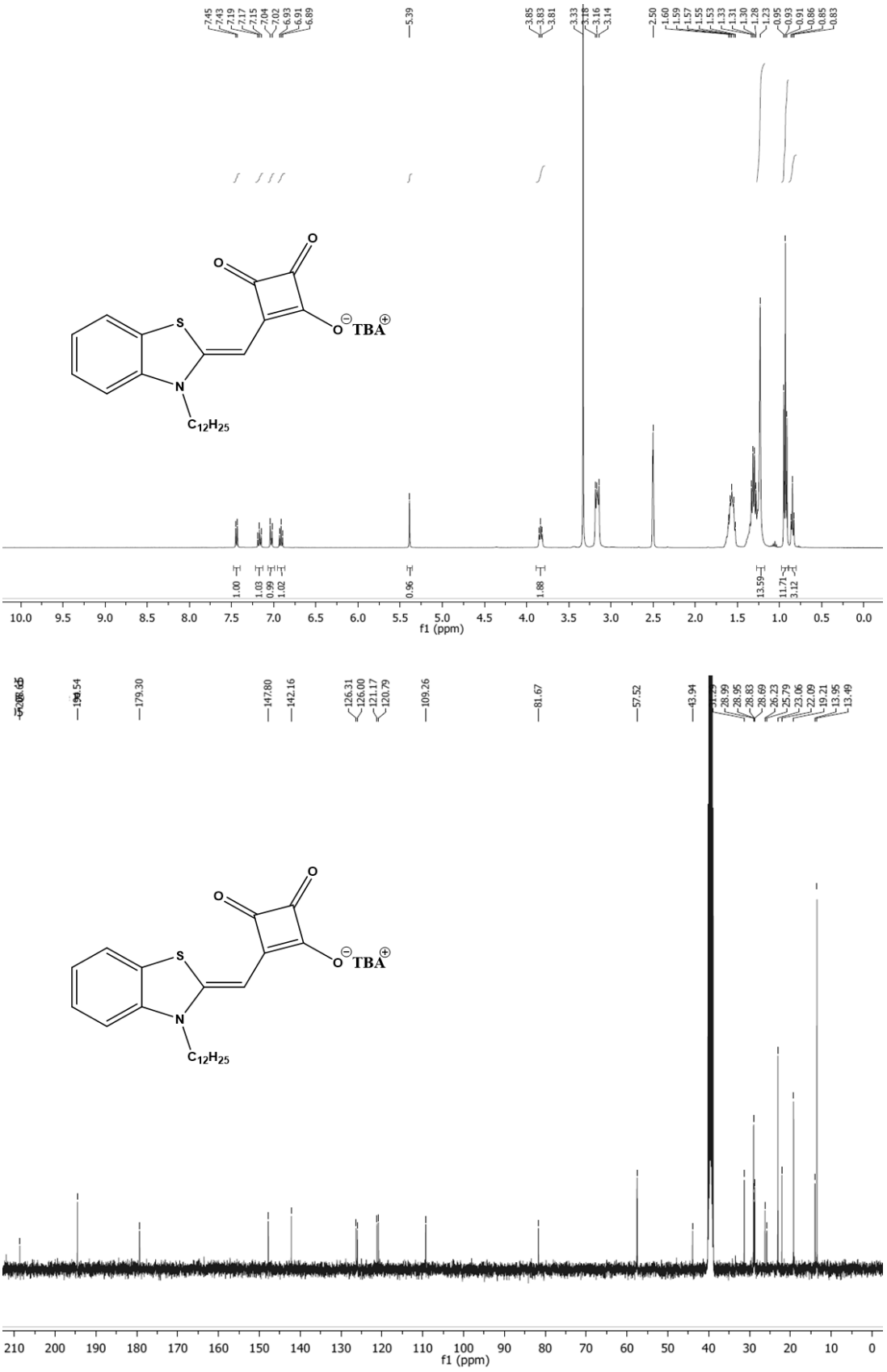

Figure 8.8 - ^{1}H (400 MHz) and ^{13}C (101 MHz) spectra of (**D1**) in DMSO

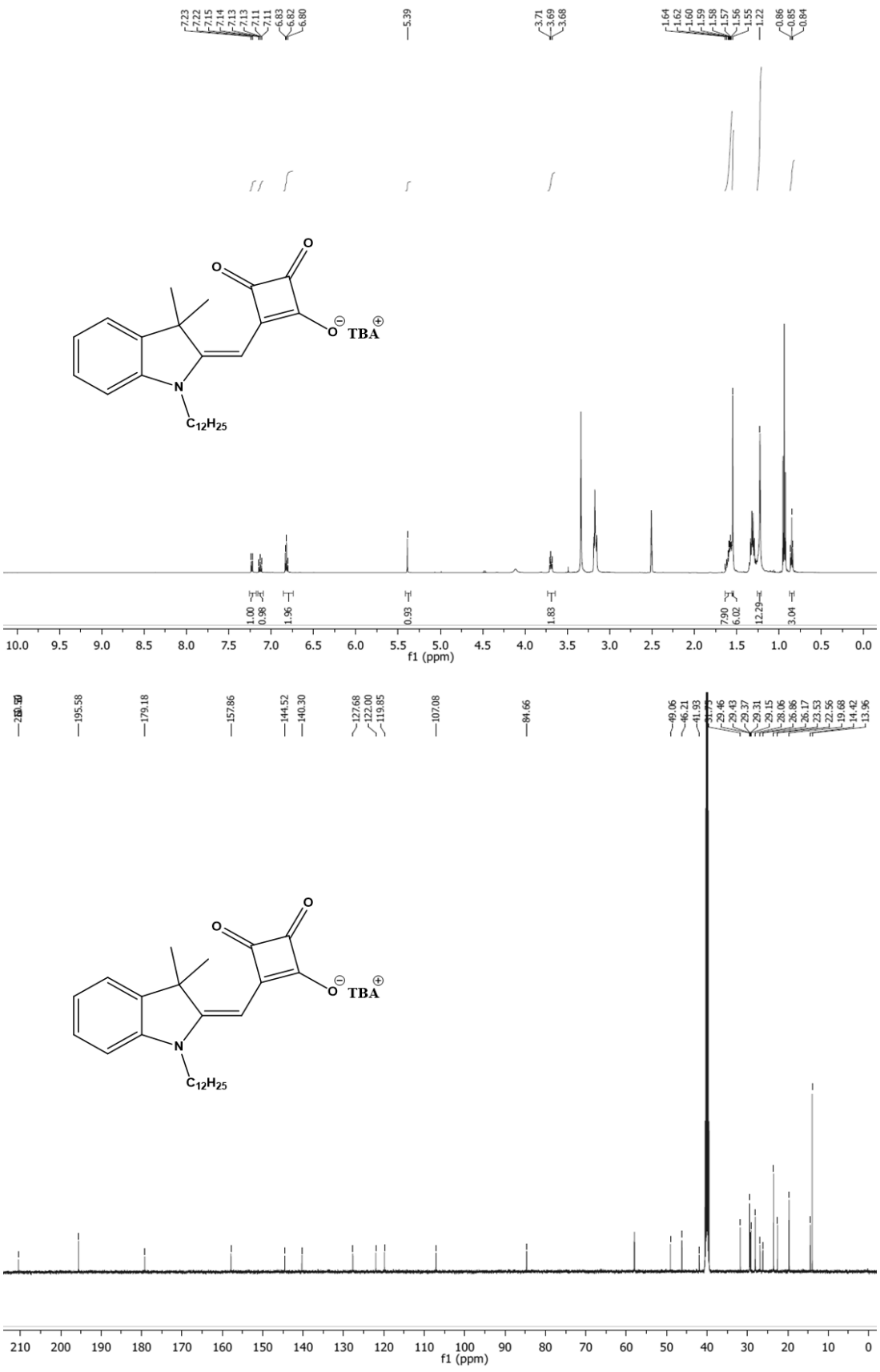

Figure 8.9 - ^{1}H (500 MHz) and ^{13}C (126 MHz) spectra of (**D2**) in DMSO

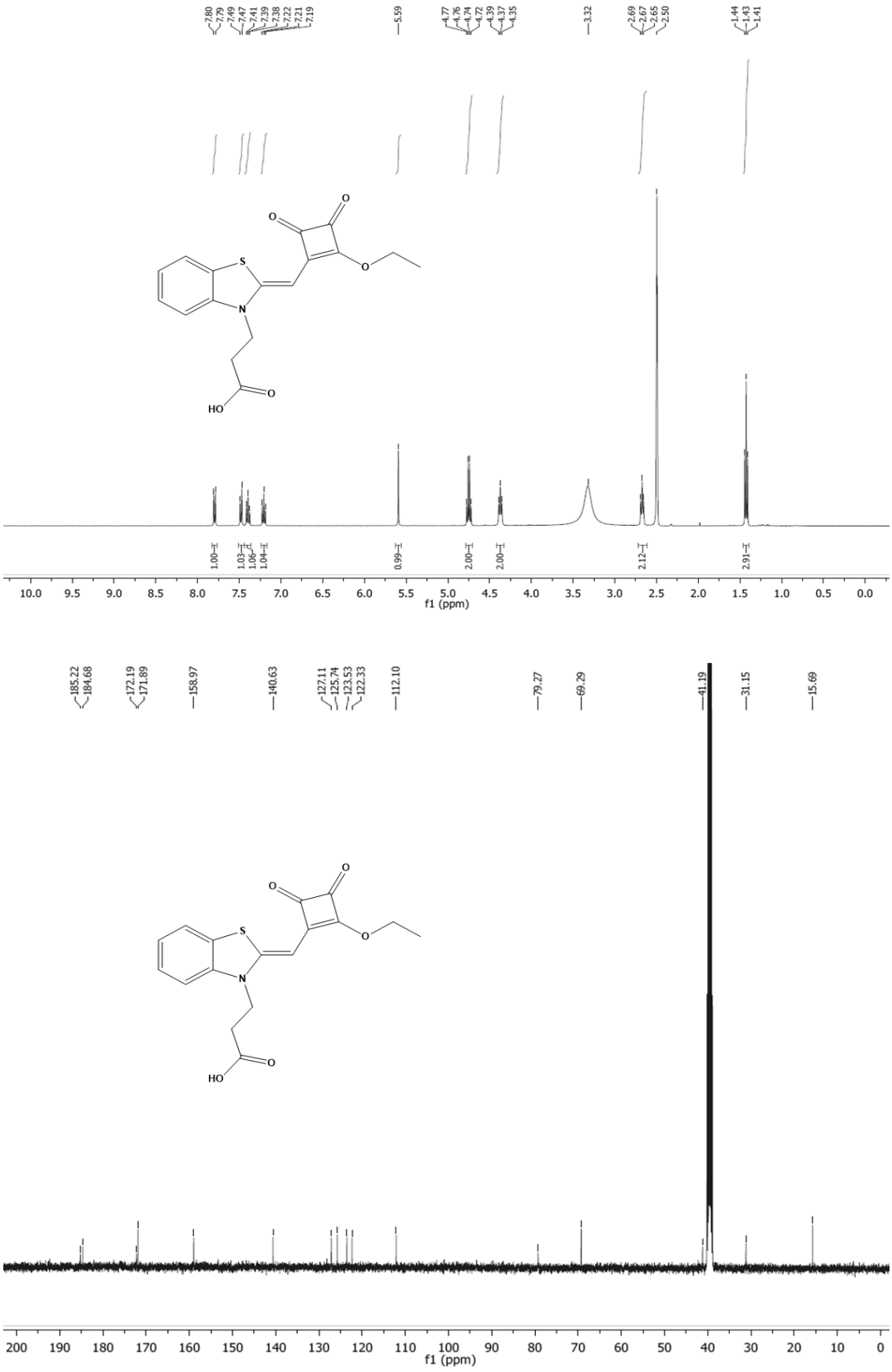

Figure 8.10 - ^{1}H (400 MHz) and ^{13}C (101 MHz) spectra of (**D3**) in DMSO

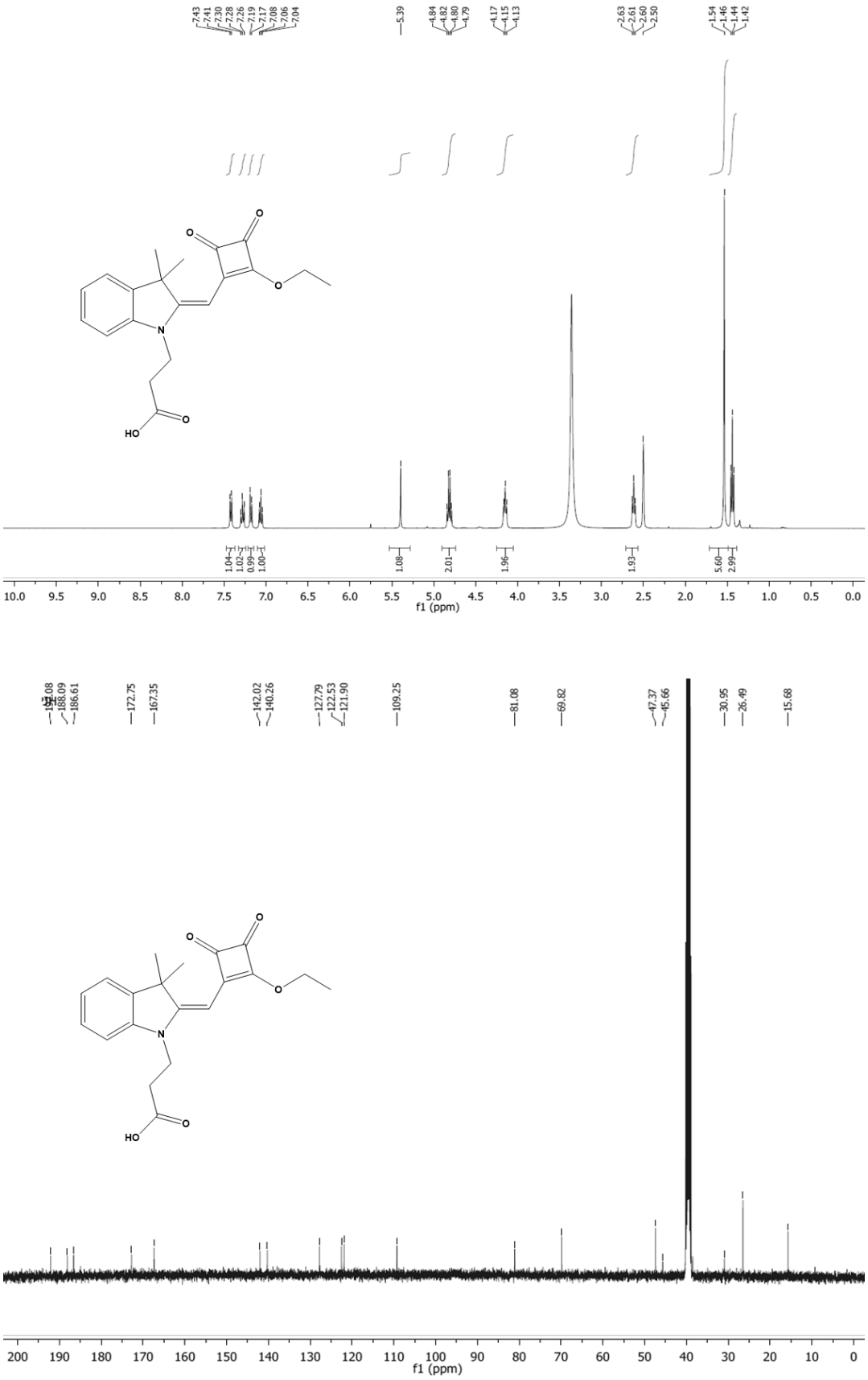

Figure 8.11 - ^{1}H (400 MHz) and ^{13}C (101 MHz) spectra of (**D4**) in DMSO

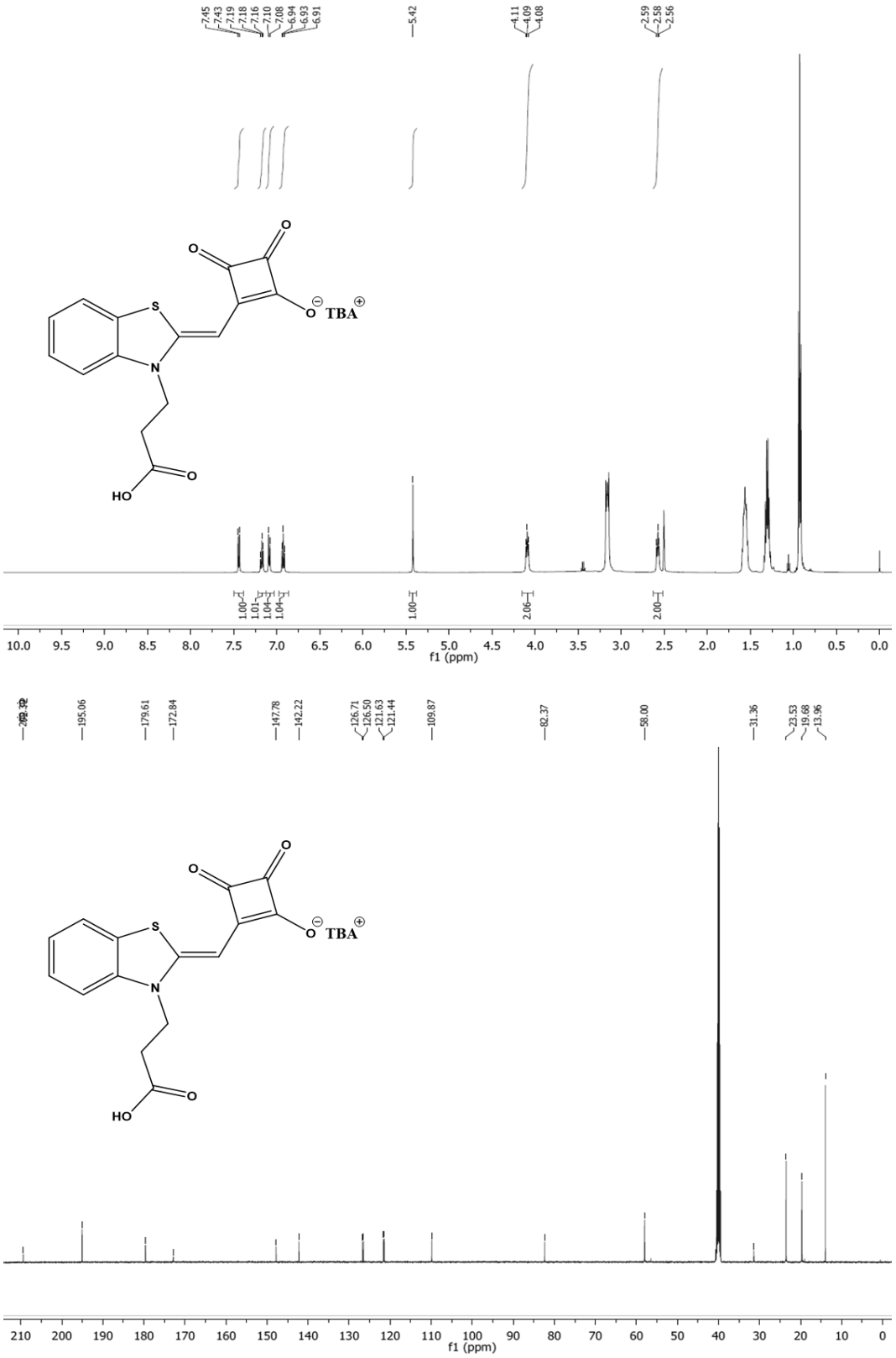

Figure 8.12 - ^{1}H (500 MHz) and ^{13}C (126 MHz) spectra of (**D5**) in DMSO

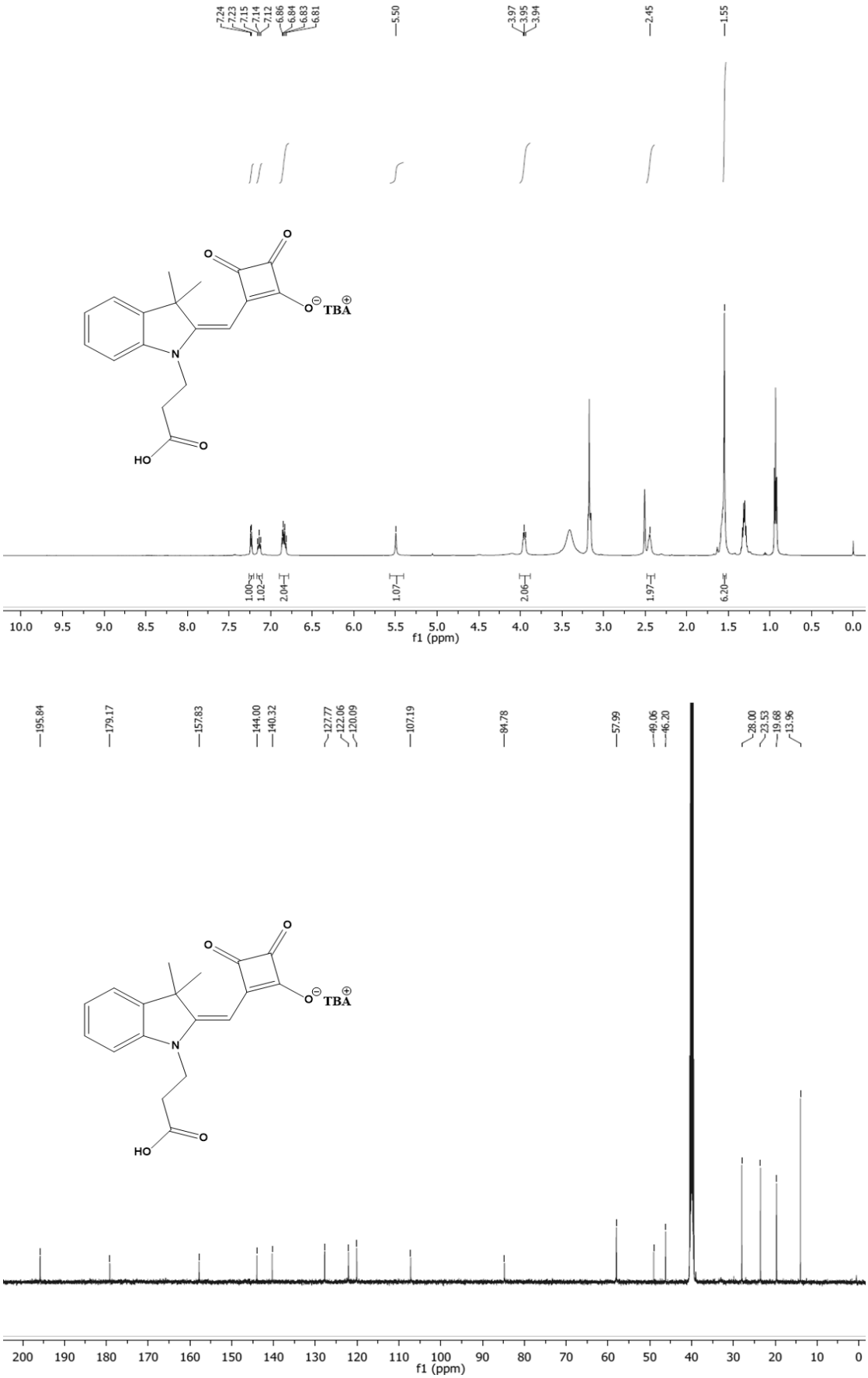

Figure 8.13 - ^{1}H (500 MHz) and ^{13}C (126 MHz) spectra of (**D6**) in DMSO

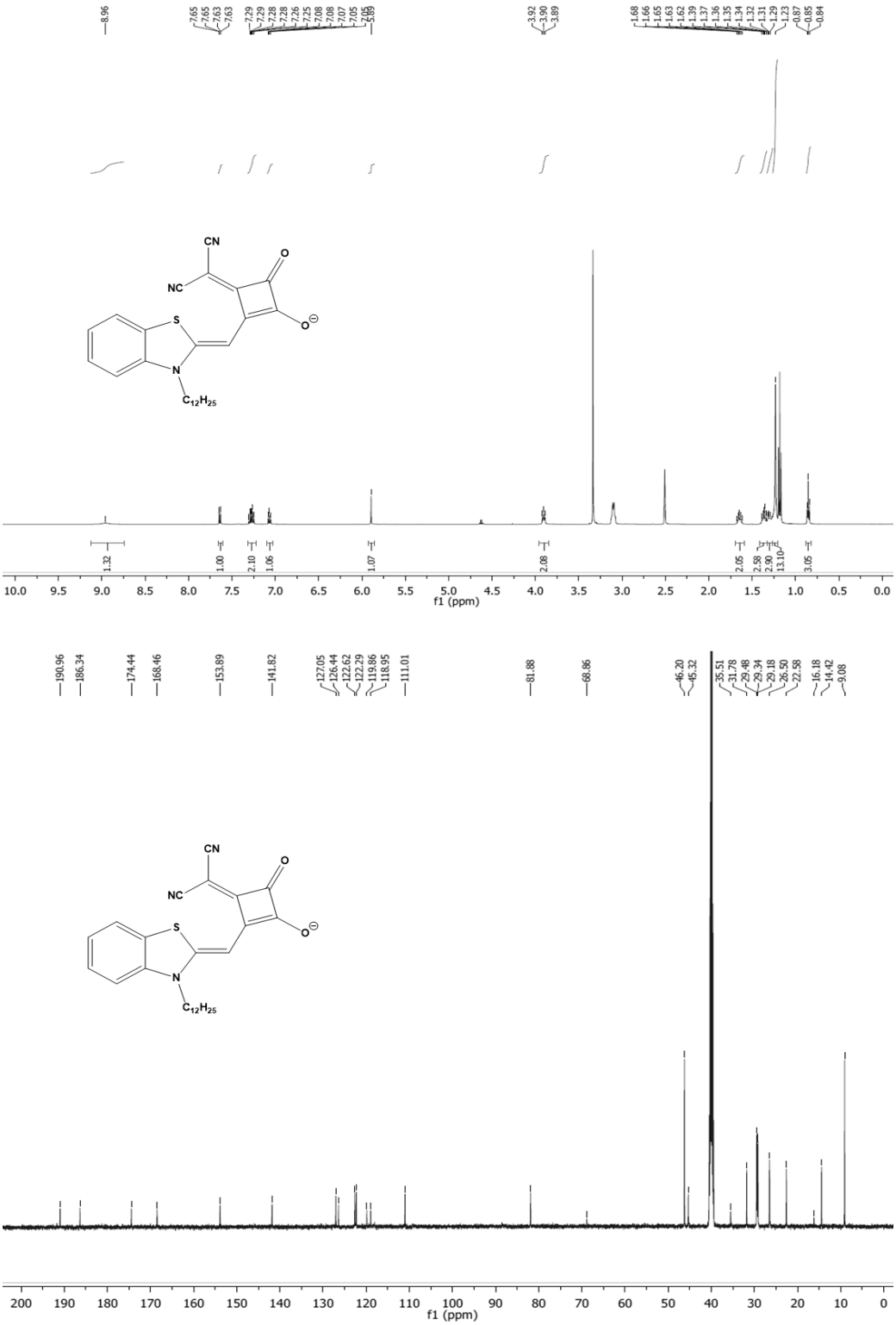

Figure 8.14 - ^{1}H (500 MHz) and ^{13}C (126 MHz) spectra of (**D7**) in DMSO

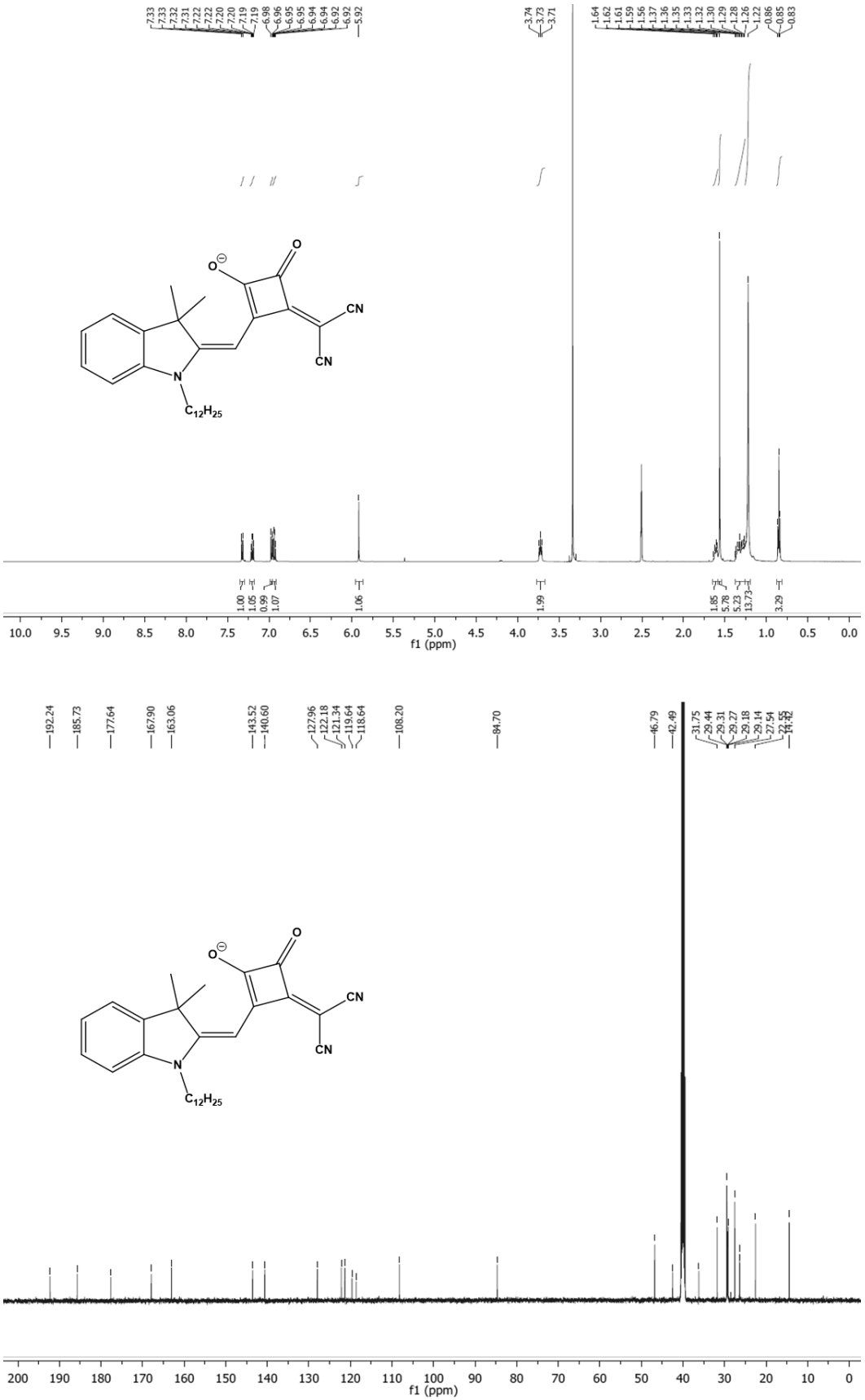

Figure 8.15 - ^{1}H (500 MHz) and ^{13}C (126 MHz) spectra of (**D8**) in DMSO

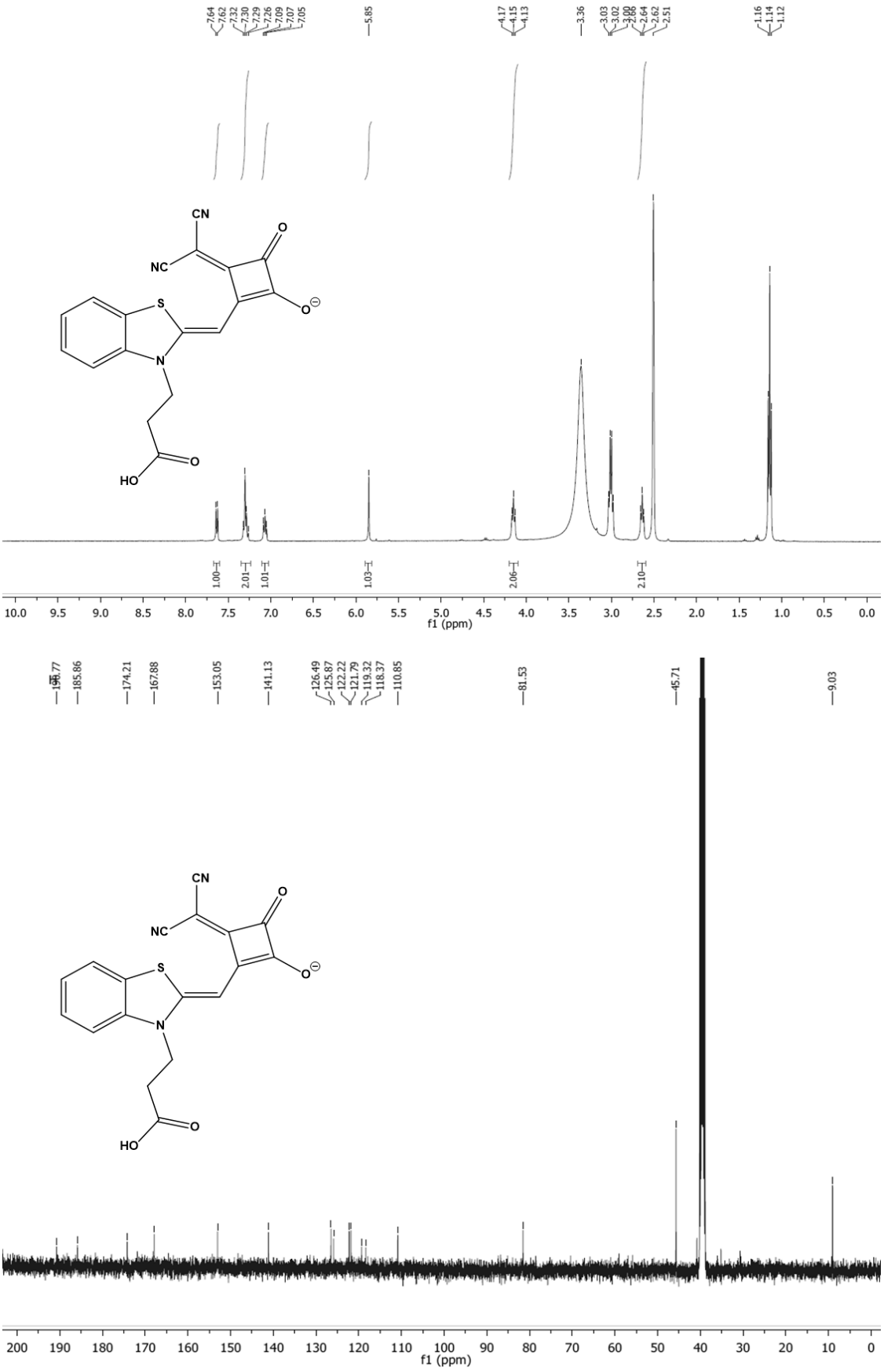

Figure 8.16 - ^{1}H (400 MHz) and ^{13}C (101 MHz) spectra of (**D9**) in DMSO

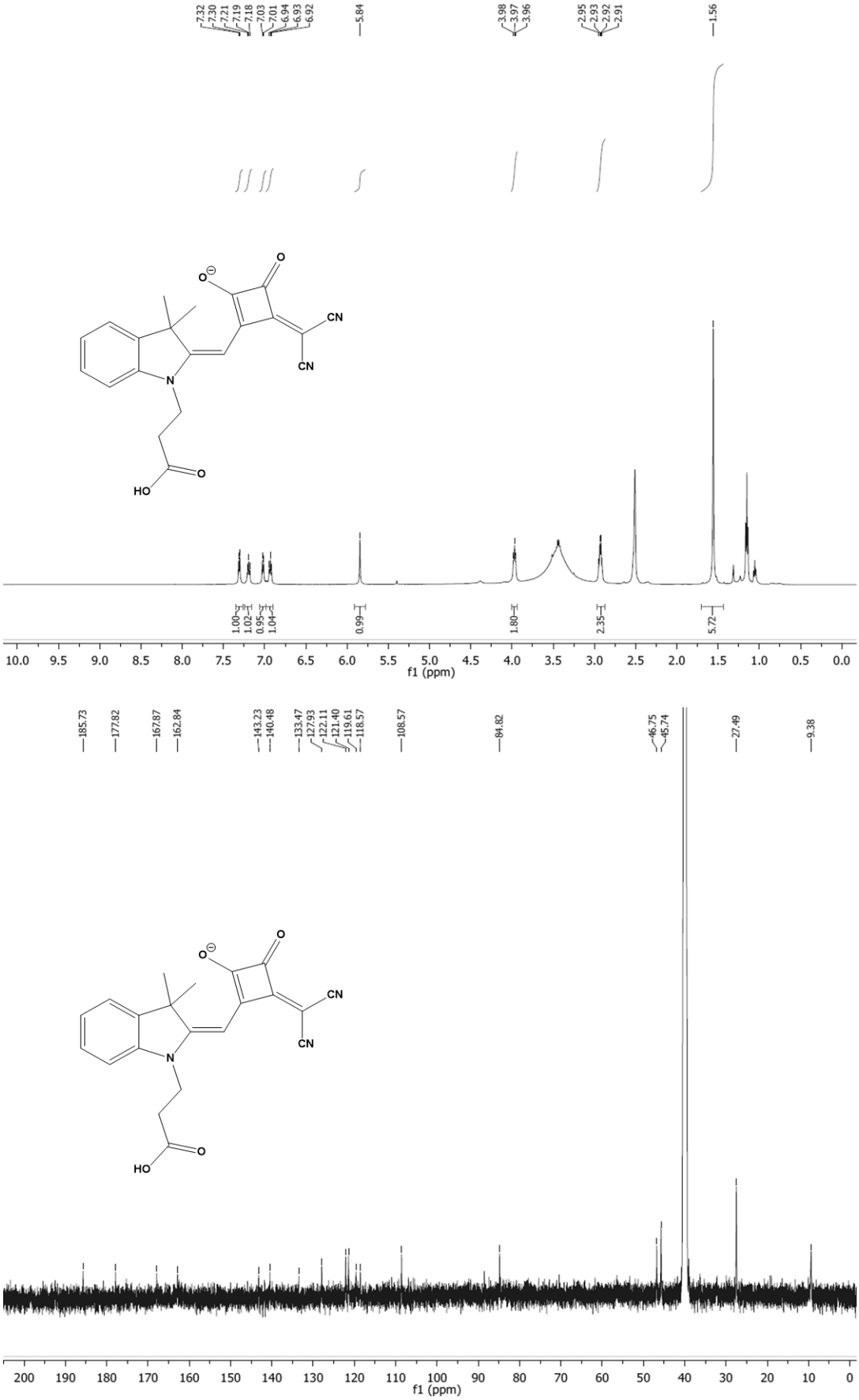

Figure 8.17 - ^{1}H (500 MHz) and ^{13}C (126 MHz) spectra of (**D10**) in DMSO

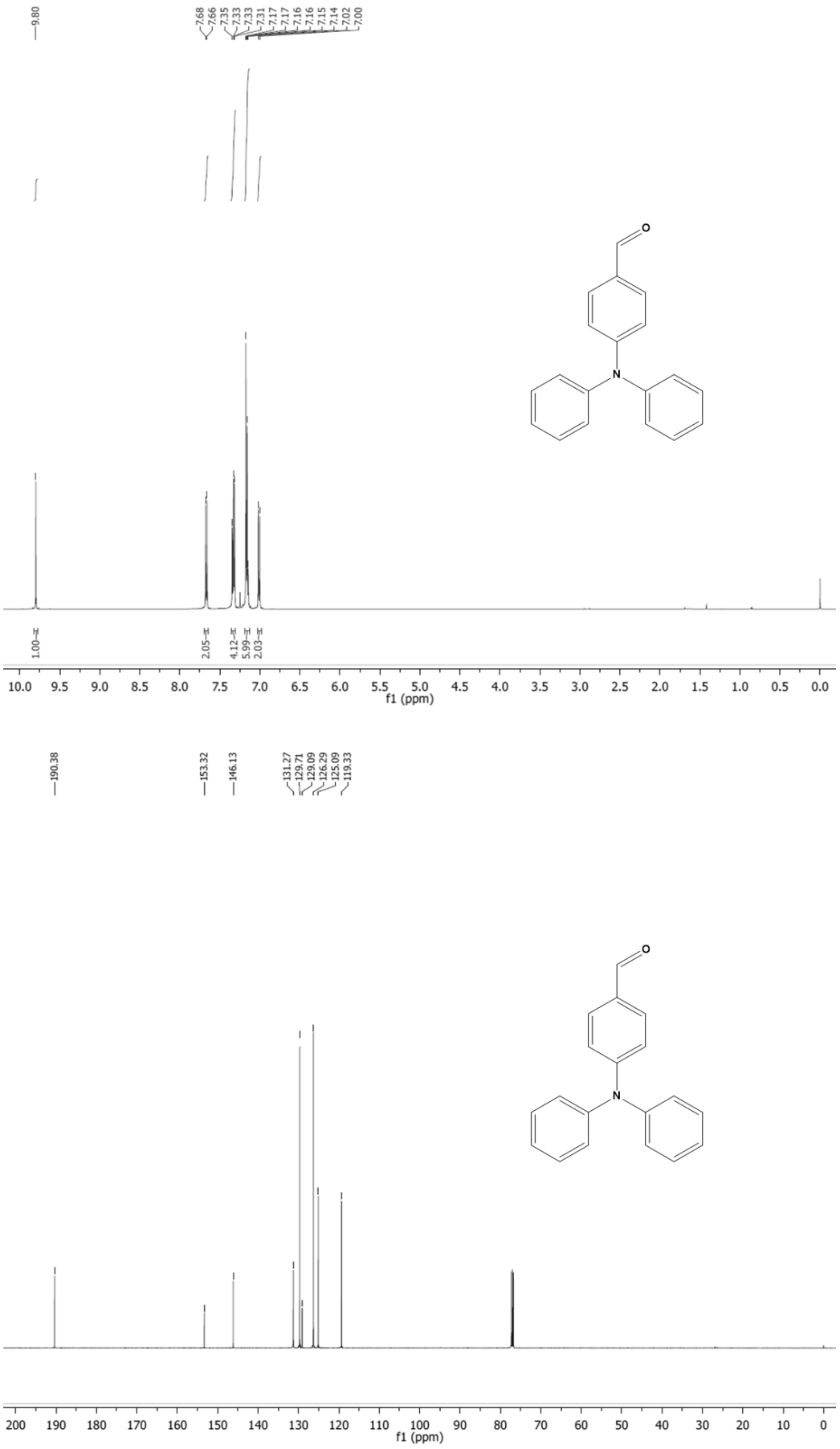

Figure 8.18 - ^{1}H (500 MHz) and ^{13}C (126 MHz) spectra of (**YD-S1**) in $CDCl_3$

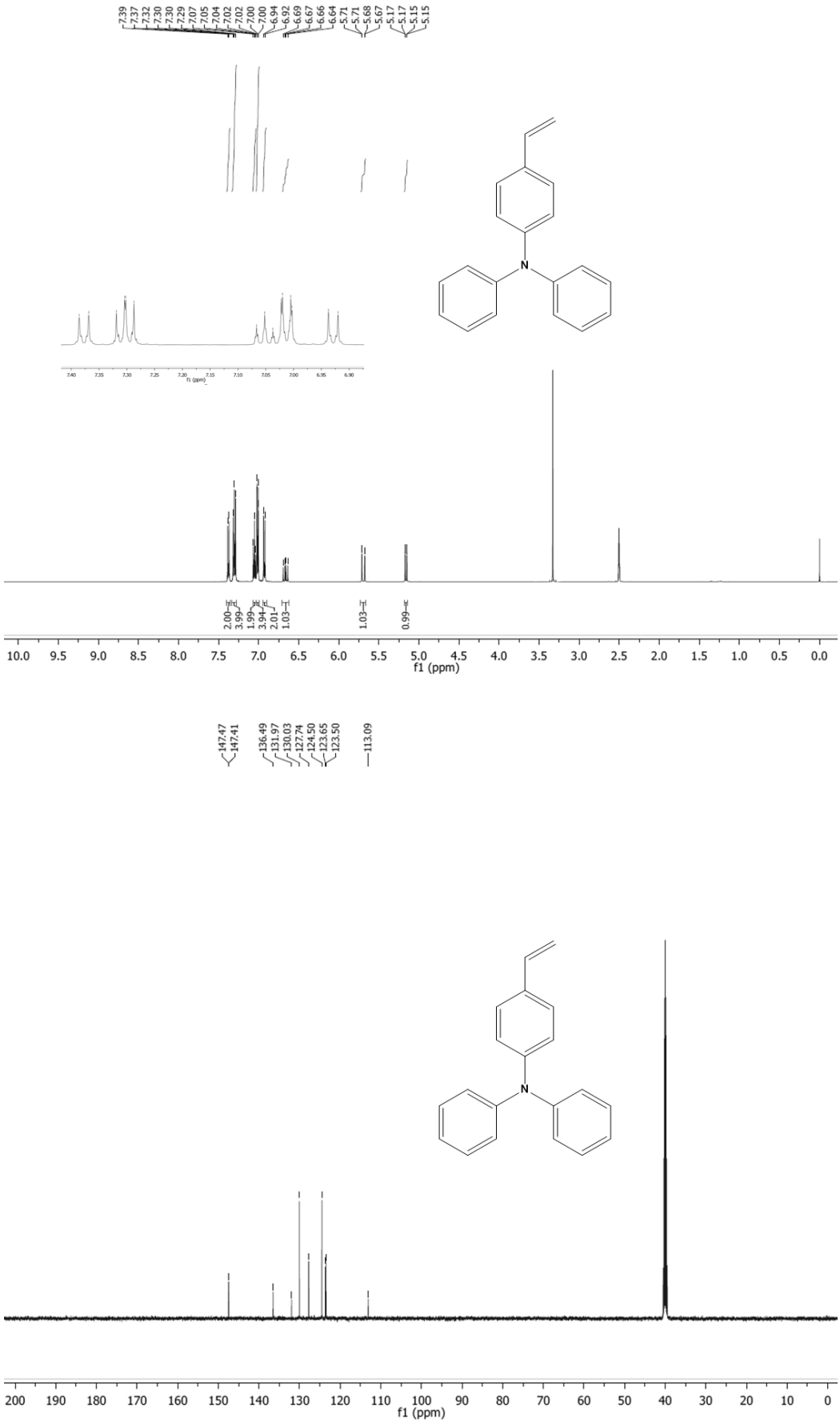

Figure 8.19 - ^{1}H (500 MHz) and ^{13}C (126 MHz) spectra of (**YD-S2**) in DMSO

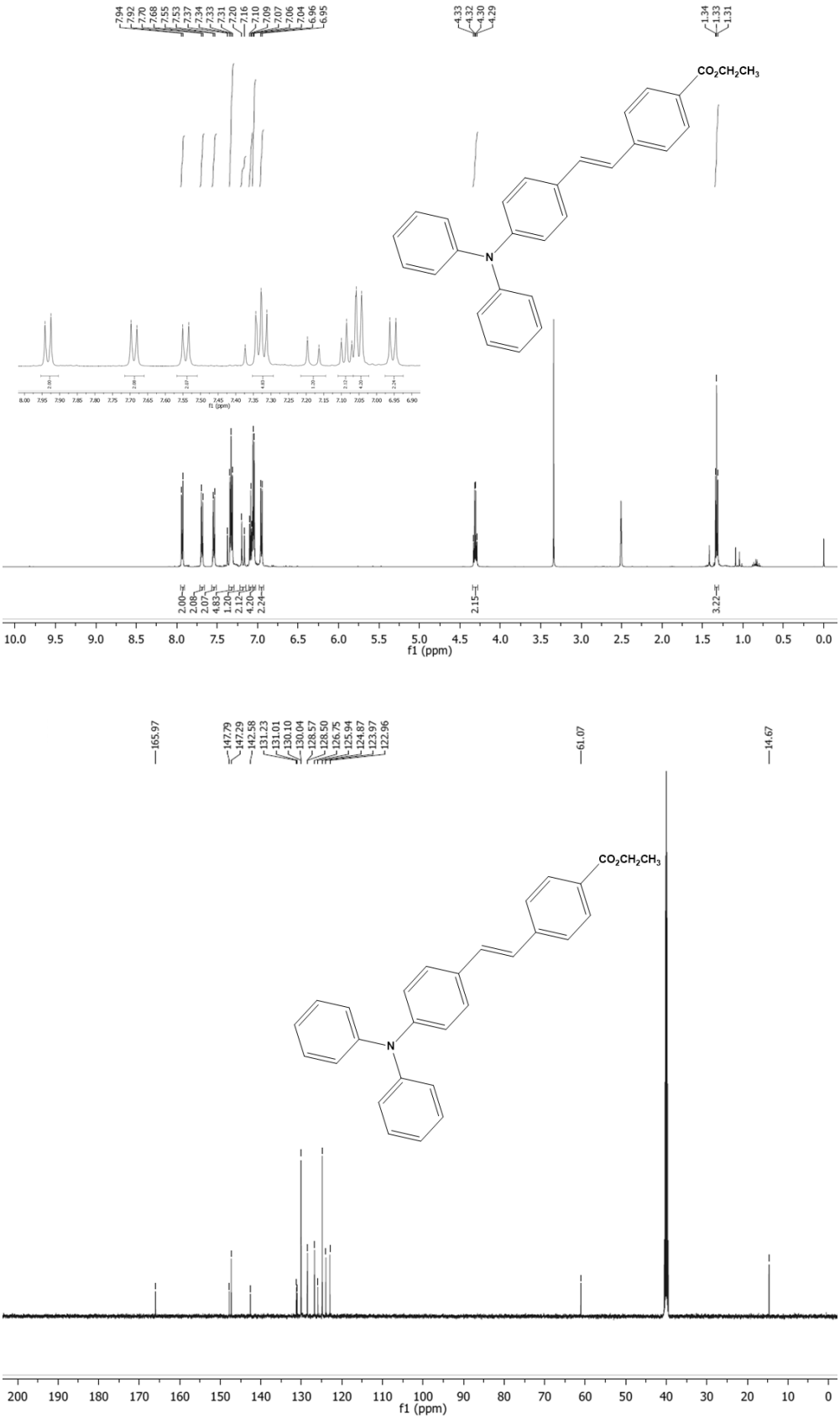

Figure 8.20 - ^{1}H (500 MHz) and ^{13}C (126 MHz) spectra of (**YD-S3**) in DMSO

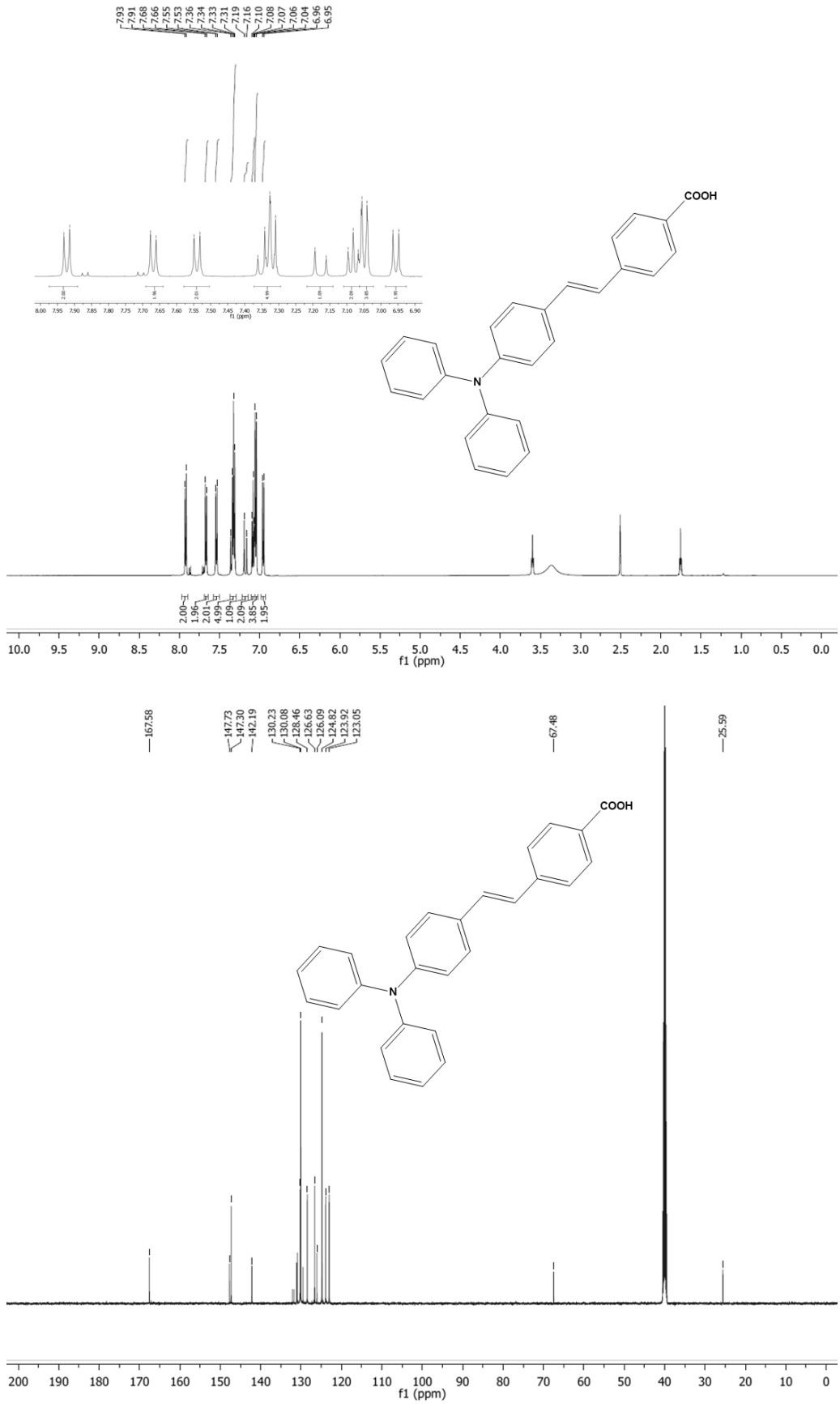

Figure 8.21- ^{1}H (500 MHz) and ^{13}C (126 MHz) spectra of (**YD-Ac**) in DMSO

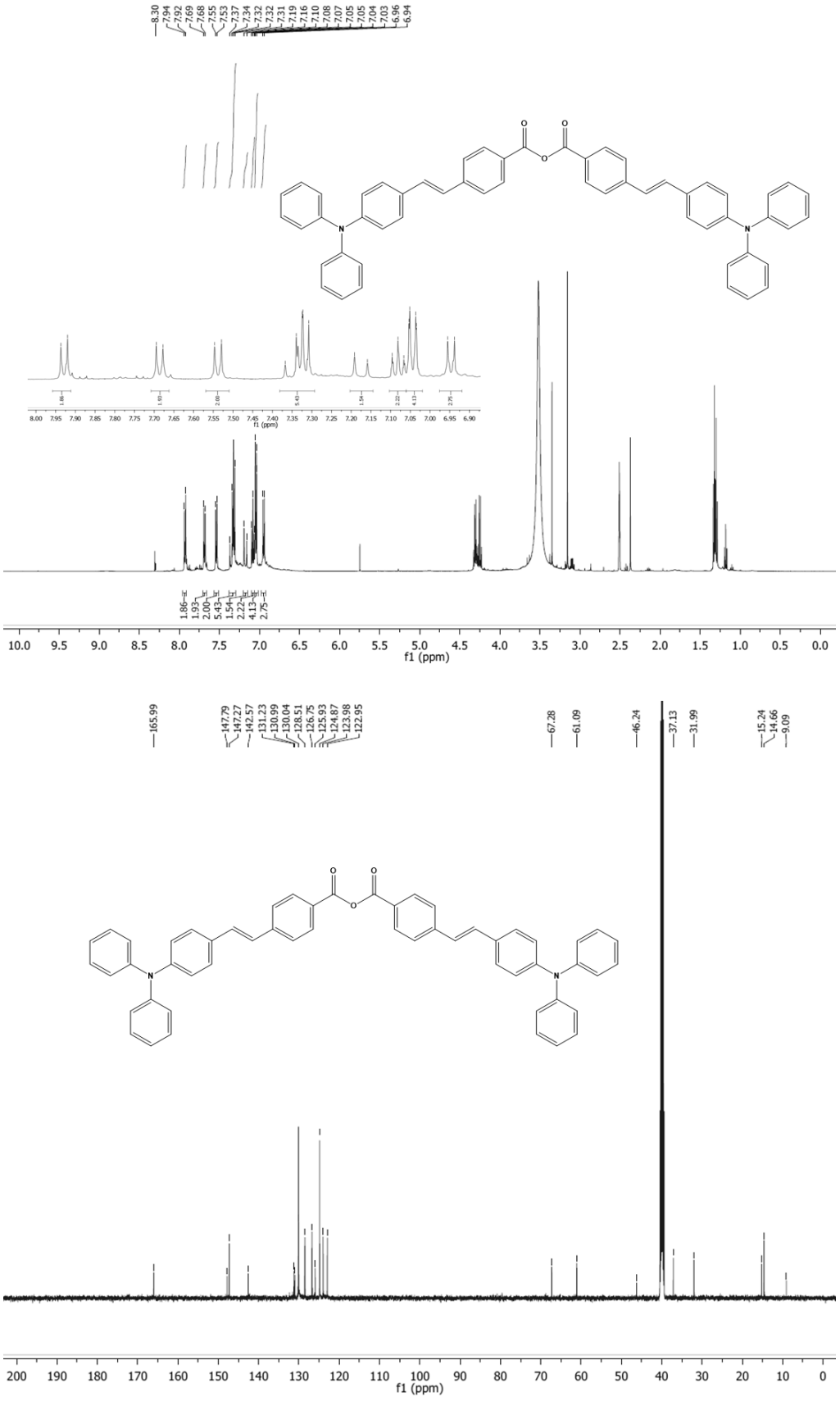

Figure 8.22 - ^{1}H (500 MHz) and ^{13}C (126 MHz) spectra of (**YD-An**) in DMSO

8.2 Mass spectrometry

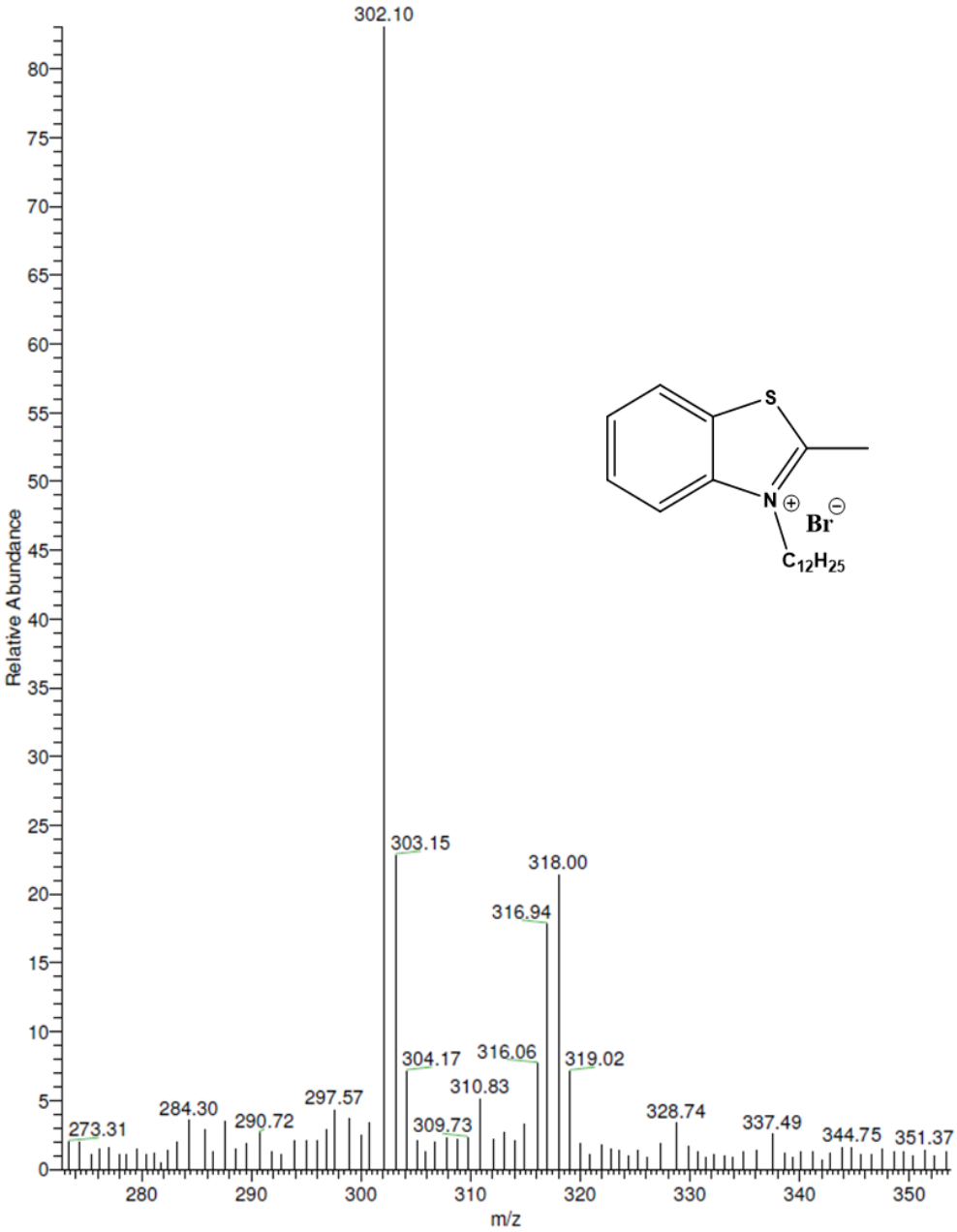

Figure 8.23 – Mass spectrometry of (**1**)

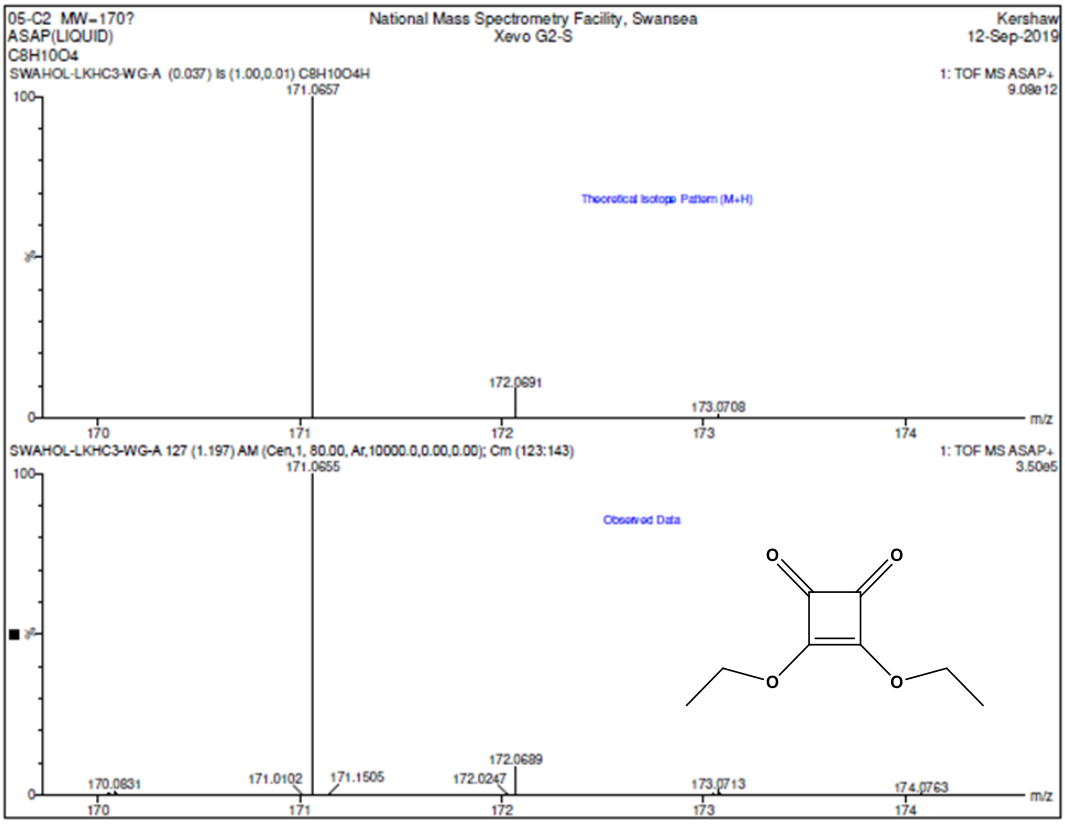

Figure 8.24 – Mass spectrometry of (**2**)

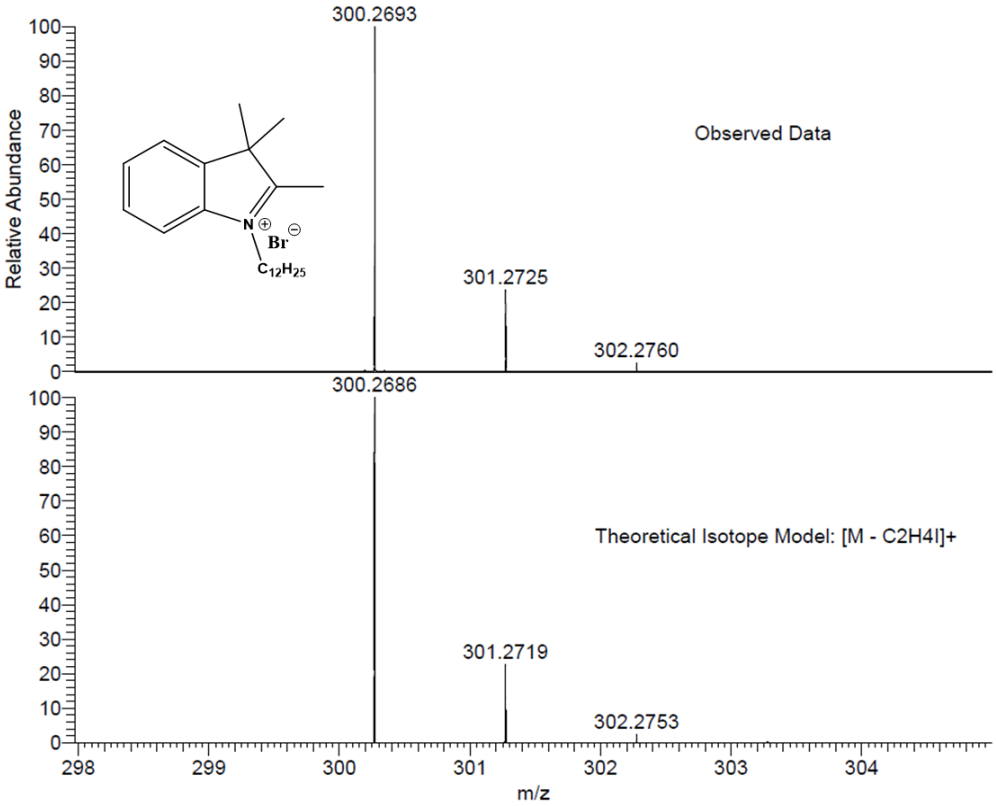

Figure 8.25 – Mass spectrometry of (**3**)

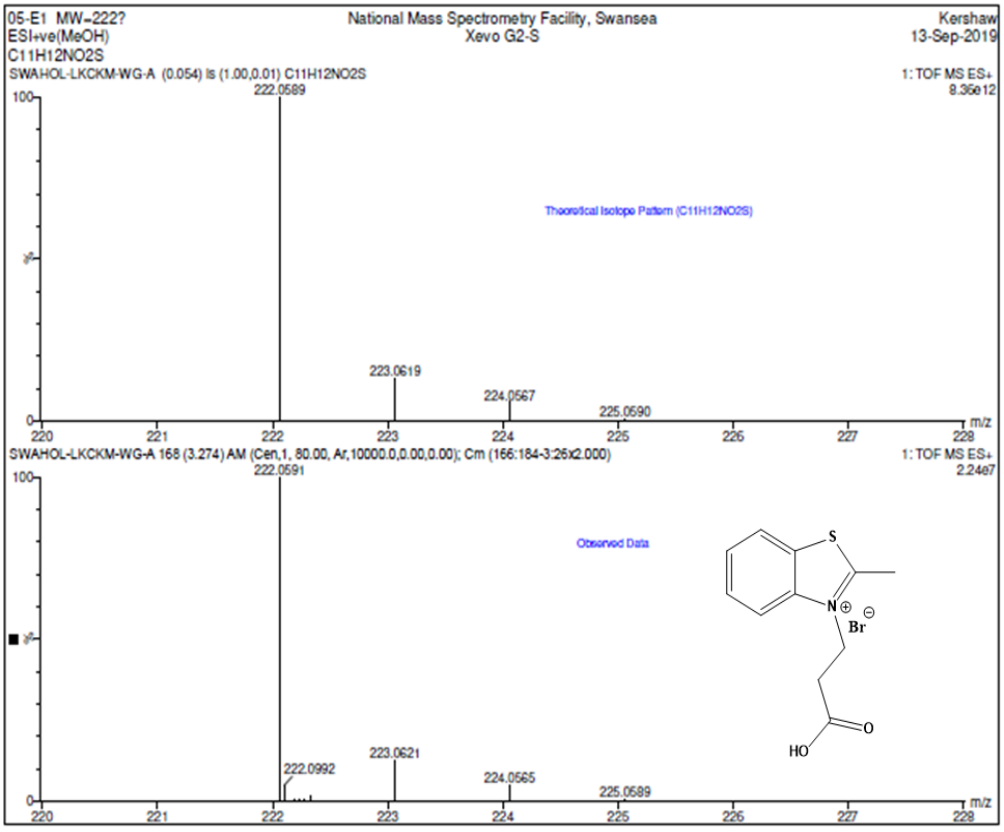

Figure 8.26 – Mass spectrometry of (**4**)

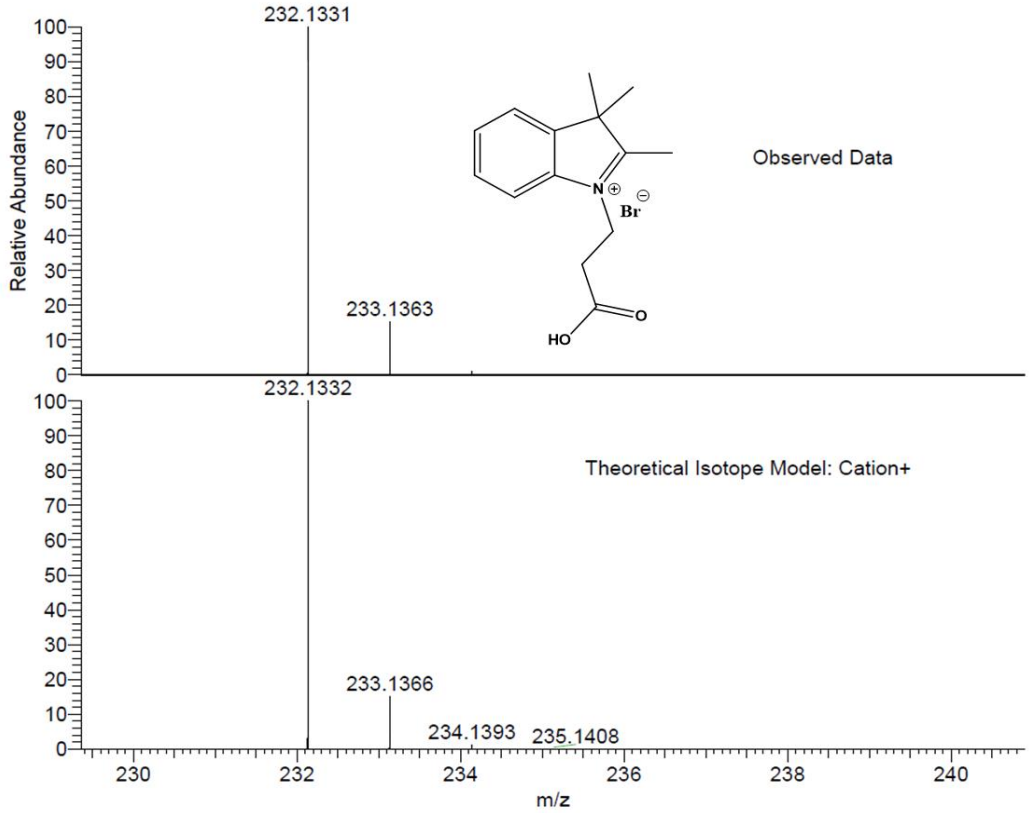

Figure 8.27 – Mass spectrometry of (**5**)

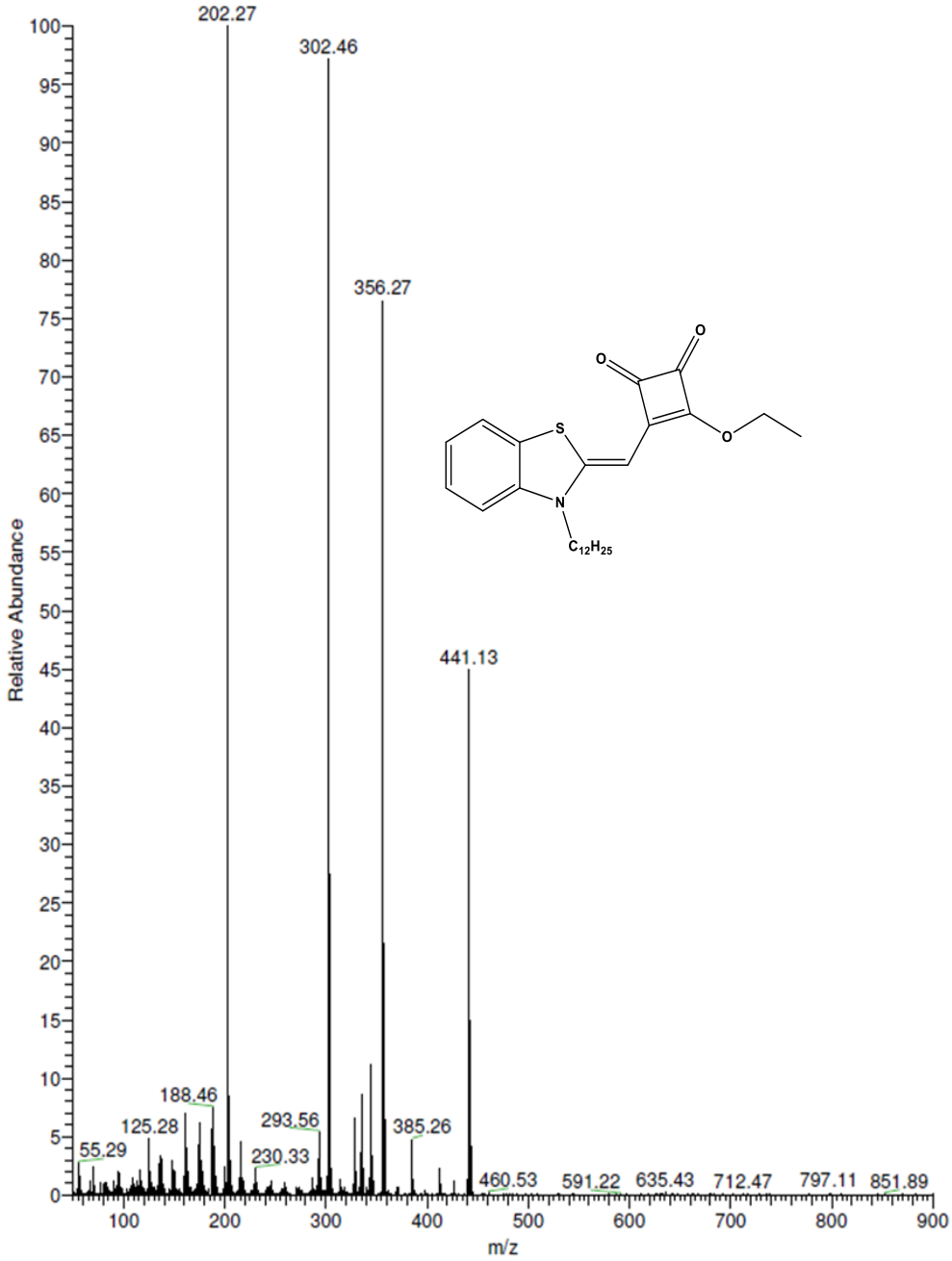

Figure 8.28 – Mass spectrometry of (**6**)

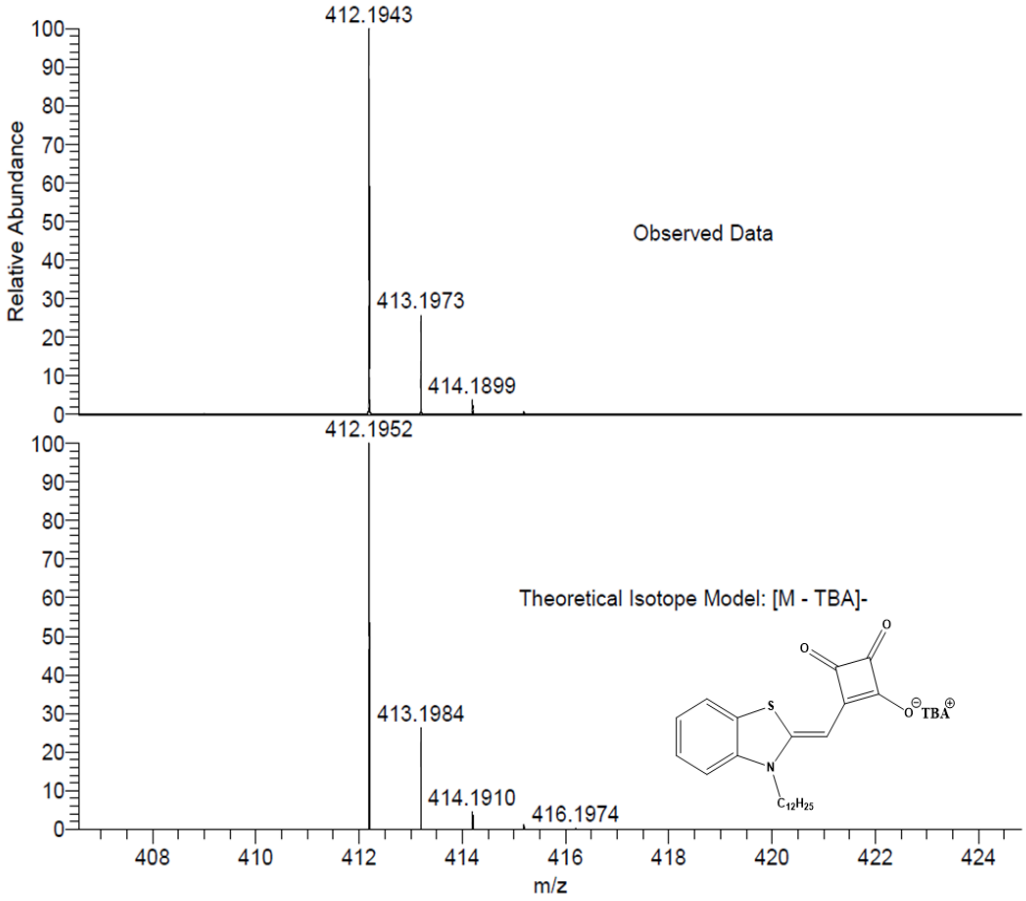

Figure 8.29 – Mass spectrometry of (**D1**)

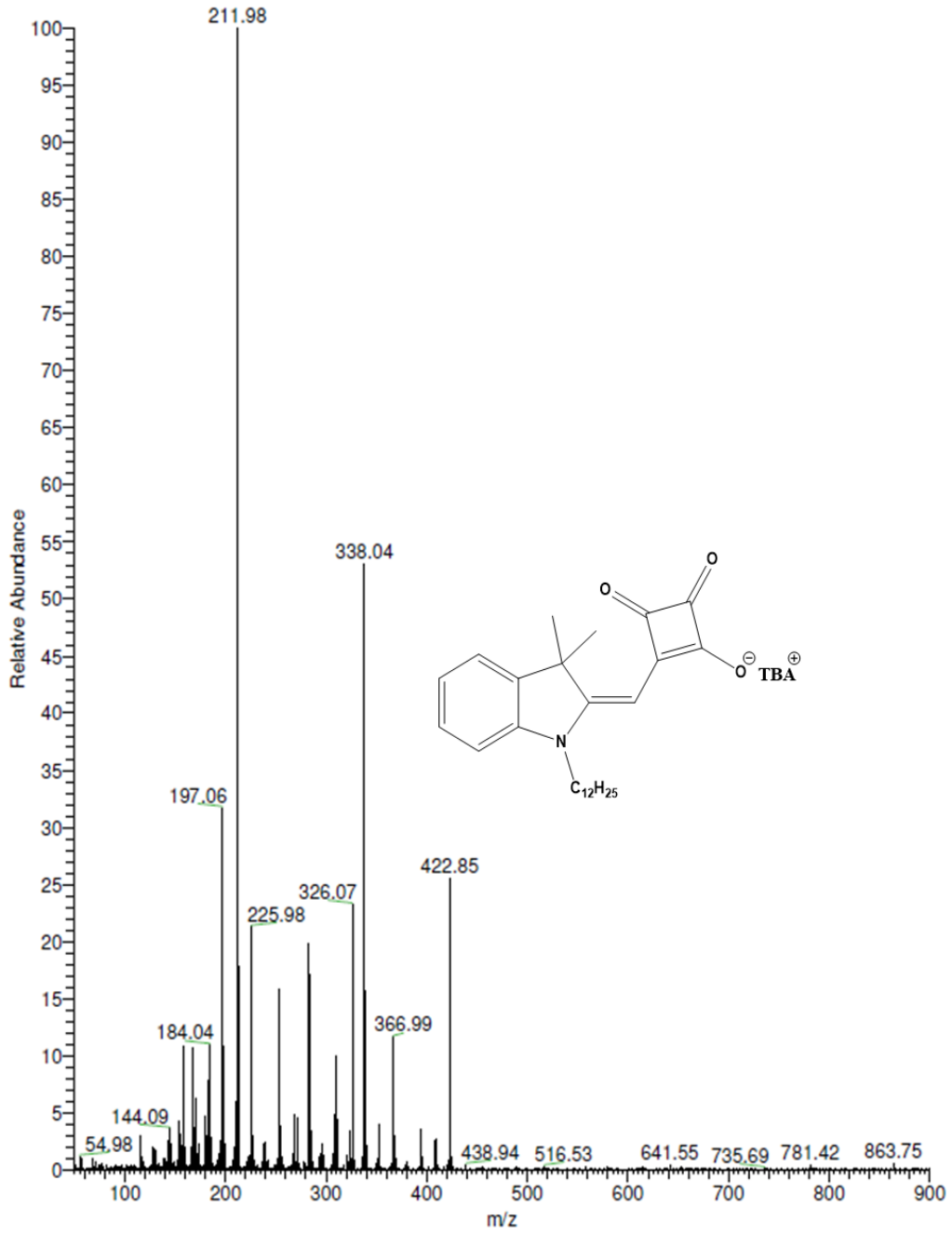

Figure 8.30 - Mass spectrometry of (**D2**)

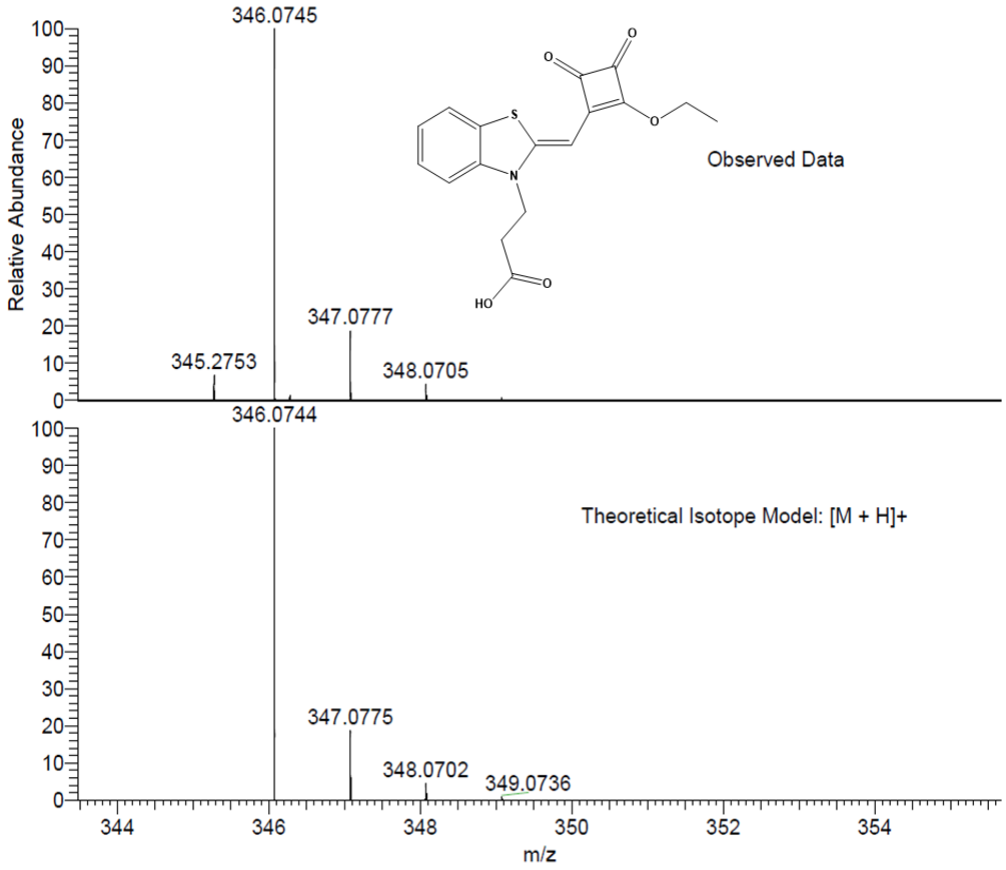

Figure 8.31 – Mass spectrometry of (**D3**)

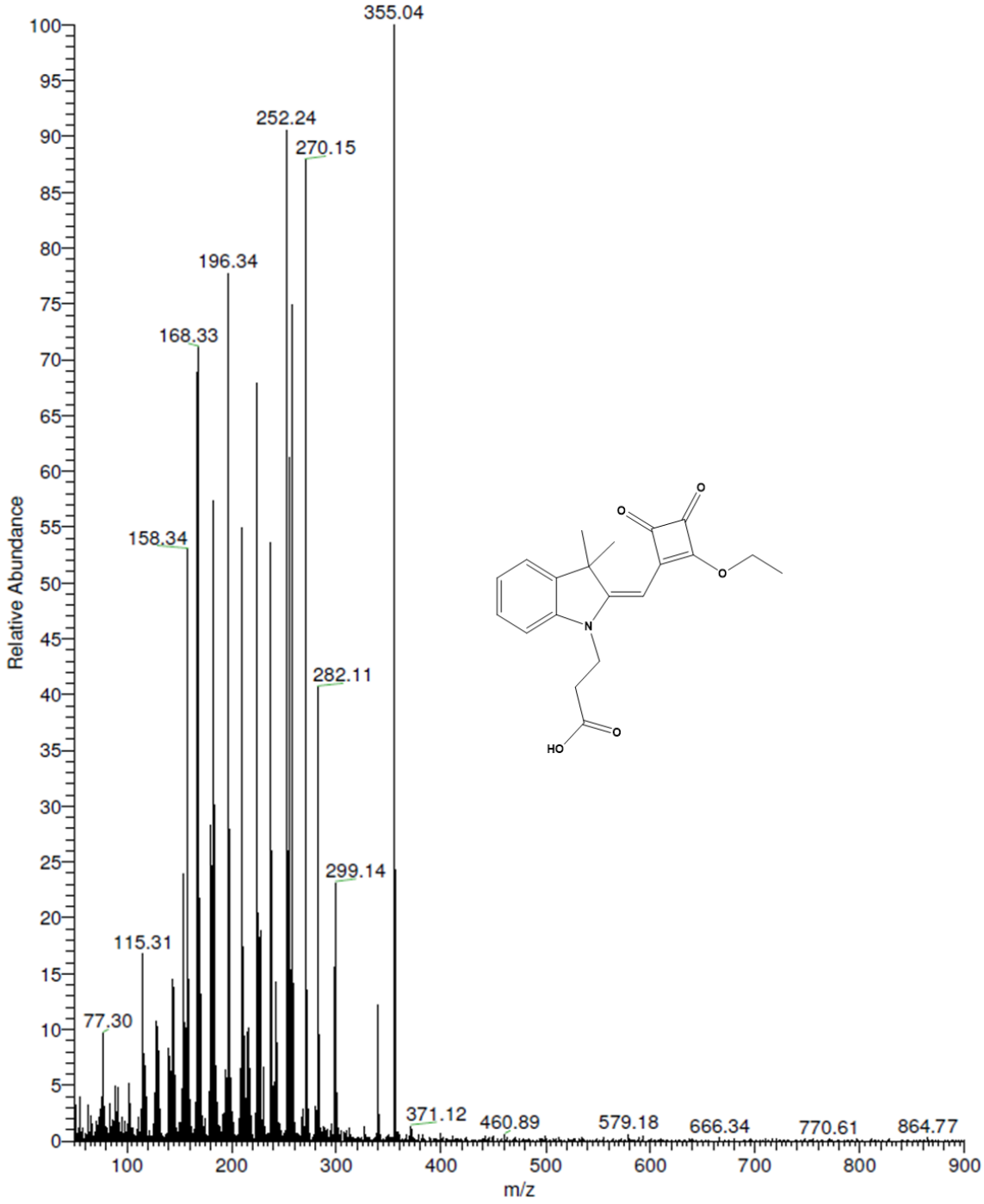

Figure 8.32 – Mass spectrometry of (**D4**)

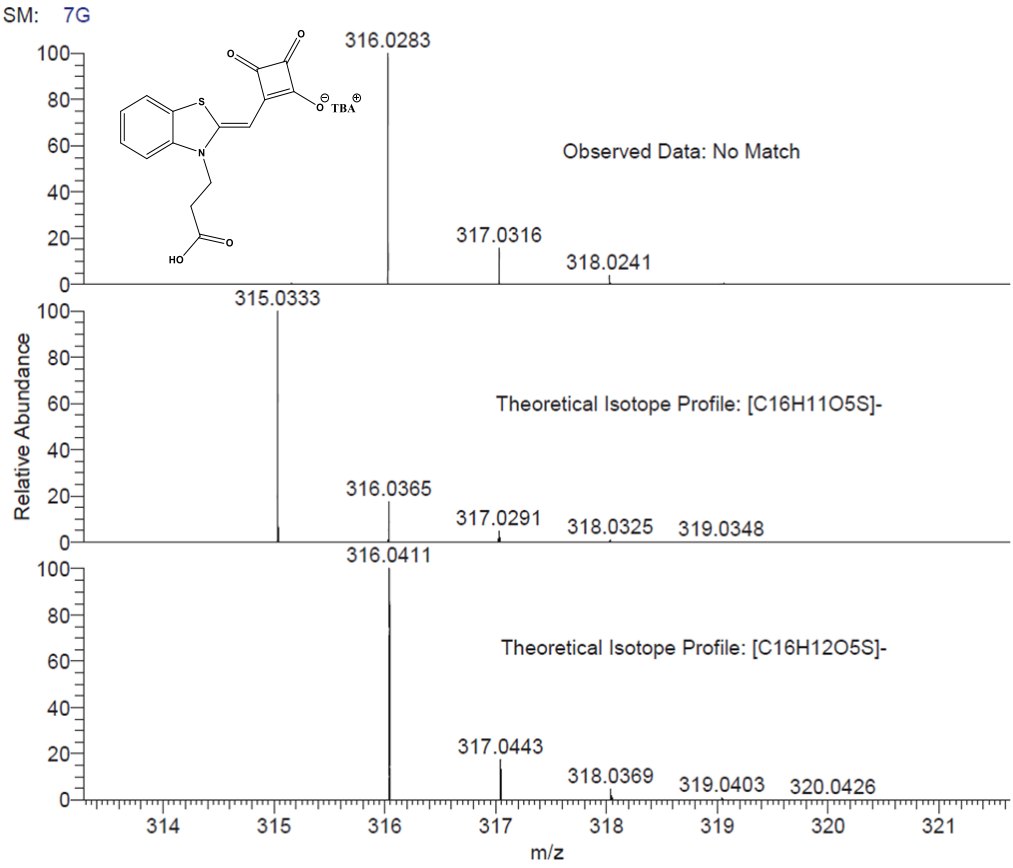

Figure 8.33 – Mass spectrometry of (**D5**)

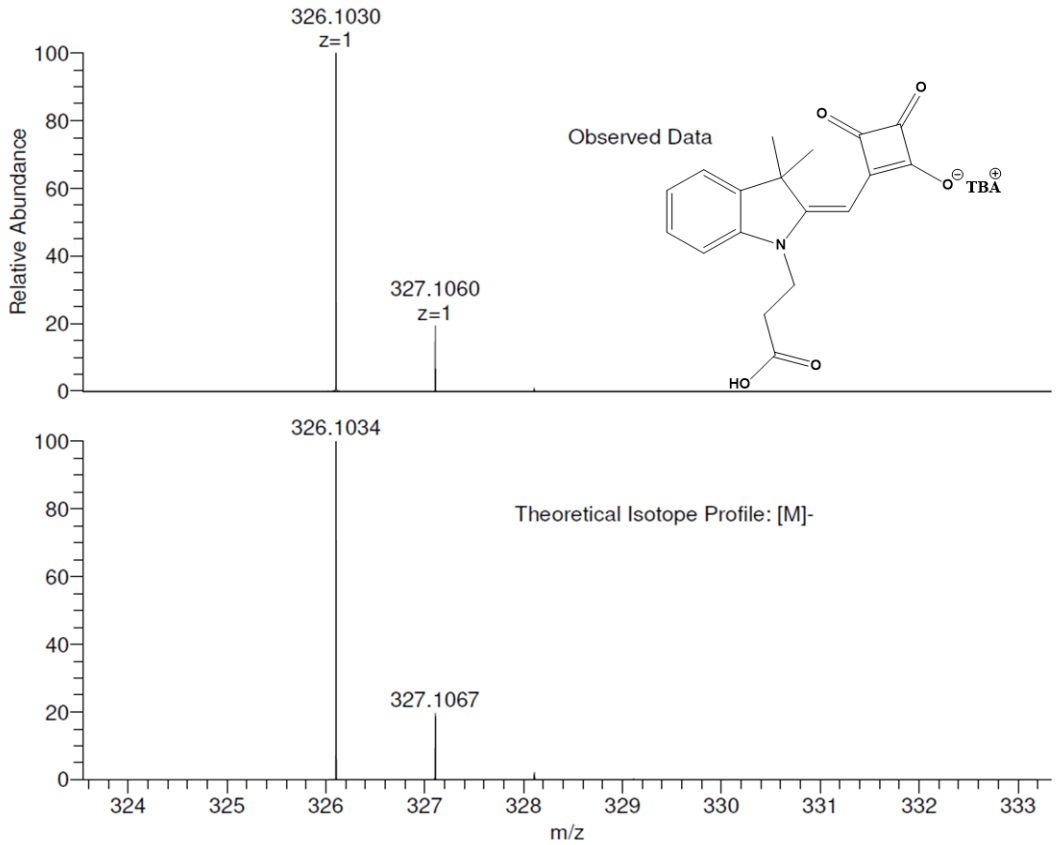

Figure 8.34 – Mass spectrometry of (**D6**)

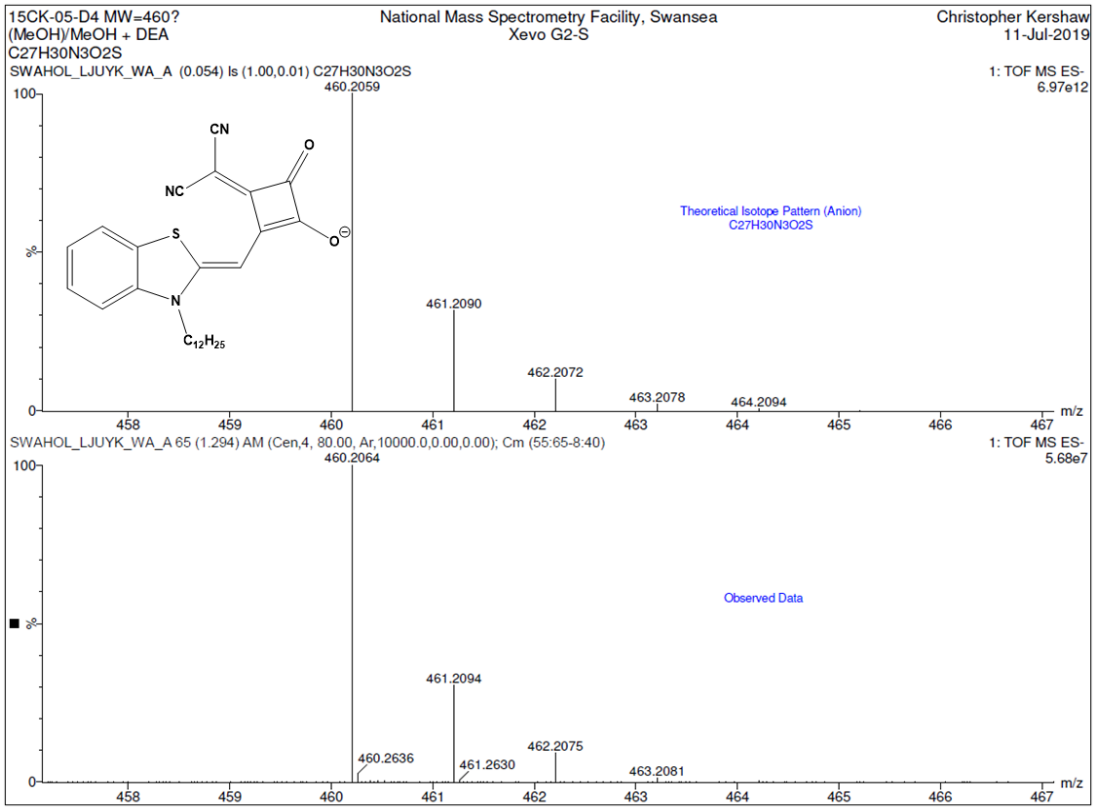

Figure 8.35 – Mass spectrometry of (**D7**)

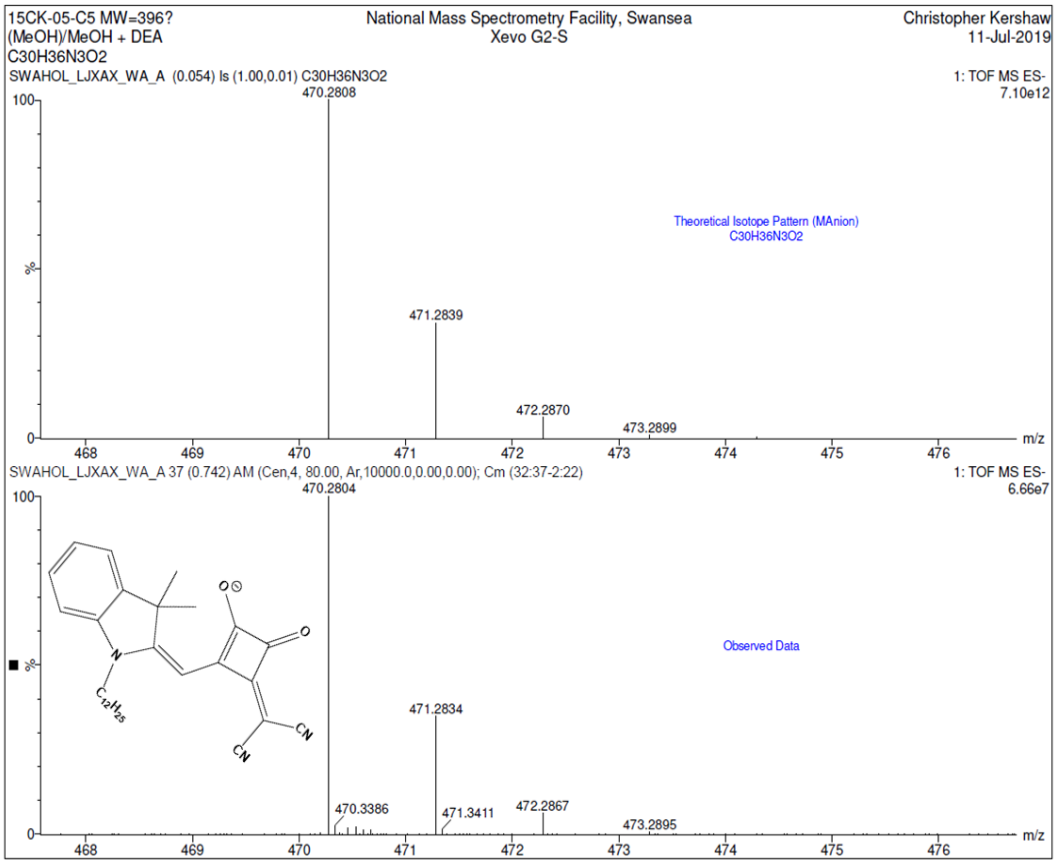

Figure 8.36 – Mass spectrometry of (**D8**)

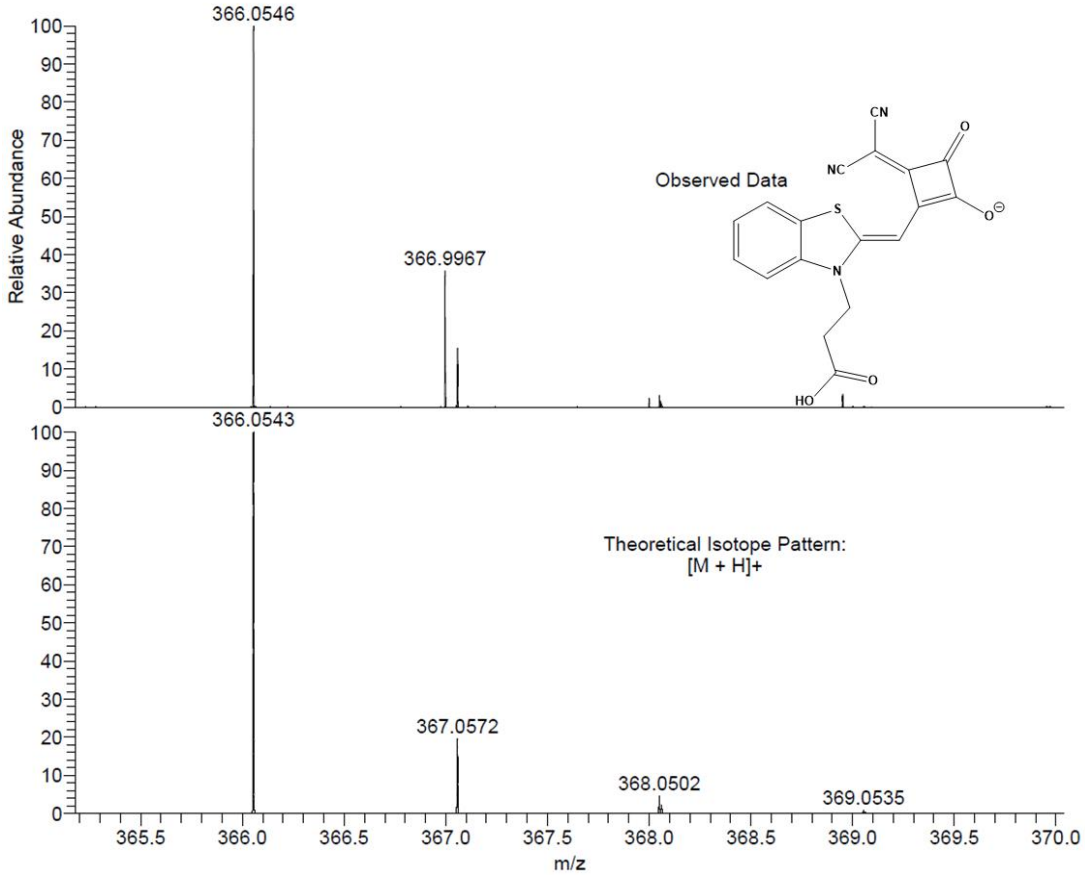

Figure 8.37 – Mass spectrometry of (**D9**)

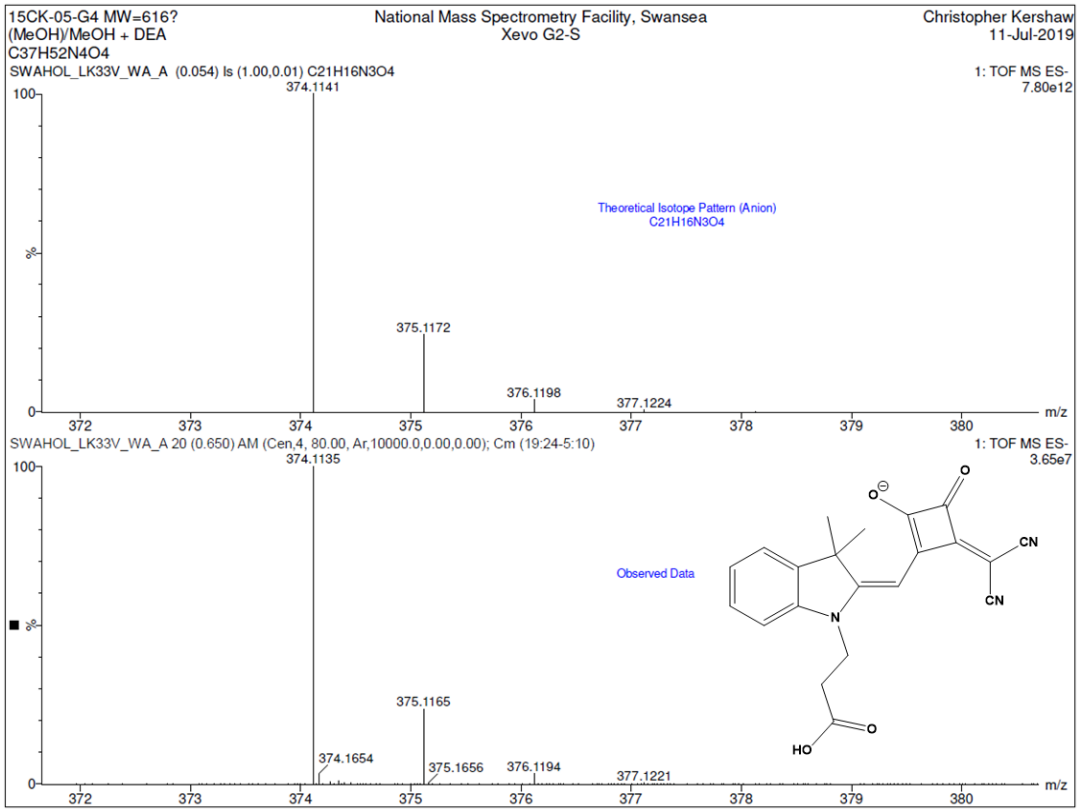

Figure 8.38 – Mass spectrometry of (**D10**)

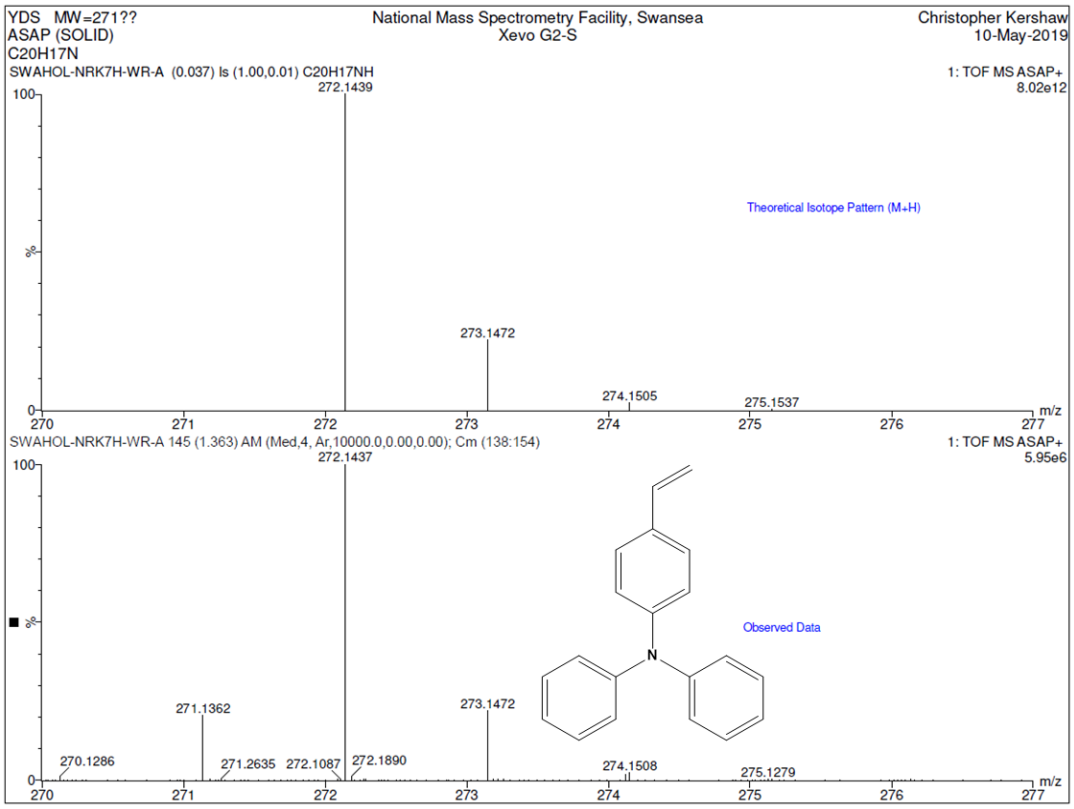

Figure 8.39 – Mass spectrometry of (**YD-S2**)

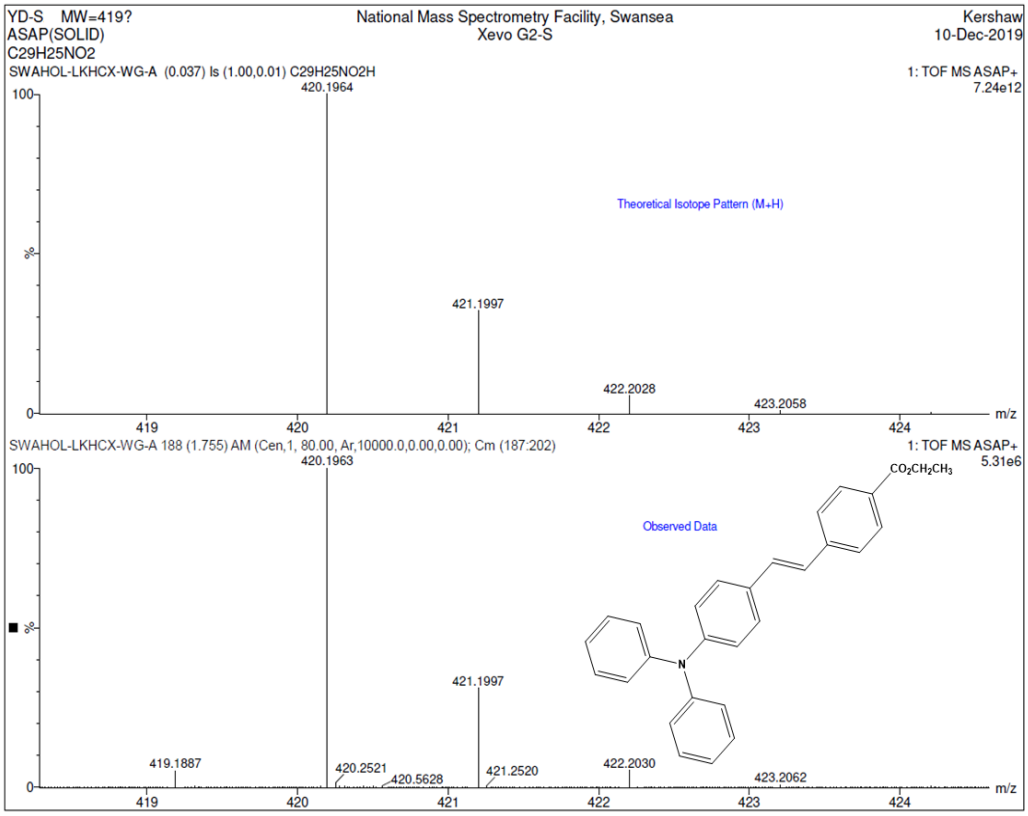

Figure 8.40 – Mass spectrometry of (**YD-S3**)

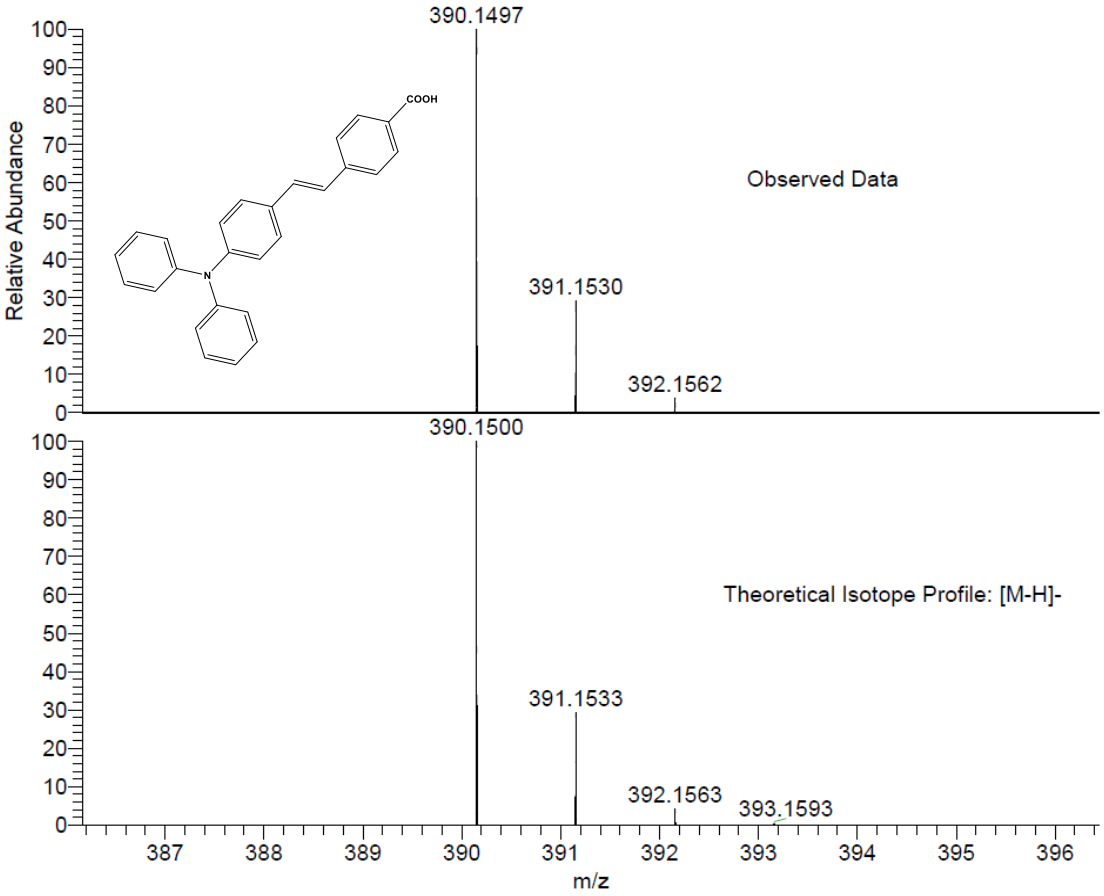

Figure 8.41 – Mass spectrometry of (**YD-Ac**)

8.3 ATR-IR spectroscopy

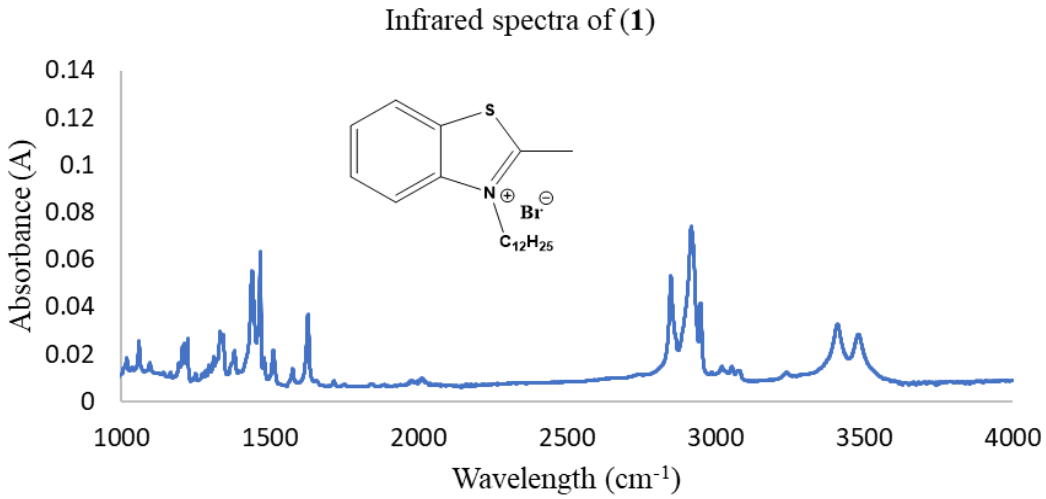

Figure 8.42 - Infrared spectra of (**1**).

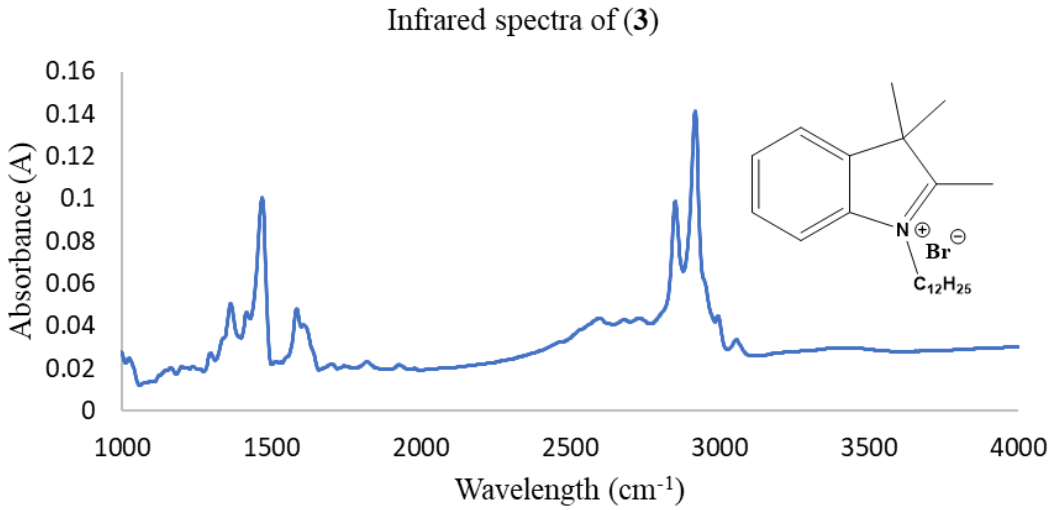

Figure 8.43 – Infrared spectra of (**3**).

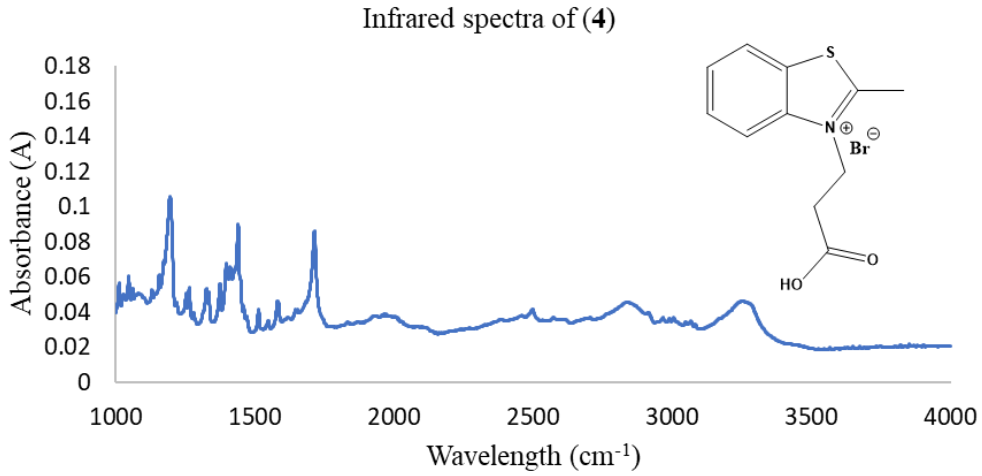

Figure 8.44 – Infrared spectra of (**4**).

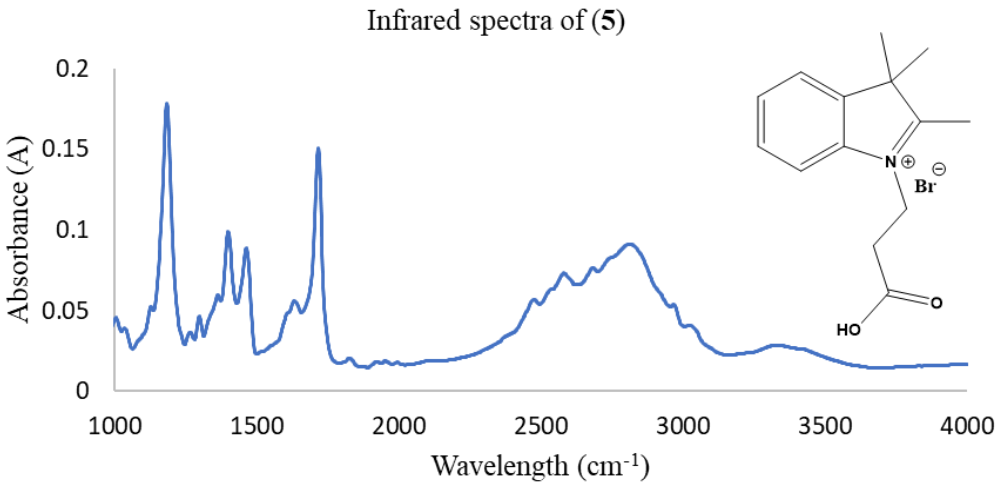

Figure 8.45 Infrared spectra of (**5**).

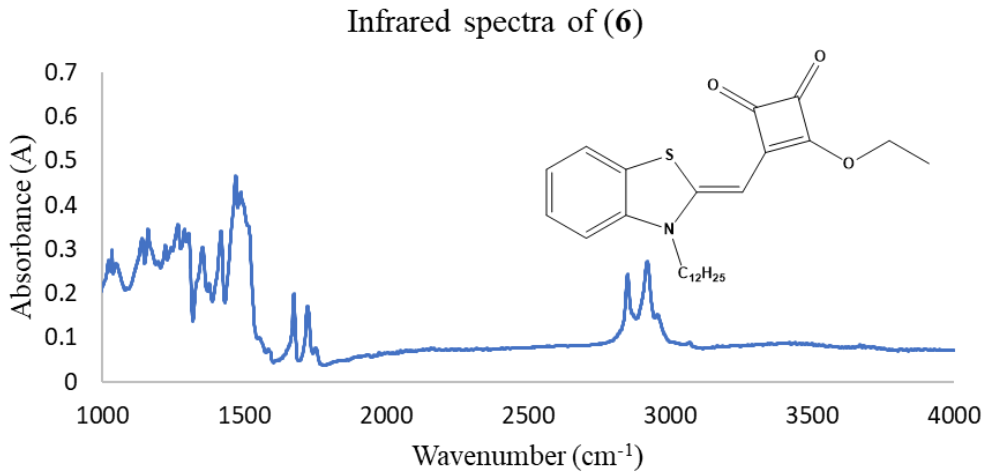

Figure 8.46 – Infrared spectra of (**6**).

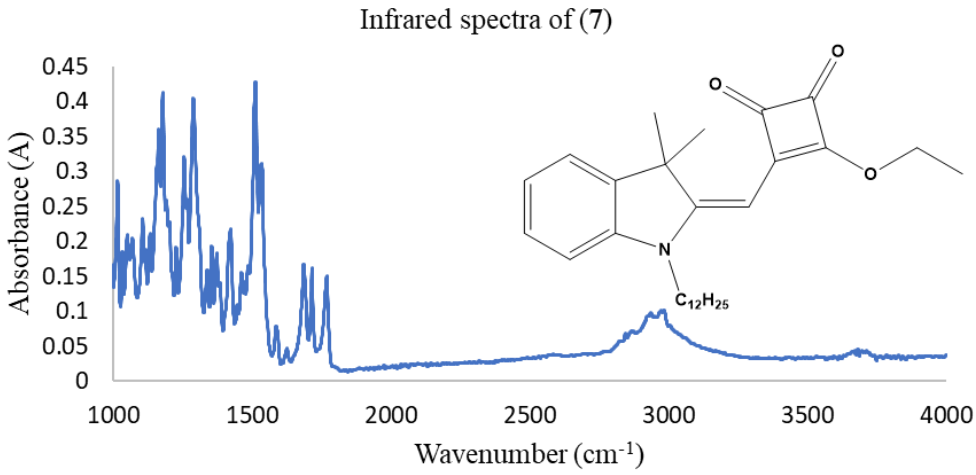

Figure 8.47 – Infrared spectra of (**7**).

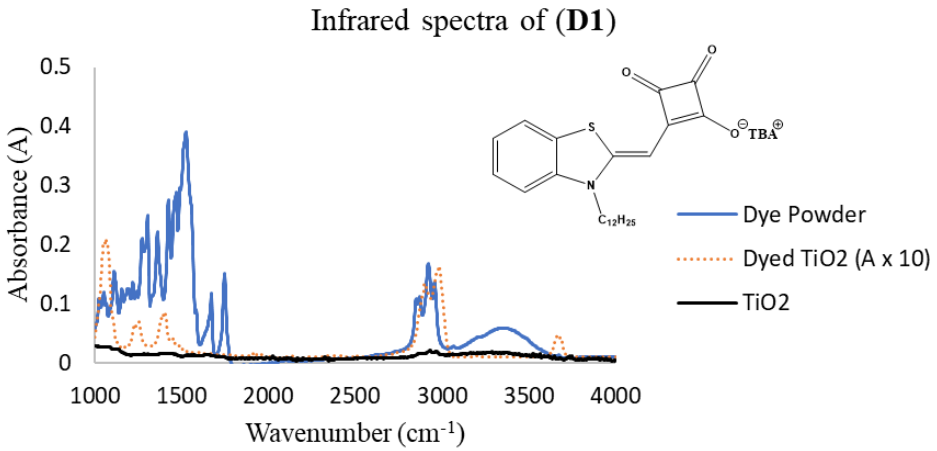

Figure 8.48 - Infrared spectra of (**D1**). Dye powder (blue solid line), Sensitised onto TiO_2 (Orange dotted line) and TiO_2 (black line).

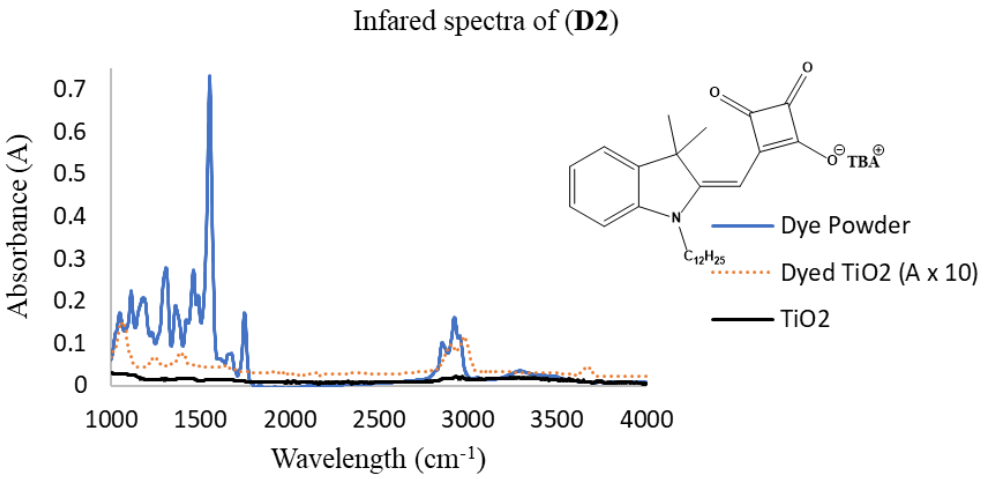

Figure 8.49 - Infrared spectra of (**D2**). Dye powder (blue solid line), Sensitised onto TiO_2 (Orange dotted line) and TiO_2 (black line).

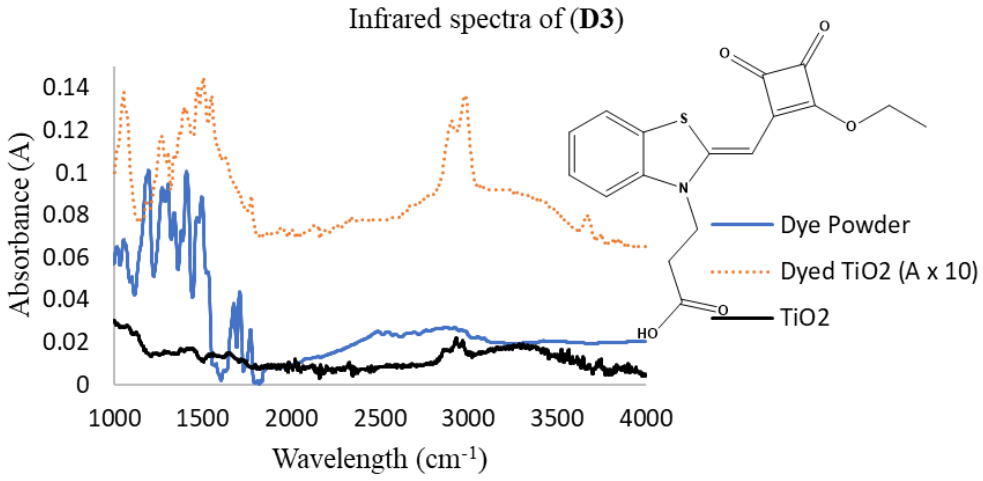

Figure 8.50 - Infrared spectra of (**D3**). Dye powder (blue solid line), Sensitised onto TiO_2 (Orange dotted line) and TiO_2 (black line).

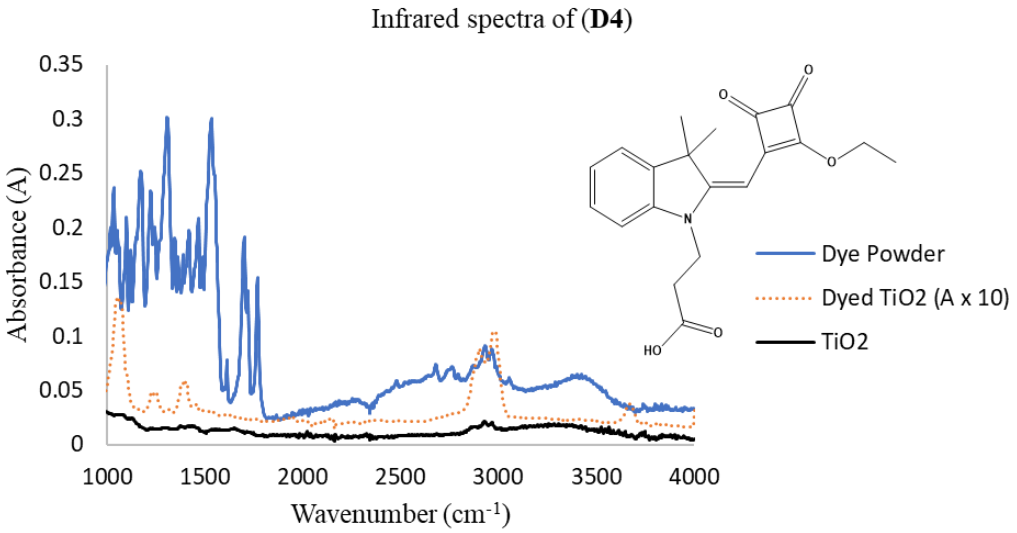

Figure 8.51 - Infrared spectra of (**D4**). Dye powder (blue solid line), Sensitised onto TiO_2 (Orange dotted line) and TiO_2 (black line).

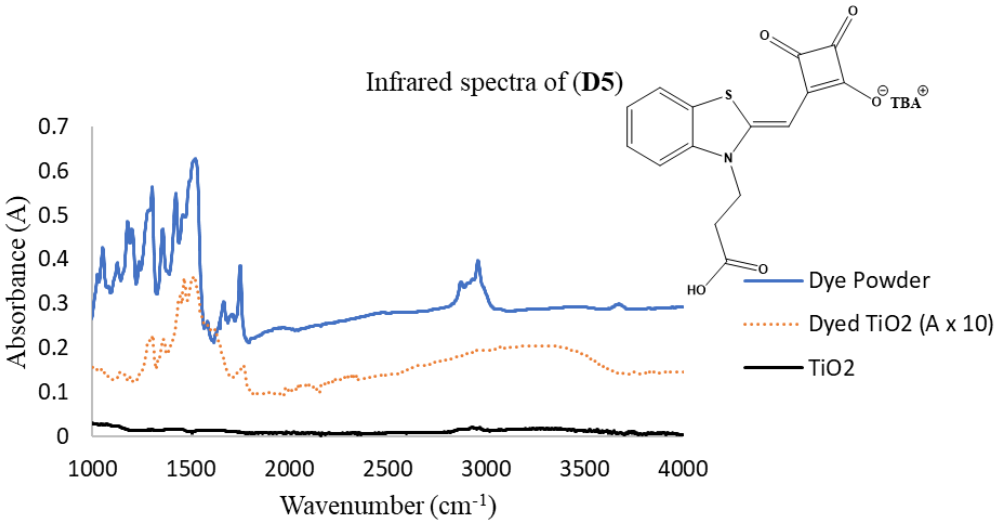

Figure 8.52 - Infrared spectra of (**D5**). Dye powder (blue solid line), Sensitised onto TiO_2 (Orange dotted line) and TiO_2 (black line).

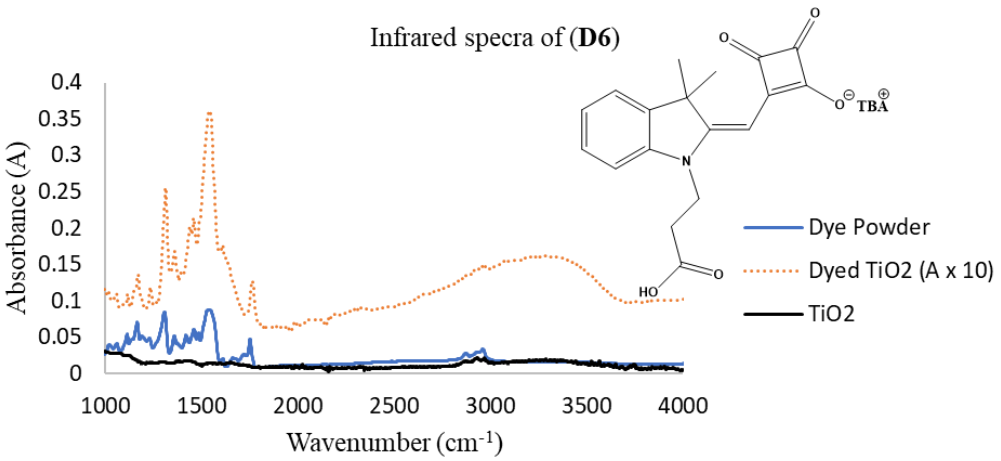

Figure 8.53 - Infrared spectra of (**D6**). Dye powder (blue solid line), Sensitised onto TiO_2 (Orange dotted line) and TiO_2 (black line).

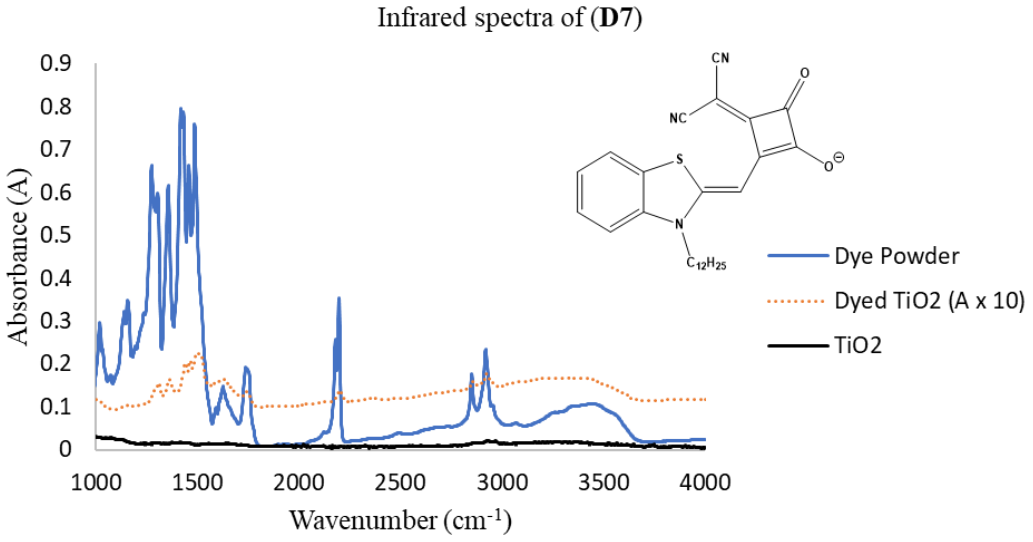

Figure 8.54 - Infrared spectra of (**D7**). Dye powder (blue solid line), Sensitised onto TiO_2 (Orange dotted line) and TiO_2 (black line).

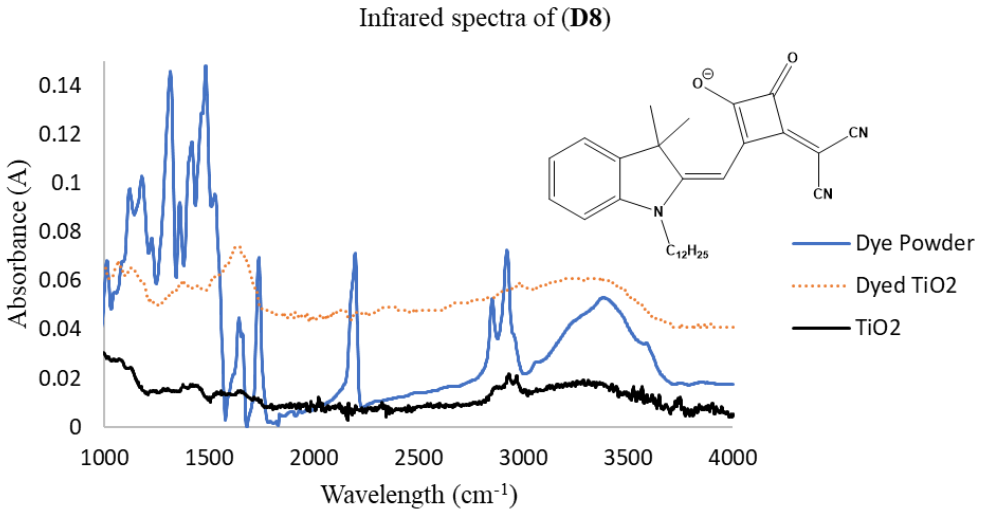

Figure 8.55 - Infrared spectra of (**D8**). Dye powder (blue solid line), Sensitised onto TiO_2 (Orange dotted line) and TiO_2 (black line).

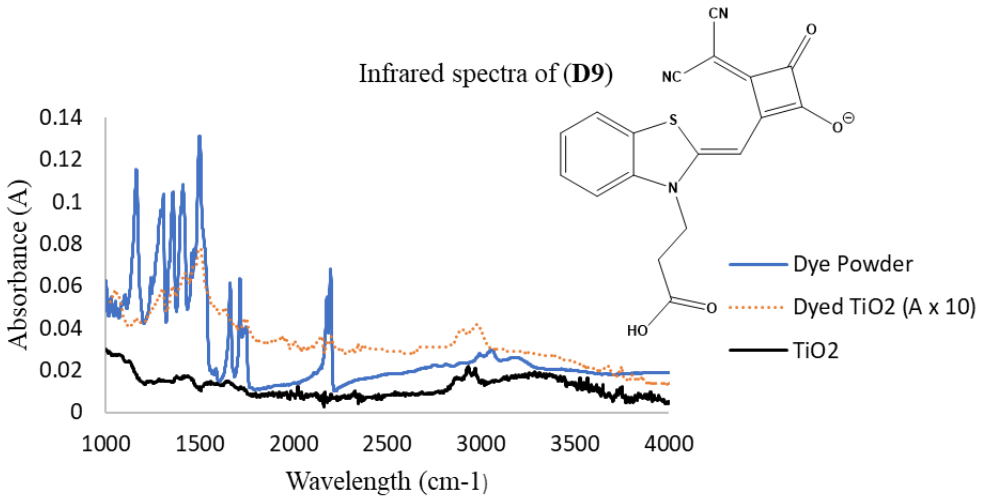

Figure 8.56 - Infrared spectra of (**D9**). Dye powder (blue solid line), Sensitised onto TiO_2 (Orange dotted line) and TiO_2 (black line).

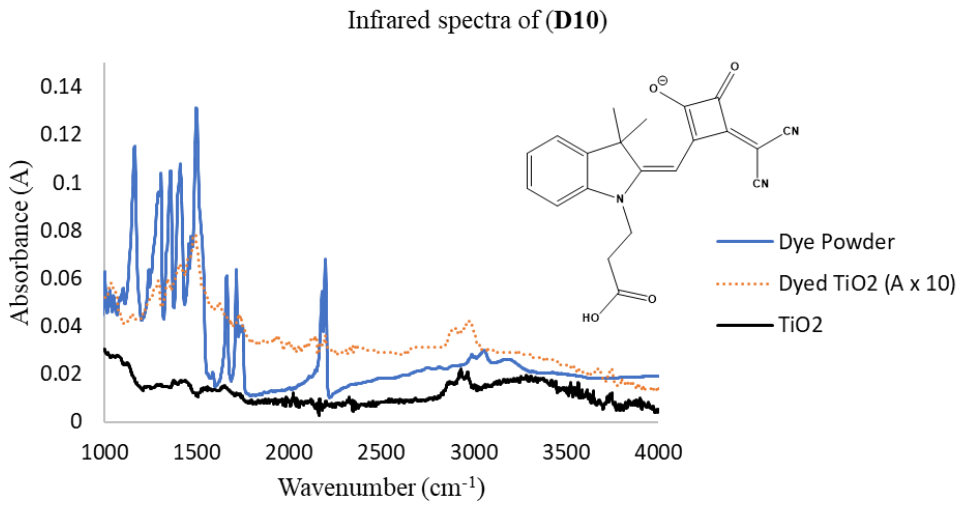

Figure 8.57 - Infrared spectra of (**D9**). Dye powder (blue solid line), Sensitised onto TiO_2 (Orange dotted line) and TiO_2 (black line).

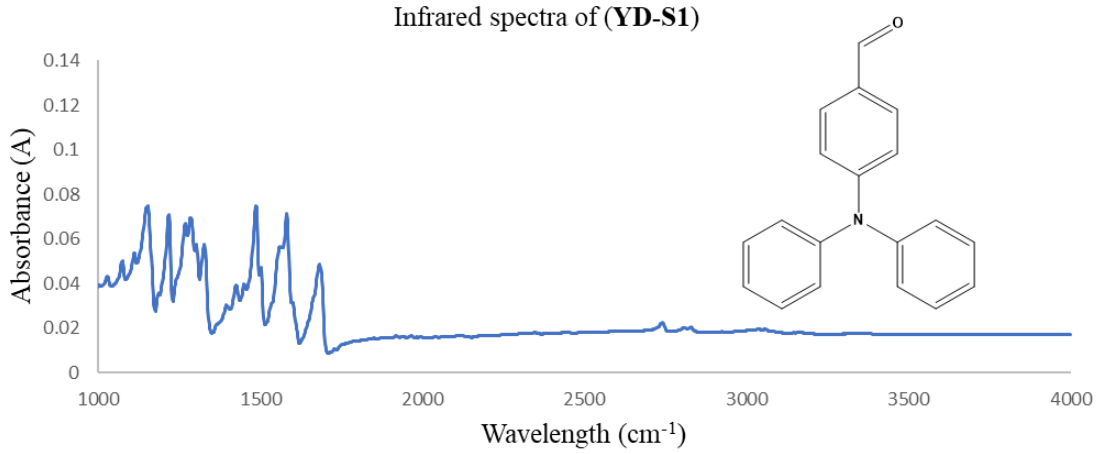

Figure 8.58 – Infrared spectra of (**YD-S1**)

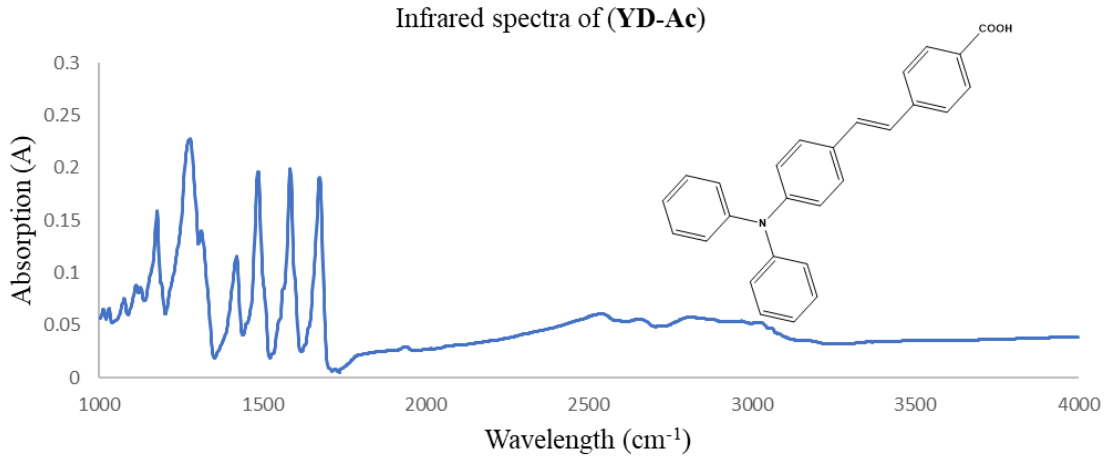

Figure 8.59 – Infrared spectra of (**YD-An**)

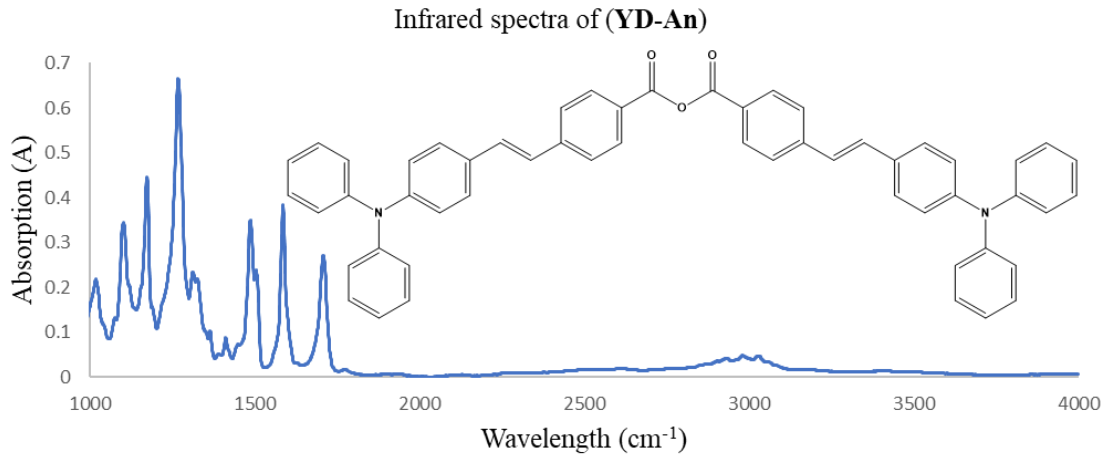

Figure 8.60 – Infrared spectra of (**YD-An**)

8.4 UV-visible spectroscopy

Dye	λ_{max} / nm	ε / 10^4 $M^{-1}cm^{-1}$	Error in ε / x 10^4
(**3**)	441	4.7	0.20
(**4**)	446	3.1	0.02
(**6**)	424	1.8	0.05
(**7**)	446	3.6	0.05
(**8**)	480	2.8	0.09
(**10**)	424	7.2	0.20
(**11**)	423	3.8	0.05
(**12**)	460	1.1	0.01
(**14**)	423	5.2	0.15
(**15**)	423	4.3	0.08
(**16**)	478	3.5	0.04
(**17**)	456	2.3	0.05

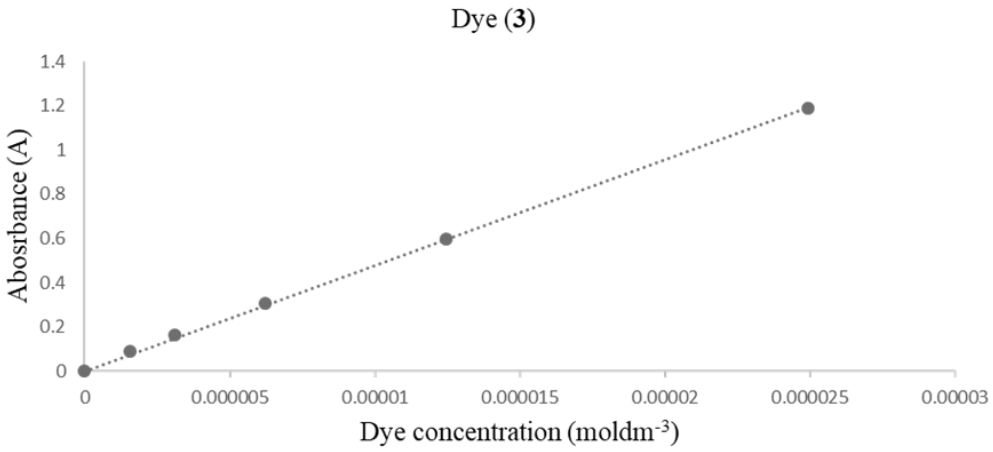

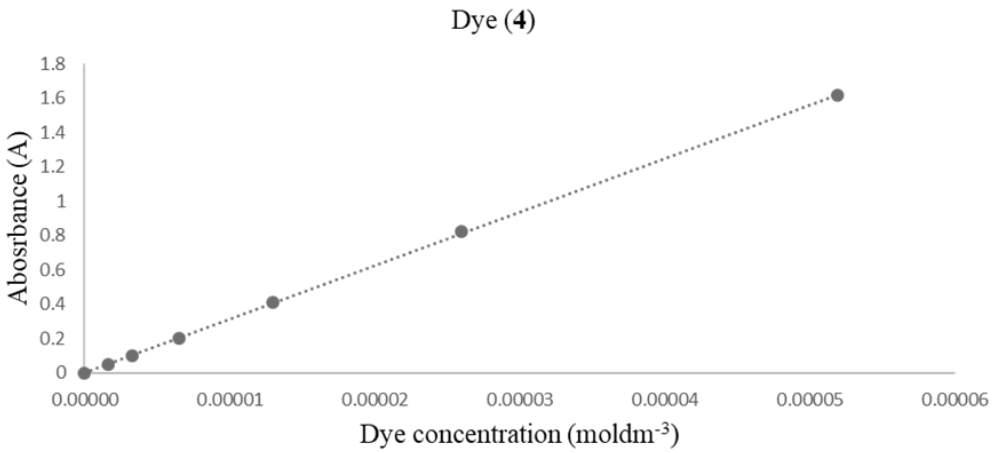

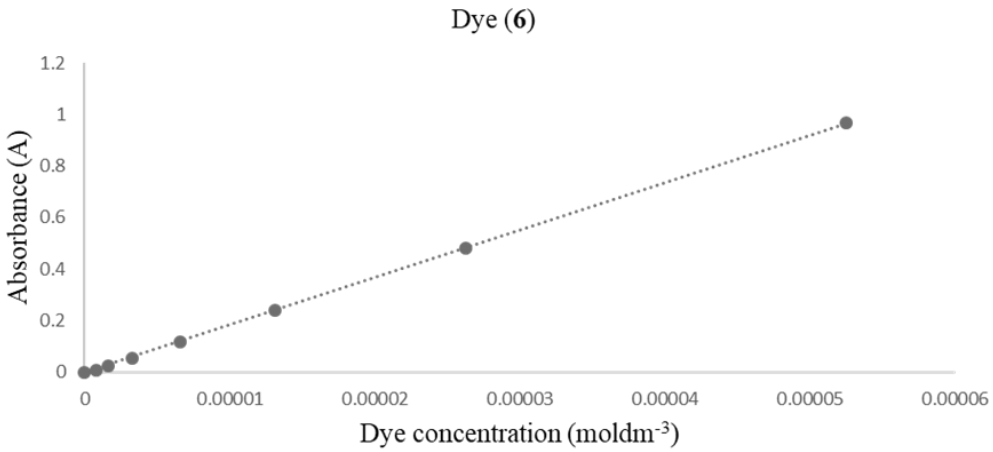

Figure 8.61 – Calibration graphs of (**3**), (**4**) and (**6**)

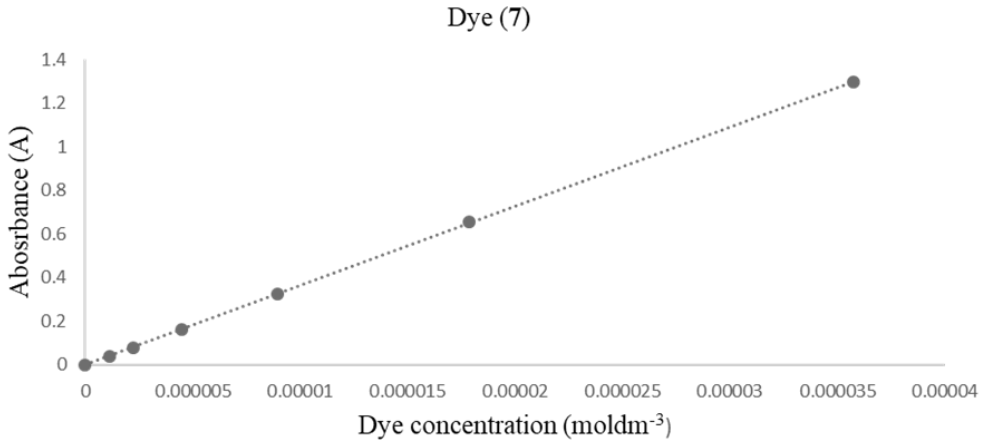

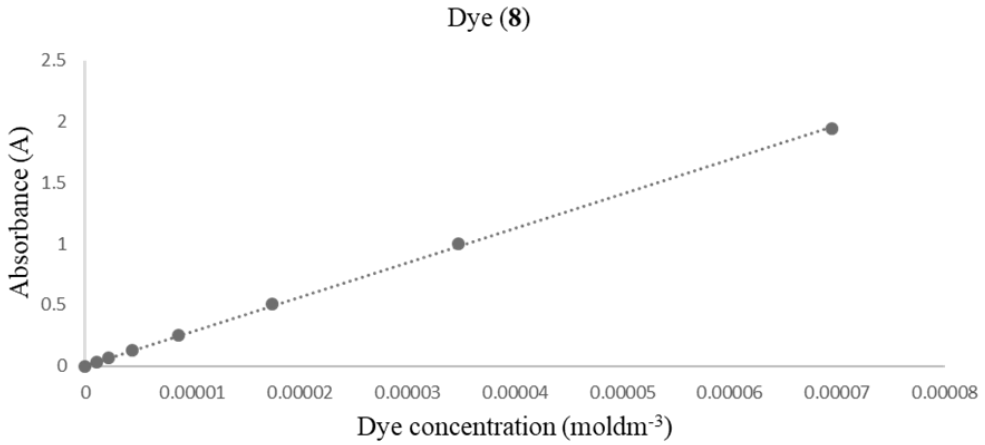

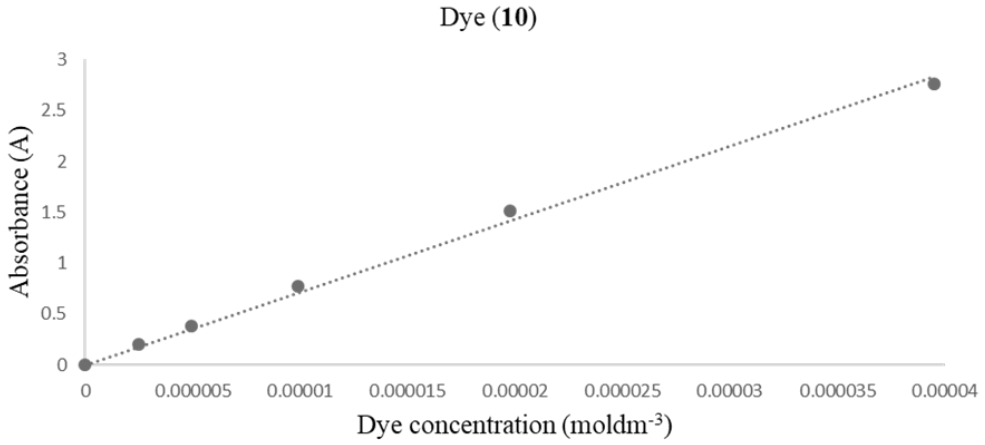

Figure 8.62 - Calibration graphs of (**7**), (**8**) and (**10**)

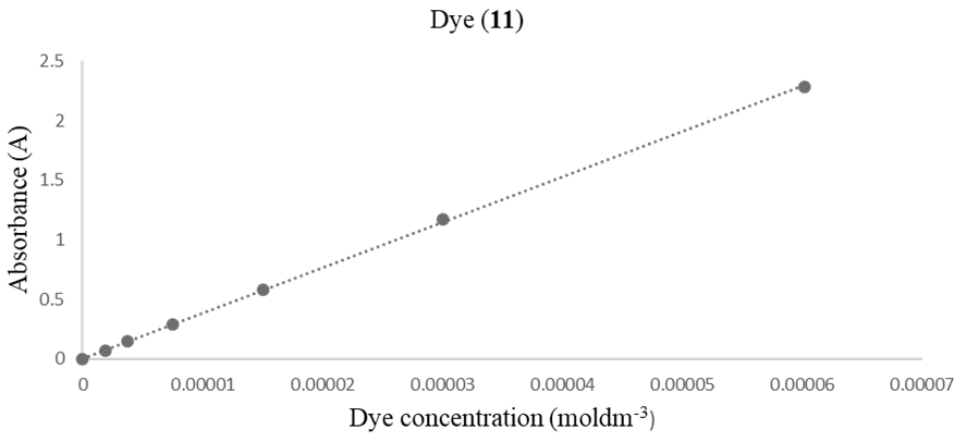

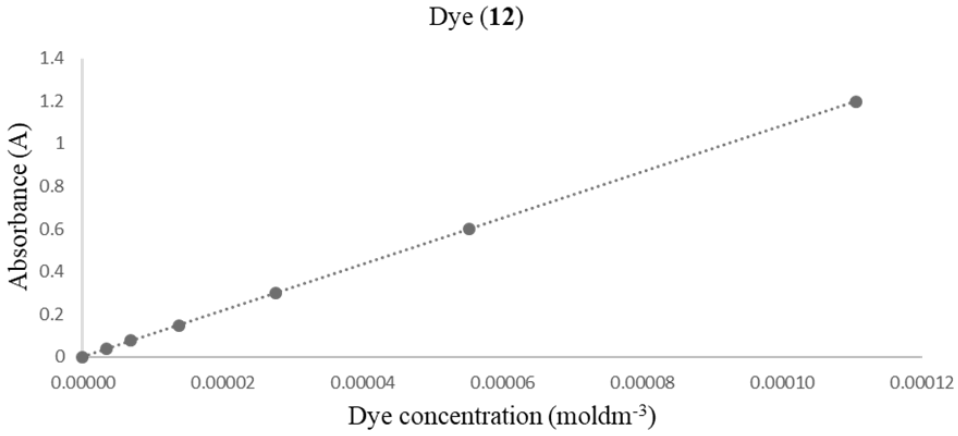

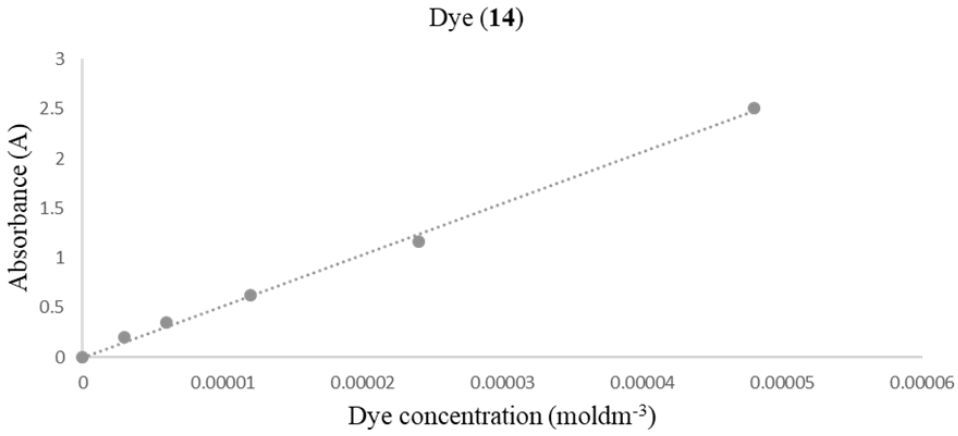

Figure 8.63 – Calibration graphs of (**11**), (**12**) and (**14**)

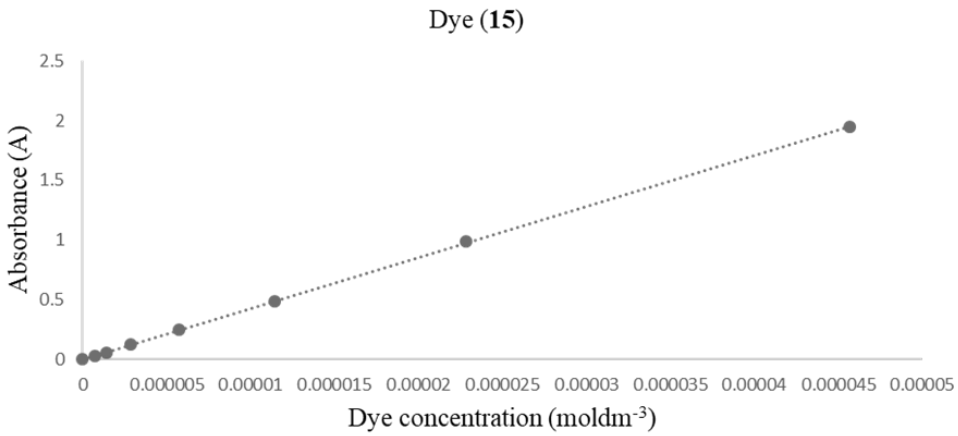

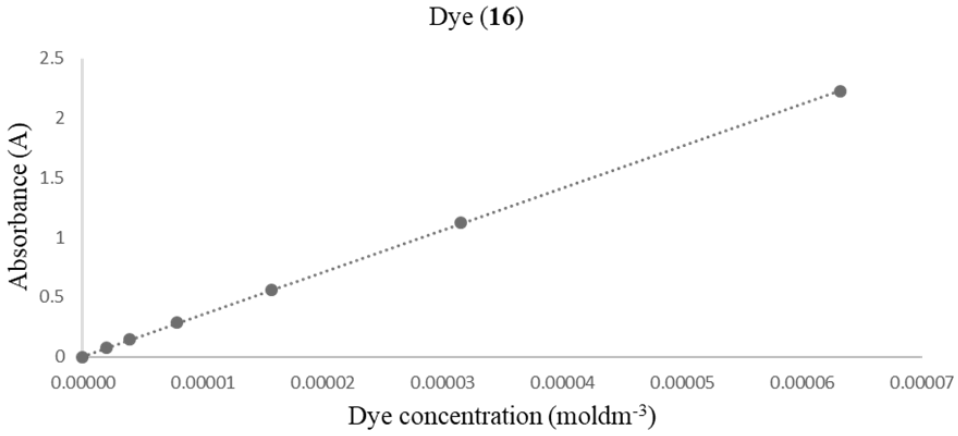

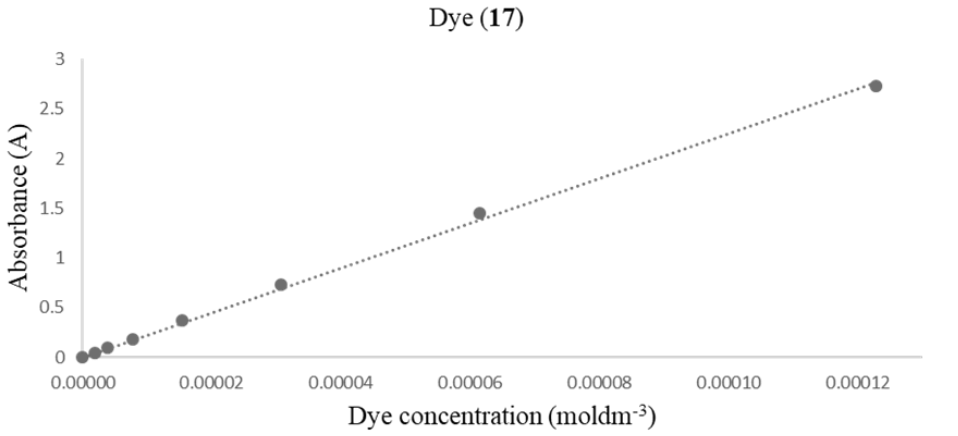

Figure 8.64 – Calibration graphs of (**15**), (**16**) and (**17**)

8.5 Crystal data

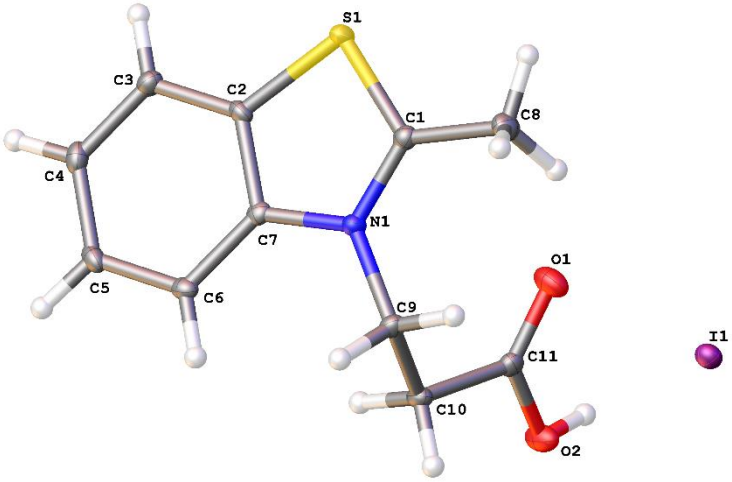

Figure 8.65 - Crystal structure of (**5**) with atom labelling scheme. Displacement ellipsoids – 50% probability

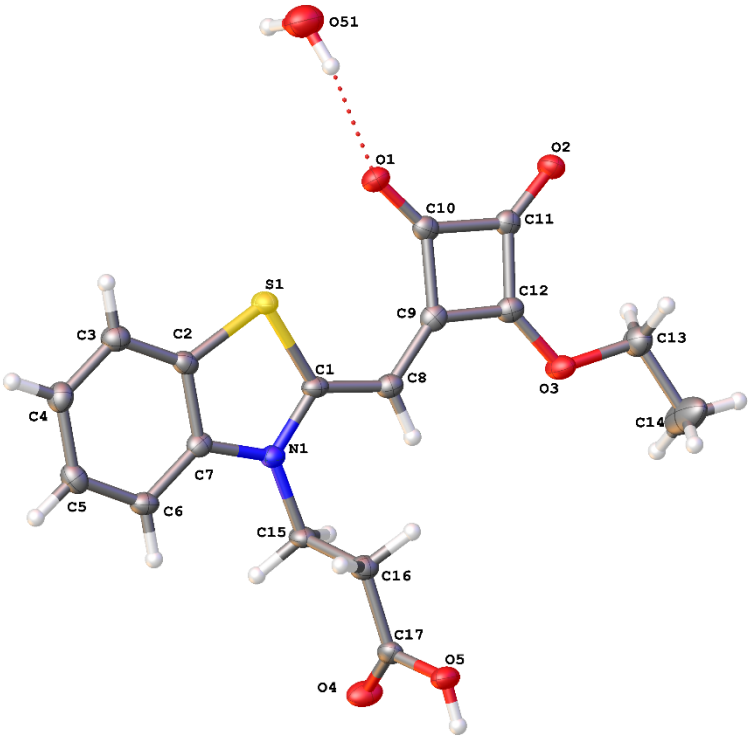

Figure 8.66 - Crystal structure of (**6**) with atom labelling scheme. Displacement ellipsoids – 50% probability

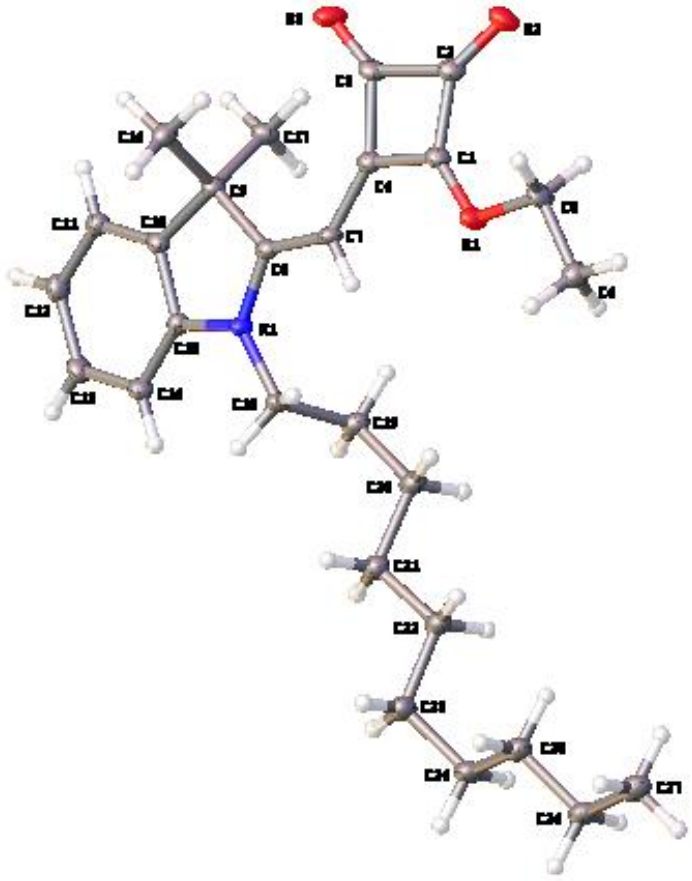

Figure 8.67 - Crystal structure of (**10**) with atom labelling scheme. Displacement ellipsoids – 50% probability

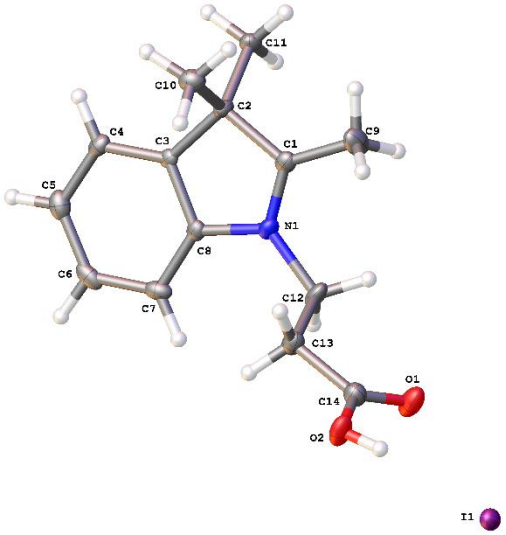

Figure 8.68 - Crystal structure of (**13**) with atom labelling scheme. Displacement ellipsoids – 50% probability

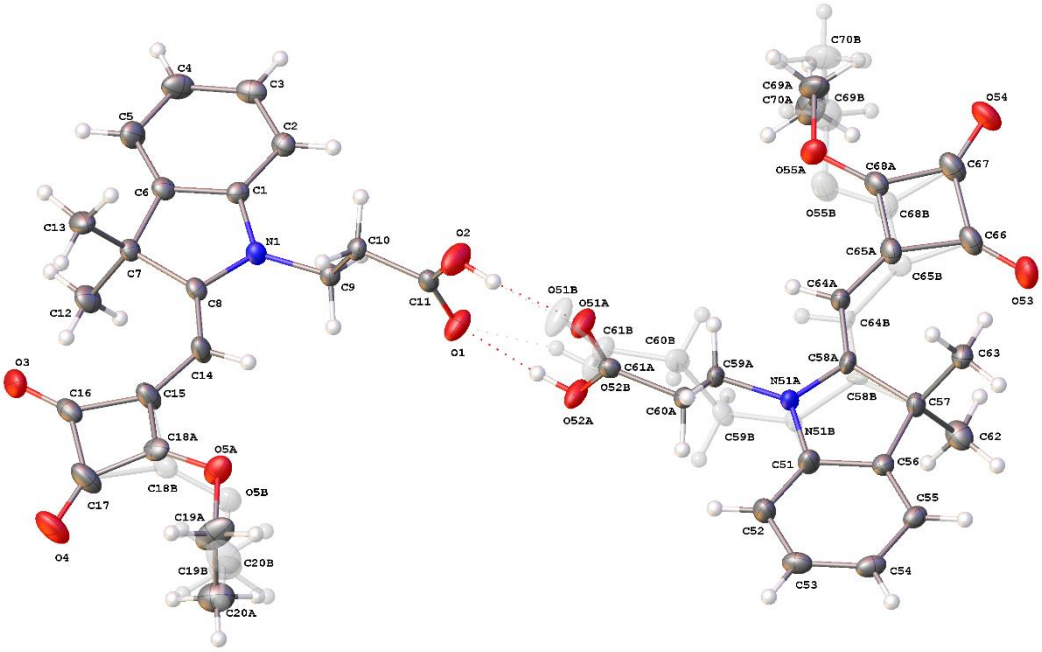

Figure 8.69 - Crystal structure of (**14**) with atom labelling scheme. Displacement ellipsoids – 50% probability

8.6 Profilometry

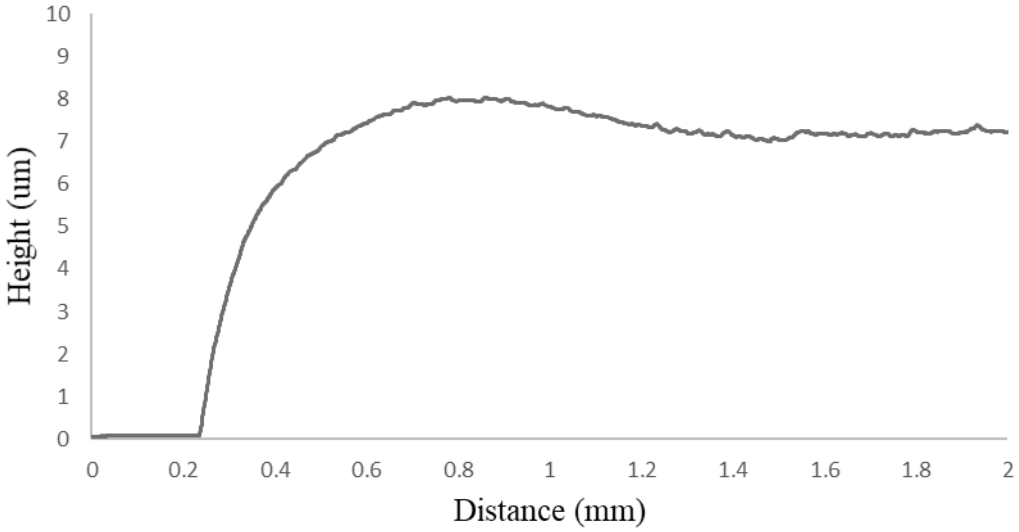

Figure 8.70 – Profilometry of SHfSQ DSC devices coated in Ti-Nanoxide T/SP (doctor bladed)

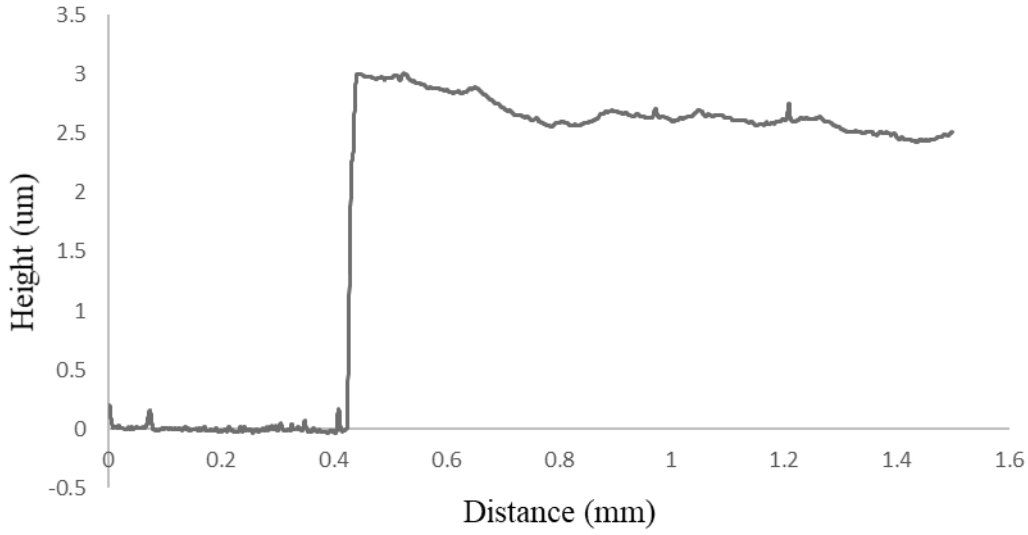

Figure 8.71 - Profilometry of ssDSC devices coated in 2:1 (ethanol:TiO_2) DSL18-NRT paste

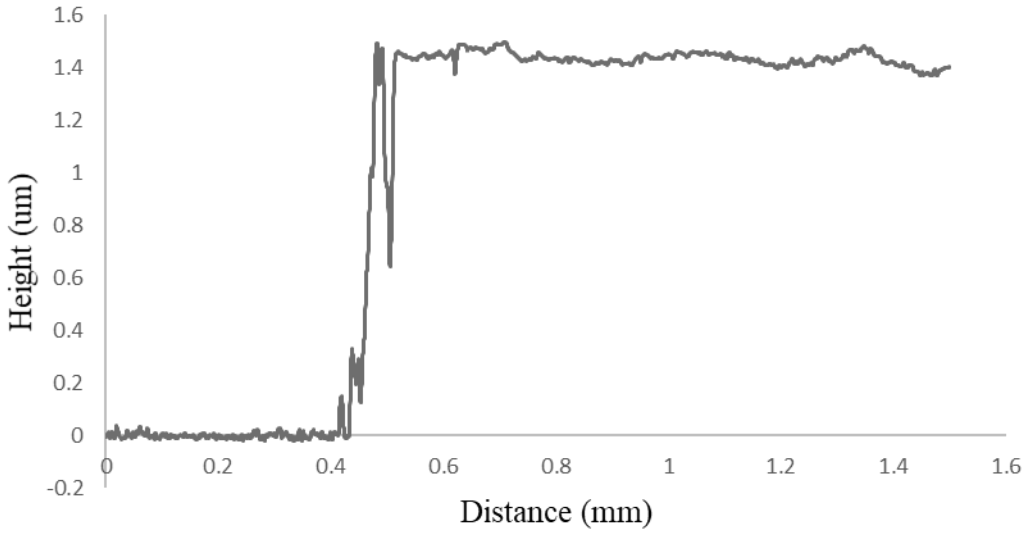

Figure 8.72 - Profilometry of ssDSC devices coated in 3:1 (ethanol:TiO_2) DSL18-NRT paste

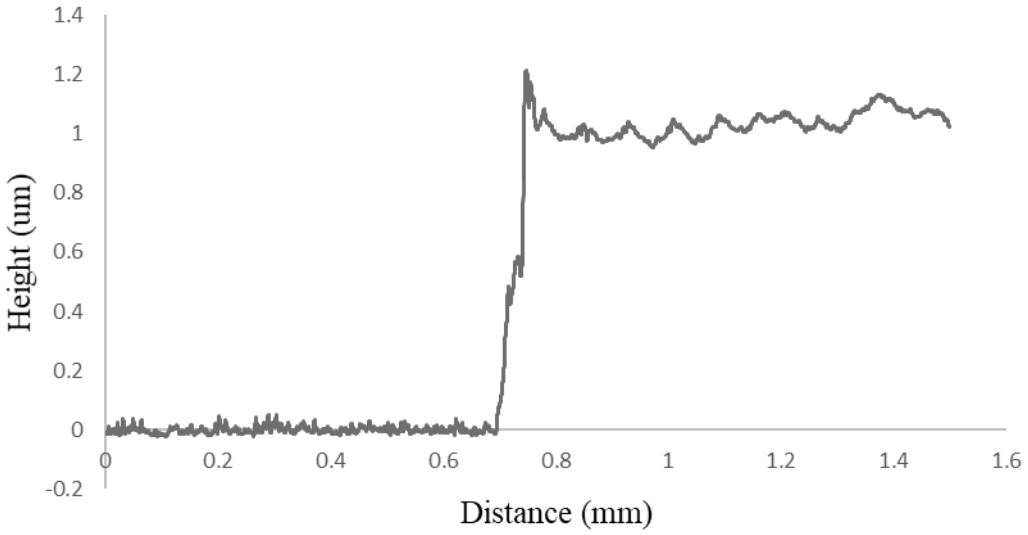

Figure 8.73 - Profilometry of ssDSC devices coated in 4:1 (ethanol:TiO_2) DSL18-NRT paste

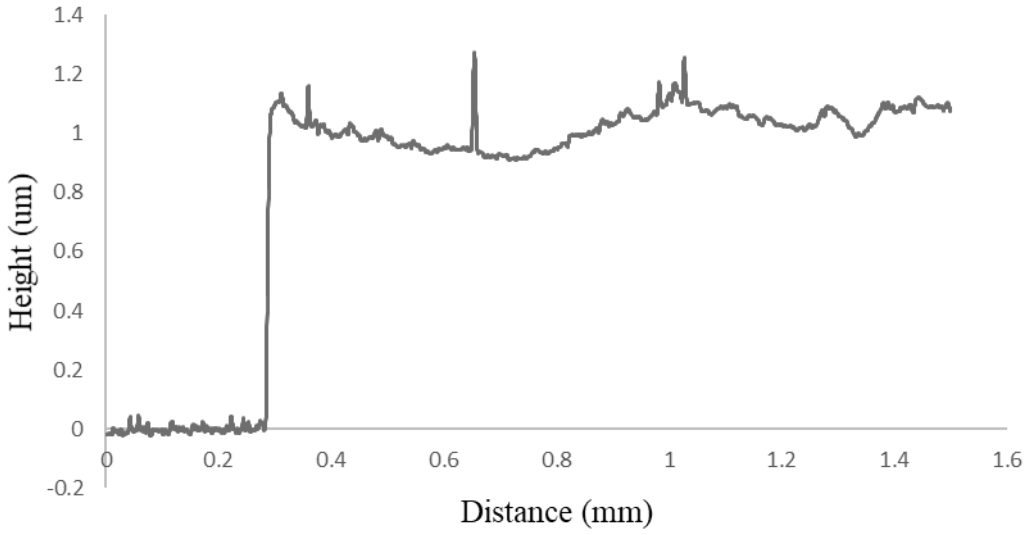

Figure 8.74 - Profilometry of ssDSC devices coated in 5:1 (ethanol:TiO_2) DSL18-NRT paste

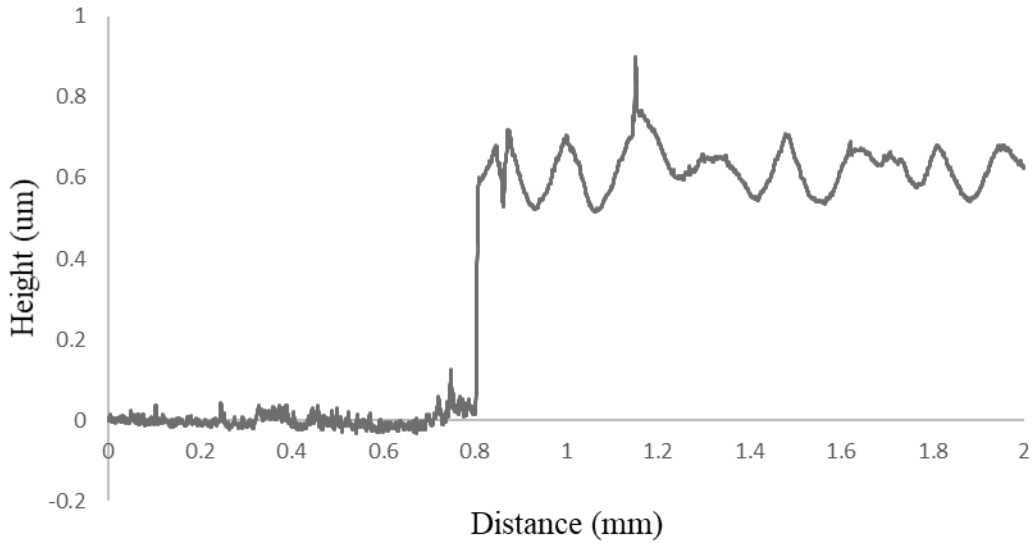

Figure 8.75 - Profilometry of ssDSC devices coated in 2:1 (ethanol:TiO_2) Ti-Nanoxide T/SP paste

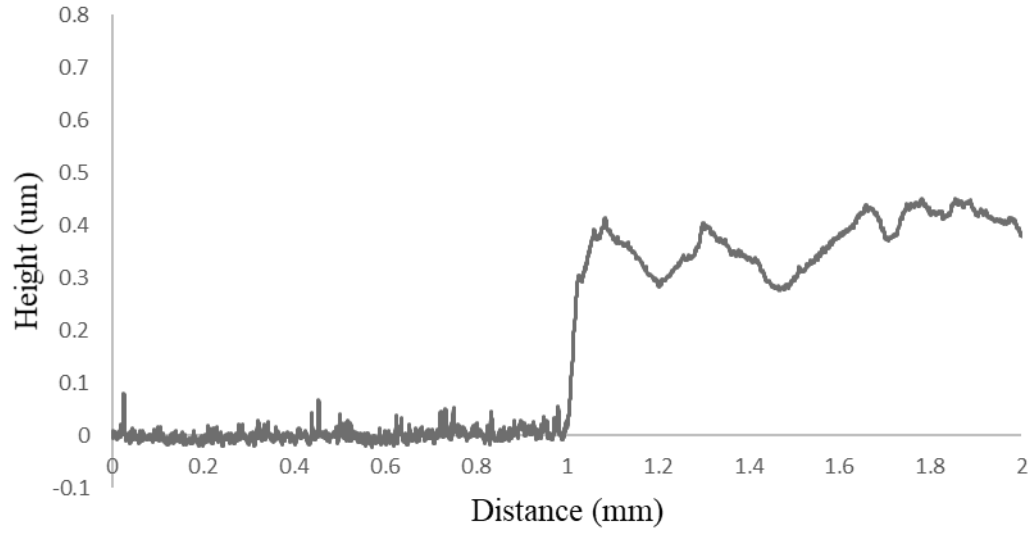

Figure 8.76 - Profilometry of ssDSC devices coated in 3:1 (ethanol:TiO_2) Ti-Nanoxide T/SP paste

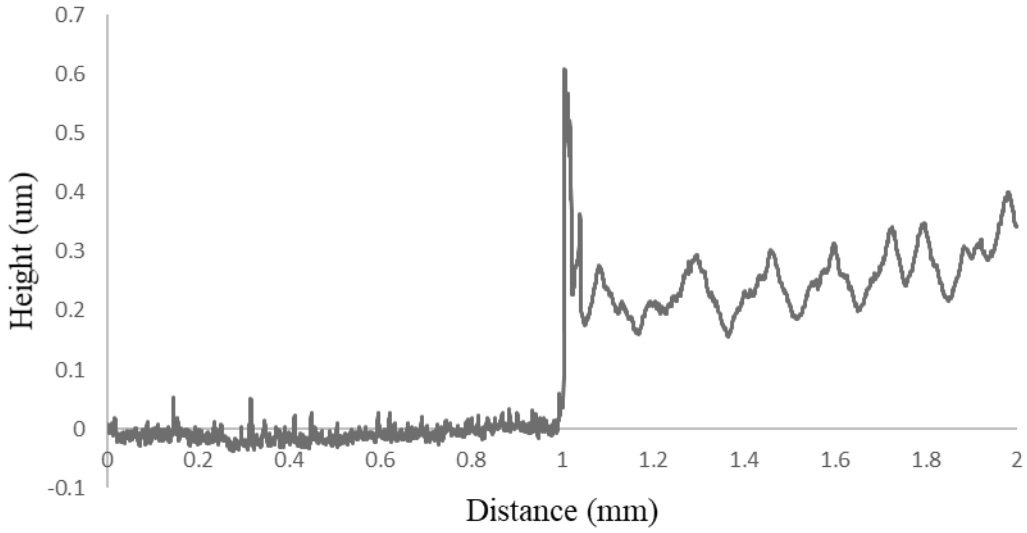

Figure 8.77 - Profilometry of ssDSC devices coated in 4:1 (ethanol:TiO_2) Ti-Nanoxide T/SP paste

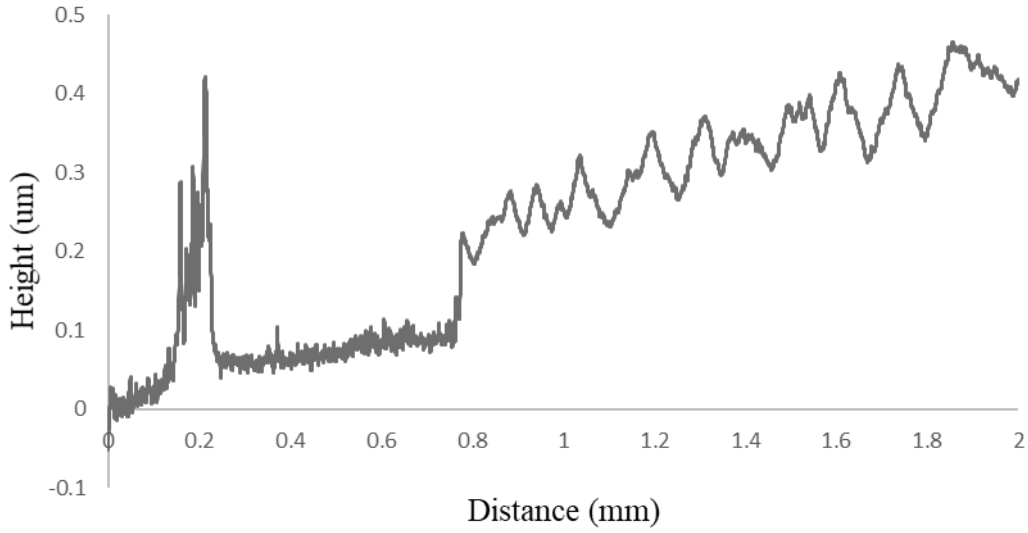

Figure 8.78 - Profilometry of ssDSC devices coated in 5:1 (ethanol:TiO_2) Ti-Nanoxide T/SP paste

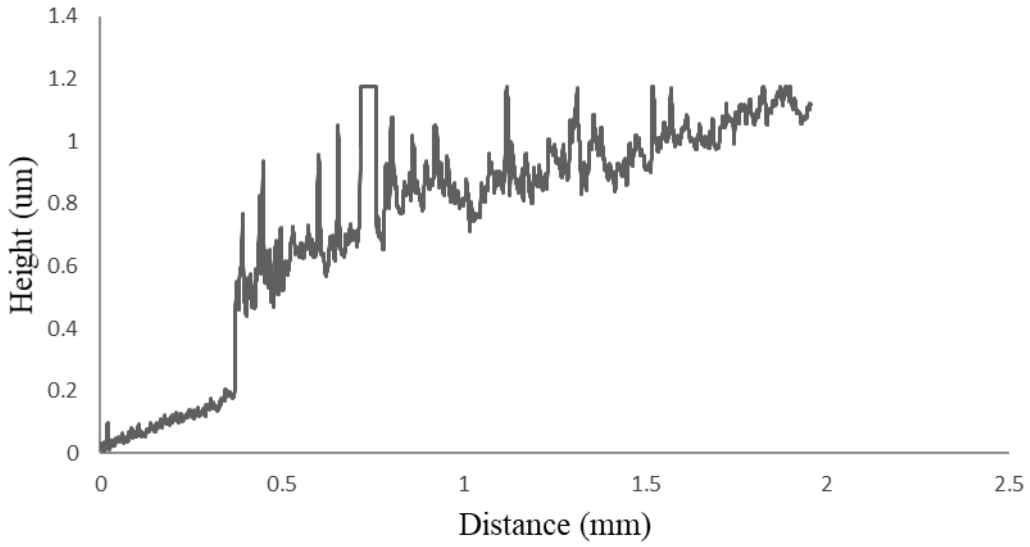

Figure 8.79 - Profilometry of ssDSC devices coated in 2:1 (ethanol:ZrO_2) Zr-Nanoxide T/SP paste

8.7 Dye injection measurements

Table 8.1 Preliminary electron injection kinetics of sHfSQ dyes synthesised in this chapter

Dye	tau1 (ps)	tau2(ps)	beta1 (ps)	beta2 (ps)
7	207	0	100	0
14	210	0	100	0
N719	319	1396	98.4	1.6
12	301	2294.1	95.4	4.6
17	159	894.9	95.3	4.7
8	200	1141.7	95.2	4.8
4	207	1271.3	95.1	4.9
11	290	1493.7	94.7	5.3
16	143	515.2	93.7	6.3
6	246	1290.2	93	7
15	106	289.5	88.2	11

[a]Sulphur containing dyes (orange), Non-sulphur containing dyes (blue), N719 standard (yellow)